Investigating electron transfer complexes using Single Molecule Force Spectroscopy

Guy Ewart Mayneord

A thesis submitted for the degree of Doctor of Philosophy at the University of Sheffield

The University of Sheffield

Faculty of Science

Department of Molecular Biology and Biotechnology

September 2019

Summary

Small diffusible redox proteins play a ubiquitous role in facilitating electron transfer (ET) in respiration and photosynthesis by shuttling electrons between large, relatively immobile membrane bound complexes. In order to sustain high ET turnover rates, the association between the cognate partners must be highly specific, yet also sufficiently weak to promote rapid post-ET separation and thus avoid 'product inhibition'. ET complexes have been investigated extensively using a variety of bulk phase structural and spectroscopic methods. While these ensemble studies have provided useful information on the general factors that facilitate efficient electron transport, the averaging involved obscures the heterogeneity inherent within the system.

In contrast, single molecule techniques allow distinct states within a heterogenous system to be accessed and through repeated observation robust statistics are acquired that provide new insights into stochastic processes. Single molecule force spectroscopy (SMFS), often performed by atomic force microscopy (AFM), has been used previously to interrogate the strength and specificity of a range of protein-protein interactions. In such experiments one protein is attached to the AFM probe and is scanned over a surface to which its binding partner is attached, and the force-distance curves measured at each point provide quantitative information on the interaction. However, classical SMFS is limited by the millisecond surface dwell times and low repetition rates which are unsuitable for investigating ET complexes which turnover on a microsecond timescale. Recently, the application of a faster AFM technique called PeakForce-quantitative nanomechanical mapping (PF-QNM) has allowed SMFS on rapid transient interactions to be investigated for the first time.

In this work, PF-QNM was applied to investigate the cytochrome b_6f : plastocyanin and photosystem I : plastocyanin ET complexes from spinach, and the RC-LH1 : cytochrome c_2 ET complex from *Rhodobacter sphaeroides*. The results provide new information on how the redox state of the participants in biological ET reactions determines their association and dissociation and allowed the forces involved to be quantified. Moreover, the work described identifies and resolves a number of commonly encountered issues with attaching ET complexes to inorganic surfaces and manipulating their stability and functional state.

Acknowledgements

First and foremost, I would like to thank my supervisor Dr Matthew P Johnson for his continued support, advice and patience over the last four years, and for the opportunity to work in his lab. No doubt he will even ask me to rewrite this section of my thesis because it 'doesn't sound right'. I would also like to thank Professor Neil Hunter and Dr Ashley Cadby for their guidance as my additional supervisors.

In relation to my work, I would like to thank Cvetelin Vasilev for his tutoring and guidance over these 4 years. My thanks also go to all the members of the Johnson and Hunter labs, in particular; Mo Brindley and Lizzy Martin for their patience with my lack of knowledge of recombinant genetics lingo, and for basically being an encyclopaedia of useful knowledge. To David Swainsbury for teaching me how to purify proteins when I started, and for teaching me too many random little things in the lab to count. To Tom Davies, for his guidance on working with liposomes and kindly donating some LHCII for experiments. To William Wood for repeatedly explaining how statistical tests work; I still don't understand a word of it. Of course, I would like to say thank you to everyone else in the Johnson and Hunter labs even if I haven't mentioned you by name.

For funding my research, I would like to thank Jeremy Grantham, for providing funding through the Sheffield Grantham Centre for Sustainable Futures.

My thanks go to my closest friends, Chris, Steve, Sean and Jack, for all the holidays and constant distractions over the past four years that likely kept me sane. I also thank my friends Ben, Prea, Reza, Alex, Christian and Denisa for the great movie nights, pub Fridays and just plain weird conversations. Most importantly, I would like to thank Oleksandra Korychenska for her love, care and support over the past few years, as well as her extensive knowledge of chemistry that ended up being invaluable to this work.

Last, but by no means least I would like to thank my parents, Susan and Roger Mayneord. Without your love, support and the upbringing you provided me, I would not have gotten this far.

Table of contents

List of figures

List of abbreviations

Å	Angstrom
AFM	Atomic Force Microscopy
Amine-NTA	Nα, Nα-Bis(carboxymethyl)-L-lysine
ATP/ADP	Adenosine triphosphate / Adenosine diphosphate
BChl	Bacteriochlorophyll
CEF	Cyclic electron flow
Cytb_6f	Cytochrome b_6f
Cyt bc_1	Cytochrome bc_1
Cyt c_2 / cyt c_2^{6His}	Cytochrome c_2 / Cytochrome c_2 + 6 x histidine tag
DMT	Derjaguin-Muller-Toporov
DOPC	1,2-dioleoyl-sn-glycero-3-phosphocholine
EDTA	Ethylenediaminetetraacetic acid
EM	Electron microscopy
ET	Electron transfer
Fd	Ferredoxin
FdC	Force-distance curve
FNR	Ferredoxin-$NADP^+$ reductase
FRET	Forster resonance energy transfer
His	Histidine

ICM	Intracytoplasmic membrane
ISP	Iron sulphur protein
LEF	Linear electron flow
LH2	Light harvesting 2
LHCI / LHCII	Light harvesting complex I / Light harvesting complex II
MQ	Milli-Q
NADPH	Nicotinamide adenine dinucleotide phosphate
OEC	Oxygen evolving complex
Pc	Plastocyanin
PF-QNM	PeakForce Quantitative Nanomechanical Mapping
P_i	Inorganic phosphate
PMF	Proton motive force
PQ / PQH_2	Plastoquinone / Plastoquinol
PSI	Photosystem I
PSII	Photosystem II
Rba. Sphaeroides	*Rhodobacter sphaeroides*
RC-LH1	Reaction centre-light harvesting 1 complex
RC^{12His}-LH1	RC-LH1 + 12x histidine tag
Rieske	Rieske iron sulphur

SATP	N-succinimidyl-S-acetylthiopropionate
SMCC	Succinimidyl trans-4-(maleimidylmethyl)cyclohexane-1-Carboxylate
$SM(PEG)_{24}$ / $SM(PEG)_{2k}$	PEGylated, long-chain SMCC crosslinker / Maleimide-PEG-NHS, MW 2000
SPM	Scanning probe microscopy
STM	Scanning tunnelling microscopy
UQ / UQH_2	Ubiquinone / Ubiquinol
X [Red] / X [Ox] / X [^{P}Ox]	Protein X is reduced / Oxidised / photo-oxidised

“All things are difficult before they are easy.”

- Dr. Thomas Fuller

“All we have to decide is what to do with the time that is given us.”

- J.R.R Tolkien, The Fellowship of the Ring

“You can’t always get what you want,

But if you try sometimes, well, you might find,

You get what you need”

- Keith Richards / Mick Jagger

1. General introduction

1.1 Photosynthesis

Photosynthesis is the mechanism by which light energy can be captured and stored, usually by molecular synthesis of carbohydrates, for use as cellular energy. Two distinct forms of photosynthetic light capture exist, usually classified as oxygenic and non-oxygenic for their ability to evolve molecular oxygen. Oxygenic photosynthesis occurs in cyanobacteria, algae and plants, whilst non-oxygenic photosynthesis occurs in purple bacteria, green- and non-sulphur bacteria, the heliobacteria and the acidobacteria. Both of these methods for photosynthesis involve the same initial stages of light capture by a chromophore, and funnelling of this energy to a reaction centre, whilst the extent of the downstream processing of energy has diverged significantly. Both will be briefly summarised below.

1.1.1 Oxygenic photosynthesis

Oxygenic photosynthesis can be performed by both prokaryotic and eukaryotic organisms. It is thought to have evolved over 3 billion years ago in cyanobacteria (Blankenship, 1992), followed by the first photosynthetic eukaryotes (around 1.5 billion years ago) which eventually evolved into land plants roughly 0.5 billion years ago (Mazor et al., 2015). The consensus has developed that oxygenic photosynthesis was transferred to eukaryotic organisms via endosymbiotic engulfment of a cyanobacterium. Following loss of most of the cellular functions, this cyanobacterium thus became the chloroplast, the organelle of oxygenic photosynthesis in plants and algae.

The reactions involved in oxygenic photosynthesis are often separated into two categories; the light reactions and the dark reactions (Miller and Burr, 1935). Although this may be an oversimplification, this separates the reactions involved into those that require light energy to drive them, and those that are independent of a light source, so long as the products from the light reactions remain. The sum of both reactions can be summarised using the single equation often seen for photosynthesis:

$$6H_2O + 6CO_2 \overset{Light}{\rightarrow} C_6H_{12}O_6 + 6O_2$$

showing the synthesis of complex carbohydrates and molecular oxygen from water and CO_2 and in doing so sequestering the light energy captured. Oxygenic photosynthesis may therefore be considered the reverse of respiration, in which water and CO_2 are generated from breaking down complex carbohydrates for energy. The division of oxygenic photosynthesis into the light and dark reactions arose from the observation that CO_2 is not required for the production of molecular oxygen while light is (Hill, 1937).

The light reactions in photosynthesis occur on or within the thylakoid membrane in the chloroplast and generate reduced Nicotinamide adenine dinucleotide phosphate (NADPH) and Adenosine triphosphate (ATP) via coupled photosynthetic electron transfer (ET). NADPH and ATP are utilised by the dark reactions in the stroma of the chloroplast to fix CO_2 into carbohydrates via the Calvin-Benson cycle (Bassham et al., 1950). The light reactions involved in oxygenic photosynthesis are described by the Z scheme of photosynthesis, which shows how the two light-driven reactions carried out by the chlorophyll proteins, Photosystem I (PSI) and Photosystem II (PSII), are connected by cytochrome b_6f leading to the reduction of $NADP^+$ via linear electron flow (LEF) (Hill and Bendall, 1960). A diagram of the redox potentials involved in this Z scheme can be seen in figure 1.1, along with the structures of the complexes involved in the thylakoid membrane.

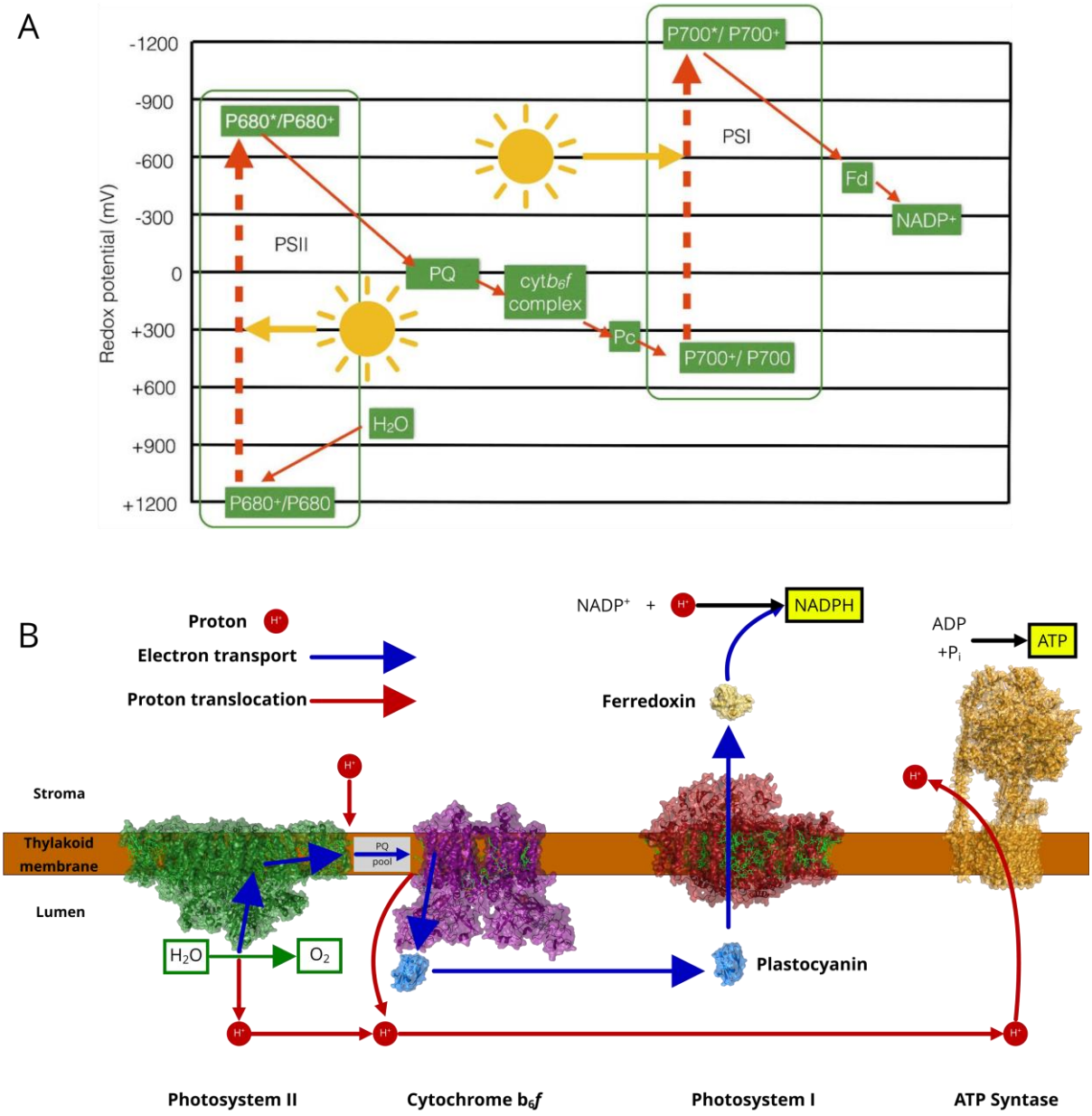

Figure 1.1 Z-Scheme components of oxygenic photosynthesis

*(**A**) The redox potentials shown for the components of the electron transport chain in the thylakoid membrane. Reprinted with permission of Portland Press from Johnson, 2016. (**B**) The components of the photosynthetic linear electron transport chain in the plant thylakoid membrane. PQ stands for plastoquinone. Light harvesting complexes are omitted. Structures used: **PSII**: 3JCU - (Wei et al., 2016), **PSI**: 4Y28 (Mazor et al., 2015), **B_6f**: 6RQF – (Malone et al., 2019), **ATP Synthase**: 6FKI - (Hahn et al., 2018), **Pc**: 1AG6 - (Xue et al., 1998), **Fd**: 1A70 - (Binda et al., 1998).*

In brief, PSII uses light energy (4 excitation events) to split 2 water molecules into 4 electrons, 4 protons and molecular oxygen (O_2). The protons are released into the thylakoid lumen and contribute to the proton motive force (PMF) across the membrane. The electrons are passed onto plastoquinone (PQ), a membrane soluble 2 electron carrier, and 2 protons are taken from the stromal side of the membrane to generate plastoquinol (PQH_2). Once PQH_2 reaches cytochrome b_6f (cytb_6f), these protons are released at the luminal side of the membrane, again contributing to the PMF. The electrons at cytb_6f go through a bifurcated path, with 1 electron undergoing the Q cycle (discussed in 1.1.2.4) to increase the number of protons translocated across the membrane per electron (Mitchell, 1975). The other electron is passed on from cytb_6f to plastocyanin (Pc), a soluble single electron carrier. Plastocyanin donates this electron to PSI which can, upon illumination, transfer this electron to Ferredoxin (Fd). In the final stages of LEF, Fd can bind to Ferredoxin-$NADP^+$ reductase (FNR), reducing $NADP^+$ to NADPH. The PMF which has been built up by several stages in this process is then utilised by ATP synthase to generate ATP from Adenosine diphosphate (ADP) and inorganic phosphate (P_i). The ratio of ATP to NADPH generated in this process is around 2.6 : 2. As the ratio of the two required by the dark reactions is 3 : 2, a method of making ATP, but no NADPH is employed to achieve this. This method is cyclic electron flow (CEF), in which electrons from Fd are recycled to PQ (Munekage et al., 2004; Nawrocki et al., 2019), in order for the electrons to continue to translocate protons across the membrane, but without generating NADPH. The internal electron transport pathways for each protein relevant to this thesis will be discussed below.

1.1.2 Components of the thylakoid linear electron transport chain

The protein complement of the thylakoid membrane is also shown in figure 1.1B. Omitted are the light capturing components of the light harvesting complex II (LHCII), which absorbs sunlight and transfers the resultant excitation energy towards reaction centres (PSI or PSII). The initial capture of light in all these complexes is performed primarily by chlorophyll, comprised of a porphyrin ring with a central magnesium ion and a phytol tail, generating a 24-member π-orbital delocalised electron field. Two forms of chlorophyll exist in higher plants, *a* and *b*, whose structures differ by the group attached to C7 on the porphyrin ring, giving slightly different spectral properties. In addition to the light capture performed by chlorophylls, some light capture is also performed by carotenoids. Energy transfer between these cofactors can occur via a nonradiative process called Forster resonance energy transfer (FRET) (Forster, 1948), requiring both short distances (due to the transfer efficiency being inversely proportional with the 6^{th} power of the distance) and overlap between the fluorescence emission spectrum of the donor and the absorbance spectrum of the acceptor (Blankenship, 2014), or

alternatively through the Dexter mechanism, which requires overlap of the molecular orbitals and involves rapid electron exchange between species. These energy transfer mechanisms facilitate the rapid transfer of energy from the light harvesting complexes to the reaction centres of PSI and PSII.

1.1.2.1 LHCII

LHCII is a heterotrimeric complex comprised of the proteins Lhcb1-3. Each monomer of the trimer contains 14 chlorophyll molecules, 8 chlorophyll a and 6 chlorophyll b, and are arranged in a circular geometry within the monomer to facilitate short transfer distances both within the LHCII trimer and to neighbouring complexes (Liu et al., 2004).

1.1.2.2 Photosystem II

Photosystem II has the biologically unique capacity to oxidise water utilising light energy. The type II (Q-Type) reaction centre uses light energy to generate the redox potential required for the Oxygen evolving complex (OEC). The OEC in PSII is the only known biological reaction capable of splitting water into protons, electrons and forming molecular oxygen which is evolved. These electrons are passed to the soluble electron carrier PQ. Whilst this H_2O – PQ oxidoreduction involves a contribution to the PMF, no actual protons are translocated across the thylakoid membrane at this stage. Instead, protons from splitting water are released into the luminal side, and protons for the reduction of PQ are taken from the stromal side, leading to a net change of 2 protons per H_2O oxidised (Reviewed in McEvoy and Brudvig, 2006). This work of PSII can be summarised as:

$$2H_2O + 2\,PQ + 4H^+_{stroma} \overset{Light}{\rightarrow} O_2 + 4H^+_{lumen} + 2\,\mathrm{PQ}H_2$$

generating 2 molecules of plastoquinol (PQH_2) that can subsequently migrate through the thylakoid membrane to cytb_6f.

1.1.2.3 Plastoquinone

The 2 electrons received from PSII are used to reduce 2 carbons on PQ, and this is stabilised by proton uptake from the stroma to generate two hydroxyl groups (figure 1.2) Following this, the newly generated PQH_2 at the Q_B site in PSII is exchanged for PQ from the membrane pool. At cytb_6f the protons are subsequently released into the thylakoid lumen, contributing to the PMF.

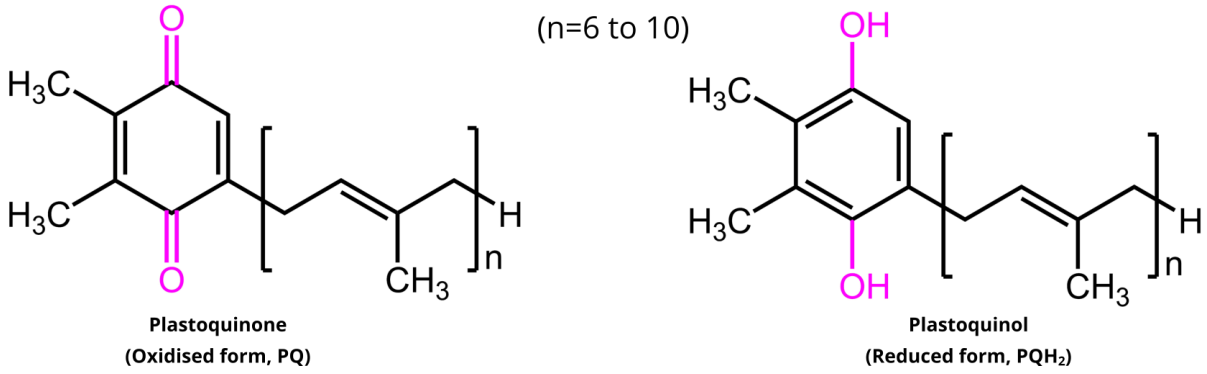

Figure 1.2 Plastoquinone and plastoquinol

Structures for the oxidised form (PQ) and reduced form (PQH_2) of plastoquinone. The change from a ketone to a hydroxyl group upon reduction is shown in pink. The length of the tail (n) can vary between organisms.

1.1.2.4 Cytochrome *b_6f*

The cyt*b_6f* complex is a homodimeric membrane protein complex, with each monomer comprised of 4 large subunits; cytochrome *f*, cytochrome b_6, Rieske iron-sulphur (Rieske) protein, subunit IV, and 4 additional smaller subunits (PetG, M, N and L). The structure of cyt*b_6f* can be seen in figure 1.3, with cyt *f* shown in green, the Rieske protein shown in blue, and the other subunits shown in purple. Its redox active cofactors are 2 *b*-type haems (housed in the cyt *b_6* subunit), two *c*-type haems (in the cyt *f* subunit and cyt *b_6* subunits) and an iron sulphur cluster (2Fe-2S, housed in the Rieske protein, figure 1.3B). High resolution structural work (Kurisu et al., 2003; Stroebel et al., 2003; Malone et al., 2019) also shows non redox active cofactors of two *9-cis β*-carotenes, two chlorophyll *a* molecules and twelve bound lipids. Acting as a PQH_2 - Pc oxidoreductase, the two electrons on PQH_2 undergo a bifurcated path (known as the Q cycle) at the Q_p site, down either a high or low potential chain shown in figure 1.3B. The high potential chain (2Fe-2S, haem *f,* shown in blue arrows) ends at plastocyanin, and the low potential chain (haem b_p, b_n and c_n, shown in purple arrows) terminates at the Q_n site to reduce another PQ. This Q cycle effectively doubles the number of protons translocated across the membrane per electron through the system (Mitchell, 1975; Tikhonov, 2014). The transfer along the high potential chain involves the movement of the Rieske protein from the Q_p site to haem *f* in order to transfer the electron. The general themes of ET binding interfaces employed by cytb_6f for Pc will be discussed later in terms of general electron transfer binding interfaces (section 1.2.2) and in specific detail in section 4.2.

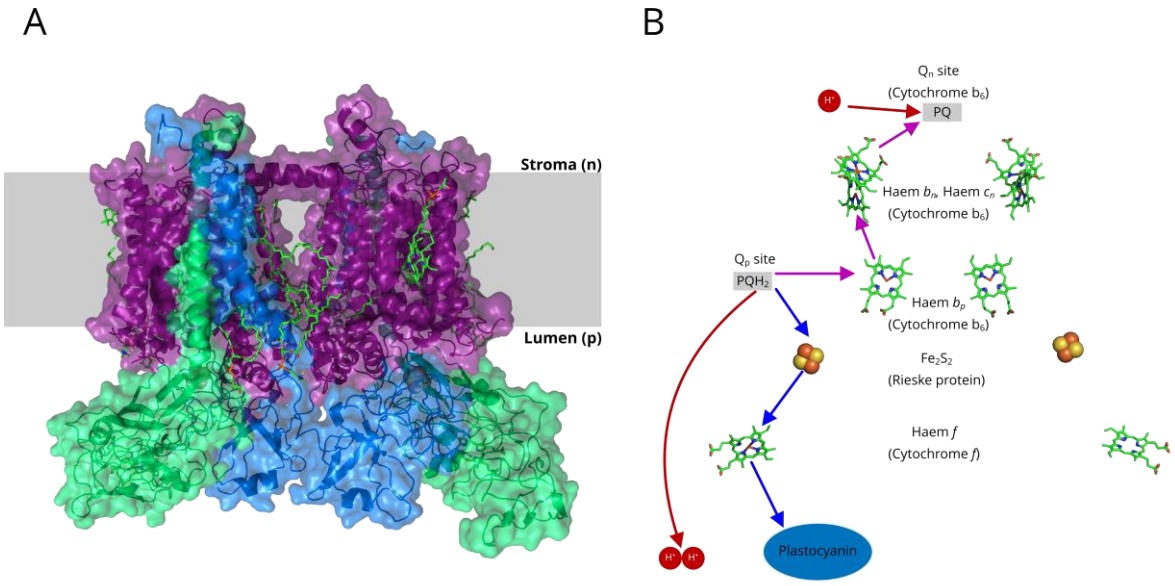

***Figure 1.3 Cytochrome b_6f* structure**

*(**A**) Translucent structure and underlying cartoon structure of the spinach cytb_6f attained from Cryo-EM in our lab by L.Malone (Malone et al., 2019). Cytochrome f is shown in green, Rieske protein in blue and the remaining subunits in purple. (**B**) Cofactors in the structure of cytb_6f that are redox active. Names of cofactors are given, along with the subunits to which they are bound in parenthesis. The low potential path for an electron is shown in purple, undergoing the Q cycle. The high potential electron path is shown in blue and donates to plastocyanin.*

1.1.2.5 Plastocyanin

Pc is the 10.5kDa soluble electron carrier between cytb_6f and PSI in the thylakoid lumen. The structure is comprised of an antiparallel β-barrel, which houses a single copper ion, capable of changing oxidation state between +1 and +2 to facilitate electron transport. The coordination of this copper ion is by two histidines, a cysteine and a methionine residue in the structure, shown in figure 1.4. The overall structure of the protein shows an isoelectric point of 3.82 (Sigfridsson et al., 1996), resulting in a net negative charge. The binding interfaces for cytb_6f and PSI will be discussed in depth in their respective chapters (section 4.2 and 5.2).

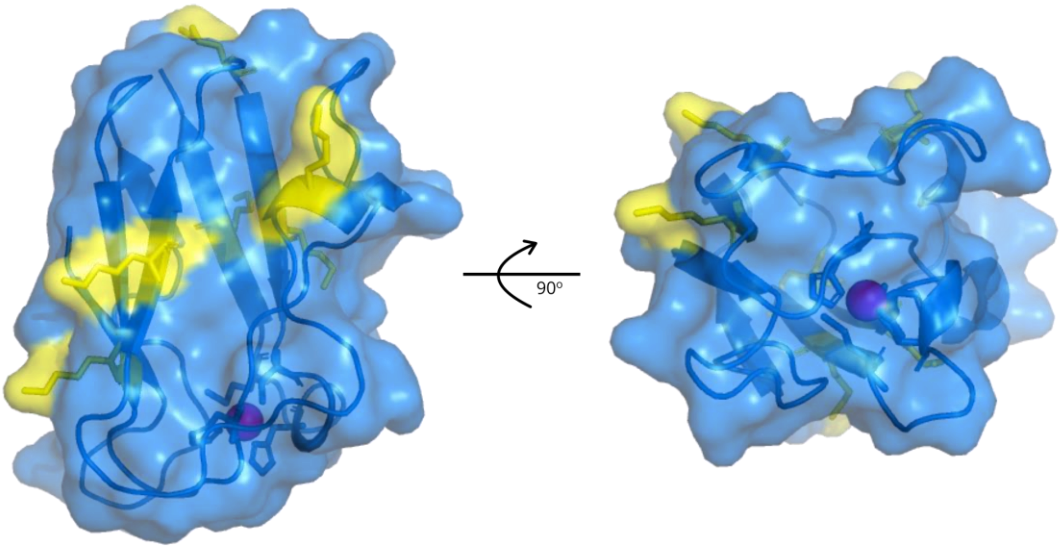

Figure 1.4 Structure of Plastocyanin

Cartoon diagram with translucent surface overlaid showing the structure of spinach Pc from two different angles. Residues involved in coordination of the copper cofactor are shown as sticks in blue. Lysine residues used for immobilisation (discussed in chapter 3) are shown in the structure as sticks in yellow, and the copper cofactor as a purple sphere. PDB: 1AG6 - (Xue et al., 1998).

1.1.2.6 Photosystem I

PSI acts as a light driven Pc – Fd oxidoreductase. It is comprised of 16 subunits, which coordinate 192 light harvesting pigments (Mazor et al., 2017). This can be seen in figure 1.5A, with the light harvesting LHCI ring shown in various green colours and the central PSI core in red. It houses a type I (FeS-type) reaction centre, which can convert light energy to a reducing potential seen in figure 1.5C. Upon activation by light, the P700* (excited) will reduce one of the nearby chlorophyll A molecules (figure 1.5B and C). Due to the close nature of the heterodimeric complex, the electron can be transferred to either side of the path shown in figure 1.5B. Both paths converge on the F_X iron-sulphur cluster located in the PsaC subunit. The electron can then be passed through PsaC via the F_X, F_A and F_B iron-sulphur clusters, before being transferred to the iron-sulphur cluster of Fd on the stromal side of the membrane. Figure 1.5C also shows the process of charge recombination (electron transfer from the cofactors back to $P700^+$, shown as dotted lines) that can occur from the cofactors. This process is slow compared to the forward electron transfer rates, meaning so long as an electron acceptor is available

from F_A/F_B, this is essentially negligible. The $P700^+$ is subsequently reduced by Pc docking at the luminal side of the complex. The specific binding interface with Pc will be discussed later (section 5.2).

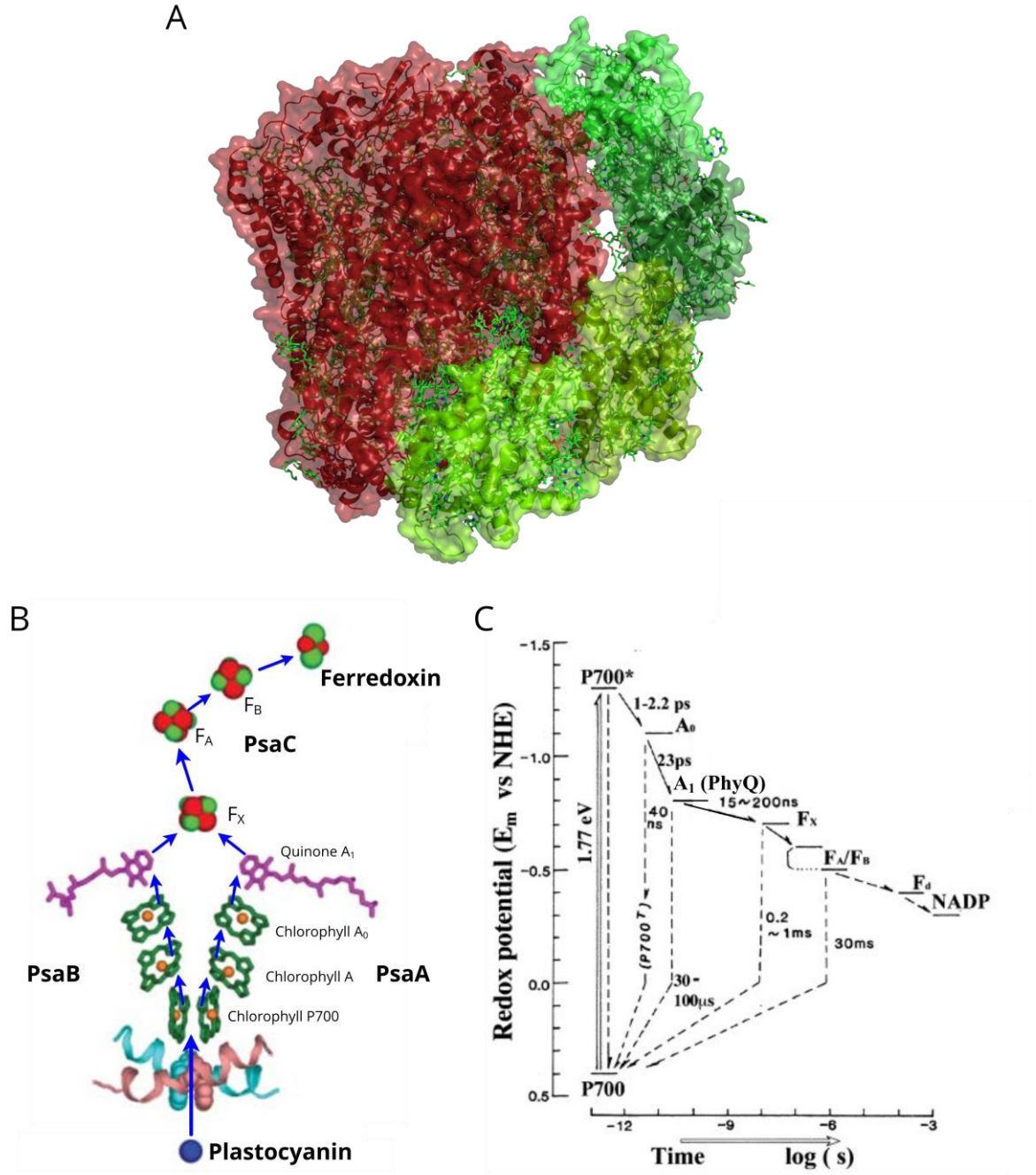

Figure 1.5 Photosystem I structure

*(**A**) PSI supercomplex of PSI – LHCI with LHCI components shown in different greens, and the core PSI structure shown in red. (**B**) Internal electron transfer pathway for PSI. The cyan/pink chains between Pc and the P700 chlorophyll are tyrosine residues involved in plastocyanin docking. Protein names are given in bold, and cofactor classifications in standard text. Reprinted with permission of Annual Reviews Inc. from Nelson and Yocum, 2006. (**C**) Energy diagram showing the redox potential of the*

chemical species in the reaction centre, and the times required for the electron transfers both forward and backward. Transfer from P700 to chlorophyll A has been too fast to measure, so the transfer to chlorophyll A_0 is shown. Reprinted with permission from BBA – Bioenergetics from Itoh et al., 2001.*

1.1.2.7 Ferredoxin

Like plastocyanin, Fd is a 10.5kDa protein capable of carrying electrons between redox partners, this time in an 2Fe-2S cofactor. It interacts with the PsaD and E subunits (Kuhlgert et al., 2012) on the stromal side of PSI to oxidise F_A/F_B (ET from either is feasible).

1.1.2.8 ATP synthase

ATP synthase is nearly ubiquitous in energy transducing membranes. It utilises the PMF across the thylakoid membrane as a source of energy to generate ATP from ADP and P_i. The complex has two distinct domains, F_0 and F_1. The F_0 domain contains 14 c subunits in thylakoid ATP synthase (Hahn et al., 2018), although this number can vary depending on the organism and even the organelle. The ATP synthase utilises the PMF through these c subunits to rotate these two domains relative to one another, producing 3 ATP per 360° rotation. As such the number of c subunits is reflective of a gearing mechanism with a higher number of c subunits reflecting a lower capacity of the available PMF to do work.

1.1.3 Non-Oxygenic photosynthesis

Rather than oxygenic photosynthesis, some bacteria such as purple-, green- and non-sulphur bacteria, heliobacteria and the acidobacteria perform photosynthesis by a process which does not evolve molecular oxygen and is therefore known as non-oxygenic photosynthesis. The evolution of non-oxygenic photosynthetic bacteria predates the evolution of oxygenic photosynthesis.

1.1.3.1 *Rhodobacter sphaeroides*

Rhodobacter sphaeroides (*Rba. Sphaeroides*) is a gram-negative purple non-sulphur bacterium. Akin to chloroplast in higher plants and algae, their photosynthetic machinery is housed in specific pseudo-organelles (Chandler et al., 2008), here called chromatophores, shown in figure 1.6.

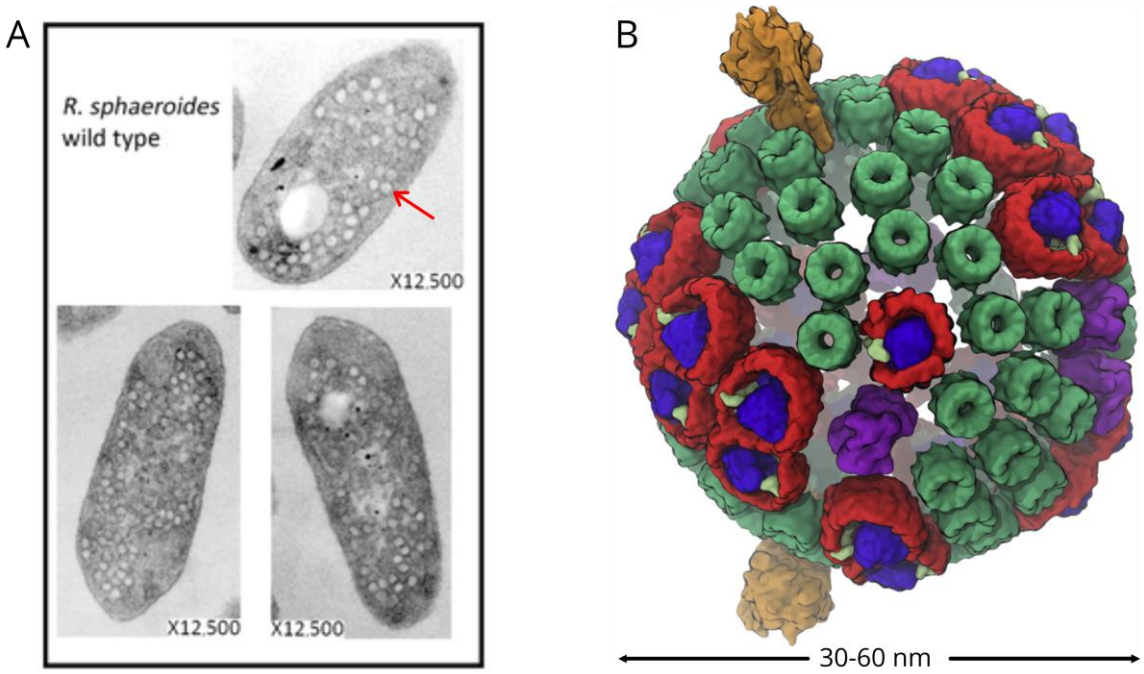

Figure 1.6 Rhodobacter sphaeroides and the chromatophore

*(**A**) Rba.sphaeroides cells under light microscopy. The red arrow indicates an example of the chromatophores seen in (B). Reprinted with permission from Springer, from Fedotova and Zeilstra-Ryalls, 2014. (**B**) Rendering of the chromatophore in Rba.sphaeroides, reprinted with permission from BBA – Bioenergetics, taken from Cartron et al., 2014.*

Under a light microscope, the chromatophores are visible in *Rba.sphaeroides* as white circles (red arrow, figure 1.6A). These are the functional units for photosynthesis, and contain the entire machinery required, from the initial capture of light to the generation of ATP from ADP and P_i. These small intracytoplasmic vesicles are formed from budding off from the cytoplasmic membrane and their size can vary from 30-60 nm depending on growth conditions. *Rba.sphaeroides* can grow heterotrophically, photoheterotrophically and photoautotrophically and produce the chromatophores under all these conditions (Cohen-Bazire et al., 1957), allowing the recombinant generation of deleterious mutations in the photosynthetic machinery.

1.1.4 Components of the chromatophore

The protein complement of the chromatophore can be seen in figure 1.8, with light harvesting II (LH2) omitted for simplicity. In brief, light energy is captured by bacteriochlorophyll (Bchl) *a* (shown in figure 1.7) in either LH2, or the LH1 ring of the Reaction centre – LH1 (RC-LH1) complex. The minor differences from chlorophyll *a* from oxygenic photosynthesis are in the porphyrin ring (figure 1.7),

with a reduced degree of conjugation in the macrocycle and the symmetry of the molecule leading to spectral changes.

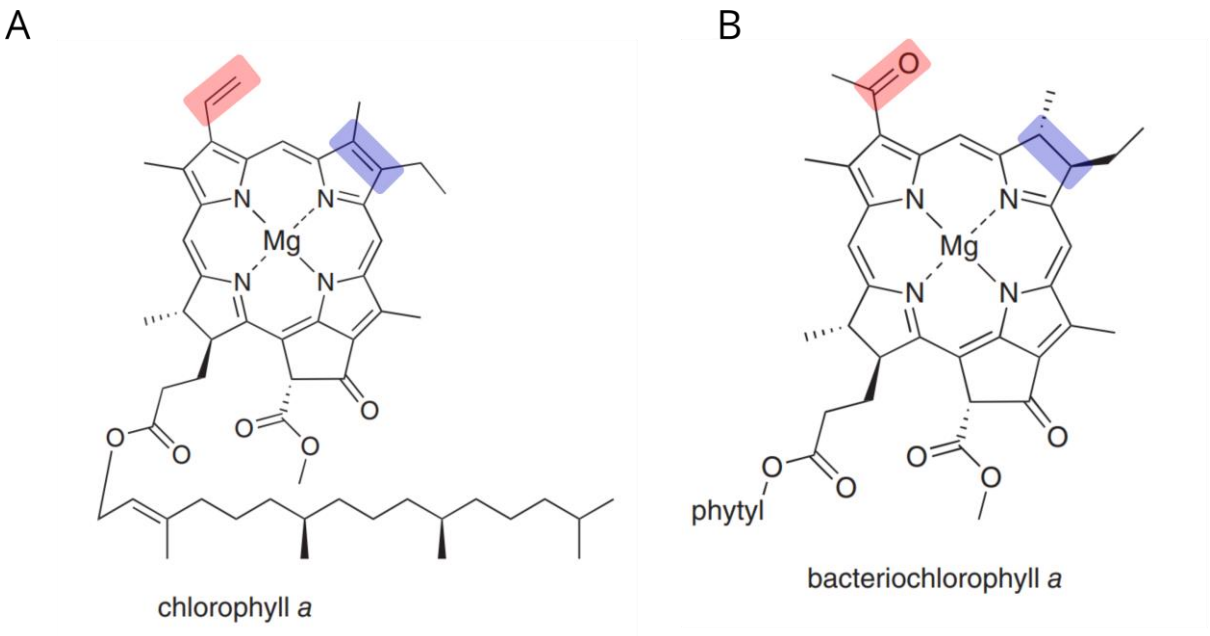

Figure 1.7 Chlorophyll a and bacteriochlorophyll a

*Structures of (**A**) chlorophyll a and (**B**) bacteriochlorophyll a, with the chemical differences highlighted. In red the acetyl group present in bacteriochlorophyll a, but not chlorophyll a is shown at position C-3. In addition, the double bond present between C-7 and C-8 in chlorophyll a, but not bacteriochlorophyll a is shown in blue. The phytyl tail is the structurally the same in both, but is shown in chlorophyll a, and abbreviated in bacteriochlorophyll a. Reprinted with permission from Wiley, from Blankenship, 2014.*

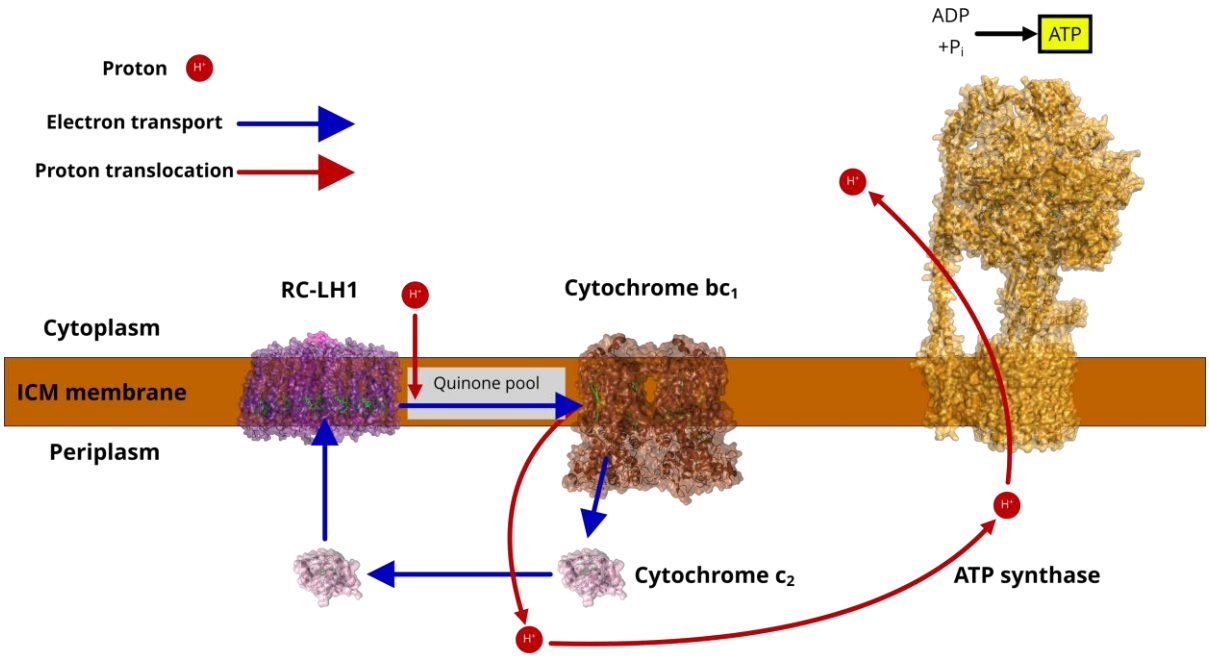

Figure 1.8 Protein complement of the chromatophore

Diagram showing the cyclic electron flow occurring in the chromatophore of Rba.sphaeroides. LH2 is omitted for simplicity. Blue arrows indicate electron transfers and red arrows the proton movement. Structures used: ***RC-LH1****: 4V9G - (Qian et al., 2013),* ***Cyt bc$_1$****: 2QJP - (Esser et al., 2008),* ***Cyt c$_2$****: 1L9J - (Axelrod et al., 2002),* ***ATP Synthase****: 6FKI - (Hahn et al., 2018).*

Following this the excitation is passed to the type 2 (Q-type) reaction centre of the RC-LH1, wherein charge separation occurs and the electron is passed to a mobile ubiquinone (UQ) molecule in the intracytoplasmic membrane (ICM). The primary donor of the RC ($P870^+$) is then reduced by an electron from the soluble electron carrier cytochrome c_2 (cyt c_2). A second light-driven charge separation leads to a second reduction of the UQ, which can then take up 2 protons from the cytoplasm forming a ubiquinol (UQH_2). The UQH_2 molecule diffuses through the membrane, and donates these electrons to the cytb_6f analogue, cytochrome bc_1 (cytbc_1). Following oxidation of UQH_2 by cytbc_1 the two electrons bifurcate, with one recycled to UQ via the Q-cycle, while the second is used to reduce cyt c_2, which can subsequently donate the electron back to RC-LH1, completing the cyclic electron flow. The protons released to the periplasm during UQH_2 oxidation at cyt bc_1 form a PMF which is utilised by ATP synthase to make ATP.

1.1.4.1 Light harvesting II complex

As with oxygenic photosynthesis, if light capture only relied on reaction centres, it would be remarkably inefficient. Instead, just as LHCII acts as an energy funnel to PSII and PSI, in *Rba. Sphaeroides* LH2 can absorb light via bacteriochlorophylls, and funnel this to RC-LH1.

1.1.4.2 Reaction-centre light harvesting I complex

Just as in oxygenic photosynthesis, the initial stable capture of light energy is performed in the reaction centres. The dimeric form of the RC-LH1 complex is shown in figure 1.9A and is comprised of the reaction centre ('Core complex'), shown in pink, and the LH1 ring shown in purple. The core complex is comprised of 3 parts, a heterodimer of L and M subunits, and the H subunit with a single transmembrane region, protruding out the cytoplasmic side of the membrane, thought to act as an effective insulator for loss of electrons from the cofactors in L and M (Moser et al., 1995). This central heterodimer forms a scaffold that encases the 10 cofactors involved in the reaction centre, shown in figure 1.9B. Figure 1.9C shows the redox potentials of all the species in the RC-LH1 reaction centre, and the times for electron transfer between them. As with PSI, the times for the charge recombination's events are also shown in dotted lines, however once again if an electron acceptor is available at the Q_B site these can be considered negligible events. The reaction centre commonly forms dimeric complex under higher light growth conditions in order to facilitate more efficient light capture. This dimerization is dependent on the protein PufX (Francia et al., 1999), and allows captured light energy in the LH1 ring to be transferred to either reaction centre in the dimer quickly. Once the light energy reaches the reaction centre, the special pair of Bchl 870 (P870) undergo charge separation, and akin to the reaction centre of PSII, this electron takes a single pathway along cofactors in the heterodimeric centre (through the L subunit, not the M subunit, shown in figure 1.9B). This pathway terminates at the mobile quinone site (Q_B), where again 2 electrons are required to generate a UQH_2 from UQ, and 2 protons are taken up from the cytoplasm. Following this, the quinone can diffuse through the membrane to cyt bc_1.

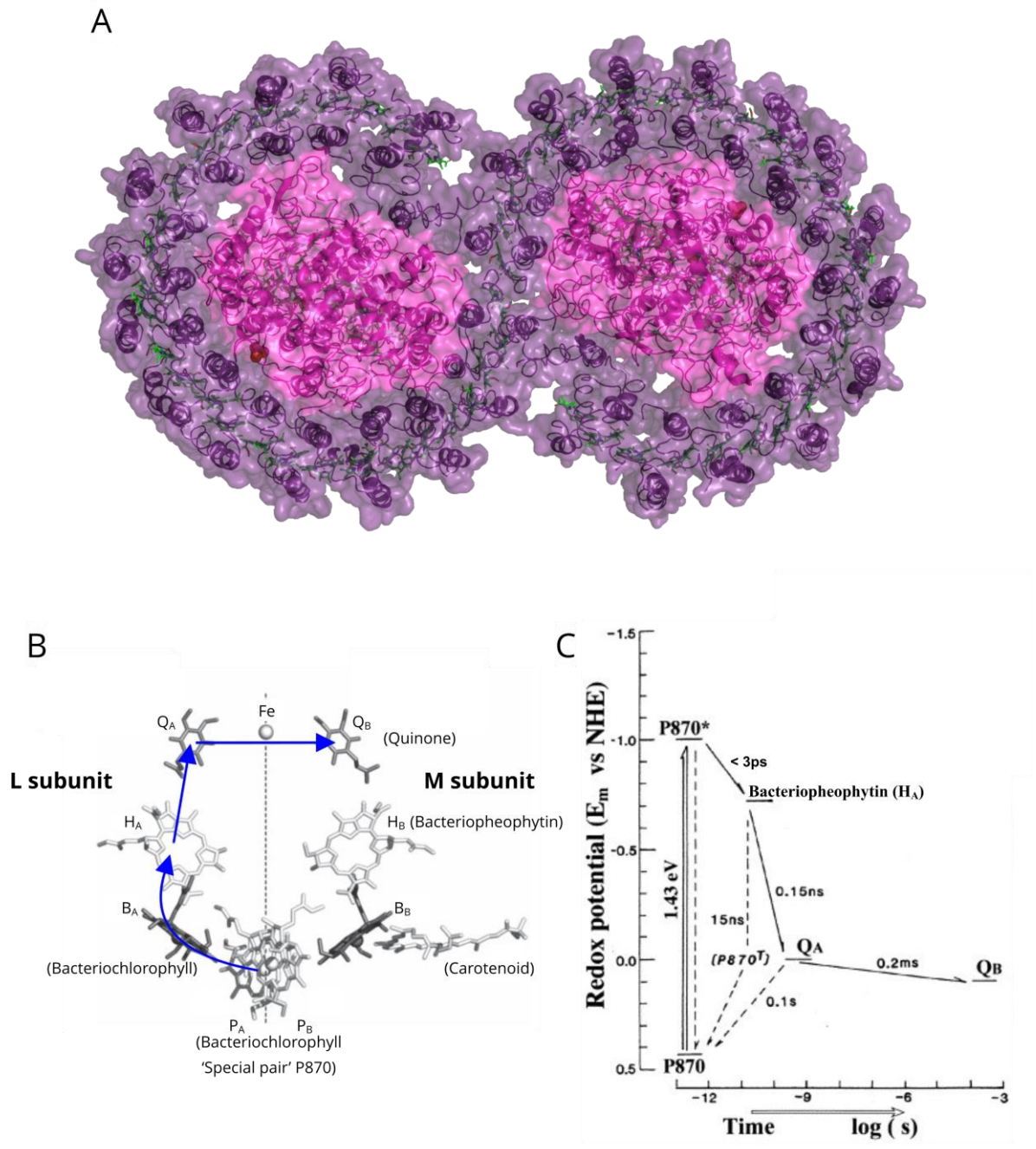

Figure 1.9 RC-LH1 structure and reaction centre

*(**A**) Structure of the RC-LH1 dimer from Rba.sphaeroides. The translucent surface has the cartoon structure visible underneath. The central reaction centre is shown in pink, and the LH1 ring shown in purple. PDB – 4V9G (Qian et al., 2013). (**B**) Reaction centre cofactors of the RC-LH1 complex, with the cofactors indicated in standard text, the protein subunits in bold text and the electron pathway shown in blue arrows. The cofactor groups are given in brackets. Reprinted with permission from Springer, edited from Hunter et al., 2008. (**C**) Redox potentials for the electron transfers involved in the initial stages of light capture in the reaction centre of RC-LH1, plotted against time for electron transfer*

events. Times for the transfers of electrons are shown at each stage, both forward and backwards, with charge recombination events being shown in dotted lines. Reprinted with permission from BBA – Bioenergetics from Itoh et al., 2001.

1.1.4.3 Ubiquinone

Similar to plastoquinone in oxygenic photosynthesis (1.1.2.3), UQ is a small membrane soluble two electron carrier (figure 1.10). It receives 2 electrons from RC-LH1 and takes up two protons from the cytoplasmic side of the membrane. Following docking with cyt bc_1 these protons are released into the periplasm of the chromatophore, contributing to the PMF.

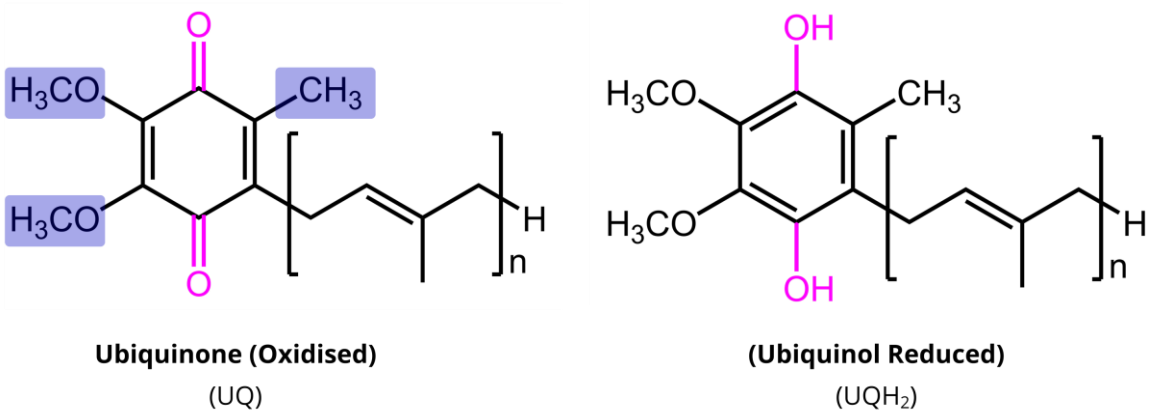

Figure 1.10 Ubiquinone structure

Structure of the oxidised and reduced UQ. The differences from plastoquinone are highlighted in blue on the oxidised form. Groups changing under reduction are shown in pink.

1.1.4.4 Cytochrome *bc₁*

Cytbc_1 is analogous to the cytb_6f seen in oxygenic photosynthesis (Esser et al., 2008). As such, it can be thought of as a UQH_2 - cyt c_2 oxidoreductase. The internal electron transfers are again analogous to that seen in cytb_6f, in which the iron sulphur cluster in the Rieske iron-sulphur protein (ISP) takes one electron from the UQH_2 along a high potential path, whilst the other electron undergoes the low potential path to a haem on cyt *b*. This involves the release of two protons on the periplasmic side of the membrane contributing to the PMF. The electron on the iron sulphur cluster is moved to the haem of the cyt c_1 subunit, and subsequently gets transferred to the haem on cyt c_2. The electron on the haem in the *b* subunit undergoes the Q cycle (as discussed in 1.1.2.4), reducing a second UQ to increase the number of protons translocated per electron (Mitchell, 1975).

1.1.4.5 Cytochrome c_2

Cyt c_2 shuttles electrons between cyt bc_1 and RC-LH1 in the periplasm of the chromatophore. It carries a single electron in the bound *c*-type haem cofactor, facilitated by the central iron atom which can change oxidation state. This iron is coordinated by the Sulphur atom on a methionine residue and the imidazole of a histidine (Axelrod et al., 1994), shown in figure 1.11.

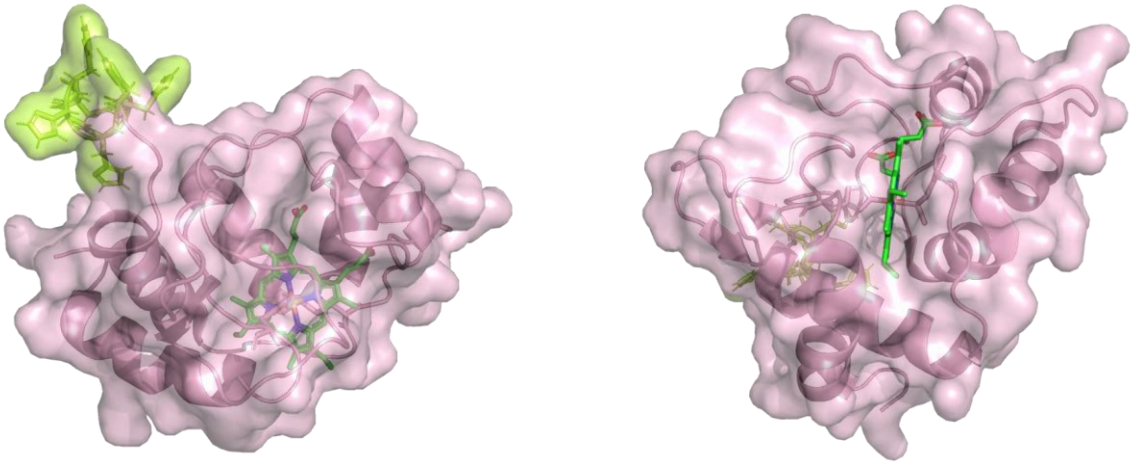

Figure 1.11 Cytochrome c_2 structure

Structure of cyt c_2 from Rba.sphaeroides from two different views. The two residues coordinating the central iron of the c-type haem are shown as sticks in pink. The location of the hexa-histidine tag used in the work presented in this thesis (Chapter 6) is shown in the structure as lime sticks. PDB 1L9J (Axelrod et al., 2002).

1.1.4.6 ATP synthase

ATP synthase is a relatively conserved protein across energy transducing membranes. The main difference often observed is the number of c subunits in the F_0 region, with only 12 in *Rba.sphaeroides* ATP synthase (Feniouk et al., 1999), slightly less than the 14 seen for thylakoid ATP synthase from spinach.

1.2 Electron transfer in proteins

A central theme becomes apparent in these photosynthetic apparatuses; that electrons are being carried between membrane bound complexes with limited mobility, by soluble, highly mobile electron carriers. This is not only true of photosynthetic membranes, but is a general rule for energy transducing membranes, including those for involved in respiration. Whilst a continuous network would be far more efficient for simple electron passage, with all transfers progressing according to first order kinetics, evolution has chosen modular systems between which electrons are shuttled to allow for adaptability to different conditions. Highly specific electron transporting proteins with their transition state metal cofactors are thus required to allow this modularity, and facilitate electron passage between complexes.

1.2.1 Electron transfers

When transferring single electrons, the energy required to reorganise the molecular environment (λ) around which the cofactor that accepts an electron resides is an important consideration. These transfers follow the kinetic regime of Marcus kinetics (Marcus, 1956), which take into account this reorganisation energy, along with the free energy release (ΔG), and the distance (R) between the donor and acceptor. Plotting the rate vs the free energy of a reaction based on Marcus kinetics finds a parabolic relationship, showing the balance between free energy and reorganisation energy. The optimum condition between these two factors is when the free energy release is equal to this reorganisation energy. When it is not, the rate will reside on either side of the parabola and become less efficient with a larger difference. A simplification of the kinetics has previously been done for room temperature:

$$\log k_{et} = 15 - 0.6R - 3.1(\Delta G + \lambda)^2 / \lambda$$

in Moser et al., 1995, where k_{et} is the rate of electron transfer.

The high dependency of electron transfer rate on distance between the two cofactors involved brings into question how electron transporting proteins efficiently receive and donate electrons with their cognate membrane bound partners. It would be expected that evolution would have finely tuned the environments of both cofactor participants in order to facilitate the fastest transfer rates. In contrast to this, electron transfer rates often appear to be quite inefficient between complexes. The reason for this is likely to do with the process by which proteins can evolve. The process of evolution, acting through insertion, deletion and mutation of residues at single locations, creates a long progression of improvement. The environment in which these cofactors are exposed to comprises of many amino acids in the surrounding structures. As such, minor changes in the amino acids are unlikely to have any

large effect in the electron transport time, relative to the other processes occurring, such as docking. With no real selection pressure, nature would only change the environment of the cofactors if these became rate limiting. As such, the large variances seen in ET times in different organisms (1µs in Rba.sphaeroides RC-LH1 : cyt c_2, to 70-130µs in cytb_6f : Pc) likely shows that the ET times are of little consequence to the proteins interaction overall, and little effect can be made to improve these without first compromising the structure of the complex (Moser et al., 1995).

1.2.2 Electron transferring binding interfaces

While the prior section addressed the kinetics of direct ET from one redox active cofactor to another in a completely bound complex, this usually represents the fastest stage in the process. Prior to this, the two cognate binding partners must be able to form the fully bound ET complex. This binding in ET complexes must meet some rather unique requirements. They must have great specificity in their binding interfaces, and come together with high affinity, yet also dissociate quickly once electron transfer has occurred in order to avoid product inhibition.

Observing an array of ET complexes, the initial feature of these complexes that becomes apparent is the smaller binding interface. Typical protein – protein interfaces will occupy ca. 1600 ± 400 Å^2 (Conte et al., 1999), whilst the typical ET complex interface occupies an average of ca. 1000 Å^2 (Nyola and Hunte, 2008; Singharoy et al., 2016; Solmaz and Hunte, 2008). In addition to this, the binding sites appear to always be comprised of two distinct regions; a uniformly charged electrostatic region and a central hydrophobic region surrounding the redox active cofactors as seen in figure 1.12. The latter of these is obvious when considering how the efficiency of electron transfer is affected by the environment, hence the generation of a hydrophobic domain excluding water molecules agrees with the expectation for electron transferring complexes. The electrostatic interactions however have found intervening water molecules when in the bound state, hence these complementary electrostatic regions are not forming specific salt bridges between oppositely charged residues on the cognate proteins but essentially forming a region of delocalised charge. This delocalised charge is also reflected in mutation studies of ET complexes, where the introduction of an additional charge near the existing region increases affinity (Hope, 2000; Illerhaus et al., 2000; Tetreault et al., 2001). It is accepted that the electrostatic regions act as long-range guides for the two proteins, whilst the hydrophobic regions act at the shorter range (Hope, 2000).

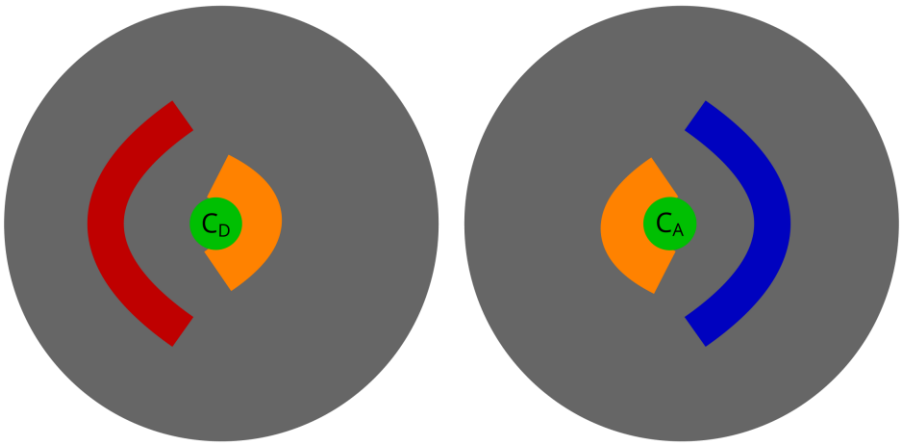

Figure 1.12 General schematic for binding interfaces

Open book view of schematic binding interfaces for the interaction between ET proteins. General protein region in grey, complementary charges are shown in blue and red, hydrophobic region in orange and the cofactors for donor and acceptor ($C_{D/A}$) in green.

Figure 1.13A shows the 3 different kinetic schematics for understanding the interaction between the two partners apparent in any electron transfer system, originally from Hervás et al., 1995. Equation 1 has been frequently used for mutation studies, observing the effect of changing residues on the donor (D) or acceptor (A) on the ET rate in the complex. While this is relatively uninformative about the mechanism, it does offer a simple comparative way to observe relative changes and assumes that ET rate (k_{ET}) >> k_{on} (association rate between D and A) and k_{off} (dissociation rate), and that electron transfer is unidirectional (hence $k_{on} \approx k_{for}$), usually a reasonable approximation. A more realistic explanation is offered by equation 2, here the fact that formation of an ET complex ({D:A}) must precede the electron transfer step is explicitly considered. This also considers the possibility that mutation of residues could lead to $k_{ET} \not> \not> k_{on}$ and k_{off}, as observed in several studies. In addition, it accounts for the possibility that the k_{on} and k_{off} may change dependent on the redox state of D and A (as seen by k^{I}_{on} and k^{II}_{on}). However, several pieces of data indicate the description in equation 2 still fails to capture the full complexity of an ET system. Firstly, bulk phase *in vitro* experiments at high concentrations of D compared to A have shown the maximum second order ET turnover rate is substantially lower than k_{ET}. This would suggest that there is an additional stage in the association between D and A, which can become rate limiting.

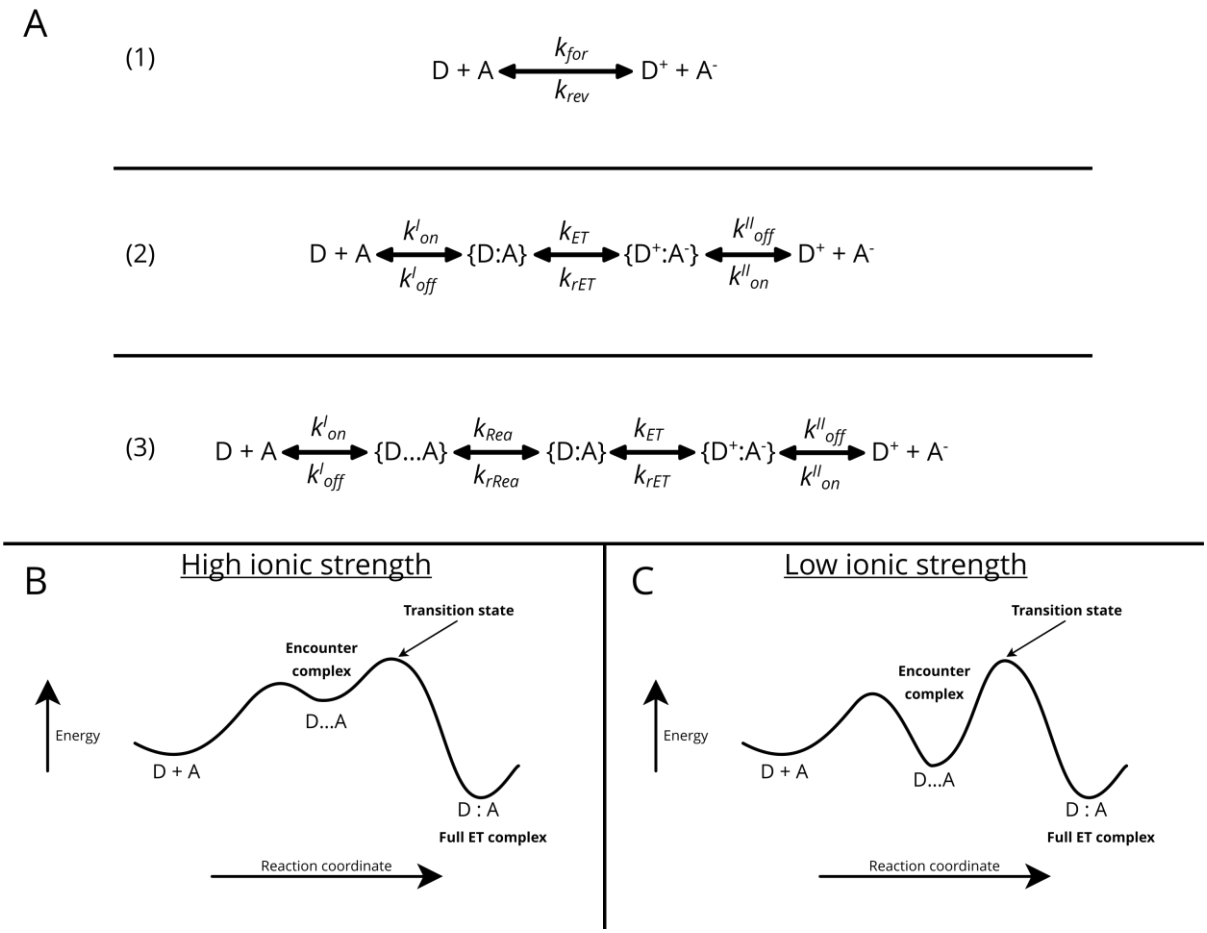

Figure 1.13 Electron transfer complex kinetics

*(**A**) Equations for the interaction schematic proposed from early experiments (Summarised in Hope, 2000). D and A represent donor and acceptor for electrons. The kinetic rate constant of k_{for} is a general measure for the overall transfer of an electron from the donor to acceptor, while k_{rev} is the summation of the reverse process. k_{on} is the second-order rate constant for binding, while k_{off} is the first-order dissociation rate constant from the bound form. k_{ET} is the first-order rate of electron transfer from donor to acceptor, and k_{Rea} is the first-order rate constant for the rearrangement from the encounter complex to the fully bound state. For each of these last two rate constants, the reverse rate is given by k_{rET} and k_{rRea} respectively. (**B**) Free energy diagram for the association between donor and acceptor at higher ionic strengths. Reproduced with permission from American Chemical Society, adapted from Tetreault et al., 2001. (**C**) Free energy diagram for the association between donor and acceptor at lower ionic strengths, leading to the stabilisation of the encounter complex and thus having an effectively larger transition state barrier.*

The nature of this first-order stage of the association between D and A became apparent in experiments where the ionic strength of the reaction medium was varied. If two electrostatically charged faces were undergoing screening provided by increasing ionic strength, then the rate would be expected to follow a single exponential decay, as the net electrostatic effect (Debye length) between D and A decreased. While this was observed at higher ionic strengths, there was also a decrease in turnover rate at lower ionic strengths that suggested that a process involved in the ET was becoming rate limiting. The proposed mechanism for this, and now thought to be the mechanism explaining ET complexes is shown in equation 3 (Ubbink, 2009). Here, generation of the full ET complex ({D:A}) is divided into two components; the initial association (k^{I}_{on}) to form an 'encounter complex' ({D…A}) which is inefficient in electron transfer, and then a rearrangement (k_{Rea}) overcoming certain electrostatic interactions to form a full ET complex capable of electron transfer. At higher ionic strengths, screening would occur in the solution, effectively decreasing k^{I}_{on} as expected. However, at lower ionic strengths, the rate of re-arrangement (k_{Rea}) would become limiting, due to the electrostatic components of the binding interface having a stronger interaction according to Coulombs law, and thus over-stabilising the encounter complex, effectively locking it in this state (Ubbink, 2009; Watkins et al., 1994). This effect on the energetic barriers is shown in figure 1.13B for high ionic strength and C for lower ionic strength, adapted from Tetreault et al., 2001 and Ubbink, 2009. As such, this balance between k_{on} and k_{Rea} results in the bell-shaped curve apparent in the ET rate versus ionic strength plot seen for a wide range of ET complexes (Ubbink, 2009). The rearrangement rate can be ignored, and hence the use of equation 2 is valid if the ionic strength of the reaction medium is sufficient to ensure $k_{Rea} >> k^{I}_{on}$. In energetic terms, the encounter complex can thus be thought of as an intermediate in the binding process, with the transition state barrier being affected by either mutation of the binding interface, or by ionic strength of the solution.

Little progress has been made in attempting to better understand the encounter complex involved in the interaction between ET proteins. While studies have made some progress using bulk phase measurements such as NMR, the heterogeneity of the proposed encounter complex has led to obscurity in these studies (Reviewed in Ubbink, 2009). In recent years, single molecule techniques have become popular in Biochemistry due to their ability to observe functional heterogeneity and probe specific interactions. Single molecule force spectroscopy (SMFS), a technique based on the use of an atomic force microscope (AFM) to quantify the forces between a scanning probe and the surface it interrogates with piconewton resolution, is one such single-molecule technique that has been successfully applied to study ET complexes (Johnson et al., 2014; Lagunas et al., 2018; Mayneord et al., 2019; Vasilev et al., 2013, 2019). This is discussed further in section 1.4, however first the methodology underpinning for SMFS and atomic force microscopy are introduced.

1.3 Atomic Force Microscopy

A conventional light microscope uses lenses to direct light into the observer's eye to magnify and focus an image. The atomic force microscope (AFM) operates on an entirely different premise. A sharp tip is traced across a surface to be imaged, and the height is recorded at each location. Performing this action over a 3D surface will thus generate a map for the corresponding height at each coordinate on the surface, and as such create a 3D topographic image. This method is described under the umbrella term of scanning probe microscopy (SPM).

1.3.1 Origins of AFM

The original SPM technique employed was the scanning tunnelling microscope (STM) (Binnig et al., 1982). This utilised the relationship between electron tunnelling current and distance. A voltage can be applied between two conductive materials in a vacuum, and the tunnelling current between them will decay exponentially as a function of the distance between them. As such, a conductive probe could be traced across a conductive surface, and the tunnelling current between them measured. Moving the conductive probe up or down in response to undulations of the surface to maintain a constant tunnelling current would thus effectively measure the height at each location. As such, the corrections needed in the Z dimension to maintain the constant tunnelling current effectively generate a topology image. Very fine motion was required for this method, both to correct in the Z dimension, and give fine motion in X and Y. This was provided by a piezo scanner, comprised of a ceramic material that acts as an electromechanical transducer. As such, the ceramic material can convert an electrical potential into fine mechanical motion, typically with an expansion coefficient of 0.1nm V^{-1} (Eaton and West, 2010). Hence, if 50V was applied across the material, it would expand by 5nm in the direction of the electric field. This fine motion response to voltage could thus be used to control the 2D scanning across a flat surface, as well as the distance between the conductive probe and surface. The development of this method won Gerd Binnig and Heinrich Rohrer the Nobel Prize in Physics in 1986.

Whilst the resolution of this instrument was very high, even capable of measuring atomic level detail, it had several obvious drawbacks for wider applications. Both materials needed to be conductive and operated in a vacuum. To avoid these drawbacks, a new method was devised, AFM (Binnig et al., 1986). Rather than measuring the distance between the probe and sample via the tunnelling current, a probe mounted on a cantilever with a suitably low spring constant (deflection/force) could be used to measure the height at the surface, by dragging this tip along. The surface was hence detected via the deflection of the AFM probe upward. As with the STM method, the height map was generated from recording the corrections performed by the piezo in the Z dimension. However, rather than

maintain a constant tunnelling current with the surface, a constant deflection of the probe on the surface was maintained. Initially, the deflection of the AFM probe was detected by a STM mounted on top of the probe, thus removing the requirement for a conductive sample, but still requiring a vacuum. In most modern AFM machines this has been replaced by a reflective material on the top of the AFM probe, and detection of motion is facilitated by directing a laser at this point and observing the deflection of the laser onto a position-sensitive photodetector as seen in figure 1.14.

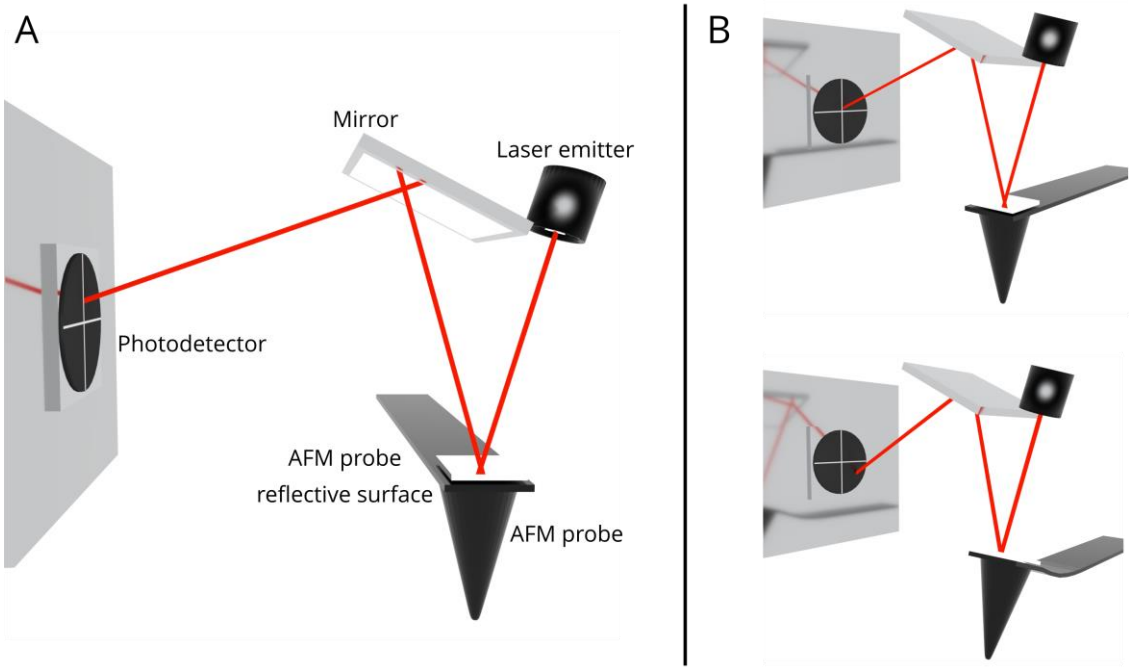

Figure 1.14 AFM schematic

*A schematic for the setup of a modern AFM instrument. (**A**) The schematic is labelled. The laser emitter focuses a laser beam onto the AFM probe's reflective surface at the end of the cantilever. This is reflected up into a steering mirror, and finally onto a photodetector split into 4 quadrants. As such, when the AFM probe moves, the deflection of the laser on the AFM probe also changes and thus can be detected by a change in the light hitting different quadrants in the photodetector, as seen in (B). (**B**) Schematic showing the effect of deflection of the AFM probe, and the subsequent change in the laser beam position on the photodetector.*

This modern method still relies on the same principle as the original AFM, however the sensitivity is lower. The benefit of this method however is no conductivity or vacuum is required, allowing imaging in the liquid phase, making it a good candidate for the study of biological system.

1.3.2 The force-distance curve

Modern AFM instruments are frequently now applied to 'soft' samples, such as those in biological systems. In these cases, a dragging motion of the AFM probe across the surface would not be desirable, as it would lead to damage of the surface and poor resolution. Instead, a mode called force-volume can apply a tapping motion, bringing the probe into contact with the surface repeatedly at each point (or pixel) in the AFM image, across a 2D plane, to generate a 3D image. This motion is shown in figure 1.15. In this method, the AFM probe starts away from the surface, and is moved down toward a sample (A). When it reaches the sample, the probe begins to deflect upwards, applying an increasing force downward on the surface. Once a set deflection of the AFM probe is reached (C) the motion of the AFM probe is reversed, and it retracts from the surface. Utilising an AFM probe with a low spring constant and maintaining a low contact force for these interactions means soft biological samples can be scanned multiple times, and theoretically remain unaffected by the imaging process. Using this method, we now have an additional piece of information. At each pixel in the image, the AFM probe and surface are bought into contact. Observing this interaction can give further information about the surface at this location. This data is frequently portrayed as a 'force-distance curve' (FdC), shown in figure 1.15.

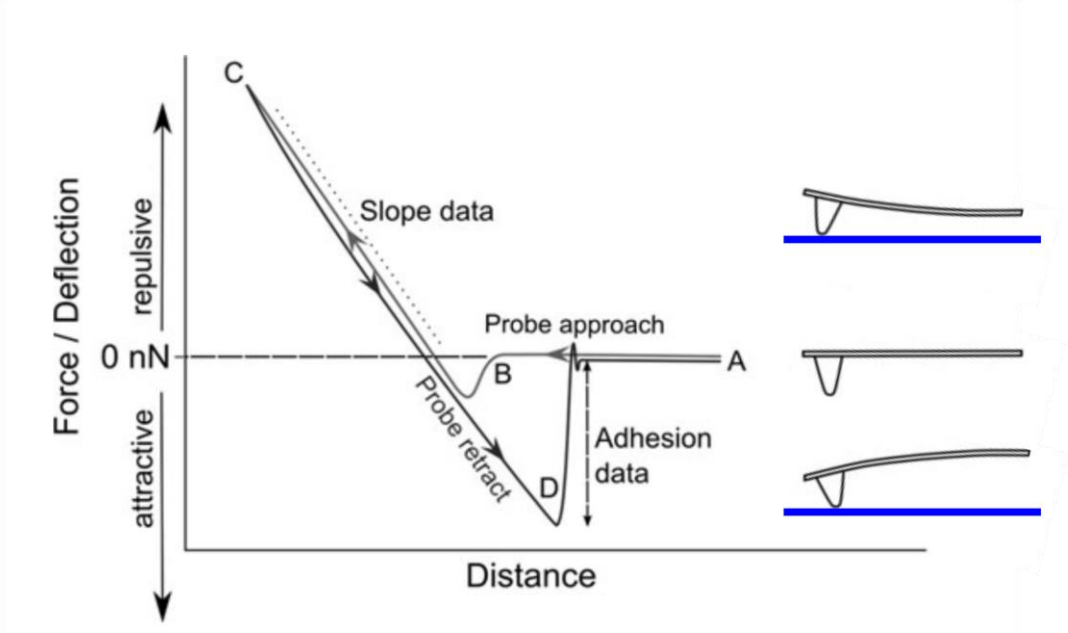

Figure 1.15 Force-distance curve

An example of a force-distance curve for an interaction with a surface, with the subsequent deflection of the cantilever seen on the right. The approach curve is in grey, while the retracting curve is in black. At point A, the AFM probe is away from the surface, hence there is no deflection of the cantilever, thus

giving a force of 0nN. As the AFM probe comes near the surface, attractive forces can allow the AFM probe 'snap' down to the surface, as seen at B. Following this, as the AFM probe is continually moved down by the piezo, the cantilever is deflected upwards, applying a linearly increasing force on the surface, as the cantilever effectively behaves as a Hookean spring. Once this force reaches a previously set maximum (C), the piezo begins moving the AFM probe away from the surface. If there is an attractive force between the surface and the probe, then as the probe is retracted it may 'stick' to the surface, and the subsequent downward deflection of the AFM probe also applies an increasing force on the surface. Once the increasing force applied from the cantilever is greater than the attractive force between AFM probe and the surface, the two are pulled apart (D) and the cantilever goes back to the normal. Reproduced with permission from Oxford Publishing Limited, Edited from Eaton and West, 2010.

Here, the approach to the surface is seen in grey, and the retraction from the surface in black. See figure legend for description of events in the FdC. The force applied in either direction on the surface can be calculated via Hooke's law, where the cantilever the AFM probe is on is considered a Hookean spring, and as such its deflection can be converted using:

$$Force = k_{spring} \times x$$

Where k_{spring} is the spring constant for the cantilever (N/m), and x is the distance displaced from the 'relaxed' position (force = 0nN in figure 1.15).

This event as a whole is often referred to as a single 'ramp' event. The distance the AFM probe moves during this ramp is set at the start of imaging and governs the magnitude of the Z motion. As such, the height image generated is the correction needed by the piezo in the Z dimension to ensure that this ramp distance is maintained, and so that the predetermined cantilever deflection is reached at the bottom of this ramp size. Using these methods, scanning across a surface can generate a height image, and a FdC at each pixel on the surface. At a repetition rate (the number of 'ramp' events occurring per second) of 10Hz, a 256 x 256 pixel image would take nearly 2 hours to obtain. Other methods such as Peak Force Tapping mode also exist, which will record lower resolution FdC's at faster rates. However, to obtain more detailed mechanical properties a newer method must be employed to obtain mechanical properties at the appropriate speed.

1.3.3 PeakForce quantitative nanomechanical mapping® AFM

PeakForce quantitative nanomechanical mapping® (PF-QNM) is an AFM imaging method developed by Bruker. It is capable of generating high pixel density topology images quickly, whilst also measuring the mechanical properties of the surface by recording FdCs.

This method oscillates the tip relative to the surface (for sample mounted systems, the sample sits on the piezo rather than the probe) at a frequency called the PeakForce frequency (which can be considered to be equivalent to the 'ramp' rate). This can vary from 0.125 – 4kHz and will form intermittent contact with the surface at the bottom of the oscillation curve. This amplitude of oscillation for the ramp cycle is also set in the parameters at the start of imaging. As described in 1.3.2, the measured height for the topology image actually comes from the correction the piezo must perform to retain the constant deflection setpoint at the bottom of the oscillation. For example, if a distance for oscillation is set to 20nm, but the peak force setpoint is achieved at 18nm, then the machine assumes that the height on the surface has risen by 2nm relative to the previous pixel, and subsequently makes the adjustment for the height of the oscillating AFM probe. The rate of this update to the baseline is set by the gain, that is, a higher gain will lead to a higher frequency of changes in the baseline, whilst a lower gain will lead to less frequent changes in the baseline. Selection of the correct level of gain is crucial to avoid noisy (from too higher gain), or low resolution (from too lower gain) images.

The cycle of approach and retract seen in figure 1.15 is repeated for each pixel location in the raster scanned 2D plane, giving the 3D image of topology and a subsequent FdC for each pixel. In this method, the generation of a 256 x 256-pixel image at a 1kHz frequency would take ca. 2 minutes, due to the methods multiple sampling for each pixel.

The data obtained in PF-QNM AFM is displayed by Bruker's software as 6 image channels. The methods for calculating 4 of the 6 image channels are shown in figure 1.16. The other two image channels not derived from the FdC in 1.16 are height (previously discussed) and PeakForce Error. The PeakForce error describes the difference between the amplitude of oscillation and the height at which the peak force is reached. Whilst this contains little information, it can give better contrast to smaller particles. The remaining 4 channels shown are all based on the Derjaguin-Muller-Toporov (DMT) model (Derjaguin et al., 1975) where each pixel in the image represents a value calculated by this model, approximating the AFM tip as a sphere, and the sample surface as a plane.

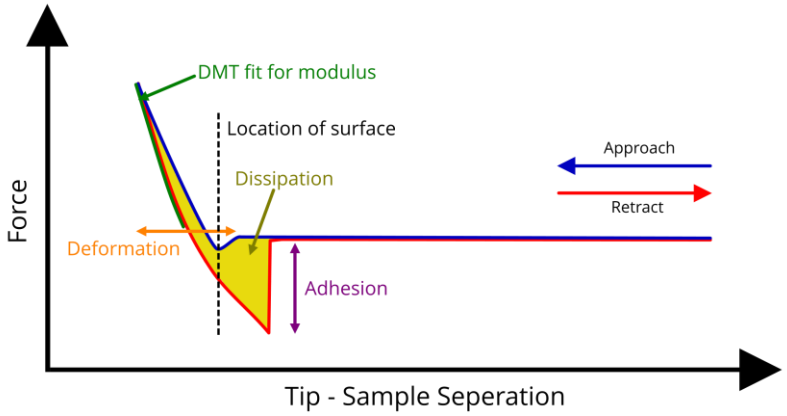

Figure 1.16 PF - QNM image channel calculations

Replicated from Bruker's own materials explaining PF-QNM. The 4 different properties that can be calculated are shown in various colours, matching the method for its calculation. The point at which the surface is reached is shown in the dotted line.

The DMT modulus is a measure of the Young's modulus and can be considered to represent stiffness of the sample. As shown in figure 1.16, this is taken from a linear region of the retraction curve after the peak force is reached. Deformation is measured by the distance travelled between the point of contact, and the point at which the peak force is reached. Once the surface has been contacted, any further downward motion thus applies a force, which can deform the sample underneath the tip. Hard surfaces would have a very short distance travelled, while softer samples would have greater distances. In practical terms rather than use the point of contact, which could be obscured by noise, the location at which 15% of the peak force is achieved is used as the effective contact point in PF-QNM. Dissipation can be defined as the work done to the sample by the AFM tip, or alternatively the energy of the tip moving lost as it is dampened by the sample. This is calculated by integrating the area between the approach and retraction curves, as both deformation and adhesion would count as work performed on the sample. Finally, adhesion is a measure of the force required to separate the AFM tip from the surface. It manifests as a negative deviation from the normal in a force curve and comes from the interactions occurring between the tip and the surface. Whilst other methods for measuring the locations of adhesions exist, such as picoTREC, these fail to give specific properties of the adhesions at the given location.

AFM images for all 6 channels are shown in figure 1.17. This data was taken from Johnson et al., 2014, where an AFM probe with Pc attached was used to scan over an extracted grana membrane patch from spinach chloroplast. As such, the white dots seen in the adhesion image on the membrane

actually represent the locations where the interaction between Pc on the probe and cytb_6f in the imaged membrane are measured. Utilising the precise motion of AFM to interrogate the interaction force between two binding partners in this way is known as single molecule force spectroscopy.

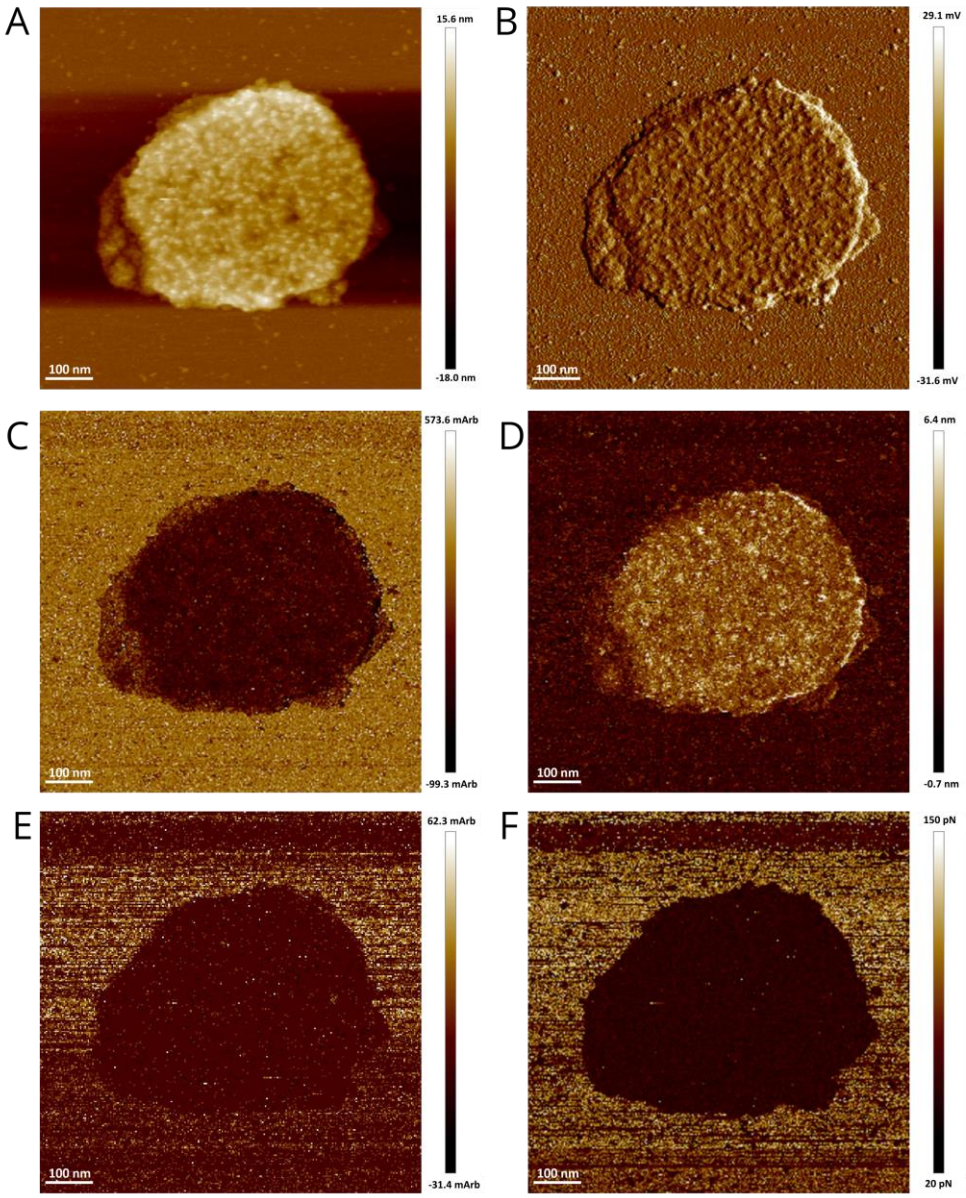

Figure 1.17 PF-QNM output channels

*AFM data taken from Johnson et al., 2014 on extracted grana membrane patches. See Johnson et al., 2014 for details. Each of the 6 channels for: (**A**) Height (**B**) Peak force error (**C**) DMT modulus (**D**) Deformation (**E**) Dissipation (**F**) Adhesion.*

1.4 Single Molecule Force Spectroscopy

Traditional biochemical views of affinity are based on bulk phase measurements such as k_D, k_{on} and k_{off}. Whilst these have previously served as suitable characterisations of the affinity between proteins, the averaging involved can hide heterogeneity intrinsic in the system. In single molecule force spectroscopy (SMFS), cognate binding partners are attached to the AFM probe and a surface and are bought into contact with one another for a set period of time, known as the 'dwell time'. If the two partners are interacting upon retraction then a constantly increasing force is applied to the bound complex (seen as adhesion), until this force exceeds the force holding the two proteins together. At this time, the interaction is ruptured, and this force can be measured by the minimum (adhesion) in the force curve. This can be used to explore underlying interactions involved in binding (discussed below), or to show the locations at which these interactions occur, in the technique known as affinity mapping (Ebner et al., 2005; Johnson et al., 2014; Stroh et al., 2004a, 2004b).

1.4.1 Origins

Lee et al., 1994 were the first group to attempt these experiments, measuring the interaction between biotin and streptavidin as it is one of the strongest interactions known in biology. As a control, they added excess biotin into the imaging buffer to block the available binding sites on the surface. When scanning over surfaces that had been exposed in this way, a significant drop in the number of adhesions was observed, indicating that the binding site had been blocked, and the interaction being probed was therefore specific. An issue with these initial experiments was the direct attachment of the binding partners to the probes. This gave an effective 'separation distance' (distance between the AFM probe tip leaving the surface and the adhesion event occurring) of 0nm. As such, any other interaction between the AFM probe itself and the surface would also manifest at this location, making it difficult in distinguishing specific from non-specific interactions. A simple solution to this was to attach the protein via a linker including a long spacer, to allow the probe to leave the surface and the linker extend before any force is applied on the bound complex, thus distinguishing the specific interactions between the cognate partners from any other non-specific adhesion seen between the AFM probe and the surface. Following the synthesis of appropriate linkers for this purpose (Haselgrubler et al., 1995), Hinterdorfer et al., 1996 used these to probe the interaction between human serum albumin, and its antibody. The setup of these experiments is shown in cartoon form in figure 1.18, with explanation in the legend.

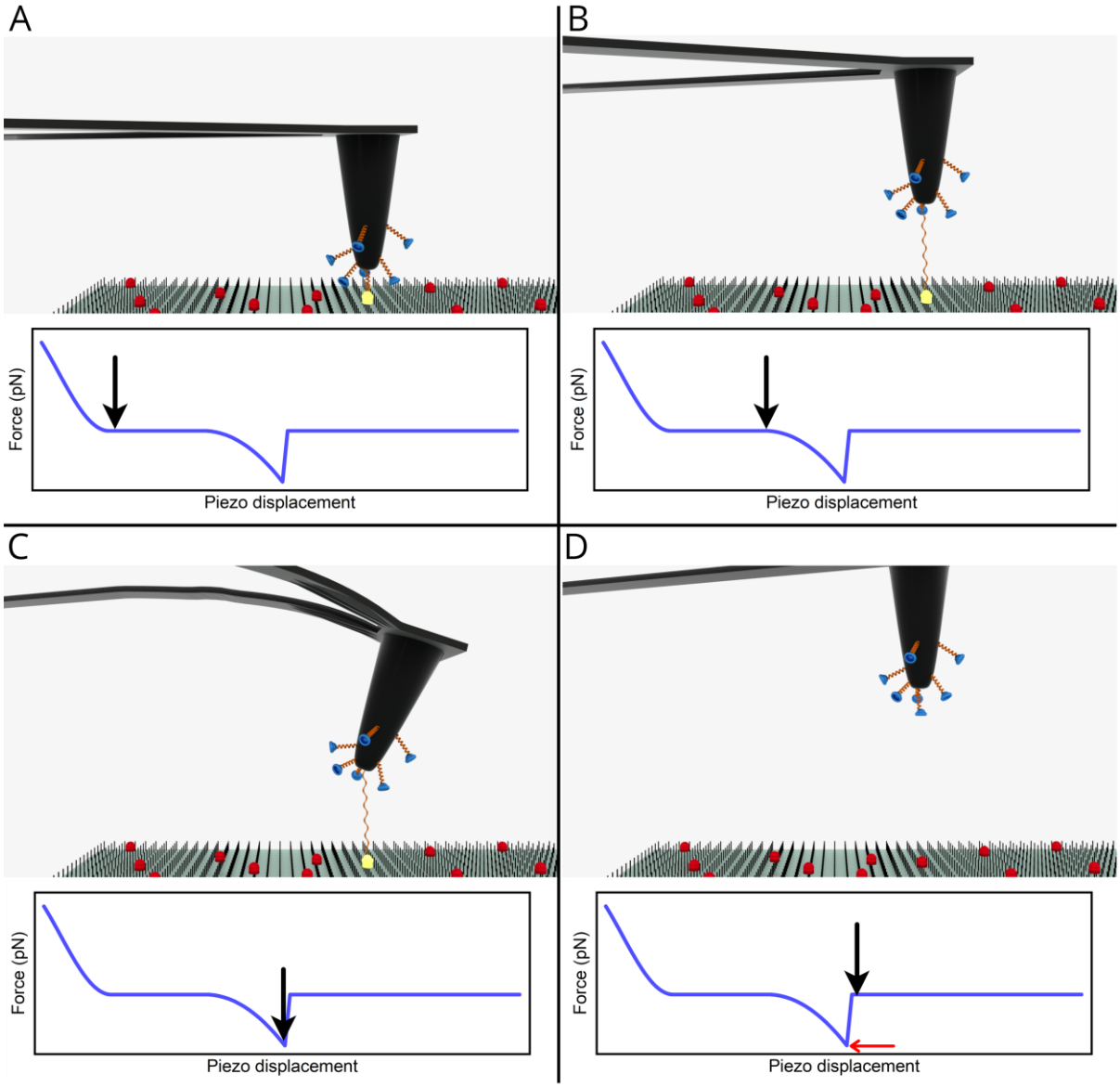

Figure 1.18 Single molecule force spectroscopy schematic

*Four successive images showing the retraction from the surface in a ramp event involved in SMFS. The corresponding location of the event on the force curve is shown below each cartoon. In this diagram, two cognate binding partners (Protein 1 in red, Protein 2 in blue) are attached to a flat surface and an AFM probe. An interaction complex of both protein 1 and 2 is shown as a yellow glowing complex. (**A**). The AFM probe begins to leave the surface, while protein 1 and 2 are interacting. (**B**). The linker attaching protein 2 to the AFM tip is pulled taut. (**C**) As the piezo continues to move the AFM probe away from the surface, the cantilever bends, acting as a Hookean spring. In this case, a constantly increasing force is applied on the interacting complex of protein 1 and 2. (**D**) The force applied to the interacting complex has exceeded the force holding the two proteins together, and thus the interaction*

is ruptured. As such, the lowest point in adhesion is considered the unbinding force for the complex (red arrow).

1.4.2 Bell – Evans model

An initial explanation of the force measured between two bound proteins in this way was offered by Bell, 1978 and later expanded upon by Evans (Evans and Ritchie, 1997) and co-workers (Merkel et al., 1999). This model shows the relationship between various parameters of the interaction and the unbinding force measured (F^U) as:

$$F^U = \frac{k_B T}{\gamma} \ln\left(\frac{\gamma\, r_f}{k_{off} k_B T}\right)$$

where k_B is Boltzmann constant, T is absolute temperature, γ is the distance between the bound state and the transition state barrier for dissociation, k_{off} is the dissociation rate constant of the complex in solution and r_f is the loading rate. The loading rate describes the rate at which the increasing force is applied to the bound complex and is usually measured from the slope of the FdC immediately prior to the interaction being ruptured. It is proposed that when performing single molecule force spectroscopy on bound complexes, the free energy landscape for dissociation is effectively tilted (figure 1.19A). The extent of this tilting is usually proportional to the loading rate in an exponential manner. This shows an important feature in single molecule force spectroscopy experiments; that varying the loading rate of the experiment can allow the probing of multiple energetic barriers in the unbinding, as when the tilting of the free energy plot is significant enough a different barrier becomes dominant in the unbinding (figure 1.19A). These are often portrayed in what is called the dynamic force spectrum, where the unbinding forces are plotted against the loading rate as shown in figure 1.19B. As such, each linear regime seen is the probing of a different barrier. Whilst other models for the unbinding force have been proposed (Dudko et al., 2008; Friddle et al., 2012), little difference is seen in the extracted parameters from these alternatives (Hane et al., 2014).

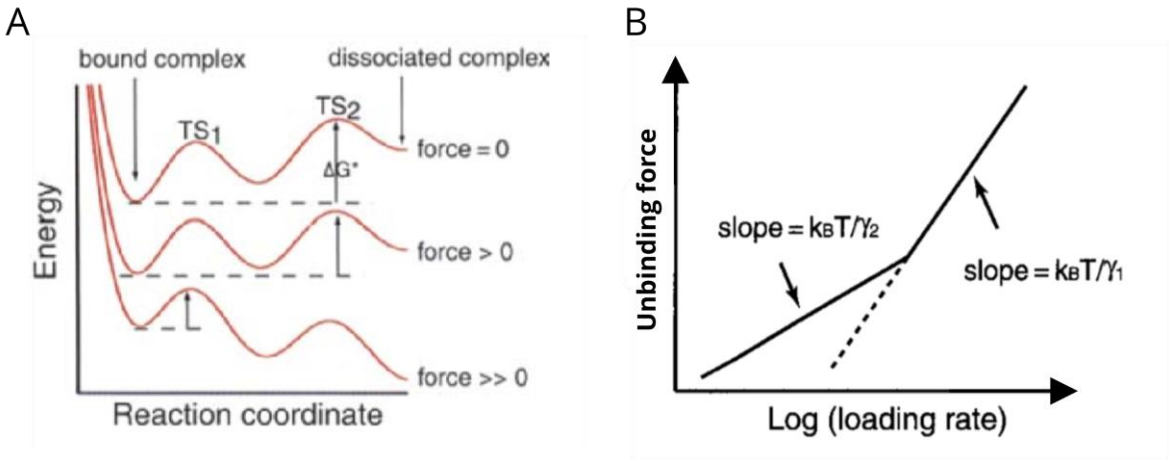

Figure 1.19 Dynamic force spectrum

*Reproduced with permission from Springer, from Hinterdorfer et al., 2009. (**A**) Free energy plot for the dissociation of a bound complex with 2 energetic barriers. As can be seen natively (force = 0) the second barrier (TS2) is the highest energetic barrier. As a slow loading rate is applied on the bound complex (force > 0), the energetic landscape is tilted, as the constantly increasing force will be larger further along the reaction coordinate. The outer energetic barrier (TS2) is still dominant though. As a larger loading rate is applied on the complex (force >> 0), the energetic landscape is tilted further so that the inner energetic barrier TS1 becomes dominant. It should be noted that this is the plot for dissociation, different from the plot for association like those in figure 1.13. (**B**) The manifestation of the effect of loading rate on the energetic barrier being probed as shown in (A). This is referred to as the dynamic force spectrum as it shows the response of unbinding force to loading rates, unveiling the energetic barriers involved in dissociation. γ here is the distance in the reaction coordinate between the bound complex and the barrier being probed (shown in dashed lines in (A)), thus γ_1 is the TS1 energetic barrier seen in (A), and γ_2 is the TS2 barrier.*

1.4.3 Utilising PF-QNM for SMFS

While SMFS experiments have traditionally been performed at slower 'ramp' rates often below 10Hz, the probing of more transient interactions requires a faster rate of motion from the AFM. Fortunately, PF-QNM offers the ideal candidate for the quantitative exploration of more transient complexes. The initial study by Vasilev et al., 2013 was used to probe the interaction between RC-LH1 and cyt c_2 from *Rba. sphaeroides*, testing the effect of light on the interacting complex at repetition rates from 0.5-1 kHz (Vasilev et al., 2013). Following this, the work was further expanded upon in Johnson et al., 2014, where the technique was used for affinity mapping to show the location of cytb_6f in a thylakoid grana

membrane, by probing it with Pc attached to the AFM tip (figure 1.17). This work again used a repetition rate of 1kHz for the PF-QNM imaging. In addition, the technique was applied to the study of the interaction between viral proteins and their cell surface receptors, in conjunction with simultaneous confocal microscopy (Alsteens et al., 2016). This technique used the slower 0.125-0.25kHz range and found a single barrier for the interaction. In the first and last of these cases, the PeakForce frequency was changed, giving a concordant change in loading rate which was measured from the generated FdCs. As the oscillation involved in PF-QNM generates natural fluctuations, there is an inherent variation in the loading rate for an experiment even if the repetition rate is not changed. However, PF-QNM involves multiple interactions with the surface for each pixel and the real-time analysis of this data is obscured. As is the nature of dealing with private companies, assurances have been given by Bruker that the forces measured from the force curves in PF-QNM are accurate for the interaction force, and do not involve averaging. However, there is not an assurance that the loading rate is correct, and as such attempting to correlate a loading rate in PF-QNM may be inaccurate, or ill advised.

1.4.4 Measurements from SMFS

The parameters obtained in bulk, ensemble studies that would describe an interaction, such as dissociation constants, can only be roughly translated to the parameters in SMFS. Generally, it is accepted that the k_{off} is related to the unbinding force in Bell-Evans (Evans, 2001; Evans and Ritchie, 1997), or Friddle-De Yoreo models (Friddle et al., 2012) via a logarithmic relationship. Given the nature of PF-QNM discussed above, dynamic force spectroscopy was not performed in this thesis due to lacking the ability to accurately obtain the loading rate. Instead, the unbinding forces measured at a single repetition rate under different conditions (eg. Ionic strengths) have been reported.

The interaction frequency could be argued to be analogous to the k_{on} or k_D for an interaction (based on the dwell time and the complex lifetime), measuring how frequently a bound state is achieved (for k_{on}) or occupied (for K_D) within the dwell time. Attempting to draw a direct relationship between interaction frequency and k_{on} is beyond the scope of this thesis, as too many variables would exist, even within a single experimental repeat. However, it is shown here and in other studies that the interaction frequency is useful as a relative measurement for comparison of different conditions on the interaction (Johnson et al., 2014; Mayneord et al., 2019; Vasilev et al., 2013, 2019).

Using these two parameters to measure affinity, we wished to probe electron transferring complexes to gain a better understanding of how they achieve their unique requirements of fast association, dissociation, and efficient electron transfer.

1.5 Bibliography

Alsteens, D., Newton, R., Schubert, R., Martinez-Martin, D., Delguste, M., Roska, B., and Muller, D.J. (2016). Nanomechanical mapping of first binding steps of a virus to animal cells. Nat. Nanotechnol. *12*, 177–183.

Axelrod, H.L., Feher, G., Allen, J.P., Chirino, a J., Day, M.W., Hsu, B.T., and Rees, D.C. (1994). Crystallization and X-ray structure determination of cytochrome c2 from Rhodobacter sphaeroides in three crystal forms. Acta Crystallogr. D. Biol. Crystallogr. *50*, 596–602.

Axelrod, H.L., Abresch, E.C., Okamura, M.Y., Yeh, A.P., Rees, D.C., and Feher, G. (2002). X-ray structure determination of the cytochrome c2: reaction center electron transfer complex from Rhodobacter sphaeroides. J. Mol. Biol. *319*, 501–515.

Bassham, J.A., Benson, A.A., and Calvin, M. (1950). The path of carbon in photosynthesis. J. Biol. Chem. *185*, 781–787.

Bell, G.I. (1978). Models for the specific adhesion of cells to cells. Science (80-.). *200*, 618–627.

Binda, C., Coda, A., Aliverti, A., Zanetti, G., and Mattevi, A. (1998). Structure of the mutant E92K of [2Fe-2S] ferredoxin I from Spinacia oleracea at 1.7 A resolution. Acta Crystallogr. D. Biol. Crystallogr. *54*, 1353–1358.

Binnig, G., Rohrer, H., Gerber, C., and Weibel, E. (1982). Surface Studies by Scanning Tunneling Microscopy. Phys. Rev. Lett. *49*, 57–61.

Binnig, G., Quate, C., and Gerber, C. (1986). Atomic Force Microscope. Phys. Rev. Lett. *56*, 930–933.

Blankenship, R.E. (1992). Origin and early evolution of photosynthesis. Photosynth. Res. *33*, 91–111.

Blankenship, R.E. (2014). Molecular Mechanisms of Photosynthesis.

Cartron, M.L., Olsen, J.D., Sener, M., Jackson, P.J., Brindley, A. a., Qian, P., Dickman, M.J., Leggett, G.J., Schulten, K., and Neil Hunter, C. (2014). Integration of energy and electron transfer processes in the photosynthetic membrane of Rhodobacter sphaeroides. Biochim. Biophys. Acta *1837*, 1769–1780.

Chandler, D.E., Hsin, J., Harrison, C.B., Gumbart, J., and Schulten, K. (2008). Intrinsic Curvature Properties of Photosynthetic Proteins in Chromatophores. Biophys. J. *95*, 2822–2836.

Cohen-Bazire, G., Sistrom, W.R., and Stanier, R.Y. (1957). Kinetic studies of pigment synthesis by non-sulfur purple bacteria. J. Cell. Comp. Physiol. *49*, 25–68.

Conte, L. Lo, Chothia, C., and Janin, J. (1999). The atomic structure of protein-protein recognition sites. J. Mol. Biol. *285*, 2177–2198.

Derjaguin, B. V, Muller, V.M., and Toporov, Y.. (1975). Effect of contact deformations on the adhesion of particles. J. Colloid Interface Sci. *53*, 314–326.

Dudko, O.K., Hummer, G., and Szabo, A. (2008). Theory, analysis, and interpretation of single-molecule force spectroscopy experiments. Proc. Natl. Acad. Sci. *105*, 15755–15760.

Eaton, P., and West, P. (2010). Atomic Force Microscopy.

Ebner, A., Kienberger, F., Kada, G., Stroh, C.M., Geretschlager, M., Kamruzzahan, A.S.M., Wildling, L., Johnson, W.T., Ashcroft, B., Nelson, J., et al. (2005). Localization of single Avidin-Biotin interactions using simultaneous topography and molecular recognition imaging. ChemPhysChem *6*, 897–900.

Esser, L., Elberry, M., Zhou, F., Yu, C.-A., Yu, L., and Xia, D. (2008). Inhibitor-complexed structures of the cytochrome bc1 from the photosynthetic bacterium Rhodobacter sphaeroides. J. Biol. Chem. *283*, 2846–2857.

Evans, E. (2001). Probing the relation between force - lifetime and chemistry in single molecular bonds. Annu. Rev. Biophys. *30*, 105–128.

Evans, E., and Ritchie, K. (1997). Dynamic strength of molecular adhesion bonds. Biophys. J. *72*, 1541–1555.

Fedotova, Y., and Zeilstra-Ryalls, J. (2014). Analysis of the role of PrrA, PpsR, and FnrL in intracytoplasmic membrane differentiation of Rhodobacter sphaeroides 2.4.1 using transmission electron microscopy. Photosynth. Res. *119*, 283–290.

Feniouk, B.A., Cherepanov, D.A., Junge, W., and Mulkidjanian, A.Y. (1999). ATP-synthase of Rhodobacter capsulatus: Coupling of proton flow through F0 to reactions in F1 under the ATP synthesis and slip conditions. FEBS Lett. *445*, 409–414.

Forster, T. (1948). Zwischenmolekulare Energiewanderung und Fluoreszenz. Ann. Phys. *437*, 55–75.

Francia, F., Wang, J., Venturoli, G., Melandri, B.A., Barz, W.P., and Oesterhelt, D. (1999). The reaction center-LH1 antenna complex of Rhodobacter sphaeroides contains one PufX molecule which is involved in dimerization of this complex. Biochemistry *38*, 6834–6845.

Friddle, R.W., Noy, a., and De Yoreo, J.J. (2012). Interpreting the widespread nonlinear force spectra of intermolecular bonds. Proc. Natl. Acad. Sci. *109*, 13573–13578.

Hahn, A., Vonck, J., Mills, D.J., Meier, T., and Kuhlbrandt, W. (2018). Structure, mechanism, and regulation of the chloroplast ATP synthase. Science (80-.). *360*, eaat4318.

Hane, F.T., Attwood, S.J., and Leonenko, Z. (2014). Comparison of three competing dynamic force spectroscopy models to study binding forces of amyloid-β (1-42). Soft Matter *10*, 1924–1930.

Haselgrubler, T., Amerstorfer, A., Schindler, H., and Gruber, H.J. (1995). Synthesis and Applications of a New Poly(Ethylene Glycol) Derivative for the Crosslinking of Amines with Thiols. Bioconjug. Chem. *6*, 242–248.

Hervás, M., Navarro, J.A., Díaz, A., Bottin, H., and De la Rosa, M.A. (1995). Laser-Flash Kinetic Analysis of the Fast Electron Transfer from Plastocyanin and Cytochrome c6 to Photosystem I. Experimental Evidence on the Evolution of the Reaction Mechanism. Biochemistry *34*, 11321–11326.

Hill, R. (1937). Oxygen Evolved by Isolated Chloroplasts. Nature *139*, 881–882.

Hill, R., and Bendall, F.A.Y. (1960). Function of the Two Cytochrome Components in Chloroplasts: A Working Hypothesis. Nature *186*, 136–137.

Hinterdorfer, P., Baumgartner, W., Gruber, H.J., Schilcher, K., and Schindler, H. (1996). Detection and localization of individual antibody-antigen recognition events by atomic force microscopy. Proc. Natl. Acad. Sci. U. S. A. *93*, 3477–3481.

Hinterdorfer, P., Oijen, A. Van, Muller, D., Schmidt, T., and Seidel, C. (2009). Handbook of Single-Molecule Biophysics.

Hope, A.B. (2000). Electron transfers amongst cytochrome f, plastocyanin and photosystem I: kinetics and mechanisms. Biochim. Biophys. Acta *1456*, 5–26.

Hunter, N., Daldal, F., Thurnauer, M., and Beatty, T. (2008). The Purple Phototrophic Bacteria.

Illerhaus, J., Altschmied, L., Reichert, J., Zak, E., Herrmann, R.G., and Haehnel, W. (2000). Dynamic Interaction of Plastocyanin with the Cytochrome b6f Complex. J. Biol. Chem. *275*, 17590–17595.

Itoh, S., Iwaki, M., and Ikegami, I. (2001). Modification of photosystem I reaction center by the extraction and exchange of chlorophylls and quinones. Biochim. Biophys. Acta - Bioenerg. *1507*, 115–138.

Johnson, M. (2016). An overview of photosynthesis. Essays Biochem. *60*, 255–273.

Johnson, M.P., Vasilev, C., Olsen, J.D., and Hunter, C.N. (2014). Nanodomains of Cytochrome b_6f and Photosystem II Complexes in Spinach Grana Thylakoid Membranes. Plant Cell *26*, 3051–3061.

Kuhlgert, S., Drepper, F., Fufezan, C., Sommer, F., and Hippler, M. (2012). Residues PsaB Asp612 and PsaB Glu613 of photosystem i confer pH-dependent binding of plastocyanin and cytochrome c 6. Biochemistry *51*, 7297–7303.

Kurisu, G., Zhang, H., Smith, J.L., and Cramer, W.A. (2003). Structure of the Cytochrome b6f Complex of Oxygenic Photosynthesis: Tuning the Cavity. Science (80-.). *302*, 1009–1014.

Lagunas, A., Guerra-Castellano, A., Nin-Hill, A., Díaz-Moreno, I., De la Rosa, M.A., Samitier, J., Rovira, C., and Gorostiza, P. (2018). Long distance electron transfer through the aqueous solution between redox partner proteins. Nat. Commun. *9*, 5157.

Lee, G.U., Kidwell, D.A., and Colton, R.J. (1994). Sensing Discrete Streptavidin Biotin Interactions With Atomic-Force Microscopy. Langmuir *10*, 354–357.

Liu, Z., Yan, H., Wang, K., Kuang, T., Zhang, J., Gui, L., An, X., and Chang, W. (2004). Crystal structure of spinach major light-harvesting complex at 2.72 Å resolution. Nature *428*, 287–292.

Malone, L.A., Qian, P., Mayneord, G.E., Hitchcock, A., Farmer, D.A., Thompson, R.F., Swainsbury, D.J.K., Ranson, N.A., Hunter, C.N., Johnson, M.P. (2019). Cryo-EM structure of the spinach cytochrome b_6f complex at 3.6 Å resolution, Nature *575,* 535–539.

Marcus, R.A. (1956). On the Theory of Oxidation-Reduction Reactions Involving Electron Transfer. I. J. Chem. Phys. *24*, 966.

Mayneord, G.E., Vasilev, C., Malone, L.A., Swainsbury, D.J.K., Hunter, C.N., and Johnson, M.P. (2019). Single-molecule study of redox control involved in establishing the spinach plastocyanin-cytochrome bf electron transfer complex. Biochim. Biophys. Acta - Bioenerg. *1860*, 591–599.

Mazor, Y., Borovikova, A., and Nelson, N. (2015). The structure of plant photosystem i super-complex at 2.8 Å resolution. Elife *4*, 1–18.

Mazor, Y., Borovikova, A., and Nelson, N. (2017). The Structure of plant photosystem I super-complex at 2.6A resolution. Nat. Plants *3*, 17014.

McEvoy, J.P., and Brudvig, G.W. (2006). Water-splitting chemistry of photosystem II. Chem. Rev. *106*, 4455–4483.

Merkel, R., Nassoy, P., Leung, A., Ritchie, K., and Evans, E. (1999). Energy landscapes of receptor–ligand bonds explored with dynamic force spectroscopy. Nature *397*, 50–53.

Miller, E.S., and Burr, G.O. (1935). CARBON DIOXIDE BALANCE AT HIGH LIGHT INTENSITIES. Plant Physiol. *10*, 93 LP – 114.

Mitchell, P. (1975). The protonmotive Q cycle: A general formulation. FEBS Lett. *59*, 137–139.

Moser, C.C., Page, C.C., Farid, R., and Dutton, P.L. (1995). Biological Electron Transfer. J. Bioenerg. Biomembr. *27*, 263–274.

Munekage, Y., Hashimoto, M., Miyake, C., Tomizawa, K.I., Endo, T., Tasaka, M., and Shikanai, T. (2004). Cyclic electron flow around photosystem I is essential for photosynthesis. Nature *429*, 579–582.

Nawrocki, W.J., Bailleul, B., Picot, D., Cardol, P., Rappaport, F., Wollman, F.A., and Joliot, P. (2019). The mechanism of cyclic electron flow. Biochim. Biophys. Acta - Bioenerg.

Nelson, N., and Yocum, C.F. (2006). Structure and function of photosystems I and II. Annu. Rev. Plant Biol. *57*, 521–565.

Nyola, A., and Hunte, C. (2008). A structural analysis of the transient interaction between the cytochrome bc1 complex and its substrate cytochrome c. Biochem. Soc. Trans. *36*, 981–985.

Qian, P., Papiz., M.Z., Jackson, P.J., Brindley, A.A., Ng, I., Olsen, J.D., Dickman, M.J., Bullough, P.A., and Hunter, C.N. (2013). Three-Dimensional Structure of the Rhodobacter sphaeroides RC-LH1-PufX Complex: Dimerization and Quinone Channels Promoted by PufX. Biochem. *52*, 7575–7585.

Sigfridsson, K., Young, S., and Hansson, O. (1996). Structural dynamics in the plastocyanin-photosystem 1 electron-transfer complex as revealed by mutant studies. Biochemistry *35*, 1249–1257.

Singharoy, A., Barragan, A.M., Thangapandian, S., Tajkhorshid, E., and Schulten, K. (2016). Binding Site Recognition and Docking Dynamics of a Single Electron Transport Protein: Cytochrome c2. J. Am. Chem. Soc. *138*, 12077–12089.

Solmaz, S.R.N., and Hunte, C. (2008). Structure of complex III with bound cytochrome c in reduced state and definition of a minimal core interface for electron transfer. J. Biol. Chem. *283*, 17542–17549.

Stroebel, D., Choquet, Y., Popot, J.-L., and Picot, D. (2003). An atypical haem in the cytochrome b(6)f complex. Nature *426*, 413–418.

Stroh, C., Wang, H., Bash, R., Ashcroft, B., Nelson, J., Gruber, H., Lohr, D., Lindsay, S.M., and Hinterdorfer, P. (2004a). Single-molecule recognition imaging microscopy. Proc. Natl. Acad. Sci. U. S. A. *101*, 12503–12507.

Stroh, C.M., Ebner, A., Geretschlager, M., Freudenthaler, G., Kienberger, F., Kamruzzahan, A.S.M., Smith-Gill, S.J., Gruber, H.J., and Hinterdorfer, P. (2004b). Simultaneous topography and recognition imaging using force microscopy. Biophys. J. *87*, 1981–1990.

Tetreault, M., Rongey, S.H., Feher, G., and Okamura, M.Y. (2001). Interaction between cytochrome c2 and the photosynthetic reaction center from Rhodobacter sphaeroides: effects of charge-modifying mutations on binding and electron transfer. Biochemistry *40*, 8452–8462.

Tikhonov, A.N. (2014). The cytochrome b6f complex at the crossroad of photosynthetic electron transport pathways. Plant Physiol. Biochem. *81*, 163–183.

Ubbink, M. (2009). The courtship of proteins: Understanding the encounter complex. FEBS Lett. *583*, 1060–1066.

Vasilev, C., Brindley, A. a, Olsen, J.D., Saer, R.G., Beatty, J.T., and Hunter, C.N. (2013). Nano-mechanical mapping of the interactions between surface-bound RC-LH1-PufX core complexes and cytochrome c 2 attached to an AFM probe. Photosynth. Res. *120*, 169–180.

Vasilev, C., Mayneord, G.E., Brindley, A.A., Johnson, M.P., and Hunter, C.N. (2019). Dissecting the cytochrome c 2 -reaction centre interaction in bacterial photosynthesis using single molecule force spectroscopy. Biochem. J. *476*, 2173–2190.

Watkins, J.A., Cusanovich, M.A., and Meyer, T.E. (1994). A " parallel plate " electrostatic model for bimolecular rate constants applied to electron transfer proteins. 2104–2114.

Wei, X., Su, X., Cao, P., Liu, X., Chang, W., Li, M., Zhang, X., and Liu, Z. (2016). Structure of spinach photosystem II-LHCII supercomplex at 3.2 Å resolution. Nature *534*, 69–74.

Xue, Y., Okvist, M., Hansson, O., and Young, S. (1998). Crystal structure of spinach plastocyanin at 1.7 A resolution. Protein Sci. *7*, 2099–2105.

2. Materials and Methods

2.1 Materials

All chemicals used were of analytical grade purity purchased from Sigma Chemical company unless stated otherwise.

2.2 Standard buffers, reagents and media

All Buffers and media discussed were prepared using distilled water purified via a Milli-Q system (MQ water herein). Buffers not containing sucrose were additionally filtered in a vacuum pump with 0.2µM filters from GE Healthcare Life Sciences at the end of preparation, prior to use. Buffers containing detergents were filtered prior to adding the detergent from stocks.

2.2.1 *Rba.sphaeroides* cultures

M22 growth media was used to grow all strains of *Rba.sphaeroides*, created as described in Hunter and Turner, 1988.

Both kanamycin and tetracycline were added for selection in the SK2 strain used for purification of cytochrome c_2. This strain was generated as discussed in Vasilev et al., 2013. For RC-LH1 purifications, ΔPuc1BA ΔPufBALM ΔPuhA (deleted LH2 and RC-LH1) was used as a background. The transformation of this strain with plasmids containing PufBALM, PuhA-His yielded mutants with photosynthetic membranes devoid of LH2, and contained an RC-LH1 His tagged complex with a C terminal 12xhis tag on the H subunit. In addition, the QE(L264) mutant was generated as previously described in Tetreault et al., 2001.

2.2.2 Spinacia oleracea

Spinach was purchased from the local market on or the day before all preparations of the proteins and stored at 4°C until use.

2.3 Standard techniques

2.3.1 Absorbance spectroscopy

Absorbance spectra were taken from the samples specified in the protocol, at room temperature using a Cary 50 spectrophotometer between the wavelengths specified in the graphs.

2.3.2 Fluorescence emission spectroscopy

77K fluorescence was performed in an Oxford Scientific OptistatDN liquid nitrogen-cooled cryostat (Oxford instruments). Minor adjustments to the sample location in the holder etc were performed prior to attaining the 77k fluorescence spectra shown. Fluorescence emission spectra were obtained using a Fluorolog®-3 spectrometer using a Xenon light source.

2.3.3 Chlorophyll quantification assay

Chlorophyll concentration of samples was measured by adding 4ul sample to 2ml of 80% acetone to liberate chlorophylls, followed by vortexing and spinning in a benchtop centrifuge at 13k for 2 minutes to pellet the apoprotein. Following this an absorbance spectrum between 800 and 500nm was taken, and the chlorophyll concentration and a/b ratio was obtained using a custom-made python script, utilising the following equation:

$A_{646}^{\text{corrected}} = A_{646} - A_{750}$

$A_{663}^{\text{corrected}} = A_{663} - A_{750}$

$[\text{Chl a}] = (12.25 \times A_{646}^{\text{corrected}}) - (2.55 \times A_{646}^{\text{corrected}})$

$[\text{Chl b}] = (20.31 \times A_{646}^{\text{corrected}}) - (4.91 \times A_{663}^{\text{corrected}})$

Total chlorophyll concentration = [Chl a] + [Chl b]

Chlorophyll ratio = [Chl a] / [Chl b]

2.3.4 Sucrose gradients

Continuous sucrose gradients were generated by using two sucrose solutions in a Hoefer™ SG Series Gradient Maker, using a peristatic pump to pour the gradient, and load the sample. Stepwise sucrose gradients were formed by layering each decreasing sucrose concentration from bottom to top. Centrifugation was performed at 4°C at the relative centrifugal force given in the protocol. Fractions

were removed from a sucrose gradient using a needle connected to a peristatic pump. The sucrose concentration of these fractions was measured using a refractometer. The buffer used for the sucrose gradient is given in the protocols.

2.3.5 Columns

Unless stated otherwise: Columns requiring a continuous gradient for elution (eg. anion columns) were run in GE healthcare AKTAprime plus pump system, recording the elution profile for the absorbance at 280nm (aromatic residues) and collecting 1ml samples automatically. Columns utilising steps for elution (eg. Ni^{2+} charged IMAC columns) were simply connected to a peristatic pump and pumped directly onto the column, with flow through from the column being collected in 1ml fractions.

2.3.5.1 Anion exchange

Columns were either bought pre-packed 5ml columns, or self-packed columns of resin for either DEAE anion resin (HiTrap™ DEAE FF, DEAE Sepharose Fast Flow anion exchange chromatography resin) for weak binding, or Q anion resins (HiTrap™ Q FF, Q Sepharose Fast Flow) for stronger binding, from GE Lifesciences. Columns were always equilibrated in 5mM NaCl, and the gradient ran according to the protocol.

2.3.5.2 Ni^{2+} charged IMAC columns

Columns were either prepacked 5ml columns (GE Lifesciences HisTrap FF) or self-packed chelating resin (GE Lifesciences Chelating Sepharose™ Fast Flow) which was then charged using 100mM $NiSO_4$. Following this it was run with the buffers given in the protocol as described by 2.3.5.

2.3.5.3 Hydroxyapatite column

The Bio-rad Bio-Scale™ Mini CHT™ Ceramic Hydroxyapatite Cartridges type I 5ml prepacked columns were initially run in 400mM sodium phosphate pH 7.5 for 10 column volumes to equilibrate the column for the first use. Following this they were equilibrated and run in the buffer given in the protocol.

2.3.5.4 Desalting column

GE Lifesciences HiTrap™ Desalting columns were run on the AKTAprime plus pump system and equilibrated with 20 column volumes of the buffer given in the protocol. Following this the sample was loaded and the columns were run at 3ml/min, collecting 1ml fractions.

2.3.5.5 Gel filtration

FPLC gel filtration column (HiLoad 16/600 Superdex™ 200 prep grade) was equilibrated in the buffer given in the protocol overnight at 0.1ml/min utilising the AKTAprime plus pump system. Following loading of the sample onto the column the column was run at 0.2ml/min overnight, taking 2 ml fractions.

2.3.6 Protein analysis methods

2.3.6.1 SDS PAGE

Protein samples were diluted appropriately to a final volume of 15µl, and then incubated with 5µl of NuPAGE® LDS sample buffer 4X loading dye for 20 minutes. The entire 20µl sample was then loaded into pre-cast NuPAGE® 12% Bis-Tris polyacrylamide gels (NuPAGE® system). 10µl of precision plus protein™ unstained standards (Bio-Rad) were loaded into each end of the gel if enough lanes remained. Gels were run at 180V for 50 minutes in NuPAGE® MES SDS Running buffer. Following this, gels were stained in Coomassie Brilliant Blue R250 (Or Bio-Rad™ SYPRO Ruby Protein Gel Stain for figure 5.2) for 20 minutes, followed by de-staining in MQ water overnight to attain a good contrast. Gels were then imaged in an Amersham Imager 600.

2.3.6.2 Immunoblotting (Western blot)

SDS-PAGE gels were run as stated in section 2.3.6.1, however Precision Plus Protein™ Prestained Standards Dual colour (Bio-Rad) was loaded in place of the unstained standard, and gels were not stained following being run. Instead, gels were transferred at 300mA for 1 hour onto an Invitrolon™ PVDF membrane, in 20% methanol, 200mM glycine, 25mM Tris 0.3% SDS. Following this these were blocked with 5% dried milk powder in washing solution (10mM Tris pH 7.5, 150mM NaCl, 0.05% Tween 20) for 30 minutes. The membranes were washed 3 x for 15 minutes in washing solution, then incubated overnight in an appropriate concentration (usually 2000-5000x dilution) of the primary

antibody at 4°C. After this, membranes were washed 3x in washing buffer for 15 minutes, then incubated in a 1000x dilution of anti-rabbit secondary antibody for 40 minutes. This was followed again by 3x15 minutes in washing buffer, followed by development of the membrane using the CYANAGEN WESTSTAR SUN development kit for western blot. This was then imaged using the chemiluminescence mode on the Amersham Imager 600. All antibodies were purchased from Agrisera™.

2.3.6.3 Blue Native PAGE

Protein samples were diluted appropriately to a final volume of 15µl, and then incubated with 5µl of blue native loading mix (125mM Tris pH 6.8, 30%(v/v) glycerol, 0.01% (w/v) bromophenol blue). The entire 20µl sample was then loaded into pre-cast NaivePAGE™ 4-16% Bis-Tris Gels (NuPAGE® system). Gels were run at 180V for 50 minutes in NuPAGE® NativePAGE running buffer with a 20x dilution of NativePAGE™ cathode buffer additive. Following this, gels were de-stained in MQ water overnight to attain a good contrast. Gels were then imaged in an Amersham Imager 600.

2.3.7 SATP treatment of Plastocyanin and confirmation

Treatment of plastocyanin with Pierce™ SATP (N-succinimidyl-S-acetylthiopropionate) and the subsequent deacetylation to expose the thiol group was performed as stated in the user guide on the ThermoFisher Scientific website. To confirm this SATP had attached correctly, following deacetylation the SATP treated plastocyanin was incubated with ca.30µM of Alexa Fluor™ 750 C5 Maleimide (ThermoFisher Scientific) in 20mM HEPES pH 7.4, 20mM NaCl for 1 hour. Following this it was run down a desalting column to observe in the fractions whether the dye would elute with the protein or separately.

2.3.8 Lowry assay

A detergent compatible kit was used for determination of protein concentration. Details of the protocol can be found on the Bio-Rad® website under DC™ Protein assay. No deviations were made from the protocol.

2.3.9 Kinetic absorbance measurements

Kinetic traces were recorded on an Olis RSM 1000 UV/Vis rapid scanning spectrophotometer, which facilitated a scan rate of 64 spectra per second, for a spectral width of 300nm centred on the wavelength given in the protocol.

2.3.9.1 Cytochrome b_6f stopped-flow

Two mixtures (A and B) were generated for stopped-flow experiments on cytb_6f : Pc. Mixture A comprised of 1.25mM decylplastoquinol, which has been reduced via the method seen in Trumpower and Edwards, 1979. Following this reduction and extraction, the decylplastoquinol powder was dissolved in DMSO to generate a stock, and mixture A was made from this stock. Mixture B comprised of 62.5 µM Pc, and 230nM cytb_6f. Both A and B were in a buffer of 20mM HEPES pH 7.4, 50mM NaCl, 0.2mM tPCC-α-M. A and B were mixed in a ratio of 1:4 in a USA stopped-flow accessory for the Olis, giving end concentrations of 185nM cytb_6f, 50 µM Pc, 250 µM decylplastoquinol. Control measurements were performed by omitting either decylplastoquinol (but still pipetting the same amount of DMSO into the sample as would come from the stock) or cytb_6f (to measure the background rate of ET from decylplastoquinol to Pc). The absorbance changes were measured as stated in 2.3.9, with the centre of the recorded spectra at 600nm, and the change in Pc[Ox] was measured using an extinction coefficient of 4.7mM^{-1} cm^{-1} at 597nm.

2.3.9.2 PSI flash excitation

The PSI mixture measured comprised of 215µM Pc, 500µM methyl viologen and 60nM PSI (when present), in 50mM HEPES pH 7.4, 50mM NaCl, 5mM $MgCl_2$, 0.03% (w/v) βDDM. Illumination of the PSI mixture was carried out by a 0.5W 420nm Thor labs LED at 70% power. Filters at 550nm were used to minimise the noise from illumination. The LED power was controlled by a DC2200 - High-Power 1-Channel LED Driver, and the signal for the 10 second illumination was provided by a custom-built Arduino setup. The absorbance changes were measured as stated in 2.3.9, with the centre of the recorded spectra at 600nm, and the change in Pc[Ox] was measured using an extinction coefficient of 4.7mM^{-1} cm^{-1} at 597nm.

2.3.9.3 RC-LH1 flash excitation

The RC-LH1 mixture for both WT and QE(L264) mutants comprised of 20 µM cyt c_2^{6His} (Pre-reduced via treatment with ascorbate then desalted into 50mM HEPES, 50mM NaCl, 0.03% (w/v) βDDM (kinetic buffer) to remove ascorbate, 2.3.5.4), 10nM RC^{12His}-LH1 and 50µM coenzyme Q_0 all in kinetic buffer. Excitation of the mixture was provided by a 0.5W 880nm Thor labs LED at 80% power. Filters of 730nm were used to minimise noise from illumination. The LED power was controlled by DC2200 - High-Power 1-Channel LED Driver, and the signal for the 10 second illumination was provided by a custom-built Arduino setup. The absorbance changes were measured as stated in 2.3.9, with the centre of the recorded spectra at 550nm. The changes in cyt c_2 [Red] were followed using an extinction coefficient of 30.8$mM^{-1}cm^{-1}$ at 550nm.

2.3.10 Electron microscopy

The brief electron microscopy in this thesis was performed by L.Malone, D. Swainsbury and P Qian from the Department of Molecular Biology and Biotechnology at the University of Sheffield.

2.4 Protein purification methods

2.4.1 Plastocyanin purification protocol

Spinach leaves were blended in ice cold 50mM sodium phosphate pH 7.4, 5mM $MgCl_2$, 300mM sucrose, and filtered through 2 layers of muslin cloth, and then 2 layers of muslin cloth and cotton wool. The flow through was then spun at 4000g for 15 minutes to pellet thylakoids. The pellet was then resuspended in 10mM Tricine pH 7.4, 5mM $MgCl_2$, left on ice for 1 minute, then diluted 2x in the previous buffer with an additional 400mM sucrose. This was spun at 4000g for 15 minutes, and the pellet was resuspended in 10mM HEPES pH 7.6, 5mM NaCl, 5mM EDTA to 2mg/ml chlorophyll concentration. This was then sonicated at 80% power in a VCX Vibra-Cell™ Ultrasonic Liquid Processor for a total of 12 minutes, in 30 bursts with 30 second rests. This was spun at 200,000g for 30 minutes to pellet the membranes, and the resulting supernatant was then filtered through a 0.45µM filter. This was then placed onto a Q Sepharose anion exchange column, equilibrated in 20mM HEPES pH 8.0, 5mM NaCl. A gradient of 5-1000mM NaCl was run over 50 column volumes. Fractions containing plastocyanin (eluted at ca. 200mM NaCl) were assessed by the appearance of a blue colour upon addition of potassium ferricyanide and could be confirmed via SDS-PAGE. The plastocyanin containing fractions were pooled and concentrated in a Vivaspin 3kDa cut off spin concentrator and loaded onto a FPLC gel filtration column, equilibrated in 50mM HEPES pH 8.0, 20mM NaCl. The resulting fractions

were again pooled and concentrated in a Vivaspin 3kDa cut off spin concentrator, and frozen at -20°C until use.

2.4.2 Cytochrome *b_6f* purification protocol (Optimised)

Cytochrome b_6f was purified as previously described (Dietrich and Kuhlbrandt, 1999), but with a brief 3-minute solubilisation step in HECAMEG (previously details not given). In addition, once the protein had been eluted from the hydroxyapatite column it was then placed onto a 10-35% continuous sucrose gradient in 20mM HEPES pH 8, 20mM NaCl, 0.3mM tPCC-α-M, and spun at 175,000g for 16 hours at 4°C. The resultant single band was harvested and then run on a FPLC gel filtration column equilibrated in 20mM HEPES pH 8, 20mM NaCl, 0.2mM tPCC-α-M to remove any remaining HECAMEG and ammonium phosphate as this was found to affect surface chemistry. The peak representing dimeric cyt*b_6f* (figure 3.8) from the eluted fractions was then taken, concentrated down in a 50kDa cut off spin concentrator and frozen at -80°C until use.

2.4.3 Photosystem I purification protocol (Small optimised)

Spinach leaves were blended in ice cold 30mM Tricine pH 8.0, 15mM NaCl, 400mM sucrose, and filtered through 2 layers of muslin cloth, and then 2 layers of muslin cloth and cotton wool. This was spun at 12,000g for 10 minutes and the pellet resuspended in 10mM Tricine pH 8.0. This spinning and resuspending step was repeated a further 2 times, with the second time resuspending in 10mM Tricine pH 8.0, 50mM NaCl. This was spun a final time and then resuspended in 20mM Tricine pH 8.0, 400mM sucrose to 3mg/ml chlorophyll concentration. This was briefly solubilised in 0.4% αDDM for 5 minutes on ice and then diluted 10-fold in 20mM Tricine pH 8.0, 400mM sucrose and spun at 200,000g for 30 minutes. The pellet was then resuspended in 15mM Tricine pH 8.0, 10mM NaCl, again to 3mg/ml chlorophyll concentration. This was then frozen at -80°C. Following thawing the membranes were solubilised in 1.5% βDDM for 1 hour at 4°C, then spun at 120,000g for 15 minutes at 4°C to pellet any un-solubilised material **. This was then applied to a 10-35% sucrose gradient in 15mM Tricine pH 8.0, 10mM NaCl, 0.04% βDDM and spun at 175,000g for 36 hours. The bottom band from the gradient was then taken, confirmed by 77K fluorescence, concentrated in a 100kDa cut off spin concentrator, and frozen at -80°C until use.

2.4.4 Photosystem I purification protocol ('Scaled up' optimised)

This protocol matched that in 2.4.3 until the first sucrose gradient (indicated with **). This was then applied to a 10-50% sucrose gradient in 15mM Tricine pH 8.0, 10mM NaCl, 0.04% βDDM and spun at 175,000g for 36 hours. The bottom band from the gradient had sucrose removed via a desalting column and then concentrated in a 100kDa cut off Vivaspin concentrator and ran on a 25-40% sucrose gradient made in the same buffer as before. The bottom fraction containing PSI was taken, confirmed by 77K fluorescence, then concentrated in a 100kDa cut off spin concentrator, and frozen at -80°C until use.

2.4.5 RC-LH1 purification protocol

Both variants of RC-LH1 were purified in the same way. Cells were grown semi-aerobically. Once cultures had reached saturation, they were harvested by centrifugation at 5000g for 15 minutes. The resultant pellet was then resuspended in a minimal volume of 50mM HEPES pH 7.4, 20mM NaCl. DNaseI and an EDTA free protease inhibitor were added, then the cells were French pressed twice at 20k psi to lyse cells. The resultant solution was spun at 27,000g for 15 minutes to pellet any un-lysed cells. The supernatant was then run on a 15/40% step sucrose gradient for 10 hours at 85,000g at 4°C. The chromatophore membranes at the interface on the step gradient were harvested and solubilised in 1% βDDM (w/v) for 75 minutes, in the dark. This was then spun at 165,000g for 45 minutes to pellet any un-solubilized material. The supernatant was filtered through a 0.45µm filter and loaded onto a Ni^{2+} charged IMAC column pre-equilibrated in 50mM HEPES pH 7.4, 5mM Imidazole, 100mM NaCl, 0.04% βDDM. This was then washed with the same buffer with 50mM imidazole for 5 column volumes, followed by elution in 400mM Imidazole. The RC-LH1 containing fractions were pooled, concentrated and ran on a FPLC gel filtration column equilibrated in 50mM HEPES pH 7.4, 50mM NaCl, 0.04% βDDM to remove the imidazole. Fractions with an 870/280nm ratio better than 1.6 were taken, pooled, concentrated using a 100kDa cut off concentrator and frozen at -80°C until use.

2.4.6 Cytochrome c_2 purification protocol

Strains were grown to saturation and harvested by centrifugation at 5000g for 15 minutes. The resultant pellet was then resuspended in a minimal volume of 50mM HEPES pH 7.4, 20mM NaCl. DNaseI and an EDTA free protease inhibitors were added, then the cells were French pressed twice at 20k psi to lyse cells. The resultant solution was spun at 27,000g for 15 minutes to pellet any un-lysed cells. At this point the supernatant was treated with 2% Triton-X100 and mixed in the dark for 90

minutes. This was then spun at 165,000g for 45 minutes to pellet any un-solubilized material. The supernatant was filtered through a 0.45µm filter and loaded onto a Ni^{2+} charged IMAC column pre-equilibrated in 50mM HEPES pH 7.4, 5mM Imidazole, 100mM NaCl. The column was then washed in 50mM HEPES, 20mM NaCl, 70mM imidazole, 0.5% triton for 10 column volumes, then a further 10 column volumes of same buffer excluding the 0.5% triton. Following this the cytochrome c_2 was eluted with 400mM imidazole. Cyt c_2 containing fractions were pooled, concentrated and ran on a FPLC gel filtration column equilibrated in 50mM HEPES pH 7.4, 50mM NaCl to remove the imidazole. Fractions with a 417/280nm absorbance ratio better than 3 were taken, pooled, concentrated using a 3kDa cut off concentrator and frozen at -80°C until use.

2.5 Preparation of SiOx wafers and AFM probes

2.5.1 Cleaning procedures

SiOx wafers and AFM probes were cleaned using a freshly prepared piranha solution (3:7 hydrogen peroxide : sulphuric acid) and submerged in this for ca. 1 hour. Following cleaning the wafers and probes were washed extensively with MQ water and dried under a stream of nitrogen.

2.5.2 Deposition of monolayers

2.5.2.1 MPTMS vapour deposition

Cleaned (2.5.1) SiOx wafers and AFM probes were placed into vacuum chamber with several Sciencewave™ Reusable Desi-Can™ boxes. The chamber underwent several evacuations down to 5kPa with a dry mechanical pump (Welch model 2027), and each time it was refilled with nitrogen to give a nitrogen atmosphere. These surfaces were left in the chamber after the final evacuation at 5kPa for 2 hours to dry. The dry surfaces were then place into the deposition chamber along with 2x10 µl of (3-mercaptopropyl)trimethoxysilane (MPTMS) in Eppendorf lids. The chamber then underwent several evacuations down to 5kPa using the same dry mechanical pump, and were refilled each time with nitrogen, generating a pure nitrogen atmosphere for deposition. This was then left overnight (at 5kPa) to facilitate the deposition. Following this, surfaces and AFM probes were washed extensively with MQ-H_2O and dried under a stream of nitrogen.

2.5.2.2 MPTMS liquid deposition

Cleaned (2.5.1) SiOx wafers were placed in 5mM MPTMS in toluene, and an argon atmosphere was provided by flushing the system with a Schlenk line. Following deposition for 30 minutes, these surfaces were removed and washed extensively with toluene and ethanol, then dried under a stream of nitrogen.

2.5.2.3 Ethanolamine liquid deposition

2.2g of ethanolamine hydrochloride was dissolved in 6ml DMSO by heating at 100°C for 30 minutes. 4Å molecular sieve beads were added and this was left for 1 hour at 100°C. Following cleaning (2.5.1), AFM probes and SiOx wafers were then left overnight in this solution at 100°C to functionalise the silicon surfaces with amines. Following this, wafers and AFM probes were washed with DMSO, ethanol, and chloroform 3 times, and dried under a stream of nitrogen.

2.5.3 Attachment of crosslinkers to monolayers

2.5.3.1 Reaction of SMCC with functionalised surfaces

Succinimidyl 4-(N-maleimidomethyl)cyclohexane-1-carboxylate (SMCC) was purchased from ThermoFisher Scientific™. Following deposition (2.5.2.1), surfaces were incubated with 2.5mM SMCC in 20mM HEPES pH 7.6 for 45 minutes. Following this, surfaces were again washed extensively with MQ-H_2O and dried under a stream of nitrogen.

2.5.3.2 Reaction of $SM(PEG)_n$ with functionalised probes

Following deposition (2.5.2.1 or 2.5.2.3), AFM probes were incubated in 1mM $SM(PEG)_{24}$ (prior to chapter 5) or 1mM $SM(PEG)_{2kDa}$ (from chapter 5 onwards) in 20mM HEPES pH 7.6 for 45 minutes. Following this, surfaces were washed extensively with MQ-H_2O and dried under a stream of nitrogen. $SM(PEG)_{24}$ was purchased from ThermoFisher Scientific™ and $SM(PEG)_{2kDa}$ was purchased from Nanocs™.

2.5.3.3 Reaction of DMS and Cytochrome *b_6f* combined

Following deposition (2.5.2.3), wafers were incubated with 10 µM DMS and 1 µM cyt*b_6f* in 10mM HEPES pH 7.4, 10mM NaCl, 0.2 tPCC-α-M. Surfaces were then washed extensively and stored in the same buffer until use.

2.5.3.4 Reaction of NHS – PEG – Biotin with functionalised probes

Following deposition (2.5.2.3), AFM probes were incubated with 1mg/ml NHS-$(PEG)_n$-Biotin (Purchased from Nanocs™, average molecular weight of 5kDa) in chloroform, with a 0.5% (v/v) triethanolamine catalyst for 3 hours. Following this, AFM probes were washed with chloroform, ethanol, then MQ-H_2O and stored in PBS until use.

2.5.3.5 Reaction of Maleimide – PEG – NTA with functionalised probes

Following deposition (2.5.2.1), AFM probes were incubated with 1mM Maleimide-$(PEG)_{2k}$-NTA for 1 hour in 20mM HEPES pH 7.6. Probes were then washed in MQ-H_2O, dried under a stream of nitrogen and stored in 20mM HEPES pH 7.4, 20mM NaCl, 5mM EDTA in piranha cleaned glassware until use.

2.5.4 Attachment of proteins to surfaces

2.5.4.1 Attachment of Cytochrome b_6f to SiOx wafers

Following generation of an SMCC monolayer (2.5.2.1 and 2.5.3.1), surfaces were incubated with 700nM cyt*b_6f* in incubation buffer for 45 minutes. Incubation buffer was different depending on the experiment:

Prior to section 3.3.13: 10mM HEPES pH 7.4, 10mM NaCl, 0.2mM tPCC-α-M.

Section 3.3.13: 10mM HEPES pH 7.4, 10mM NaCl, 10µM Tris, 0.2mM tPCC-α-M.

After section 3.3.14: 10mM HEPES pH 7.4, 10mM NaCl, 10µM Tris, 0.05% (w/v) GDN.

Section 3.3.14: 10mM HEPES pH 7.4, 10mM NaCl, 10µM Tris*, and one of the following: 0.2mM tPCC-α-M**, 0.03% (w/v) αDDM**, 0.05% (w/v) GDN**.

* Tris used only when stated in experiments

** Only 1 selected detergent from section 3.3.14 was used, as noted in the experiment.

Following incubation, surfaces were washed with incubation buffer, and stored in the fridge until use.

2.5.4.2 Attachment of Plastocyanin to AFM probe – Non-SATP method

Following the generation of the $SM(PEG)_n$ functionalised probe (2.5.2.1 and 2.5.3.2), this left a layer of NHS esters on the end of the AFM probe that could be reacted with lysine residues on the Pc surface. 750nM Pc was incubated with the AFM probes, in 10mM HEPES pH 7.4, 10mM NaCl (incubation buffer) for 1 hour. The AFM probes were then washed and stored in the incubation buffer until use.

2.5.4.3 Attachment of Plastocyanin to AFM probe – SATP method

Following the generation of the $SM(PEG)_n$ functionalised probe (2.5.2.3 and 2.5.3.2), this left a layer of maleimide groups on the end of the AFM probe that could be reacted with SATP treated Pc (Pc^{SATP}). The chemically modified Pc was generated by reacting 2mM SATP with 500 µM Pc for 1 hour in PBS. Following this, the mixture was applied to a desalting column to separate out unreacted SATP from the now modified protein. Immediately prior to the incubation with the AFM probe, the sample could be reacted with 50mM hydroxylamine, 2.5mM EDTA in PBS to deacetylate the SATP protection group. Following separation via desalting column, 750nM Pc^{SATP} was incubated with the AFM probes, in 10mM HEPES pH 7.4, 10mM NaCl (incubation buffer) for 1 hour. The AFM probes were then washed and stored in the incubation buffer until use.

2.5.4.4 Attachment of PSI to SiOx Wafers

Following generation of an SMCC monolayer (2.5.2.1 and 2.5.3.1), wafers were incubated with 30nM PSI in 10mM HEPES pH 7.4, 10mM NaCl, 0.03% βDDM (incubation buffer) for 45 minutes. Following this, wafers were washed and stored in incubation buffer until use.

2.5.4.5 Attachment of RC-LH1 to SiOx Wafers

Following generation of an SMCC monolayer (2.5.2.1 and 2.5.3.1), wafers were reacted with 1mM amine-NTA in 20mM HEPES pH 7.6 for 1 hour. Wafers were then washed with MQ-H_2O, dried under a stream of nitrogen and could be stored in 20mM HEPES pH 7.4, 20mM NaCl, 5mM EDTA (storage buffer) until the day of use. Immediately prior to use, surfaces were taken out of storage buffer and

washed extensively with MQ-H_2O. These surfaces were then incubated with 100mM $CuSO_4$ in H_2O for 10 minutes. After washing extensively with MQ-H_2O, the wafers were then incubated with 500nM RC-LH1 for 10 minutes in 10mM HEPES pH 7.4, 10mM NaCl, 0.03% βDDM (incubation buffer). Wafers were then washed and stored in incubation buffer until use.

2.5.4.6 Attachment of Cytochrome c_2 to AFM probes

Following generation of an NTA monolayer (2.5.2.1 and 2.5.3.5), the stored AFM probes were washed extensively with MQ-H_2O and incubated with 100mM $CuSO_4$ in H_2O for 10 minutes. Following this they were washed extensively in MQ-H_2O and then incubated with 10µM cyt c_2 in 10mM HEPES pH 7.4, 10mM NaCl (incubation buffer) for 10 minutes. Probes were then washed and stored in incubation buffer until use.

2.5.4.7 Attachment of Avidin to mica surface

An avidin stock solution of 1mg/ml in PBS was diluted with 100mM NaCl to a concentration of 0.5ug/ml. Freshly cleaved mica surfaces were incubated with this solution for 15 minutes, followed by washes with 100mM NaCl, and then PBS. These surfaces were then imaged immediately in PBS.

2.5.4.8 Immobilisation in liposomes – DOPC method

18:1 (Δ9-Cis) PC (DOPC) was purchased from Avanti® Polar lipids inc. and dissolved into chloroform at a concentration of 20mg/ml and stored at -20°C. Prior to use, an aliquot from this stock was placed in piranha cleaned glassware and left in a fume cupboard for the chloroform to evaporate and form a lipid cake. This was then dissolved in 20mM MOPS, pH 7.8, 20mM NaCl to a concentration of 1mg/ml and vortexed. This suspension was downsized by extruding 50 times through a 0.2µM pore polycarbonate membrane (Whatman Nucleopore) to form small uni-lamellar vesicles. The liposome solution was incubated with 0.2mM (end concentration) tPCC-α-M for 30 minutes. Following this, purified cytb_6f was introduced to the sample at the various mol/mol ratios to the lipids given in image in figure 3.26, and the proteoliposome solution was left for 1 hour at 4°C. The redundant tPCC-α-M was then removed slowly by the addition of nonpolar polystyrene biobeads (Bio-Rad, Bio-Beads™ SM-2 Adsorbents) gradually to the mix, with slow rocking at 4°C. When a sucrose gradient was present (figure 3.26), the step gradient was made in a buffer of 20mM MOPS pH 7.8, 20mM NaCl with steps from 10-50% (w/v) increasing by 10% for each layer, and centrifuged at 154,000g for 15 hours. Bands had some slight colour and had concentrated at the 20-30% interface. The extracted bands were

incubated with a freshly cleaved mica surface for 30 minutes, followed by washing with 20mM MOPS, 20mM NaCl and imaged in this buffer.

2.5.4.9 Immobilisation in liposomes – Thylakoid lipid method

A stock lipid solution was produced comprised of 50% Monogalactosyldiacylglycerol (MGDG), 10% Phosphatidylglycerol (PG), 30% Digalactosyldiacylglycerol (DGDG) and 10% Sulfoquinovosyldiacylglycerol (SQDG), all purchased from Avanti® Polar lipids inc. in chloroform and stored at -20°C. For use, an aliquot of the solution was placed into a piranha cleaned glass vial and the chloroform allowed to evaporate, generating a lipid cake. This lipid cake was resuspended in 20mM HEPES pH 7.4, 40mM NaCl, pH 7.5 by vigorous vortexing. This suspension was downsized by extruding 20 times through a 0.2µM pore polycarbonate membrane (Whatman Nucleopore) to form small uni-lamellar vesicles. The liposome solution was incubated with 0.2mM (end concentration) tPCC-α-M for 30 minutes. Following this, purified cytb_6f was introduced to the sample at the various mol/mol ratios to the lipids given in image in figure 3.26, and the proteoliposome solution was left for 1 hour at 4°C. The redundant tPCC-α-M was then removed slowly by the addition of nonpolar polystyrene biobeads (Bio-Rad, Bio-Beads™ SM-2 Adsorbents) gradually to the mix, with slow rocking at 4°C. When a sucrose gradient was present (figure 3.26), the step gradient was made in a buffer of 20mM HEPES pH 7.4, 20mM NaCl with steps from 10-50% (w/v) increasing by 10% for each layer, and centrifuged at 154,000g for 15 hours. Bands had some slight colour and had concentrated at the 20-30% interface. The extracted bands were incubated with a freshly cleaved mica surface for 30 minutes, followed by washing with 20mM HEPES pH 7.4, 20mM NaCl and imaged in this buffer. Also, some experiments included LHCII (Prepared by T.Davies) in addition to cytb_6f, and in these cases the ratios of cytb_6f : LHCII : Lipids were 1 : 1 : 200.

2.5.5 Fixing SiOx wafers for AFM imaging

For all processed encompassed in section 2.5 which functionalised a SiOx wafer, for AFM imaging the wafer was fixed down to a 0.75cm radius magnetic puck by Reprorubber® Thin pour kit.

2.6 Atomic Force Microscopy

2.6.1 Instrumentation

Atomic force microscopy measurements were made on a Bruker Multimode VIII, with software of Nanoscope 9.1/9.2. Bruker's Peak Force Quantitative Nanomechanical Mapping™ (PF-QNM) mode was used for all imaging and force spectroscopy work, unless stated otherwise.

2.6.2 Imaging

All imaging (non – SMFS work) was performed in PF-QNM liquid mode. Unless stated otherwise, a buffer of 10mM HEPES pH 7.4, 10mM NaCl, along with the detergent the protein was in, was used at room temperature (ca. 20^{o}C). Repetition rates of 1-2kHz imaging were used to obtain images. An interaction setpoint of 150mV was consistently used for imaging, resulting in a ca. 100-300pN force applied to the surfaces. Pixel density of either 256 x 256 or 512 x 512 pixels were used. Brukers SNL probes were used for nearly all imaging, in rare cases AC-40 tips were also used for imaging.

2.6.3 Force spectroscopy measurements

All force spectroscopy measurements were performed with PEAKFORCE-HIRS-SSB probes. Spring constants were nearly uniformly around 0.1 N/m and deflection sensitivity ca. 10 nm/V. Redox states of the participants were set by incubation with 1mM sodium ascorbate for reduction, or 1mM potassium ferricyanide for oxidation prior to imaging, followed by extensive washing. Redox states of the participants were then maintained (when it was proposed they could change) in the experiment by re-incubation of the functionalised wafer and AFM probe every 2 images taken. When illumination was present, it was provided from a white light source through an optical fibre (Fibre-Lite MI150, Dolan-Jener) and the power density of the illumination of the sample was approximately 11W m^{-2}. Due to differences in tip functionalisation that could occur, each measurement in the change of affinity was a relative measurement between datasets using the same probe / surface (apart from experiments on mutant/WT complexes seen in section 6.3.7). This meant that at the start of each experiment, one state of the system (e.g. cytb_6f[Red] – Pc[Ox]) was set, and a number of images were obtained, recording FdC's. Following this, the conditions of the system were changed (e.g. cytb_6f[Ox] – Pc[Ox]), and further data was recorded, leading to a relative measurement between the same probe/surface.

Imaging parameters were as follows:

Scan size: 500nm

Scan Rate: The imaging rate was adjusted in a way that ensured two force–distance curves recorded per image pixel.

Samples/Line: 128

Feedback gain was controlled by ScanAsyst software. No other parameters were changed by ScanAsyst Autocontrol.

PeakForce setpoint : 0.2-0.3V (converted to a force of ca. 200pN)

PeakForce amplitude: 30-40nm

PeakForce Frequency: 0.5kHz

Force curves were recorded for each pixel. An engage PeakForce of 0.3V was used to ensure that the AFM probe did not suffer damage upon engaging with the surface.

Buffers used unless indicated otherwise:

cytb_6f : Pc - 10mM HEPES pH 7.4, 10mM NaCl, 0.05% (w/v) GDN

PSI : Pc - 10mM HEPES pH 7.4, 10mM NaCl, 0.03% (w/v) βDDM

RC-LH1 : cyt c_2 – 10mM HEPES pH 7.4, 10mM NaCl, 0.03% (w/v) βDDM

Tip parameters were attained using inbuilt methods in the Bruker NanoScope 9.1 software. In brief, once AFM measurements had been attained, the sample was changed to the Veeco Saphire-15M sample included in the PF-QNM sample kit. This was used to obtain the deflection sensitivity by driving the AFM probe into this surface and measuring the resultant deflection of the probe (Setpoint of 1V used). The slope was taken from the linear region of the resultant force distance curve, and used as the deflection sensitivity. Following this the sample and tip were moved apart, and the inbuilt thermal tune system was used to attain the power spectral density of the cantilever, followed by fitting and integration of the peak to attain the power. This was then used by the inbuilt program to calculate the spring constant of the cantilever.

2.6.4 Data analysis of force spectroscopy images

The analysis script used for all the SMFS analysis is presented in appendix (section 8.1). In brief, the user would input directory for the PF-QNM files, then input the analysis parameters as seen in the panel in figure 3.17B. This involved the AFM probe parameters of the deflection sensitivity (nm/V) and spring constant (N/m) to allow the initial raw read out of the photodetector (V) to be converted into force (N). In addition, some analysis parameters could be set out, to provide the location on the force curves to search for troughs in. These analysis parameters were the minimum adhesion force, and the minimum and maximum piezo movement from the location where the PeakForce was reached. While the piezo movement could be converted into the separation distance this relied on the ability to attain a baseline for the data. While this is attempted in the MATLAB script, it was not reliable enough to ensure the correction was valid, and thus this baseline was not then used to convert the raw piezo movement to separation distance. The user would be shown the force curve which passed the initial filtering parameters, and the location on the surface where it occurred, and they would be able to

select the adhesion location on the curve to have the final input. If the baseline in the data was incorrect, then this could be corrected for by selecting two locations of the FdC. When selecting two locations in the data, the script assumes that the first is the correct baseline according to the user, and the second is the adhesion location. Following the analysis of a data set (all the PF-QNM files in a directory) the program would output several csv files with different organisations of the data to make analysis easier. For example, one output would simply be the number of selected adhesions per image, while another would have all the sizes of the adhesions and their locations for each image.

As previously stated, the data sets measured differences in affinity based on different conditions, and were always a relative measurement between the same probe and surface under the different conditions. Once the outputs from the MATLAB program had been generated, the mean for each tip in each condition was obtained. The mean of the initial condition for each experiment (e.g. cytb_6f[Red] – Pc[Ox] for experiments of redox state on cytb_6f and Pc) was then used to adjust the frequency in each image (for both conditions), giving the adjusted frequency. As such, an experiment in which the initial condition saw a mean of 100 adhesions per image, and the second condition saw 50 adhesions per image would be equal to another repeat in which a different probe only yielded a mean of 60 adhesions per image on the initial condition, and 30 adhesions in the second condition. Once this had been performed, the adjusted frequencies for all probes in each condition were collected, and could be statistically analysed, with each image representing an experimental repeat. For testing of two different conditions, an unpaired T-test was used to assess the statistical significance of any difference seen. For testing of more than two conditions, one-way ANOVA's were used to compare differences between all pairs in the data (as seen in figure 4.4), or to search for trends (as in figure 4.5). These adjusted frequencies were also then used to adjust the cumulative frequencies of the forces shown in the histograms in all the experiments, so that the cumulative frequencies represented the adjusted frequencies seen in the interaction frequencies. The measured unbinding forces were collected and statistically analysed in Graphpad Prism 7, and plotted in Origin 2017/8/9, according to the above description. For each result in this thesis, the results of the statistical tests are given in the figure legend.

2.7 Bibliography

Dietrich, J., and Kuhlbrandt, W. (1999). Purification and two-dimensional crystallization of highly active cytochrome b6f complex from spinach. *463*, 97–102.

Hunter, C.N., and Turner, G. (1988). Transfer of Genes Coding for Apoproteins of Reaction Centre and Light-harvesting LH1 Complexes to Rhodobacter sphaeroides. Microbiology *134*, 1471–1480.

Trumpower, BL, Edwards, C.A, Purification of a reconstitutively active iron-sulfur protein (oxidation factor) from succinate. cytochrome c reductase complex of bovine heart mitochondria, J. Biol. Chem. 254 (1979) 8697–8706.

Vasilev, C., Brindley, Aa, Olsen, JD., Saer, R.G., Beatty, J.T., Hunter, C.N. Nano-mechanical mapping of the interactions between surface-bound RC-LH1-PufX core complexes and cytochrome c 2 attached to an AFM probe., Photosynth. Res. 120 (2013) 169–80.

3. Establishing Single Molecule Force Spectroscopy experiments

3.1 Summary

Single molecule force spectroscopy (SMFS) experiments require purified proteins to be attached to an AFM probe. These probe-protein conjugates can be used to interrogate the binding of the probe borne protein with a cognate partner attached to a surface. Attaching proteins to inorganic surfaces, whether it be the AFM probe or a silicon wafer, is not trivial. Initially, the inert surface must have some form of functionalisation in order to create a monolayer which presents a more reactive chemical group. Next, a linker molecule is added, one end of which reacts with the monolayer chemistry while the other end harbours a specific chemical group allowing it to be coupled to a protein. Finally, the protein itself is attached to the linker molecule, with various methods available to control the final density.

The aim of the experiments in this chapter were to establish the optimal conditions for the attachment of the small soluble electron carrier protein plastocyanin (Pc) to the AFM probe and its cognate electron transfer partner cytochrome b_6f (cytb_6f) to a silicon surface. Whilst previous SMFS studies on bacterial systems (e.g. Vasilev et al., 2013) utilised recombinant proteins engineered for specific attachment via hexa-histidine tags, this option was unavailable for the spinach complexes. Therefore, methods for the purification of native Pc and cytb_6f from spinach were adopted and developed.

Cytb_6f could be prepared at high purity using an existing protocol based on extraction from thylakoids using the detergent Methyl-6-O-(N-Heptylcarbamoyl)-α-D-Glucopyranoside (HECAMEG). Cytb_6f was attached to an MPTMS monolayer on a silicon wafer via SMCC linker which reacts an NHS-ester to lysine residues on the protein. Unfortunately, due to HECAMEG's high critical micelle concentration (CMC), incubation of the purified complex with the MPTMS-SMCC monolayer resulted in non-specific absorption of the detergent to the surface preventing a covalent attachment. Therefore, the cytb_6f protocol was adapted to include an additional step exchanging the complex into HEPES buffer and the detergent 4-trans-(4-trans-Propylcyclohexyl)-cyclohexyl α-maltoside (tPCC-α-M). The combination of tPCC-α-M and HEPES allowed surfaces of cytb_6f complexes to be generated at a suitable density. The activity and intactness of the cytb_6f preparation under these new conditions was further verified by both activity and structural studies (Structural studies conducted by L. Malone).

Whilst the attachment of cytb_6f to the silicon wafer could be verified by the height image generated in AFM imaging, there was no analogous way of assessing whether the linkage of Pc to the AFM probe had been successful. Since initial Pc : cytb_6f SMFS experiments provided no evidence of specific interactions subsequent efforts focused on improving the reliability of Pc attachment to the probe.

The method described in Johnson et al., 2014 involved an initial functionalisation step which required deposition of (3-Mercaptopropyl)trimethoxysilane) (MPTMS) in vapour phase. As an alternative, attempts were made to deposit MPTMS via liquid phase, but these also proved inadequate with the materials available. Following this, the switch to an alternative functionalisation method involving ethanolamine attachment chemistry was made. Following verification by the traditional biotin : avidin experiments (Lee et al., 1994), which has been seen as a baseline to assess new methods of surface chemistry (Riener et al., 2003), the specific interactions between Pc and cytb_6f could be successfully detected by SMFS. The mean unbinding force from this was significantly lower than previously measured by Johnson et al., 2014 on native membranes. This was thought to stem from the modification involved in Pc attachment to the probe via the ethanolamine method affecting the cytb_6f binding site on Pc.

The arrival of a new vacuum chamber in the laboratory provided an opportunity for the MPTMS attachment method of Pc to the probe in Johnson et al., 2014 to be revisited. Utilising the new hardware Pc probes were generated that allowed specific interactions between Pc and cytb_6f to be successfully detected by SMFS with an unbinding force similar to that reported in Johnson et al., 2014 (~310 pN). In addition, a second 230pN population was also detected. Observing the heights measured for the cytb_6f on the surface it appeared that a significant number of the complexes were orientated with their membrane plane perpendicular to the SiOx wafer (figure 3.23A). We therefore sought to investigate if this mis-orientated cytb_6f was responsible for the lower force population. As an alternative a number of conditions were trialled in attempts to orient the cytb_6f attached to the surface, and showed that 10 µM Tris, along with 0.05% (w/v) GDN could be used to retain cytb_6f in an 'upright' conformation on the silicon surface for prolonged periods.

Attempts were made to incorporate cytb_6f into proteoliposomes in either DOPC, or native thylakoid lipids that could then be deposited onto a mica surface with the aim of generating uniformly oriented complexes. Unfortunately, none of the initial tests showed any signs of cytb_6f being correctly incorporated into the membrane, and this method was abandoned.

The experiments described in this chapter therefore establish a robust system in which we could probe the interaction between cytb_6f and Pc, and observe the effect of ionic strength and redox state (Chapter 4, and the basis of Mayneord et al., 2019).

* A version of this work was published in Biochimica et Biophysica Acta (Mayneord et al., 2019). All rights and permissions for all visual data and artwork have been granted.

3.2 Introduction

In oxygenic photosynthesis the small soluble electron carrier protein Pc accepts an electron from the c-type haem of cytochrome *f* and delivers it to the P700 special-pair chlorophylls of PSI (section 1.1.2.5, and reviewed in Hope, 2000). The redox active cofactor in Pc is a copper ion, which cycles between a +1 and +2 oxidation state to carry electrons. This type 1 copper results in a broad absorbance in the oxidised (+2) state centred around 600nm, giving rise to a distinct blue colour. This allows an easy identification of fractions containing Pc during purification, and the ratio of absorbance at 600 and 280 nm is often used for an assessment of purity during purifications (Navarro et al., 2011). Several purification methods have been developed for the purification of untagged, native Pc directly from higher plants, green algae and cyanobacteria (Navarro et al., 2011). Detail on the interaction of Pc with cytb_6f and PSI can be found in chapters 4.2 and 5.2 respectively.

The membrane embedded complex cytb_6f is comprised of several subunits; the larger units visible via SDS-PAGE are Cytochrome *f* (31kDa), Cytochrome b_6 (18kDa), Reiski protein (18kDa) and subunit IV (14kDa) (Dietrich and Kuhlbrandt, 1999). Whilst earlier purification methods relied on general solubilisation of the thylakoid membrane, followed by chromatography steps in order to enrich cytb_6f (Huang et al., 1994), the development of the detergent Methyl-6-O-(N-Heptylcarbamoyl)-α-D-Glucopyranoside (HECAMEG) allowed the specific enrichment of cytb_6f at the stage of solubilisation, first used in *C. reinhardtii* (Pierre et al., 1995), and then in spinach (Dietrich and Kuhlbrandt, 1999). This permitted a simpler purification, only requiring the solubilisation, a sucrose gradient and then a type 1 ceramic hydroxyapatite column to yield high purity viable complex (Dietrich and Kuhlbrandt, 1999).

Traditional bulk-phase kinetic measurements have been extensively used to characterise purified electron transferring proteins both *in vitro* and *in vivo*. While these ensemble studies have been useful in defining the general characteristics of electron transfer (ET) complexes, the averaging involved can obscure heterogeneity inherent in the system. Studies of single molecules interacting, in particular force spectroscopy measurements, have become a popular way of probing previously hidden aspects of interactions since the initial work in Lee et al., 1994. Since this inception, many different systems have been probed using the technique of single molecule force spectroscopy (SMFS) including not only protein-protein interactions (Adams et al., 2016; Bonanni et al., 2005; Vasilev et al., 2013, 2019), but protein – ligand (Fritz et al., 1998; Merkel et al., 1999; Yu et al., 2007) and protein – DNA interactions (Krasnoslobodtsev et al., 2007). Whilst these studies followed the same general schematic as seen in section 1.4.1, the chemistry used for attachment has varied from study to study (Summarised in Ebner et al., 2008).

Many options are now available for the attachment of proteins to surfaces, either by specifically engineered sites such as a cysteine residue, or a hexa-his tag, or by less specific methods such as attachment to primary amines of lysine residues on the protein's surface. These methods of covalent or coordination chemistry for attachment of proteins to linkers are well established, and relatively flexible. Issues with the successful attachment of biomolecules to crystalline silicon or gold surfaces generally arises from the functionalisation chemistry employed. Both silicon and gold are relatively chemically inert surfaces, and thus the first stage in these experiments is the creation of a monolayer to present more chemically reactive groups for attachment of the biomolecule. On silicon, the modifications are commonly to primary amine groups, such as those in (3-Aminopropyl)triethoxysilane (APTES) or ethanolamine, or thiol groups such as (3-Mercaptopropyl)trimethoxysilane (MPTMS). Following this these chemical groups offer a wide range of linkages, usually through a heterobifunctional (two ends, with different reactivities) linker to allow attachment to the surface at one end, and to the protein/ligand/DNA at the other.

Issues with the initial stages of functionalisation of either silicon or gold surface can stem from poor cleaning of the initial surface, or with issues in the deposition of the monolayer itself. Generally, use of gold surfaces requires fresh samples to be prepared each time (by depositing the gold on another adhesion layer such as chromium), as once deposited, many cleaning methods can damage or strip the surface entirely. Silicon is a good alternative, as crystalline silicon wafers can be extensively cleaned using harsh methods, such as piranha cleaning (H_2O_2 + H_2SO_4). In addition, this generates a layer of silicon oxide (terminating in hydroxyl groups) for simple functionalisation with MPTMS, APTES or ethanolamine.

The initial experiments using SMFS probed the interaction between Biotin and Streptavidin, one of the strongest known non-covalent interactions in biochemistry (Lee et al., 1994). In more recent years, the interaction between Biotin and Avidin has been used as an effective test method (Ebner et al., 2007a, 2007b; Riener et al., 2003; Wildling et al., 2011) for new linkage chemistry, due to the interaction's strength and reliability, as well as the commercial availability of both components. As a result, it can be used to troubleshoot problems in experiments where measurements such as surface density are not available.

Whilst most previous SMFS studies have focussed on bound complexes that exist from seconds to hours using force volume ramping, the study of more transient complexes requires faster movement. This can be provided by the peak-force quantitative nanomechanical mapping (PF-QNM) AFM mode (section 1.3.3), initially used to probe the interaction between cytochrome c_2 and RC-LH1 from *Rba.sphaeroides* (Vasilev et al., 2013). Whilst this study relied on both proteins being attached to gold surfaces, the work using PF-QNM was developed further by studying on the interaction between Pc

and attached to a Silicon nitride AFM probe, and cytb_6f in the native grana membranes adsorbed to a mica surface (Johnson et al., 2014). In both studies, the lifetime of the bound complex was well below 1ms, requiring the speed only available via PF-QNM. As previously summarised in section 1.3.3, with speeds up to 4kHz available for imaging in liquid, PF-QNM offers the time resolution required to probe such transient interactions. In addition, the high-resolution simultaneous height and adhesion images that are generated in PF-QNM also allow for the easy correlation of locations of adhesions on the surface, offering another method for data verification.

Previous SMFS studies have generally been on soluble proteins, which did not require the presence of detergents. Whilst the aforementioned methods of linkage have proven functional, the ideal scenario would be the incorporation of purified proteins into a native lipid environment which could then be adsorbed to a flat surface. Liposomes have not previously been applied to SMFS experiments but have been used to characterise a number of different spectral and energy transferring properties from higher plant photosynthetic components (Moya et al., 2001). Due to their ability to easily adsorb to a mica surface, it would appear that liposomes present the ideal candidate for SMFS experiments on membrane proteins.

A crucial factor in attaching molecules to surfaces for SMFS work, whether in direct covalent linkages to the surface or via proteoliposomes, is the control of protein density. Whilst the previous affinity mapping study of cytb_6f : Pc in Johnson et al., 2014 utilised isolated grana membranes, the data sets for the interaction were understandably limited by the number of cytb_6f in a membrane patch. The goal with using purified cytb_6f was to achieve high enough surface density of active protein that large datasets on the interaction could be easily obtained as in Vasilev et al., 2013 and 2019.

3.3 Results

3.3.1 Purification of Plastocyanin

The purity of protein samples required for SMFS work is relatively high, especially for circumstances where proteins are attached non-specifically (As opposed to attachment by engineered specific linkage sites such as a cysteine residue or hexa-His tag). No recombinant methods were currently available in our lab for purification of Pc, but relatively extensive methods already exist for the purification directly from spinach. A simplified method from the original Navarro et al., 2011 spinach method was used, with a number of steps removed for time and yield sake. This method was described in Mayneord et al., 2019 and in the Materials and Methods section 2.4.1 of this thesis. The SDS – PAGE in figure 3.1A displays the end purified product, running at ca. 12.5 kDa due to charge (Actual molecular weight (MW) of 10.5 kDa). The faint upper band at ca. double the apparent MW was thought to be due to the presence of an additional acidic isoform that runs aberrantly on SDS-PAGE, and thus was tested via western blot seen in figure 3.1B, where reactivity of both bands to a Pc antibody is shown, as previously seen (Agrisera Website). Following treatment of the sample with Laemmli buffer however yielded a single band, indicating that the double MW band was in fact dimerised complex via disulphide bonds upon unfolding. Figure 3.1C shows the absorbance spectra for Pc, with the given broad peak centred at ca. 600nm from the type 1 copper cofactor. The purification gave a 280/597nm ratio of 1.9 (Oxidised form). This, along with the SDS-PAGE confirmed the sample was sufficiently pure for use in SMFS experiments.

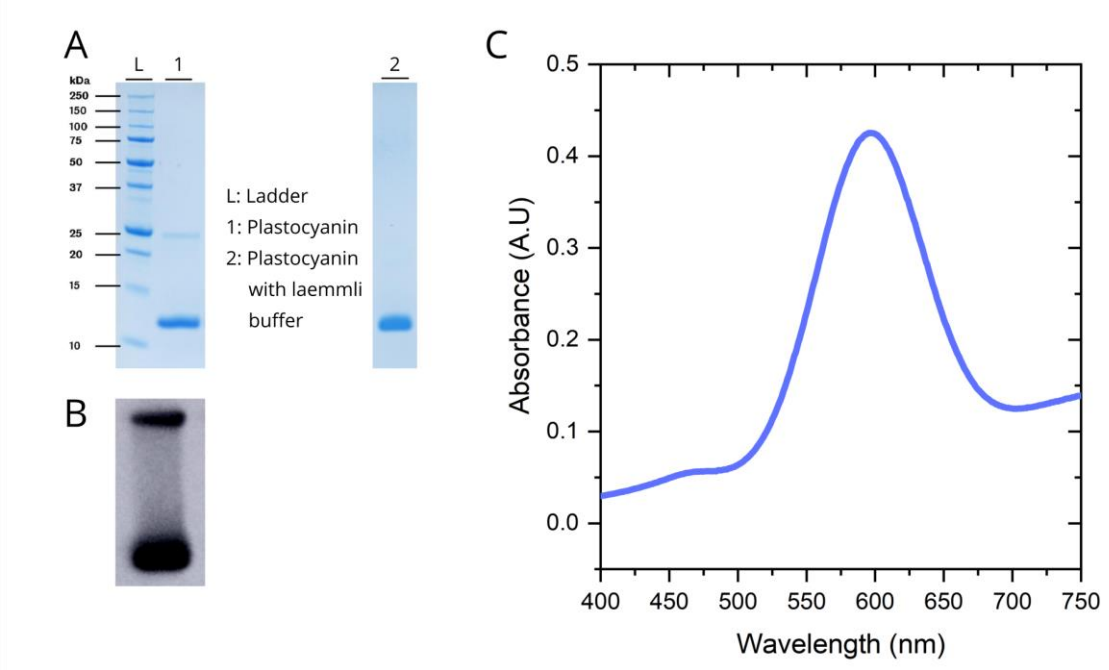

Figure 3.1 Proof of purification of Plastocyanin from native spinach

*(**A**) SDS-PAGE of end purified product, showing the normal ca. 12.5kDa band for Pc. An additional band is seen at ca. twice the molecular weight. This was initially believed to be a more acidic isoform of the protein, as addition of reducing agents to remove disulphide bonds did not remove it. However, running the sample in Laemmli loading buffer removed the now identified dimer band, as seen in lane 2. (**B**) Western blot using a Pc antibody, showing the reactivity of both bands seen in A. (**C**) Absorbance spectra showing the peak from the copper cofactor in the structure.*

3.3.2 Purification of Cytochrome b_6f

Previous methods have shown a simple, effective purification of cytb_6f from both spinach (Dietrich and Kuhlbrandt, 1999) and *C.reinhardtii* (Pierre et al., 1995) using the detergent HECAMEG. These methods relied on the ability of HECAMEG to specifically extract cytb_6f from its lipid rich regions in the thylakoid membrane. As the previous protocol for spinach contained no details on solubilisation conditions (Dietrich and Kuhlbrandt, 1999) initial optimisations needed to be performed. Given the spectra of cytb_6f, a simple method was devised for the quick analysis of purity and yield of cytb_6f fractions. Tracking the absorbance signal at 420nm (the unique Soret band from the bound haems and chlorophyll) could be used to observe the amount of cytb_6f. The ratio between 420nm (cytb_6f) and 440nm (from other photosynthetic components' chlorophyll) would allow a test for the enrichment of the solubilised fractions. Using these two measurements, solubilisation trials were carried out testing the effect of both time and concentration of the detergent. Following this, solubilised samples

were centrifuged for 15 minutes at 80,000g to pellet unsolubilised material. The supernatant was extracted and an absorbance spectrum was taken. The results are shown in figure 3.2. Red data points (figure 3.2 B,D) show the ratio of 420/440nm for thylakoid membranes prior to solubilisation. The solubilisation time (A/B, all performed at a concentration of 1% HECAMEG) had no apparent effect on either the relative amount (A) or the purity (B), thus suggesting that the HECAMEG acts quickly on the sample and following this no further effect is seen.

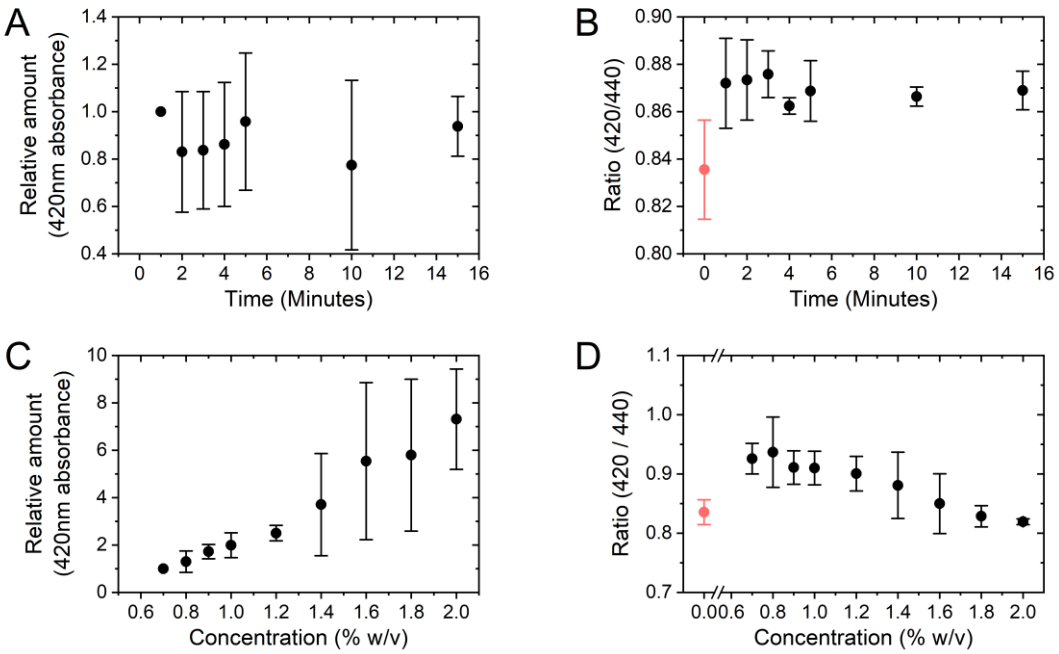

Figure 3.2 Solubilisation trials of Cytochrome b_6f in HECAMEG, Time and Concentration

*Effect of time of solubilisation (in 1% HECAMEG) on (**A**) the amount of material obtained (adjusted relative to 1 minute in each trial) and (**B**) the purity of the material. (**C**) Effect of concentration on the amount of material obtained and (**D**) on the purity of the material for a 2-minute solubilisation. Relative amount in A and C is from the comparison of the absorbance at 420nm in the sample vs the absorbance seen at (A) 1 minute or (C) 0.7%.*

The effect of increasing the concentration of HECAMEG was an increase in the amount of material solubilised, as seen in figure 3.2C. However, the purity of the 'enriched' supernatant decreased at higher concentrations of HECAMEG (figure 3.2D), most noticeably over 1.2% w/v, ultimately decreasing to the equivalent of non-solubilized thylakoids at 1.8%. This showed that while the time for solubilisation had little to no effect, higher concentrations of HECAMEG were not effective at enriching cytb_6f. From this, a concentration of 1% HECAMEG was chosen, and a time of 3 minutes, as

later used in Mayneord et al., 2019. Following the solubilisation, the enriched supernatant was placed onto a 10-35% sucrose gradient in 0.8% HECAMEG and spun at 125,000 g for 16 hours (See materials & methods section 2.4.2). The resultant gradient can be seen in figure 3.3A. From this, the dark brownish band (indicated arrow) was taken and loaded onto a type-1 Ceramic Hydroxyapatite column (CHT column). This was washed with 5 column volumes of 100mM Ammonium phosphate buffer pH 8.0, removing any remaining green colour from the column and leaving a brown band which was then eluted by 400mM ammonium phosphate buffer. All column stages were performed in the presence of 0.8% HECAMEG. See materials and methods section 2.4.2 for more detail. This sample was then frozen and stored at -80°C until use, and an SDS-PAGE of the purification process can be seen in figure 3.3B, with visible cytb_6f subunits highlighted.

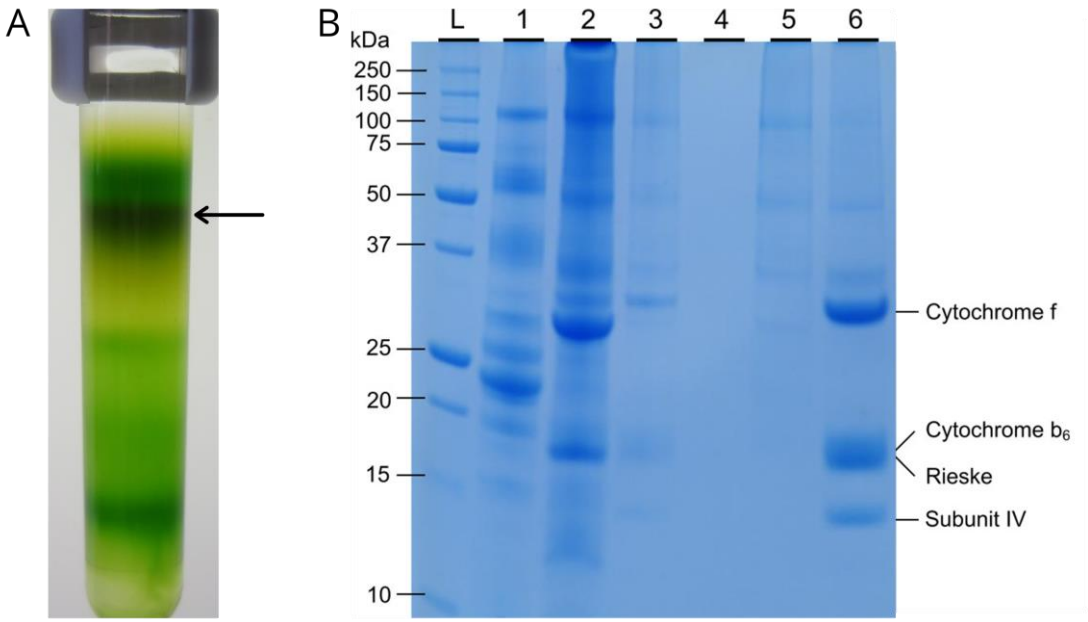

Figure 3.3 Purification of Cytochrome b_6f

*(**A**) Sucrose gradient of the supernatant following HECAMEG solubilisation. The dark band indicated (arrow) was extracted. (**B**) SDS-PAGE of the cytb_6f purification process. Lanes: L) Ladder, 1) Thylakoid membranes, 2) Supernatant from HECAMEG solubilisation, 3) Fraction taken from sucrose gradient (A, arrow), 4) Flow through loading CHT column, 5) CHT column elution with 100mM Ammonium phosphate (Wash), 6) CHT column elution with 400mM Ammonium phosphate.*

3.3.3 Initial surface immobilisation of Cytochrome b_6f

A diagram for the surface immobilisation chemistry used is shown in figure 3.4, with A and C showing the components of the linkages, and B and D showing the final products for protein immobilisation on

both the SiOx wafer (A,B) and AFM probe (C,D). While other detergents such as n-Dodecyl β-D-maltoside (βDDM) have been used previously for surface immobilisation of membrane proteins (Vasilev et al., 2013, 2019), no previous studies using HECAMEG could be found. The final linkage stage to the protein (reaction of the N-Hydroxysuccinimide (NHS) esters with primary amines on the protein) is susceptible to hydrolysis in aqueous solvents (Figure 3.4B, RHS showing a hydrolysis product). As such, changing the concentration of the protein can be an easy was to control surface density, as the water effectively competes with the primary amines for linkage. Initial immobilisation experiments were performed, using the chemistry shown in figure 3.4 and with a protein concentration ranging

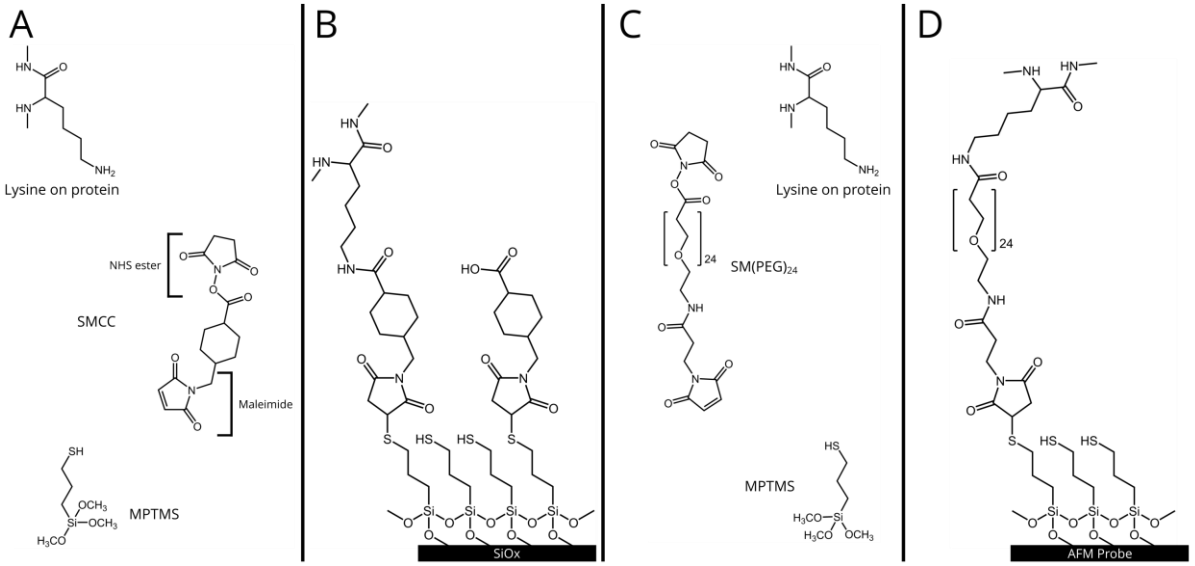

Figure 3.4 Surface chemistry for immobilisation proteins

*Surface chemistry used for protein immobilisation. (**A**) Individual components used to attach cytb$_6$f to SiOx wafers (with NHS ester and maleimide groups hightlighted), and (**B**) the end product of the linkage. (**C**) Components used for attachment of Pc to the AFM probe, and (**D**) the end product of the linkage. For B and D, by-products of the reactions are omitted. (SMCC: (succinimidyl 4-[N-maleimidomethyl]cyclohexane-1-carboxylate). SM(PEG)24: (succinimidyl-[(N-maleimidopropionamido)-tetracosaethyleneglycol] ester) MPTMS: (3-Mercaptopropyl)trimethoxysilane))*

from 5nM to 1µM. Figure 3.5 shows AFM images taken of the wafers following the immobilisation steps, at two different concentrations and times for incubation, showing no distinguishable difference. Previous work has shown that this range of concentrations is optimal for the immobilisation (Ebner et al., 2007a, 2007b; Johnson et al., 2014; Vasilev et al., 2013, 2019). While some aggregation of the

cytb_6f on the surface can be seen, this was not thought to be responsible for the lack of response to protein concentration. Instead it is believed that the high critical micelle concentration (CMC) of HECAMEG results in the surface effectively being coated, allowing the protein to adsorb to the surface, and not covalently attach. At this point it was decided that the cytb_6f should be transferred into a different detergent with a lower CMC.

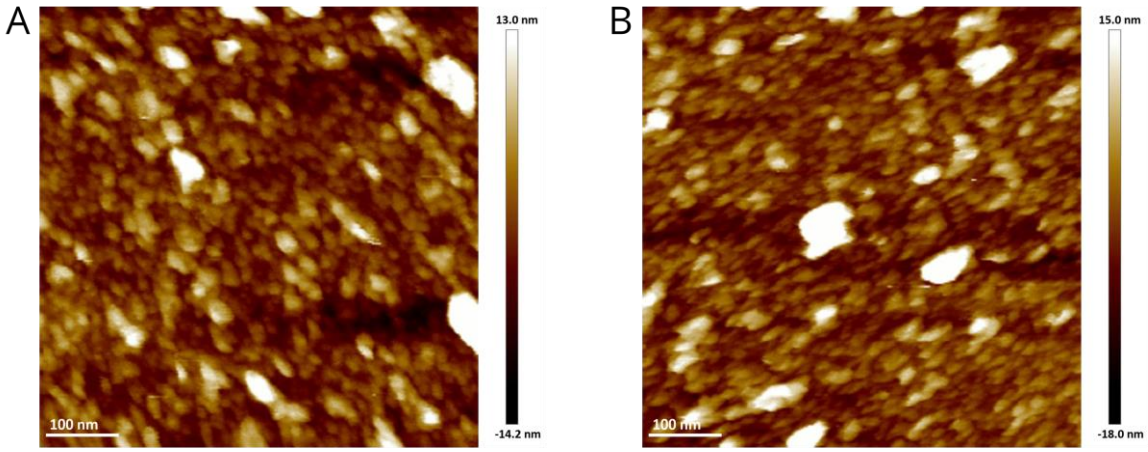

Figure 3.5 Testing of surface immobilisation of the Cytochrome b_6f complex

*AFM images of the surface generated from incubating (**A**) 500nM of cytb_6f, for 45 minutes and (**B**) 50nM cytb_6f for 10 minutes. As both appeared to be effectively coating the surface, it was assumed the high concentration of detergent was allowing the protein to be adsorbed on the surface non-specifically.*

The detergent 4-trans-(4-trans-Propylcyclohexyl)-cyclohexyl α-maltoside (tPCC-α-M) had previously displayed the ability to retain high cytb_6f activity, even following long storage at room temperature (Hovers et al., 2011). Previous studies using this detergent had relied on his-tagged cytb_6f to allow for simple purification by immobilised metal affinity chromatography (IMAC) columns. As this was not available for our experiments, our original HECAMEG purification method could still be used, with the cytb_6f then being exchanged into the new detergent. A sucrose gradient was used for exchanging the protein, still containing the 400mM ammonium phosphate, however with 0.4mM tPCC-α-M for exchange. Figure 3.6A shows the sucrose gradient, with the arrow indicating the band taken onwards. Following this the sucrose was removed by a desalting column, being exchanged into 400mM ammonium phosphate pH 8.0, 0.3mM tPCC-α-M, and the protein was again incubated with freshly prepared NHS-ester terminated surfaces (figure 3.4) and imaged by AFM, shown in figure 3.6B.

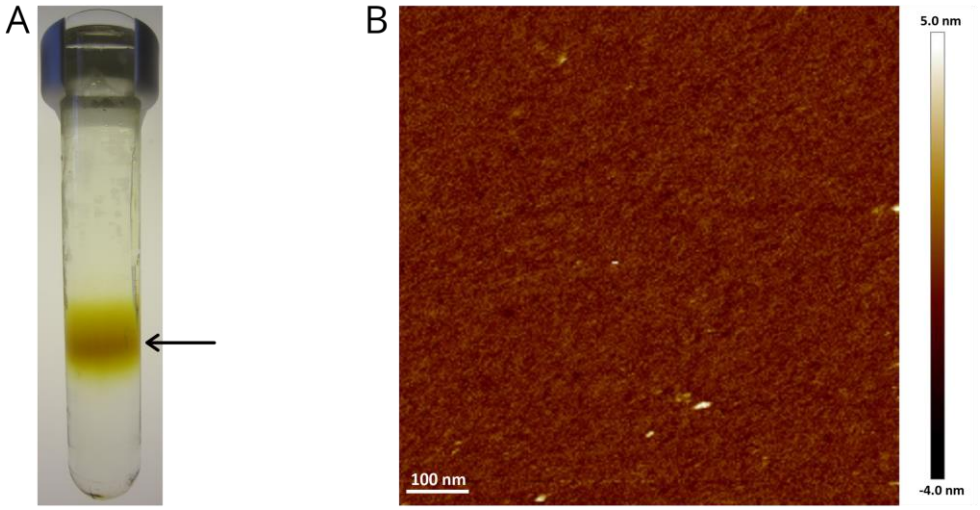

Figure 3.6 Cytochrome b_6f in tPCC-α-M, 400mM Ammonium phosphate

*(**A**) Continuous sucrose gradient (10-35% w/v) for exchanging cytb_6f into tPCC-α-M. Arrow indicates the band extracted. (**B**) An AFM image of the surface as prepared in the materials and methods (section 2.5.4.1) with the band seen in A for the protein incubation stage following desalting to remove sucrose. No clear topology is seen, indicating no linkage has occurred.*

No apparent surface topology was present, and it was suggested that a small amount of the 400mM ammonium phosphate could be decomposing to ammonia, which would thus outcompete the lysine residues on the protein's surface. If the ammonia represented even 0.01% of the 400mM ammonium phosphate, 40 µM of ammonia would be generated, dwarfing the 0.2 µM concentration of the cytb_6f. As a result, the preparation was amended so that the sucrose gradient exchange step in figure 3.6A would also exchange the buffer to 20mM HEPES pH 8.0, 50mM NaCl. In addition, a size exclusion column was also added to the end of the preparation to ensure that following extraction from the sucrose gradient, any residual ammonium phosphate was removed. This was the method then used in Mayneord et al., 2019. AFM images of the surfaces generated with this sample as previously described are shown in figure 3.7. Average heights measured are ca. 5 – 5.5nm, corresponding with cytb_6f being in a 'laying down' (membrane plane perpendicular to the silicon surface) conformation.

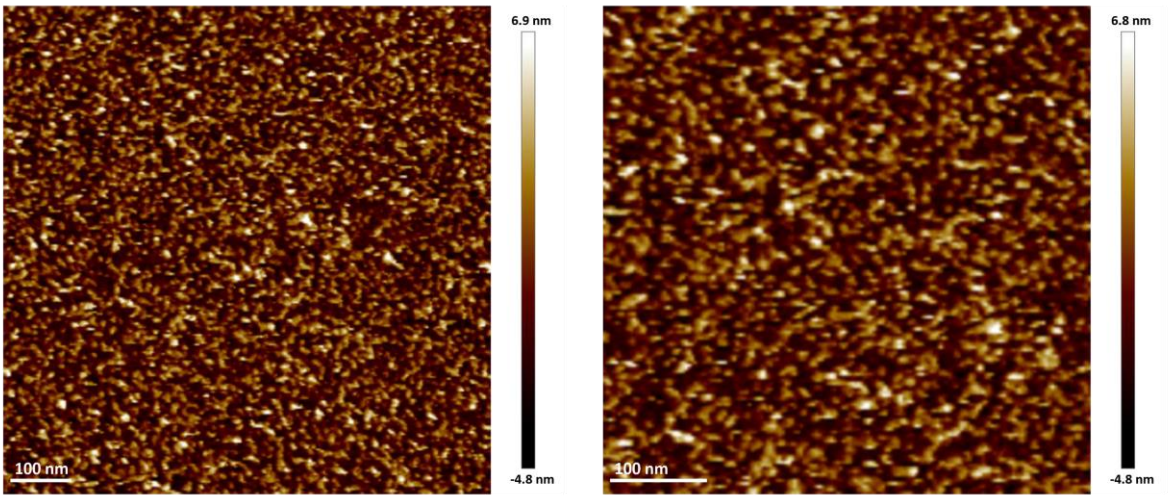

Figure 3.7 Surfaces of Cytochrome b_6f in tPCC-α-M, 10mM HEPES

AFM images of surfaces of cytb_6f generated with cytb_6f in 10mM HEPES, 10mM NaCl, 0.3mM tPCC-α-M. Average heights measured were around 5 – 5.5 nm, in agreement with cytb_6f in a 'laying down' conformation, with the plane of the detergent micelle perpendicular to the surface.

3.3.4 Verification of the viability of Cytochrome *b_6f*

Following the additional steps added to the original Dietrich and Kuhlbrandt method, we wished to verify that the cyt*b_6f* was still dimeric and functional. βDDM has been previously shown to monomerise cyt*b_6f* if involved in the purification stages (Luján et al., 2017). As a result, during one round of purifications, a small amount of the product of the CHT column was exchanged on a sucrose gradient into a buffer containing 50mM HEPES pH 8.0, 20mM NaCl, 0.03% βDDM. The sample was then run on a size exclusion column, in the same buffer, alongside the original. Figure 3.8 shows the results from these samples generated in parallel, with the sucrose gradients in A and B showing clear contrast between the single (dimeric) band in the tPCC-α-M sample, and the double band shown in the βDDM sample, with the suspected monomeric cyt*b_6f* indicated by the red arrow.

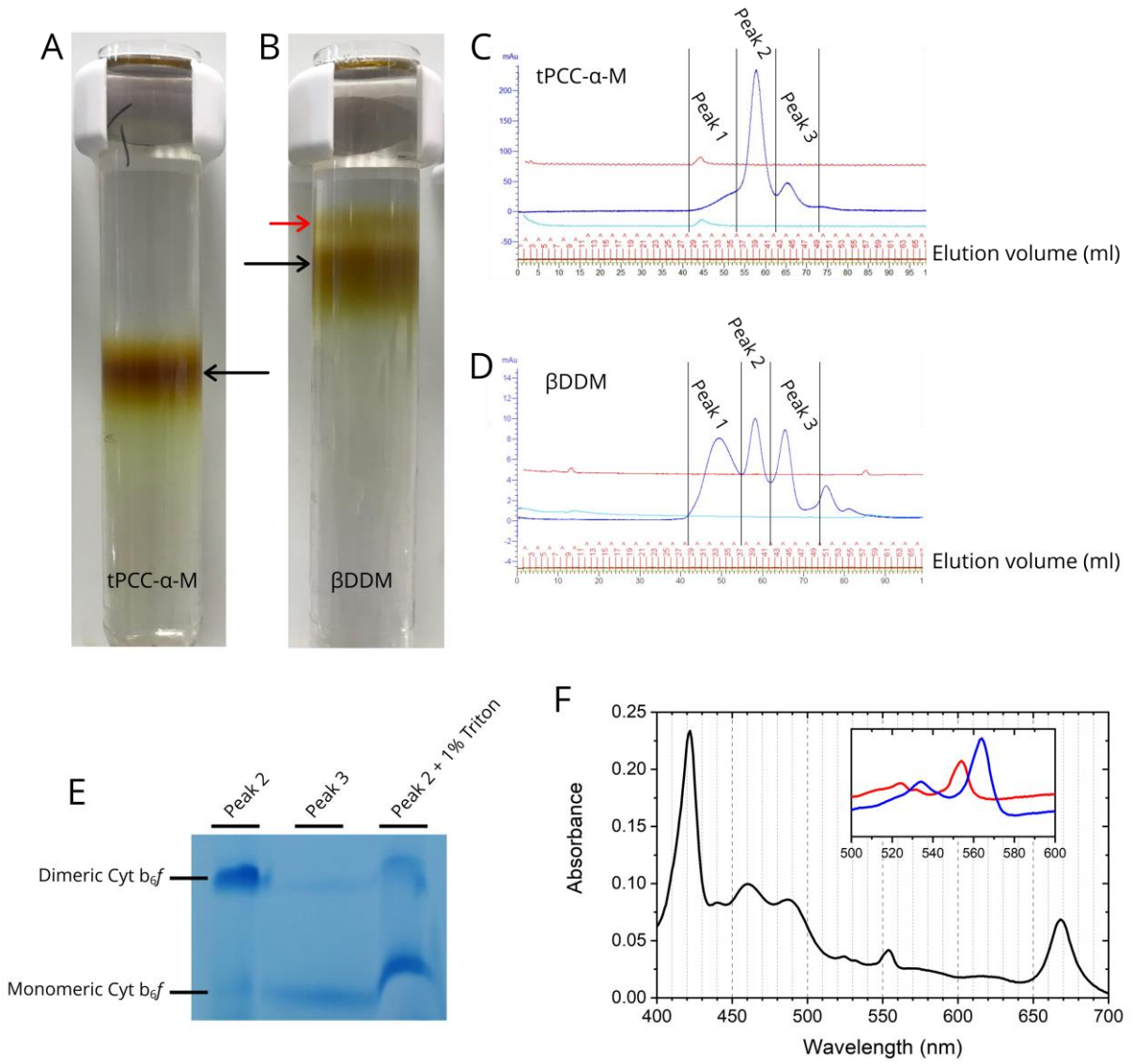

Figure 3.8 Gel filtration results of the Cytochrome b_6f complex

*(**A**) Exchange sucrose gradient for cytb_6f exchanged into buffer base (50mM HEPES, pH 8.0, 20mM NaCl) + 0.3mM tPCC-α-M and (**B**) Exchanged into buffer base + 0.03% βDDM. Bands extracted are denoted by black arrows. Small Red arrow shows a more diffuse band above the dimeric cytb_6f band previously linked to monomerised complex (Hovers et al., 2011). (**C**) Gel filtration elution profile (absorbance traces at 280nm are in dark blue) for the cytb_6f complex being eluted into buffer base + 0.3mM tPCC-α-M, and (**D**) Eluted into buffer base + 0.03% βDDM. (**E**) Blue Native PAGE showing the final 2 peaks seen in (C) (tPCC-α-M samples), along with Peak 2 after treatment with 1% triton for 30 minutes, to deliberately monomerise cytb_6f. (**F**) Absorbance spectra of the end cytb_6f from peak 2 treated with ascorbate, with an inlay showing the difference spectra for ascorbate – ferricyanide (Red) and dithionite – ascorbate (blue). This found a calculated haem b / haem c ratio of 2, in agreement with the complete complex (Cramer and Whitmarsh, 1977).*

The different heights of the same bands in tPCC-α-M (figure 3.8A) and βDDM (figure 3.8B) samples are due to the different MW of the micelles. The dimeric bands (indicated by the black arrow in both A and B) were extracted and placed on a size exclusion column, pre-equilibrated in 50mM HEPES pH 8.0, 20mM NaCl and either 0.03% (v/w) βDDM or 0.3mM tPCC-α-M as indicated. The elution profile for the size exclusion column of each sample is shown in figure 3.8 C/D. Peak 2 (central peak, suspected to be dimeric) and peak 3 (suspected to be monomeric) from the tPCC-α-M preparation was then run on a blue native PAGE, along with a sample of peak 2 which had been treated with 1% w/v triton for 30 minutes to cause the deliberate monomerisation of the sample. The result can be seen figure 3.8E. If the samples represented the monomeric (peak 2) and degraded (peak 3) forms of the protein, other bands would be expected from the blue native PAGE of peak 3 but were not seen. The results agree with our hypothesis that the peaks represent dimeric (peak 2) and monomeric (peak 3) cytb_6f with the earliest peak (1) representing some aggregation of the complex. In addition, the elution profile for the βDDM treated sample (figure 3.8D) shows the material nearly evenly distributed between all 3 peaks, suggesting that the monomerisation caused by βDDM continues following the sucrose gradient, and matches the elution seen previously in Luján et al., 2017. As an additional measure, the absorption spectrum for ascorbate-reduced cytb_6f from peak 2 is shown in 3.8F. From the difference spectra seen in the inlay, a ratio of b-type haem to c-type haem of 2 was calculated, in agreement with the complete complex (Cramer and Whitmarsh, 1977).

No high-resolution structure existed for the higher plant cytb_6f complex. As a result, with a preparation we were confident in we wished to use the recent developments in electron microscopy to obtain the complex's structure. A sample was given to L.Malone, D.Swainsbury and P.Qian in our lab for initial negative stain EM. A sample of the negative stain EM results are shown in figure 3.9A. From these images, the size of the longest visible edges of the particles were measured in ImageJ, and the histogram generated shown in figure 3.9B. Gaussian fitting shows that two peaks are present, with means at 6.9 ± 0.1nm and 9.5 ± 0.1nm. These arguably respond to the regions of 'highest density' for the cytb_6f as shown in figure 3.9C/D, in which the *C.reinhardtii* cytb_6f structure (Stroebel et al., 2003, pdb: 1Q90) is shown, with an overlay for the size of the entire complex (green) and the regions of highest density (blue). These regions of highest density would represent what would be visible from the low contrast of the negative stain EM.

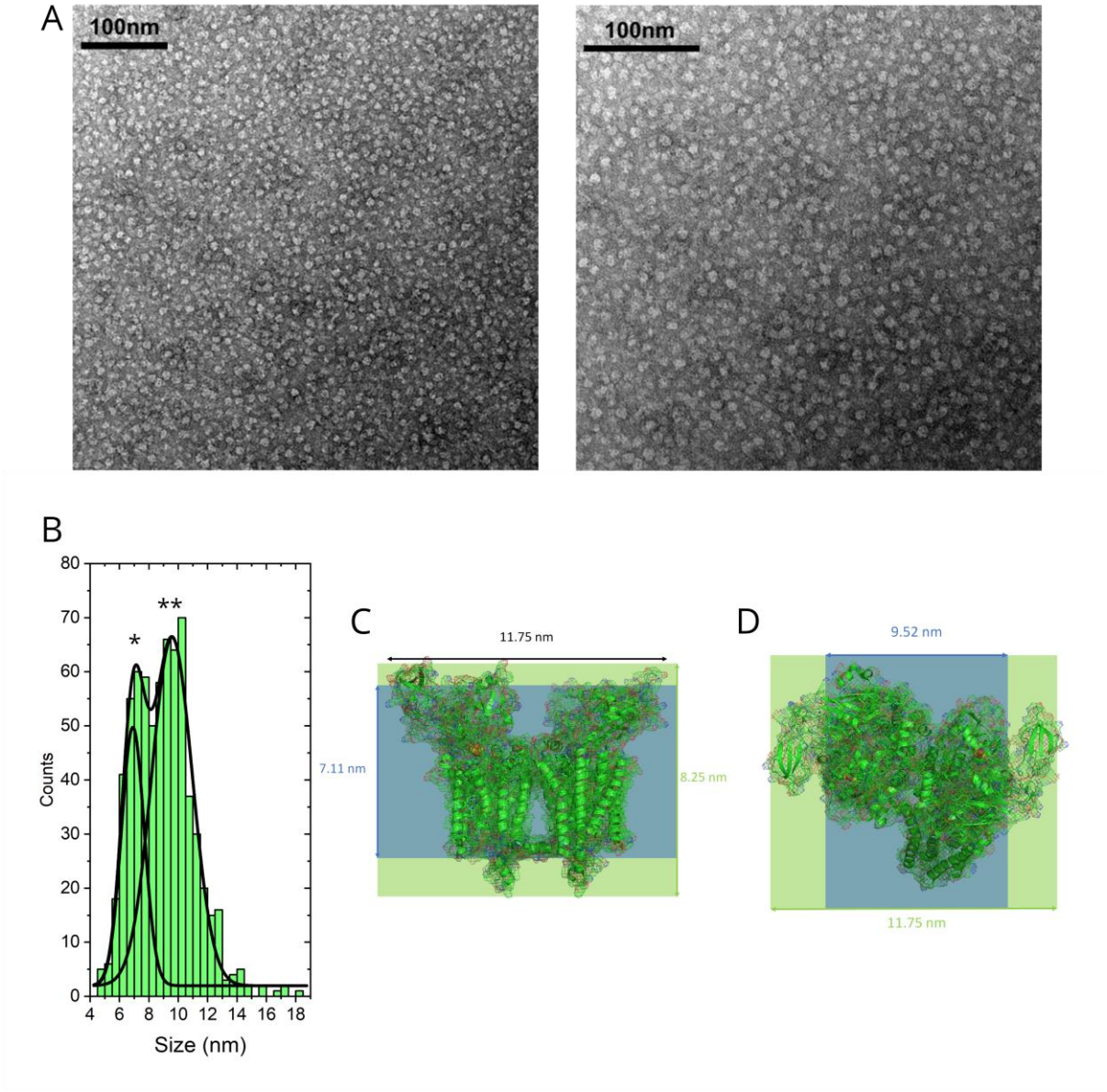

Figure 3.9 Negative stain EM on Cytochrome b_6f sample

*(**A**) Negative stain electron microscopy performed by L.Malone, D.Swainsbury and P.Qian, on the end sample of cytb_6f. (**B**) Histogram of the 'longest edge' particle sizes measured in imageJ on the images such as those in (A). Gaussian fit over the histogram shows peaks with means at 6.9 ± 0.1 nm (*) and 9.5 ± 0.1 nm (**). Errors given are ± standard errors of the mean. (**C/D**) Cytb_6f structure from C.reinhartii (Stroebel et al., 2003, pdb: 1Q90) with full dimensions highlighted in green, and regions of 'high density' highlighted in blue. The measured dimensions of these high-density regions are in agreement with the longest edge particle sizes in B.*

In addition to observing if the cytb_6f was still dimeric, we also wished to ensure the interaction between the purified Pc and cytb_6f would match the previously published results in bulk phase experiments (Black et al., 1987; Dietrich and Kuhlbrandt, 1999) and the measured native ET rate (Hope, 1993) of 300 electrons s^{-1}. For this purpose, a newly obtained stopped-flow system in our lab could be used to perform an activity assay and show the initial rate at which the cytb_6f complex was catalysing the transfer of electrons from plastoquinone to Pc. Decylplastoquinone was reduced via the method seen in Trumpower and Edwards, 1979, and the generated decylplastoquinol was dissolved into DMSO, due to methanol causing complications with cytb_6f kinetics (Dietrich and Kuhlbrandt, 1999). Figure 3.10 shows the absorbance traces at 597nm (Oxidised Pc) for the stopped-flow experiments.

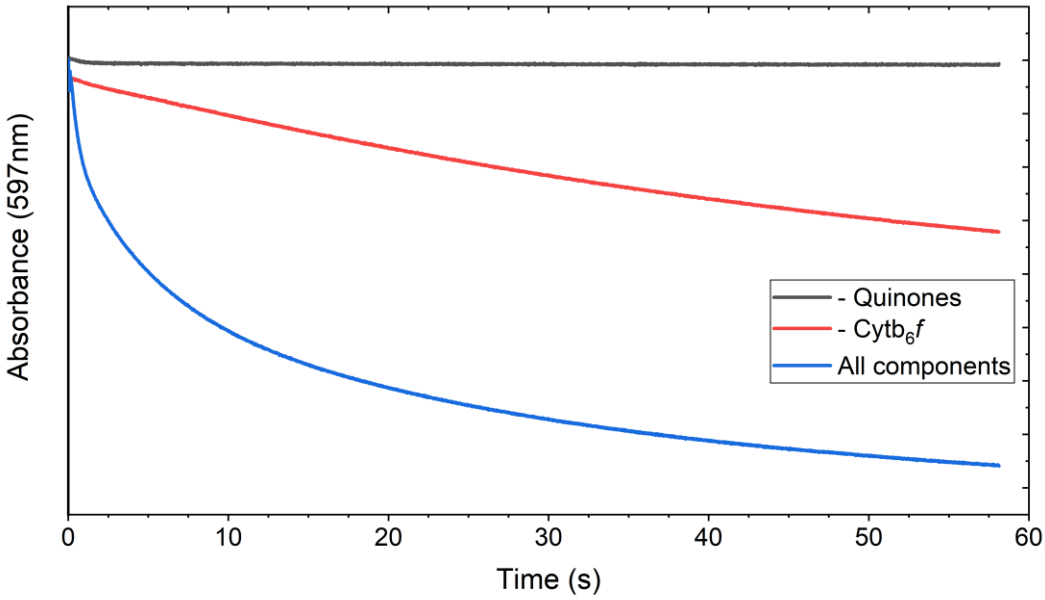

Figure 3.10 Stop flow measurements of the Cytochrome b_6f and Plastocyanin.

Stop flow experiments testing the catalytic rate of the purified cytb_6f complex, along with controls. End concentration of all constituents (when present) were 185nM cytb_6f 50µM Pc, 250µM decylplastoquinol. Each experiment was repeated 3 times, and the mean plotted. Quinones were omitted (grey) to show there was no other source of electrons, and any residual DMSO from the decylplastoquinol stock had no effect. Cytb_6f was omitted (red) to obtain the background rate for ET from decylplastoquinone to Pc when uncatalyzed. All components (blue) display the rate for ET from decylplastoquinone to Pc (Catalysed + Background). Absorbance at 597nm was tracked to observe the reduction of Pc, and the rate of reduction calculated using an extinction coefficient of 4.7mM^{-1} cm^{-1} for oxidised Pc (Yoshizaki et al., 1981).

Experiments were initiated by addition of decylplastoquinol to pre-mixed Pc and cytb_6f, to give final concentrations of 185nM cytb_6f, 50µM Pc and 250uM decylplastoquinol (figure 3.9, Blue, 'All components'). To ensure the residual DMSO from the decylplastoquinol stock had no effect upon mixing, decylplastoquinol was omitted (figure 3.9, Grey, '- Quinones'). As the electron potentials of both decylplastoquinol and Pc facilitate ET between the two in solution, this background rate needed to be quantified. The red absorbance trace (figure 3.9, '- cytb_6f') shows a slow rate of transfer from decylplastoquinol to Pc in solution. When calculating the catalysed rate of ET this background rate was removed. The rate of ET catalysed by cytb_6f was found to be 200 electrons s^{-1}, in good agreement with previous studies on cytb_6f from spinach (Dietrich and Kuhlbrandt, 1999), *C.reinhardtii* (Hovers et al., 2011; Pierre et al., 1995) and native spinach membranes (Hope, 1993).

In addition to this, the sample previously given to L.Malone, D.Swainsbury and P.Qian was also analysed by Cryo-EM to obtain a high-resolution structure. From the cryo-EM grids generated, over 420,000 particles were picked by L.Malone, and the structure of the spinach cytb_6f complex was obtained to 3.6 Angstrom resolution (Malone et al., 2019). This structure can be seen in figure 3.11, and again showed the sample generated by this method was complete and could be taken on to SMFS experiments.

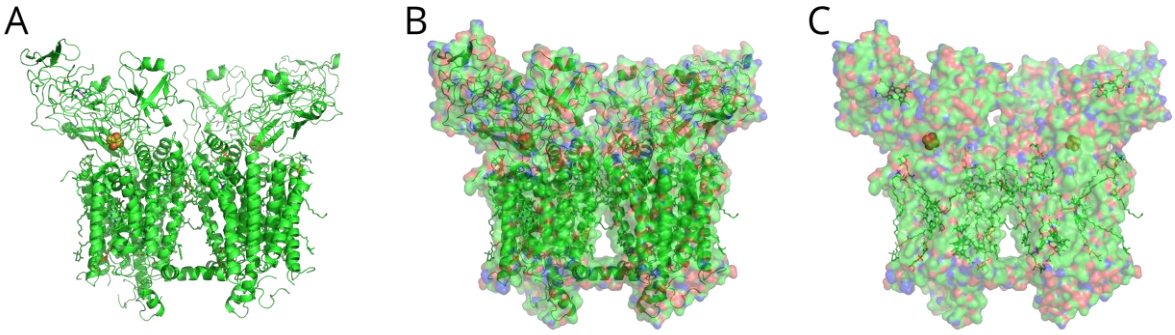

Figure 3.11 Cytochrome b_6f structure from Spinach.

*The structure obtained by L.Malone using cryo-EM from samples prepared in tPCC-α-M. The complex had a resolution of 3.6 Angstrom. The cytb_6f is shown in (**A**) cartoon form, (**B**) cartoon + surface overlay and (**C**) surface form. PDB: 6RQF - (Malone. et al. 2019).*

3.3.5 Initial SMFS experiments on Cytochrome b_6f : Plastocyanin binding

Surfaces of cytb_6f were generated as described in Materials and Methods section 2.5.4.1, using the chemistry shown in figure 3.4 A/B. Pc was attached to the AFM probe (Bruker AC40) via the same chemical linkages, however a 24 unit polyethylene glycol spacer was also present in the linker, to give a final tip to protein separation distance of 10nm, as seen in figure 3.4 C/D (materials and methods section 2.5.4.2). This could thus be used as an initial selection criterion for distinguishing between specific adhesion (which would yield up to 10nm separation prior to applying a force on the complex) and non-specific adhesion (which would occur at a separation distance of 0). Cytb_6f surfaces were incubated in 1mM sodium ascorbate to reduce cytochrome *f*. They were then initially scanned across via PF-QNM AFM with a 'clean' (unfunctionalised) probe, to assess surface density in the height image. Following this the probe was replaced by a Pc functionalised probe, which had been pre-oxidised in 1mM potassium ferricyanide, at which time the machine was switched to also record the FdC in the data set. Each pixel in the height image thus had a concordant FdC (discussed in 1.3.2) describing the interaction with the surface at that point. Whilst PF-QNM offers several characterisations beyond simply height (section 1.3.3), only adhesion is of interest in SMFS experiments. Observing the height and adhesion image, rather than extracting and assessing every FdC allows a quick initial test of the experiments. Figure 3.12 shows the simultaneously obtained height (A/C) and adhesion (B/D) images from early experiments on the interaction between cytb_6f and Pc.

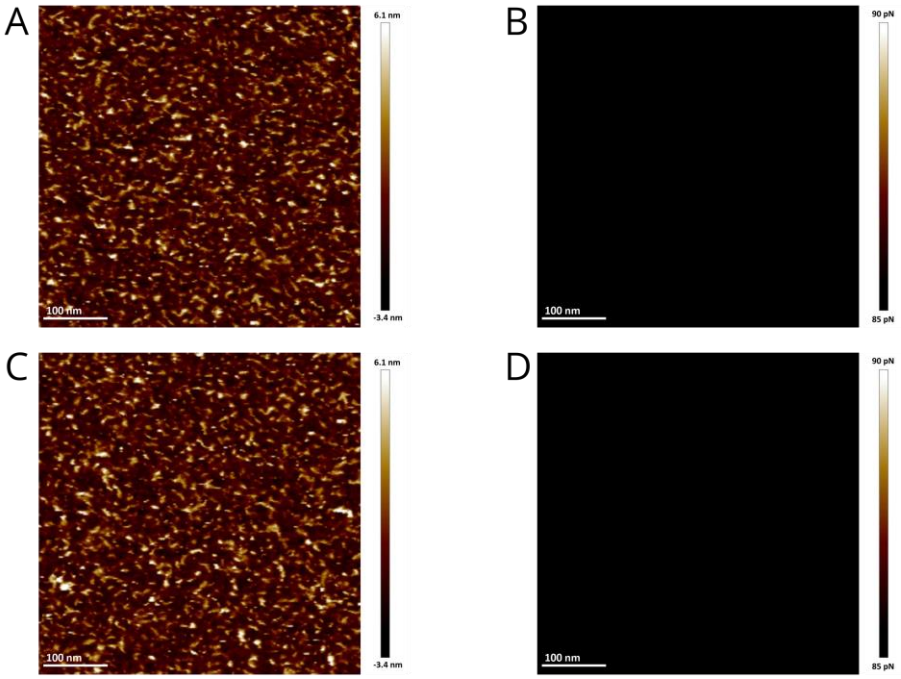

Figure 3.12 SMFS on Cytochrome b_6f and Plastocyanin interaction

AFM Height (A/C) and corresponding adhesion (B/D) images from imaging in PF-QNM mode for the initial experiments on the interaction between cytb_6f on the surface, and Pc on the AFM probe. The Z scale in B and D is set to only a small range at a relatively low force (90pN upper limit) to effectively act as a threshold, showing adhesions higher than 90pN as white dots. This method was frequently used to perform an initial assessment of the adhesion data.

As previously mentioned, the height measured for the *cytb_6f* on the surface was ca. 5nm, in agreement with the cytb_6f complex being in a 'laying down' conformation. Previous experiments on the cytb_6f – Pc interaction in native grana membranes (Johnson et al., 2014) had found a mean unbinding force of ca. 310pN, and as such a threshold value of 90pN was placed on the adhesion image so that only adhesions over this threshold were visible in the image.

No adhesion is observed in figure 3.12 above the 90pN threshold. These experiments were repeated 10 times, yielding the same result each time. The attachment chemistry for the surfaces had already been verified from prior experiments showing its absence under various conditions (figure 3.6), and surface density was visible from the height image. However, the attachment of Pc to the AFM probe could not be verified as no method was available to observe the AFM probe functionalisation. Whilst it is generally assumed that the silicon on the AFM tip should be no different from a SiOx surface, it would appear that some difference in functionalisation was occurring. As the vacuum chamber used for MPTMS deposition was old, and no longer held vacuum for periods longer than 3 hours, this was

considered to be a likely explanation for this issue. Whilst the deposition was generally performed under argon or nitrogen (materials and methods section 2.5.2.1), a loss of vacuum would result in air, and thus moisture, being introduced into the chamber. As MPTMS requires strictly dry conditions, this could be detrimental to the deposition of a monolayer on the AFM probe. Whilst the SiOx surface may be capable of tolerating some loss in surface deposition, the AFM probe may be more sensitive as only a very small area of the probe (the tip apex) is relevant for SMFS experiments. As a result, other avenues for the creation of a reactive monolayer were pursued.

3.3.6 Alternatives for MPTMS immobilisation

Whilst our previous attempts at surface functionalisation had been performed in the vapour phase, MPTMS can also be deposited in the liquid phase. To assess whether this avenue was worth pursuing cleaned SiOx wafers were given to O.Korychenska in the Department of Chemistry for liquid phase deposition. This method uses a concentration of 5mM MPTMS in toluene, under an argon atmosphere as reported in Ramanath et al., 2003 (materials and methods section 2.5.2.2). These surfaces were then assessed by AFM to observe the quality of the deposition, and the images can be seen in figure 3.13. Figure 3.13A shows the starting sample (Piranha cleaned AFM surface), whilst figure 3.13B shows the surfaces following liquid phase MPTMS deposition. The protrusions seen on the surface could either be due to MPTMS polymerisation (due to exposure to moisture during deposition) or non-covalently attached MPTMS. Previous experiments have removed the latter by heating the sample to 85°C for 10 minutes (Gothe et al., 2018), which produced the surface shown in figure 3.13C. Some MPTMS appears to have been removed from the surface, however uncontrolled polymerisation is occurring. As such this showed that liquid phase deposition was not appropriate for the functionalisation steps with the available equipment.

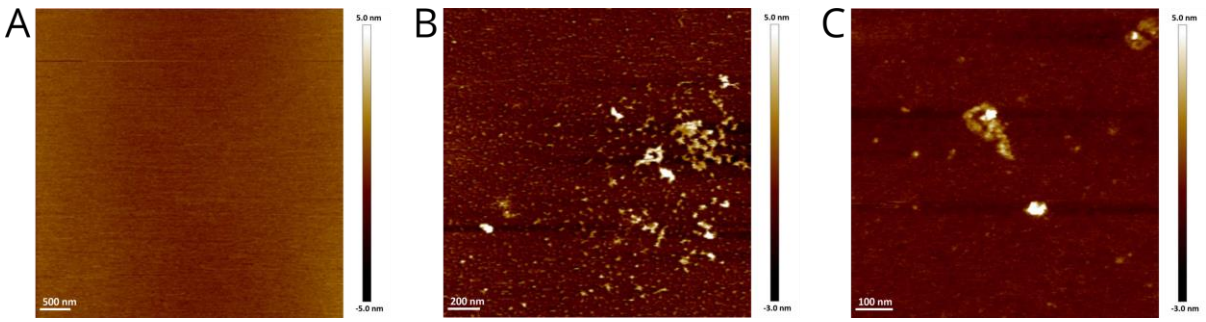

Figure 3.13 Liquid MPTMS monolayer deposition.

*Testing of monolayer deposition by the liquid phase method. AFM images taken of: (**A**) Blank piranha cleaned silicon wafer (starting material). (**B**) Surface following liquid phase deposition of MPTMS before baking step and (**C**) after baking at 85°C for 10 minutes. Clear inconsistencies are observed both before and after baking.*

3.3.7 Ethanolamine deposition and the Biotin : Avidin test bed experiments

With the deposition of MPTMS not available in vapour phase, due to the poor chamber, or in liquid phase due to the strict requirement for dry conditions, another deposition was required in order to allow chemical attachment to the silicon surface. The creation of an amine functional layer was also possible via incubation of silicon with ethanolamine in DMSO (Hinterdorfer et al., 1996; Riener et al., 2003), again requiring dry conditions, however not as strict as with MPTMS. To assess this functionalisation method, a solution of 2.2g Ethanolamine HCl in 4ml DMSO was used for the deposition. Silicon wafers were placed in custom designed glassware to allow for 4Å molecular sieve beads to be present in the solution, aiding a dry environment, and left in this solution overnight at 100°C. Surfaces were then washed in DMSO 3 times, followed by ethanol 3 times and finally dried under a stream of nitrogen. Following this they were incubated with a homobifunctional linker dimethyl suberimidate (DMS) and cytb_6f simultaneously (Chemistry diagram shown in figure 3.15 C/D, See materials and methods section 2.5.3.3 for details). Any attachment of cytb_6f to the surface would thus give an initial indication that the linkage was functioning. These surfaces were imaged by AFM and can be seen in figure 3.14. As expected, some aggregation is observed from the crosslinking of multiple cytb_6f together, however as this was only used as a verification of ethanolamine functionalisation this was not an issue.

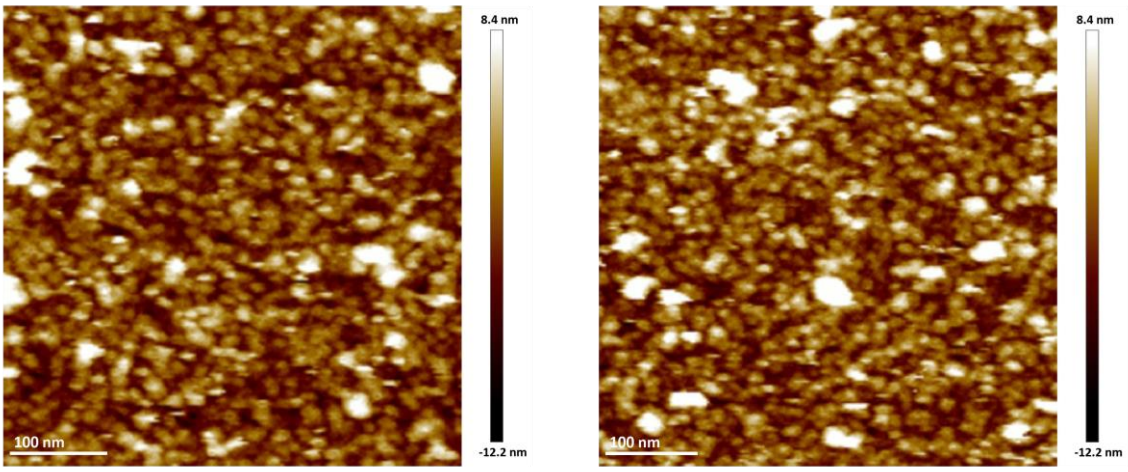

Figure 3.14 Cytochrome b_6f surfaces via ethanolamine linkages

AFM images taken of surfaces generated by incubation of cytb_6f and DMS linker with ethanolamine functionalised surfaces. Clear topology shows that the cytb_6f has linked to the surface, with some aggregation seen due to the crosslinking causing aggregation of cytb_6f.

Following this initial verification, we needed to also assess the functionalisation on the AFM probe. We chose the well characterised SMFS experiment of measuring the interaction between Biotin and Avidin as both Avidin and linkers terminating in Biotin were commercially available. Repeating this widely reported experiment (Evans, 1999; Florin et al., 1994; Izrailev et al., 1997; De Paris et al., 2000; Riener et al., 2003) would verify that no other factors in the experiments were responsible for the failures seen previously, and show whether the ethanolamine method was suitable. The principle of using this test system to investigate linkage methods has been previously established (Ebner et al., 2007a, 2007b; Riener et al., 2003). The proposed linkage chemistry can be seen in figure 3.15, with A showing the individual components, and B showing the end conjugate structure. The NHS-$(PEG)_n$-Biotin linker was attached to the ethanolamine generated surface by a 3-hour incubation at a concentration of 1mg ml^{-1} in a solution of chloroform, with 0.5% (v/v) triethanolamine as a catalyst (as in Hinterdorfer et al., 1996). In this linker, *n* represents the variable number of PEG units, with an average MW of 5kDa for the entire molecule, thus corresponding to ca. 100 PEG units, giving a tip – Biotin separation distance of ca. 40nm.

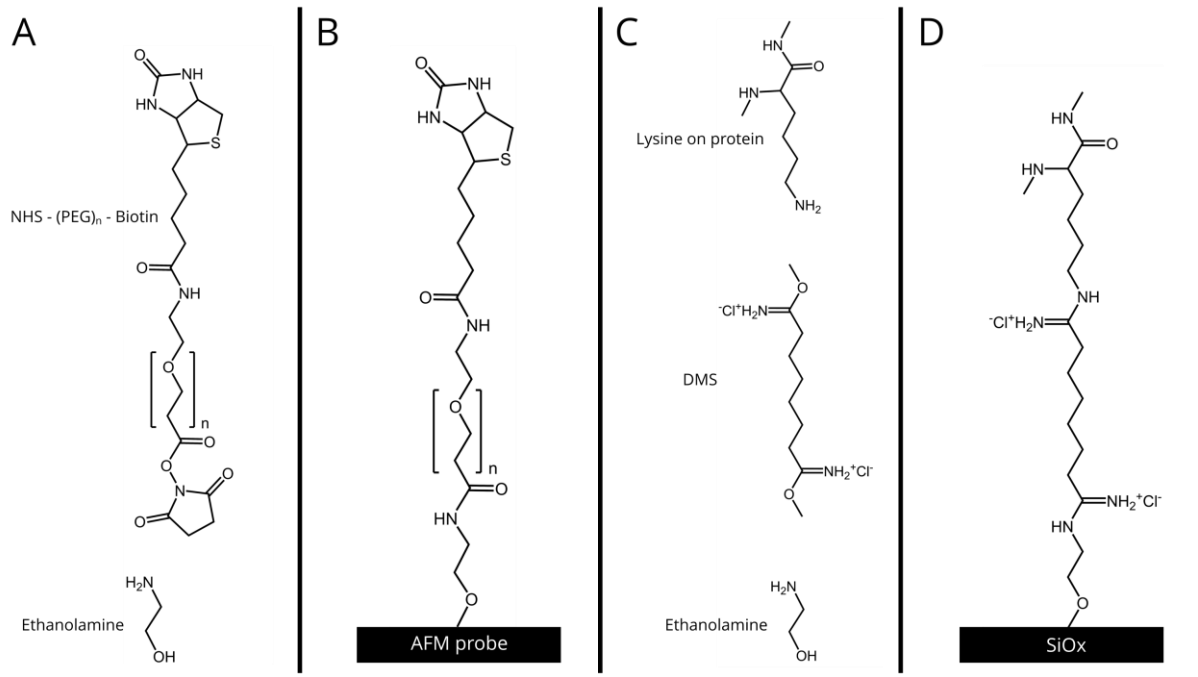

Figure 3.15 Ethanolamine linkage of proteins to surfaces

*The linkage method for attaching Biotin to an AFM probe. (**A**) Linkage components prior to reaction, and (**B**) The final conjugate formed from the reaction. (**C**) The linkage method for attaching cytb$_6$f to the surface, with the components for attaching cytb$_6$f to the SiOx surface and (**D**) the final conjugate formed from the reaction. The length of the PEG units in A and B was determined by the MW of the entire linker, having an average of 5kDa.*

Avidin could readily be adsorbed to a surface by simple incubation as shown in Riener et al., 2003 (materials and methods section 2.5.4.7). Due to its small size however, observing surface topology to assess density would be difficult. As a compromise, a 'scratch test' was performed to confirm the presence of avidin as in Ebner et al., 2007b. In this case, the peak force for AFM could be increased to a high force, and a small region could be scanned. This high force would remove the protein adsorbed to the surface. When the peak force was subsequently lowered again, and a larger image taken, the region which has had protein removed can be seen, as shown in figure 3.16, confirming that avidin was successfully attached. Now scanning across the surface using force volume (FV) mode gave clear specific adhesions on the surface, with a separation distance between 15 and 45 nm in the FdC's.

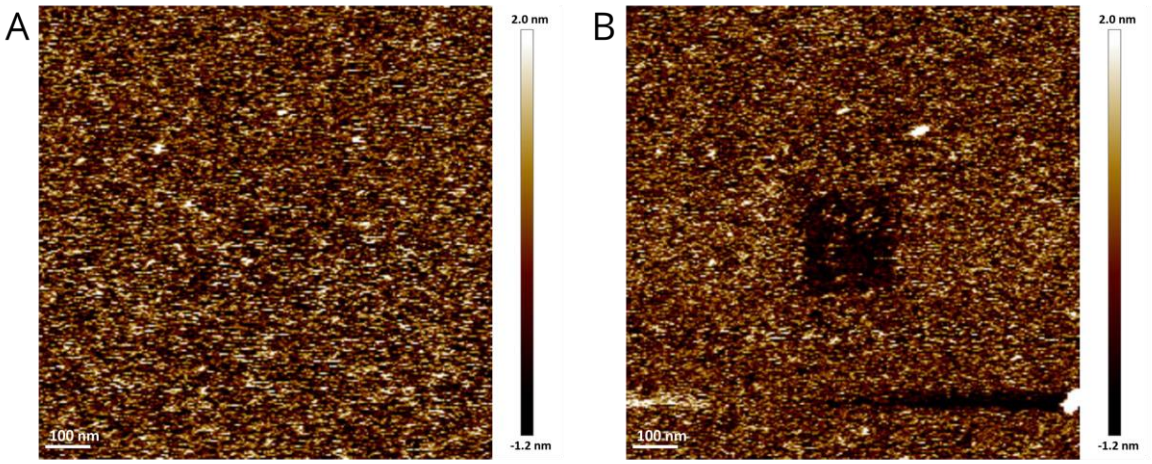

Figure 3.16 Avidin surface scratch test

*AFM images for surfaces of immobilised avidin. (**A**) AFM image taken on avidin surface. Following this, the scan size was decreased to 200 x 200nm and the scanning peak contact force was increased to several nano-newtons (scratch test). (**B**) Image taken at same size as in A, following the scratch test, showing a central region in which the avidin has been removed, leaving the underlying mica surface.*

3.3.8 MATLAB analysis tool

The analysis of a SMFS experiment in either FV or PF-QNM modes requires the opening of each pixel's FdC data, a correction for the baseline of the curve, followed by initial filtering of the data by set parameters. The Nanoscope software that comes with Bruker's AFM machines is not well equipped to handle this task, requiring the user to first save each FdC before making all the corrections manually. Rather than pursue this time-consuming process, Bruker's own MATLAB toolbox can be used to open the files, and all subsequent requirements can be met by MATLAB's own inbuilt tools. A simple flow chart for the logic of an analysis program is shown in figure 3.17, displaying the reasoning behind the initial filtering and how the analysis program would work. The script for the MATLAB program used throughout SMFS analysis can be found in the appendix section 8.1. Whilst the syntax for opening FV and PF-QNM files is different in Bruker's MATLAB toolbox, this only required changing two lines, one to open the FdC, and the other to open the height image. As a result, the program shown in the appendix is for opening the PF-QNM files.

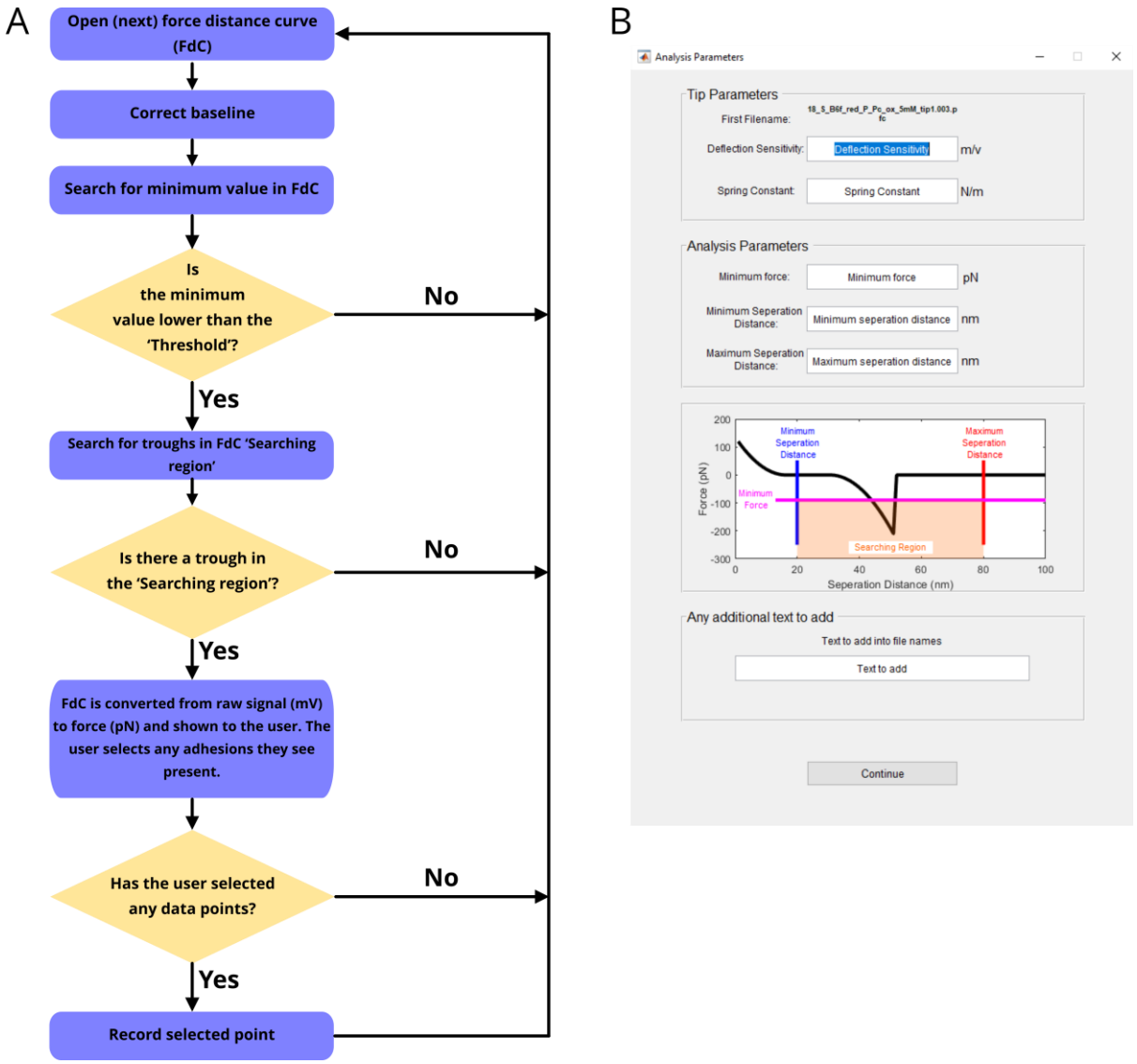

Figure 3.17 Analysis tool flowchart and MATLAB script.

*(**A**) Flowchart showing the logical steps for the analysis tool generated in MATLAB for data analysis. Filtering parameters (the 'Threshold' and 'Scanning region') are given by the user at the start of the analysis, in the popup window seen in (B). (**B**) The popup window the user is shown at the start of analysis and can be used to input the tip parameters (Deflection sensitivity and spring constant). Following this the user inputs the analysis parameters, the minimum force here representing the 'Threshold' seen in A, and the minimum and maximum separation distance giving the 'Searching region'. The third panel in the analysis window offers a graphical representation of this, with the highlighted orange region being the region the program searches for adhesions (troughs) in. The minimum force ('Threshold') is converted into the equivalent raw data signal (mV) for the initial filtering seen in A, so that minimal conversion of values from raw data to force needs to be performed.*

Following this curves that fit the filtering parameters given are shown to the user, and adhesion maxima can be selected (Appendix 8.1).

3.3.9 Biotin : Avidin results

The biotin – avidin binding system has already been extensively studied via SMFS utilising AFM, amongst other tools. The purpose of the experiment here was simply to show it could be repeated using our surface chemistry to ensure the ethanolamine deposition was functioning on our AFM tip. Figure 3.18 shows the distribution of forces measured from the SMFS experiment of biotin and avidin, along with the traditional blocking control that is usually performed for these experiments (Lee et al., 1994). These experiments were performed in force volume (FV) mode of AFM, which is considerably slower than the PF-QNM method previously discussed. Blocking the biotin on the tip by introducing 0.1mg/ml avidin into the imaging buffer showed a greater than 10-fold drop in the number of unbinding events that were being detected. The average loading rate was found to be ca. 2000pN/s, as measured by the slope of the FdC immediately prior to rupture. The measured mean unbinding force was 48 ± 1pN, in agreement with previous studies at this loading rate (Evans, 1999; De Paris et al., 2000).

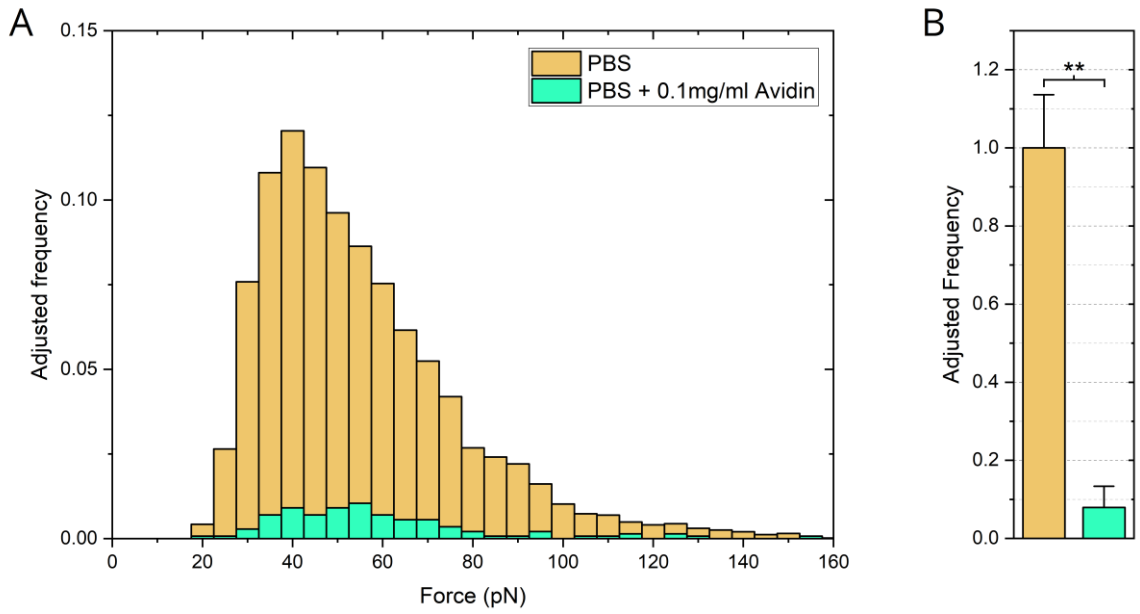

Figure 3.18 Biotin : Avidin force distribution and interaction frequency

*SMFS on the Biotin – Avidin system for testing the linkage to the AFM probe and analysis program. (**A**) The distribution of forces measured for the biotin avidin test system in Phosphate buffered saline (PBS). In addition, 0.1mg/ml Avidin was added to the solution, showing a decrease in the interaction*

*frequency. Adjusted frequencies changed so the cumulative frequencies represent those in (B). (**B**) Interaction frequencies measured in the interaction, with colours matching those seen in (A). Unpaired t-test analysis was performed on the adjusted frequencies. Asterisk denotes a p-value of 0.0025. Error bars are ± standard error of the mean, n = 3-5 independent analysed images for each condition.*

These results showed that the ethanolamine functionalisation method was working, and that the generated analysis script in MATLAB was also useful for the analysis.

3.3.10 Ethanolamine - Plastocyanin linkage to an AFM probe

Having established that an amine monolayer could be created using the ethanolamine method, efforts now focused on finding a way to couple Pc to the AFM probe. One possibility was to use homobifunctional crosslinkers, with the same chemical group at either end. However, these are notoriously inefficient unless protection groups are used (Wildling et al., 2011). As an alternative, chemical modification of Pc to create an altered linkage site was attempted (as previously used in Haselgrubler et al., 1995 and Kamruzzahan et al., 2006). Utilising N-succinimidyl-S-acetylthiopropionate (SATP), surface lysine residues on Pc could be functionally converted into free thiol groups, then allowing chemical attachment via maleimide groups (such as on the previous heterobifunctional linker $SM(PEG)_{24}$ seen in figure 3.20). To ensure the SATP chemical modification of Pc had worked correctly, a simple test was performed. Utilising the same maleimide group as on the $SM(PEG)_{24}$, the Alexa Fluor® 750 – maleimide dye could be attached to the protein. Following this, the dye protein mixture could be run on a desalting column. If the two had linked together, the protein and dye would elute together, otherwise they would elute separately. Figure 3.19A shows this result, along with the control experiment in 3.19B of mixing non-SATP treated Pc with the dye, leading to the elution of the dye separately. See materials and methods section 2.3.7 for details on SATP functionalisation and dye attachment.

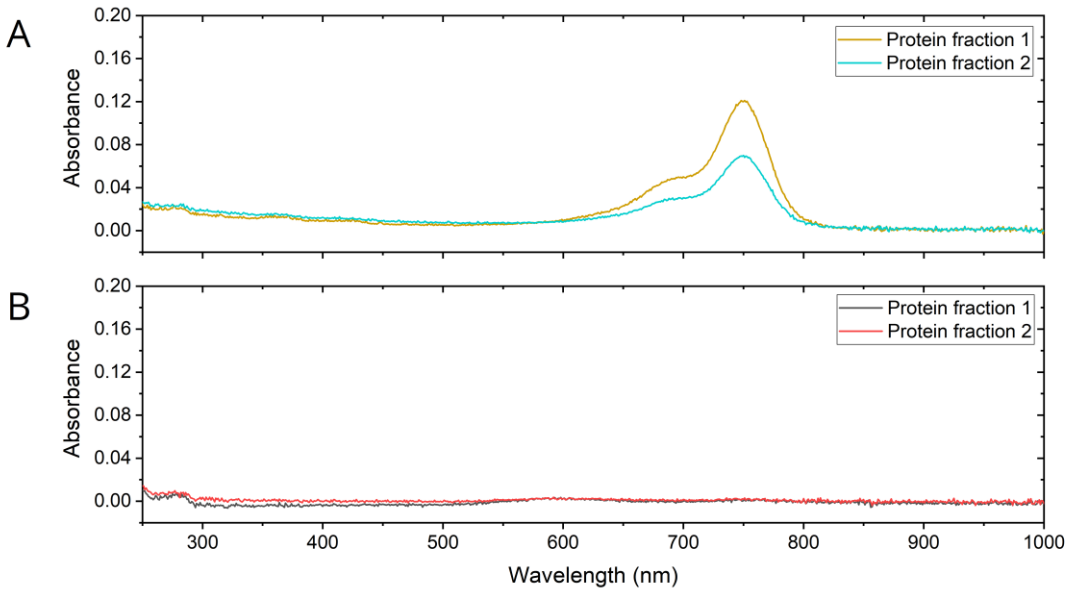

Figure 3.19 Testing of SATP labelled Plastocyanin

*Absorbance spectra for the protein containing fractions when (**A**) SATP-treated Pc and (**B**) non- SATP-treated Pc is mixed with Alexa Fluor® 750 – maleimide dye for 1 hour and run down a desalting column.*

Having confirmed that the SATP modification of Pc was successful, the chemical linkage of SATP-Pc to the amine terminated AFM probe was now undertaken, with the linkages shown in figure 3.20. These probes were then used for initial SMFS experiments.

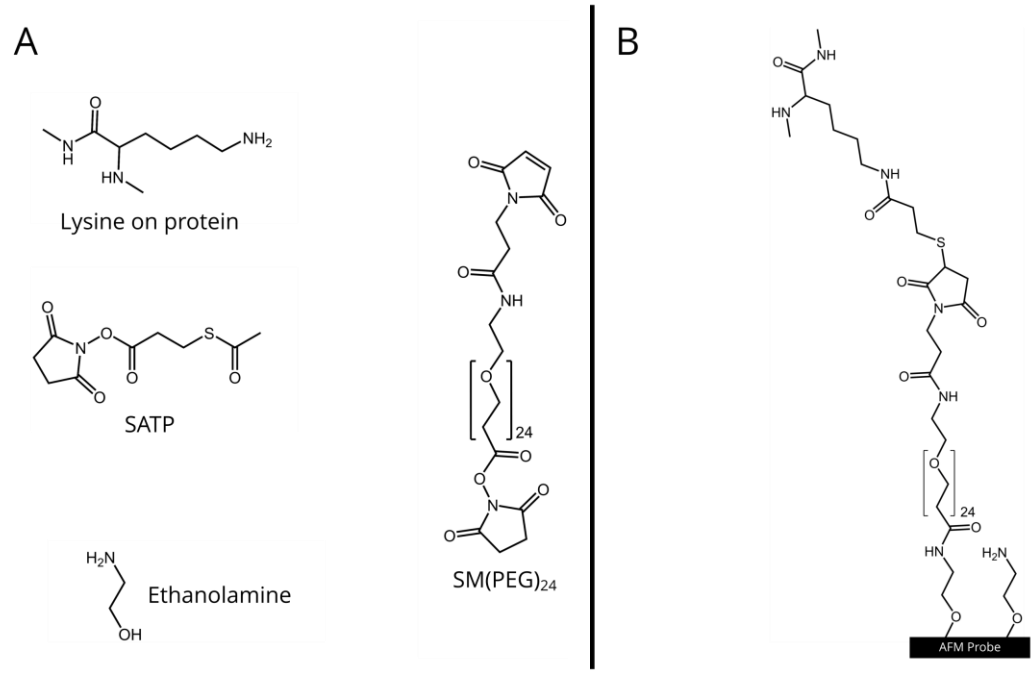

Figure 3.20 Chemical linkage of Plastocyanin to an AFM probe with Ethanolamine

*Linkage chemistry used to attach SATP treated Pc to the AFM probe. (**A**) The individual components of the linkages, and (**B**) The product of the linkage stages, with by-products omitted.*

3.3.11 Initial SMFS of SATP treated Plastocyanin

SMFS experiments utilising the SATP treated Pc yielded the results seen in figure 3.21, on cytb_6f surfaces generated as discussed previously (figure 3.4, Materials and methods section 2.5.4.1). The traditional blocking control (Lee et al., 1994) yielded an over 5-fold decrease in the number of unbinding events observed. The distribution of forces deviated from those originally observed in Johnson et al., 2014 with mean forces of 217 ± 4 pN and 371 ± 25pN, presumed to be single (217pN) and double (371pN) unbinding events (i.e. double events occur when two Pc on the AFM probe interact with two cyt*f* in cytb_6f complexes on the surface, and both are ruptured upon retraction).

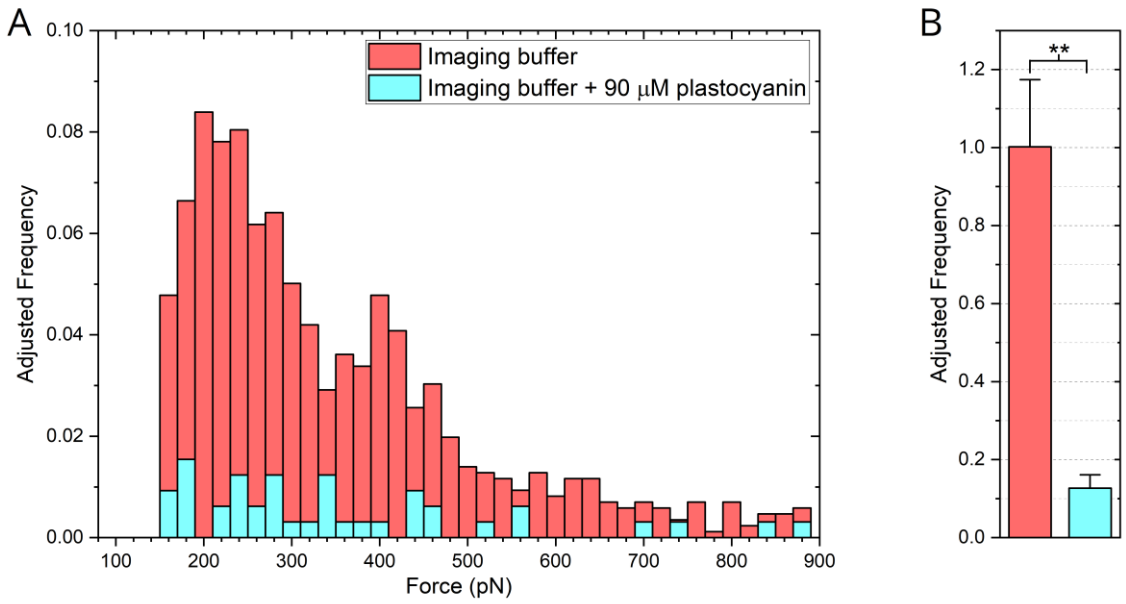

Figure 3.21 Initial experiments on Cytochrome b_6f : Plastocyanin - Thiol linkage

*SMFS data for the interaction between cytb_6f and Pc using the attachment chemistry seen in figure 3.20 for Pc. Imaging buffer of 10mM HEPES pH 7.4, 10mM NaCl, 0.2mM tPCC-α-M. (**A**) The distribution of forces seen for the interaction between Pc and cytb_6f. The adjusted frequency reflects the cumulative frequencies of the histogram being equal to the frequencies seen in (B). (**B**) Interaction frequency for the interaction before and after addition of 90μM (final concentration) Pc into the imaging buffer, set relative to the frequency before addition. Colours match those used in (A). Unpaired t-test analysis was performed on the adjusted frequencies. Asterisk denotes a p-value of 0.0079. Error bars are ± standard error of the mean, n = 5 independent analysed images for each condition.*

The original study in Johnson et al., 2014 found a mean unbinding force of 312 ± 5 pN in the native grana membranes. The discrepancy in the forces recorded between the two experiments may be due to the chemical modification of all lysine residues on Pc by SATP. A blanket chemical modification of this nature would affect K81, a residue close to the 'large' electrostatic region involved in binding (figure 2.1), irrespective of whether K81 was also the attachment point to the AFM probe. This situation contrasts with the method used in Johnson et al., 2014 (and figure 3.4) where only one of the six lysine residues on Pc is presumed be coupled to the AFM probe. Therefore, while chemical modification would affect all lysine residues (thus K81 would always be affected), the single linkage point would only affect K81 ca. 17% of the time (assuming equal reactivity of all lysine residues on the

surface). With these limitations in mind the decision was taken to return to the original method used in Johnson et al., 2014.

3.3.12 SMFS utilising original Plastocyanin attachment method

Following the purchase of a new vacuum chamber to facilitate deposition, the original method for MPTMS deposition could be repeated. Utilising this, and the same $SM(PEG)_{24}$ linkers discussed previously, Pc could be attached to the AFM probe as seen in figure 3.4 (materials and methods section 2.5.4.2). The results from this are shown in figure 3.22, displaying the force distribution (A) and interaction frequency (B) observed during these experiments, and for addition of 90 µM excess of free Pc into the imaging buffer. Whilst the data set here was small, the unbinding forces this time have means of 237 ± 20 pN and 311 ± 126pN. This second population agreed with the previous studies (Johnson et al., 2014). In addition, higher harmonics (that could not be fit with a Gaussian) of the initial force populations are also seen, at ca. 460pN and 600pN, again suggested to be 'double events' for the two lower populations. The decrease in interaction frequency observed upon addition of the 90µM Pc is ca. 3-fold, smaller than before. This may be due to the 'unmodified' Pc on the probe having a higher affinity for the cytb_6f on the surface compared to the SATP modified Pc described in Section 3.3.11, thus competing more effectively with the free Pc in the buffer.

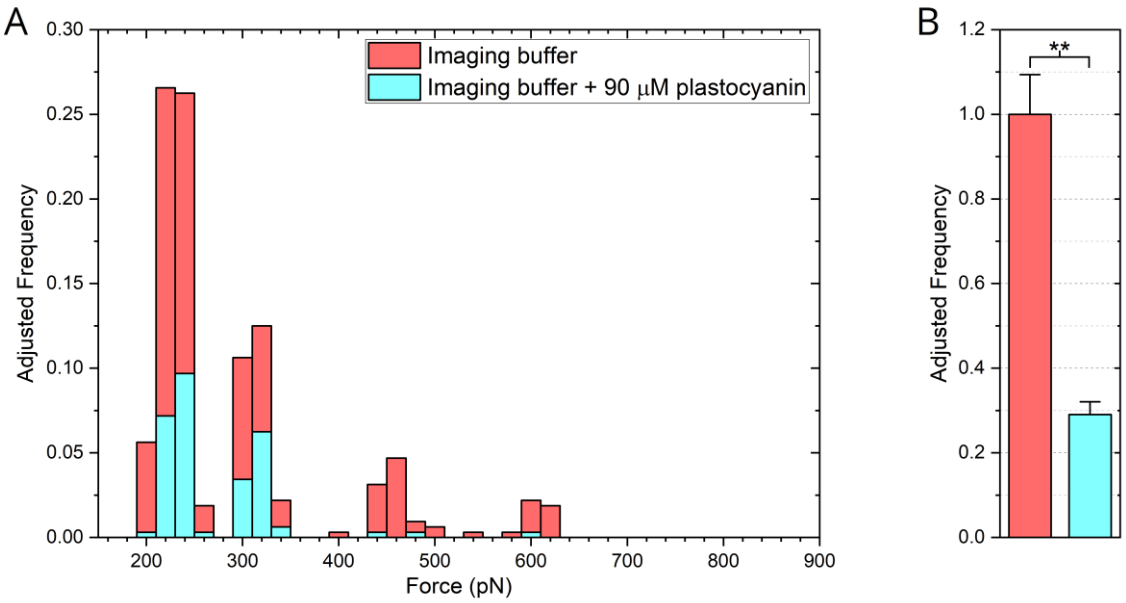

Figure 3.22 Initial experiments on Cytochrome b_6f : Plastocyanin - Amine linkage

*Initial results from the interaction between cytb_6f and Pc in imaging buffer of 10mM HEPES pH 7.4, 10mM NaCl, 0.2mM tPCC-α-M. (**A**) Distribution of forces for the interaction, with the cumulative frequency being equal to that seen in (B). (**B**) Interaction frequency for the interaction, with the*

frequencies being set relative to before addition of 90µM Pc. Colours match those seen in (A). Unpaired t-test analysis was performed on the adjusted frequencies. Asterisk denotes a p-value of 0.0079. Error bars are ± standard error of the mean, n = 5 independent analysed images for each condition.

The lower force population observed in figure 3.21 persisted in figure 3.22, despite a lower probability of chemical modification of K81. While the presence of the ca. 310pN population would suggest that changing the attachment chemistry made the Pc-probe conjugate more native, the continued presence of the ca. 230pN population would suggest that the Pc attachment chemistry is not the only factor responsible. To investigate the possibility that the 230pN population represents a complex that is not oriented correctly, the attachment chemistry of cytb_6f to the SiOx wafer was reviewed.

3.3.13 Manipulation of Cytochrome b_6f surface attachment – Tris Spiking

As discussed previously, the heights measured for the cytb_6f on the surface suggested that significant proportions were in a 'laying down' conformation, with the plane of the transmembrane region perpendicular to the SiOx, shown in cartoon form in figure 3.23A. This was proposed to originate from multiple linkage points on the cytb_6f to the silicon surface, tethering both the stromal and luminal sides of the complex. Lowering the concentration of cytb_6f in this case would not be effective, as once a single side of the complex had been tethered, the reaction with the distal side was effectively under first order kinetics. Instead, a competitive agent could be introduced in the linkage stage, to reduce the probability of multiple linkages occurring, thus promoting only a single linkage site on the immobilised cytb_6f. For this purpose, small amounts of Tris were added to the protein incubation stage, competing with lysine residues for linkage. Figure 3.23B-C shows AFM images of the resultant surfaces, with B showing the surfaces without Tris incubation, and C having 10µM present in the incubation stage.

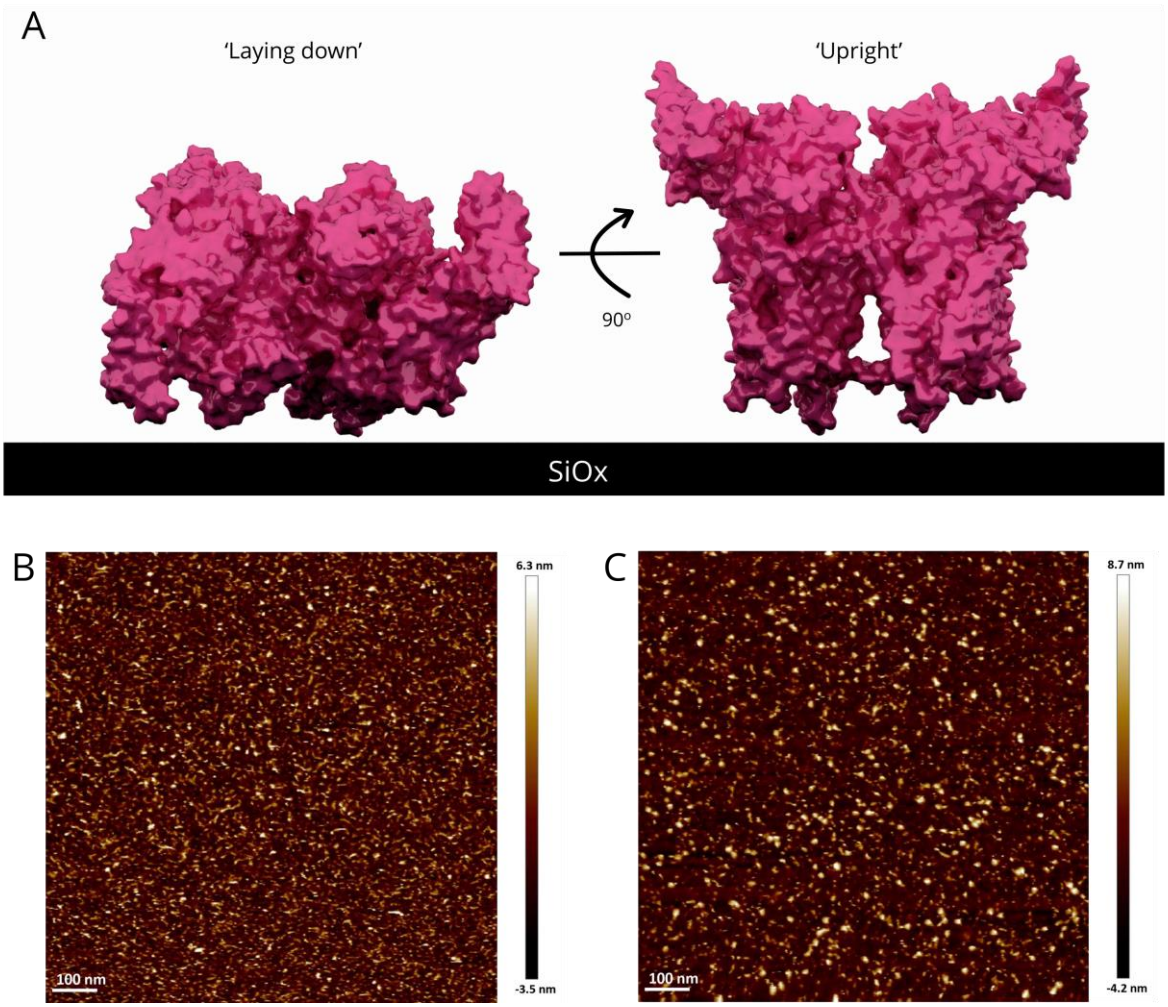

Figure 3.23 Testing of TRIS spiking for surface immobilisation.

*(**A**) Cartoon diagram showing the orientations of cytb_6f on the SiOx surface. Linkage at both luminal and stromal faces simultaneously will result in the 'laying down' orientation shown on the left. Linkage at only one of these sites will result in the 'upright' conformation seen on the right, with either the stromal or luminal faces distal to the SiOx surface. Linkers and detergent omitted for simplicity. (Structure from Stroebel et al., 2003 used, PDB: 1Q90). (**B-C**) AFM images of the surface produced following 500nM cytb_6f incubated with the surface in the absence (**B**) and presence (**C**) of 10µM Tris. Greater heights are observed in B when Tris is present, suggesting that particles are linked so the plane of the membrane would be parallel to the surface.*

A range of Tris concentrations were tested, however all appeared to have the same effect. As this gave the desired effect, it was not probed further, and hence 10 µM Tris was used in all further experiments. The particles on the surface appear to be larger in height, suggesting that they are in an 'upright' conformation, with either their stromal or luminal faces presented to the incoming AFM probe. To

facilitate easy comparisons between datasets, a custom MATLAB script was written which could open the AFM height data (following corrections made in Nanoscope) and measure the height of topological peaks on the surface (see Appendix 8.2). Figure 3.24 shows the distribution of the heights for the peaks measured. A lower threshold of 3nm was used. Curiously the 10µM Tris incubation resulted in greater heights for a short while (imaged for around 3 hours), however it appeared that over time (including when not imaged continuously by AFM) the heights went back down to the original observed without Tris.

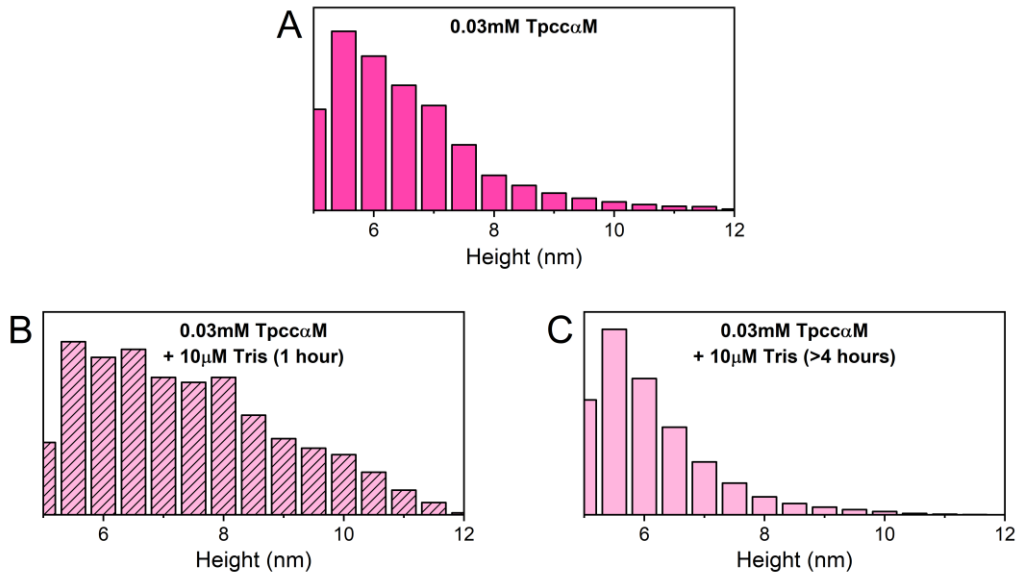

Figure 3.24 Surface heights for Tris spiking surface immobilization.

*Surface heights measured from a custom MATLAB script (Appendix 8.2) that obtains the size of peaks in an AFM height image. (**A**) Heights of the surface measured when no Tris is present in the incubation phase (Such as in Figure 3.23B). (**B**) Measured heights for cytb_6f surfaces imaged immediately after surface incubation with Tris present in incubation buffer (Such as in Figure 3.23C). (**C**) Surface heights of the surfaces imaged either the day after, or at least 4 hours after incubation with cytb_6f.*

As tPCC-α-M had already been shown to stabilise the cytb_6f complex and facilitate long storage and high activity in solution (Hovers et al., 2011), it was not thought that the detergent itself was damaging the complex. However, the activity in cytb_6f does involve movement in the protein; the Rieske protein moves to facilitate internal electron transfer via the iron-sulphur cluster from the Q_0 site to Haem *f* (See chapter 1.1.2.4). If this movement was occurring whilst the protein was tethered to the surface, this may apply a pressure on the structure and thus pull the protein apart, leading to parts not

covalently attached to the surface being allowed to move off. As such, although tPCC-α-M allowed for stable storage and high activity of the protein, another detergent would be required to effectively slow or eliminate the movement of the Rieske protein during and following incubation.

3.3.14 Manipulation of Cytochrome *b_6f* surface attachment – Detergent testing

Unfortunately, detergents that effectively reduce the activity of a protein are rarely reported, and no mention of any in the literature could be found. As a result, an optimisation test was performed, in which cyt*b_6f* was incubated with the surface in a range of different detergents to improve its stability. The detergents tested were Glyco-diosgenin (GDN), n-Dodecyl-α-D-Maltopyranoside (αDDM), and tPCC-α-M. All detergents were tested with and without 10 µM Tris, and at a concentration of 10x their CMC, as is the usual working concentration (See Materials & methods section 2.5.4.1 for individual concentrations used). Figure 3.25 shows the resultant heights measured when different detergents are present at incubation, storage and imaging stages with cyt*b_6f*. Following incubation, surfaces were stored overnight and imaged the following day, measuring the height of cyt*b_6f* on the surface. As figure 3.25 shows, the only detergent which appeared to retain the cyt*b_6f* height over time was GDN, when combined with 10 µM Tris. This showed that the best combination would be to have both GDN and Tris present at the incubation stage, and then use an imaging buffer of 10mM HEPES pH 8.0, 10mM NaCl and 0.05% (w/v) GDN as used in Mayneord et al., 2019.

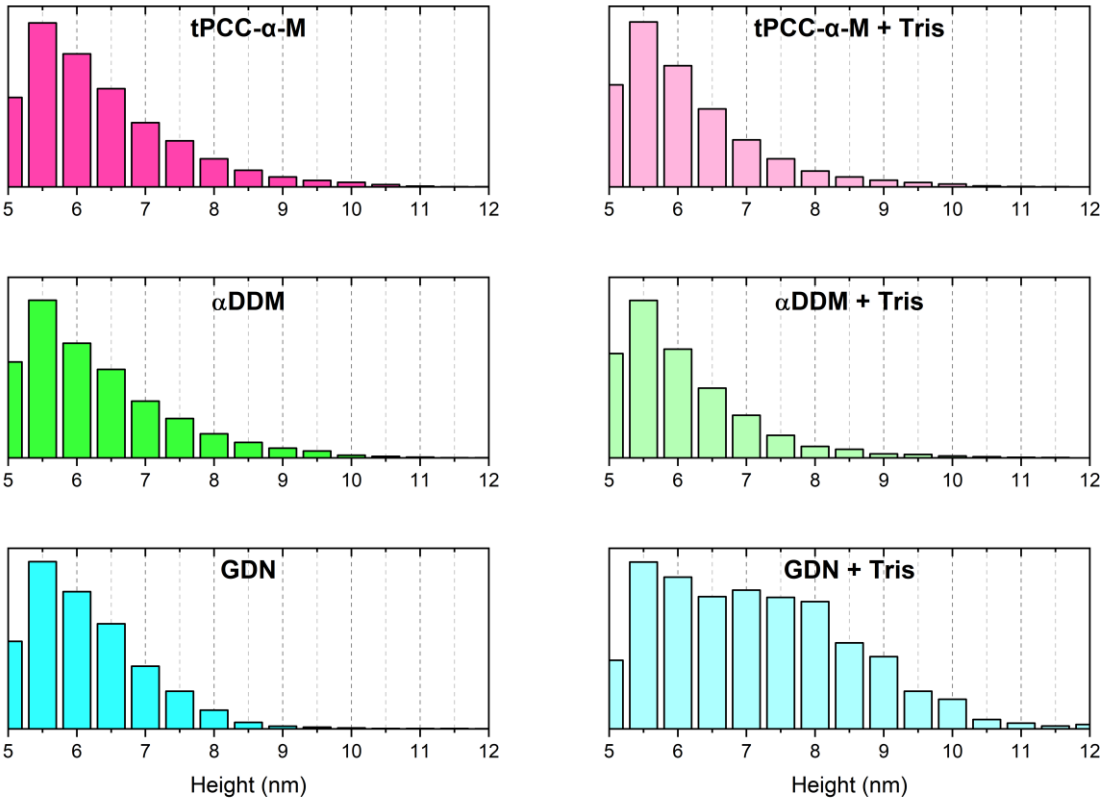

Figure 3.25 Detergent and Tris testing for immobilisation optimisation.

Surface heights measured as in figure 3.24. All detergents were tested in the presence and absence of 10µM Tris as indicated and were imaged the day after the incubation stage. The GDN + Tris combination was found to maintain the heights observed for the tPCC-α-M + Tris following several days of incubation. GDN: Glyco-diosgenin, αDDM: n-Dodecyl-α-D-Maltopyranoside, tPCC-α-M: 4-trans-(4-trans-Propylcyclohexyl)-cyclohexyl α-maltoside.

3.3.15 Attempted liposome reconstitution of Cytochrome b_6f

An alternative way of ensuring that cytb_6f was orientated in an upright conformation, with either its stromal or luminal face exposed on the surface, would be to reconstitute it into a native lipid environment, allowing effectively the original experiment in Johnson et al., 2014, however with the assurance that only cytb_6f was present in the membrane, and the ability to increase the density for a given imaging area to obtain large data sets. Methods for the incorporation of thylakoid proteins into liposomes comprised of native thylakoid lipids and their adsorption to mica surfaces have been described (Methods reviewed in Goddard et al., 2015, Yang et al., 2005; Zhou et al., 2009). Previous

studies have utilised such liposomal systems for the study of photosynthetic energy transfer, however no previous attempts to reconstitute cytb_6f into liposomes were found in the literature.

Initial attempts at reconstitution of cytb_6f into liposomes used 1,2-dioleoyl-sn-glycero-3-phosphocholine (DOPC), for which an established liposome protocol existed in our laboratory. The detergent was removed by hydrophobic adsorption using polystyrene beads (Lévy et al., 1990). For the method used for liposome creation and protein reconstitution, see materials and methods section 2.5.4.8. These proteoliposomes could then be adsorbed onto a mica surface, in a similar manner to the adsorption of native grana membranes (Sznee et al., 2011). Figure 3.26 shows AFM images of the surfaces of DOPC proteoliposomes generated, at different lipid/protein ratios. No significant topology above the lipids is seen in at protein:lipid ratios less than 1:100 (figure 3.26 A/B). The protrusions out of the membrane seen in 3.26C/D are thought to be unincorporated protein at a height of ca. 5-6nm, compared to the expected incorporated protein protrusions of ca. 3nm (shown in 3.26E). Where incorporation did appear to occur, the cytb_6f complexes appeared to be preferentially at the edges of the liposome patches. This matches previous data in our attempts to incorporate spinach thylakoid ATP synthase into DOPC, which also saw incorporation preferentially at the edges of patches (Wood et al., 2018, Supplemental). The thickness of the bilayer formed with DOPC is ca.3 nm, smaller than the 4nm for thylakoid membranes in plants. This would explain why the complexes were preferentially incorporating to the edges of the membrane, as this may be the only way to seclude the 4nm hydrophobic transmembrane region on the protein. As an alternative we attempted to incorporate cytb_6f into liposomes comprised of native thylakoid lipids.

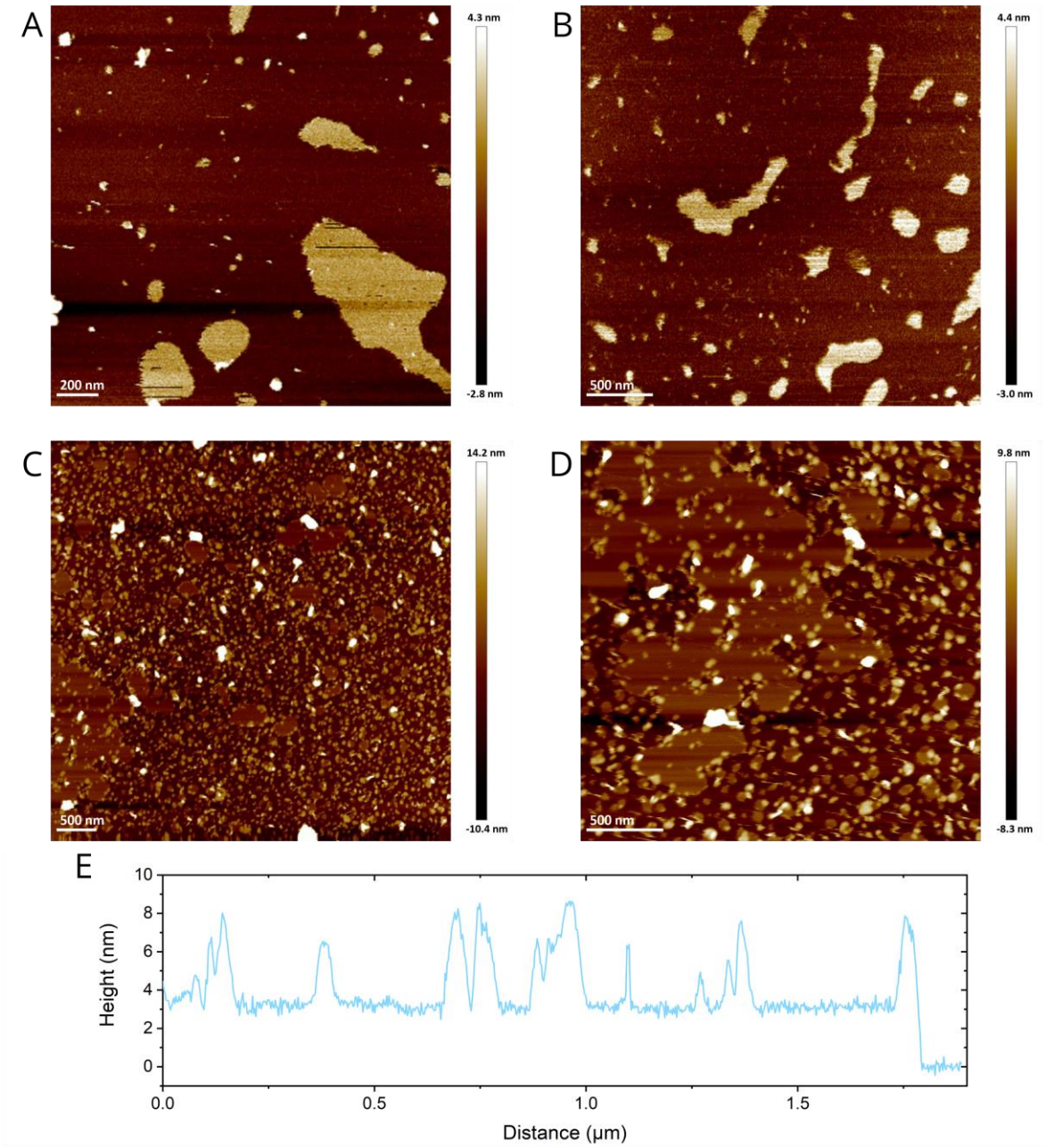

Figure 3.26 Liposome reconstitution of Cytochrome b_6f into DOPC.

*AFM images of the surfaces produced following the attempts to reconstitute cytb_6f into DOPC liposomes. At protein : lipid ratios of (**A**) 1:500 (**B**) 1:300 (**C,D**) 1:100 on mica surfaces incubated with proteoliposome mix for 30 minutes. (**E**) Cross section taken from the AFM image seen in (C) showing the DOPC bilayer height of 3nm along with the ca. 5nm height of protrusions.*

Using published methods (Goddard et al., 2015; Moya et al., 2001), liposomes were generated for the native ratio of the lipids; 50% Monogalactosyldiacylglycerol (MGDG), 10% Phosphatidylglycerol (PG), 30% Digalactosyldiacylglycerol (DGDG) and 10% Sulfoquinovosyldiacylglycerol (SQDG) as described in materials and methods, section 2.5.4.9. Initially, the use of a mix of both LHCII (Prepared by T.Davies) and cytb_6f were tested, with LHCII thought to aid adsorption of the proteoliposome patches to the mica surface for AFM imaging. A stepwise sucrose gradient from 10-40% sucrose in 10% steps was used to separate out proteoliposomes from unincorporated liposomes. The extracted bands from the gradient could be incubated with a freshly cleaved mica surface at different concentrations and lengths of incubation. Figure 3.27 shows the AFM images taken of these surfaces. A and B show surfaces incubated with LHCII / cytb_6f proteoliposomes following the sucrose gradient with very little surface coverage seen, and no apparent incorporation. C and D show the proteoliposomes also generated with LHCII and cytb_6f, but with the sucrose gradient stage excluded. Following this EM performed by T.Davies on proteoliposomes containing only LHCII found that the complex was forming crystalline arrays. As LHCII does not have any features protruding out of the membrane, this could explain the apparent lack of protrusions seen in A-D, as LHCII forming crystalline arrays could be detrimental to the incorporation of cytb_6f. Finally, excluding LHCII from the proteoliposomes generated samples as those seen in E and F, again with the sucrose gradient stage excluded (no proteoliposomes could be obtained following the sucrose gradient step).

Once again, poor incorporation and apparent aggregation at the edges of the liposome patches was observed. Following these attempts, other methods for the removal of detergent were attempted, such as rapid dilution and freeze-thawing, however none yielded any useful results. In the interest of time, the liposome attempts were abandoned and the surface attachment of cytb_6f using Tris and GDN as discussed in 3.3.14 was taken forward to probe the interaction between cytb_6f and Pc.

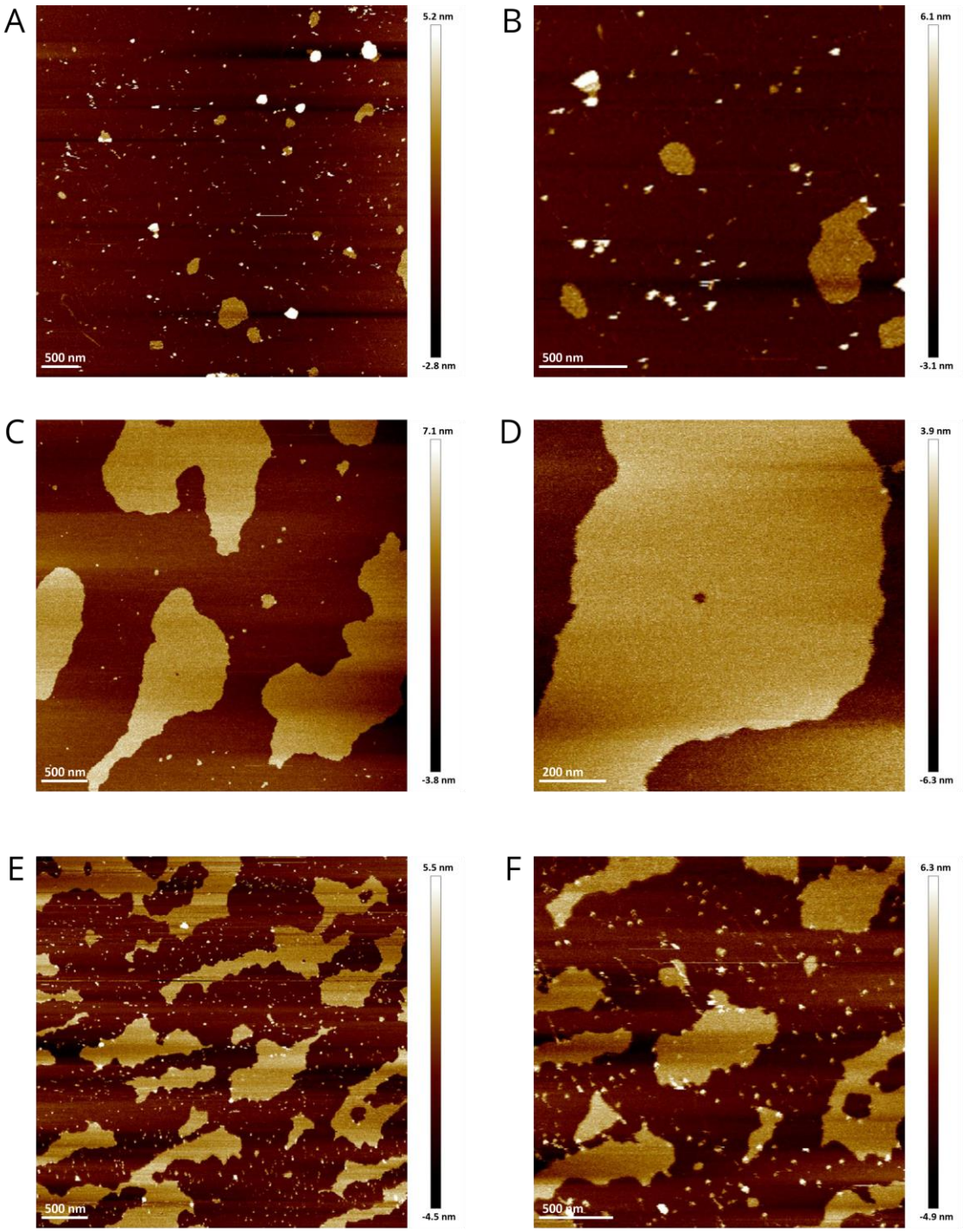

Figure 3.27 Liposome reconstitution of Cytochrome b_6f into native lipids.

*Reconstitution attempts to place cytb_6f into native thylakoid lipids. AFM surfaces of (**A/B**) Proteoliposomes generated with both LHCII and cytb_6f and enriched on a stepwise sucrose gradient, incubated with surface for 1 hour, no dilution. (**C/D**) Proteoliposomes generated with LHCII and cytb_6f with no enrichment step, incubated for 5 minutes at 10x dilution. (**E/F**) Liposomes generated with only cytb_6f, with no enrichment step, again incubated for 5 minutes at 10x dilution.*

3.4 Concluding remarks

In SMFS experiments, establishing a reliable and reproducible method of linking active biomolecules to the inorganic surfaces on the probe and substrate is the primary challenge to overcome. Since such experiments generally require different equipment compared to that commonly found in biochemical laboratories, it is important to match what is feasible with what is available. While all the techniques used in this chapter have been used for published SMFS studies, the suitability for our equipment still needed to be explored. The purifications of Pc and cytb_6f described in this chapter could be used to probe their interaction (chapter 4). The remaining work performed in this chapter optimising surface chemistry was the basis for the experiments performed in the following 3 chapters, in which this attachment chemistry, or slight deviations from it are used to probe the complexes between cytb_6f : Pc, PSI : Pc and RC-LH1 : cyt c_2 to better understand electron transfer complexes.

3.5 Bibliography

Adams, N.B.P., Vasilev, C., Brindley, A.A., and Hunter, C.N. (2016). Nanomechanical and Thermophoretic Analyses of the Nucleotide-Dependent Interactions between the AAA + Subunits of Magnesium Chelatase. J. Am. Chem. Soc. *138*, 6591–6597.

Black, M.T., R, W.W., and Cramer, W.A. (1987). Large-Scale Purification of Active Cytochrome b_6f complex from Spinach Chloroplasts. Arch. Biochem. Biophys. *252*, 655–661.

Bonanni, B., Kamruzzahan, A.S.M., Bizzarri, A.R., Rankl, C., Gruber, H.J., Hinterdorfer, P., and Cannistraro, S. (2005). Single molecule recognition between cytochrome C 551 and gold-immobilized azurin by force spectroscopy. Biophys. J. *89*, 2783–2791.

Cramer, W.A., and Whitmarsh, J. (1977). Photosynthetic Cytochromes. Annu. Rev. Plant Physiol. *28*, 133–172.

Dietrich, J., and Kuhlbrandt, W. (1999). Purification and two-dimensional crystallization of highly active cytochrome b_6f complex from spinach. *463*, 97–102.

Ebner, A., Wildling, L., Kamruzzahan, A.S.M., Rankl, C., Wruss, J., Christoph, D., Hlzl, M., Zhu, R., Kienberger, F., Blaas, D., et al. (2007a). A New , Simple Method for Linking of Antibodies to Atomic Force Microscopy Tips. 1176–1184.

Ebner, A., Hinterdorfer, P., and Gruber, H.J. (2007b). Comparison of different aminofunctionalization strategies for attachment of single antibodies to AFM cantilevers. Ultramicroscopy *107*, 922–927.

Ebner, A., Wildling, L., Zhu, R., Rankl, C., Haselgrubler, T., Hinterdorfer, P., and Gruber, H.J. (2008). Functionalization of probe tips and supports for single-molecule recognition force microscopy. Top. Curr. Chem. *285*, 29–76.

Evans, E. (1999). Energy landscapes of biomolecular adhesion and receptor anchoring at interfaces explored with dynamic force spectroscopy. Faraday Discuss. *111*, 1–16.

Florin, E., Moy, V.T., and Gaub, H.E. (1994). Adhesion Forces Between Individual Ligand-Receptor Pairs. Science (80-.). *264*, 415–418.

Fritz, J., Katopodis, A.G., Kolbinger, F., and Anselmetti, D. (1998). Force-mediated kinetics of single P-selectin/ligand complexes observed by atomic force microscopy. Proc. Natl. Acad. Sci. *95*, 12283–12288.

Goddard, A.D., Dijkman, P.M., Adamson, R.J., Dos Reis, R.I., and Watts, A. (2015). Reconstitution of Membrane Proteins: A GPCR as an Example. In Methods in Enzymology, pp. 405–424.

Gothe, P.K., Gaur, D., and Achanta, V.G. (2018). MPTMS self-assembled monolayer deposition for ultra-thin gold films for plasmonics. J. Phys. Commun. *2*.

Haselgrubler, T., Amerstorfer, A., Schindler, H., and Gruber, H.J. (1995). Synthesis and Applications of a New Poly(Ethylene Glycol) Derivative for the Crosslinking of Amines with Thiols. Bioconjug. Chem. *6*, 242–248.

Hinterdorfer, P., Baumgartner, W., Gruber, H.J., Schilcher, K., and Schindler, H. (1996). Detection and localization of individual antibody-antigen recognition events by atomic force microscopy. Proc. Natl. Acad. Sci. U. S. A. *93*, 3477–3481.

Hope, A.B. (1993). The chloroplast cytochrome bf complex A critical focus on function. BBA - Bioenerg. *1143*, 1–22.

Hope, A.B. (2000). Electron transfers amongst cytochrome *f*, plastocyanin and photosystem I: kinetics and mechanisms. Biochim. Biophys. Acta *1456*, 5–26.

Hovers, J., Potschies, M., Polidori, A., Pucci, B., Raynal, S., Bonneté, F., Serrano-Vega, M.J., Tate, C.G., Picot, D., Pierre, Y., et al. (2011). A class of mild surfactants that keep integral membrane proteins water-soluble for functional studies and crystallization Supplemental information. Mol. Membr. Biol. *28*, 171–181.

Huang, D., Everly, R.M., Cheng, R.H., Heymann, J.B., Schagger, H., Sled, V., Ohnishi, T., Baker, T.S., and Cramer, W.A. (1994). Characterization of the Chloroplast Cytochrome b_6f Complex as a Structural and Functional Dimer†. Biochemistry *33*, 4401–4409.

Izrailev, S., Stepaniants, S., Balsera, M., Oono, Y., and Schulten, K. (1997). Molecular dynamics study of unbinding of the avidin-biotin complex. Biophys. J. *72*, 1568–1581.

Johnson, M.P., Vasilev, C., Olsen, J.D., and Hunter, C.N. (2014). Nanodomains of Cytochrome b_6f and Photosystem II Complexes in Spinach Grana Thylakoid Membranes. Plant Cell *26*, 3051–3061.

Kamruzzahan, A.S.M., Ebner, A., Wildling, L., Kienberger, F., Riener, C.K., Hahn, C.D., Pollheimer, P.D., Winklehner, P., Holzl, M., Lackner, B., et al. (2006). Antibody linking to atomic force microscope tips via disulfide bond formation. Bioconjug. Chem. *17*, 1473–1481.

Krasnoslobodtsev, A. V, Shlyakhtenko, L.S., and Lyubchenko, Y.L. (2007). Probing Interactions within the synaptic DNA-SfiI complex by AFM force spectroscopy. J. Mol. Biol. *365*, 1407–1416.

Lee, G.U., Kidwell, D.A., and Colton, R.J. (1994). Sensing Discrete Streptavidin Biotin Interactions With Atomic-Force Microscopy. Langmuir *10*, 354–357.

Lévy, D., Bluzat, A., Seigneuret, M., and Rigaud, J.L. (1990). A systematic study of liposome and

proteoliposome reconstitution involving Bio-Bead-mediated Triton X-100 removal. BBA - Biomembr. *1025*, 179–190.

Luján, M.A., Lorente, P., Zazubovich, V., and Picorel, R. (2017). A simple and efficient method to prepare pure dimers and monomers of the cytochrome b_6f complex from spinach. Photosynth Res *1*, 305–309.

Malone, L.A., Qian, P., Mayneord, G.E., Hitchcock, A., Farmer, D.A., Thompson, R.F., Swainsbury, D.J.K., Ranson, N.A., Hunter, C.N., Johnson, M.P. (2019). Cryo-EM structure of the spinach cytochrome b_6f complex at 3.6 Å resolution, Nature *575,* 535–539.

Mayneord, G.E., Vasilev, C., Malone, L.A., Swainsbury, D.J.K., Hunter, C.N., and Johnson, M.P. (2019). Single-molecule study of redox control involved in establishing the spinach plastocyanin-cytochrome b_6f electron transfer complex. Biochim. Biophys. Acta - Bioenerg. *1860*, 591–599.

Merkel, R., Nassoy, P., Leung, A., Ritchie, K., and Evans, E. (1999). Energy landscapes of receptor-ligand bonds explored with dynamic force spectroscopy. Nature *397*, 50–53.

Moya, I., Silvestri, M., Vallon, O., Cinque, G., and Bassi, R. (2001). Time-resolved fluorescence analysis of the photosystem II antenna proteins in detergent micelles and liposomes. Biochemistry *40*, 12552–12561.

Navarro, J.A., Hervás, M., and la Rosa, M.A. (2011). Purification of Plastocyanin and Cytochrome c_6 from Plants, Green Algae, and Cyanobacteria. In Photosynthesis Research Protocols, R. Carpentier, ed. (Totowa, NJ: Humana Press), pp. 79–94.

De Paris, R., Strunz, T., Oroszlan, K., Guntherodt, H.-J., and Hegner, M. (2000). Force Spectroscopy and Dynamics of the Biotin:Avidin Bond Studied by Scanning Force Microscopy. Single Mol. *1*, 285–290.

Pierre, Y., Breyton, C., Kramer, D., and Popot, J.-L. (1995). Purification and Characterization of the Cytochrome b6f Complex from Chlamydomonas reinhardtii. J. Biol. Chem. *270*, 29342–29349.

Ramanath, G., Cui, G., Ganesan, P.G., Guo, X., Ellis, A. V., Stukowski, M., Vijayamohanan, K., Doppelt, P., and Lane, M. (2003). Self-assembled subnanolayers as interfacial adhesion enhancers and diffusion barriers for integrated circuits. Appl. Phys. Lett. *83*, 383–385.

Riener, C.K., Stroh, C.M., Ebner, A., Klampfl, C., Gall, A.A., Romanin, C., Lyubchenko, Y.L., Hinterdorfer, P., and Gruber, H.J. (2003). Simple test system for single molecule recognition force microscopy. Anal. Chim. Acta *479*, 59–75.

Stroebel, D., Choquet, Y., Popot, J.-L., and Picot, D. (2003). An atypical haem in the cytochrome b_6f complex. Nature *426*, 413–418.

Sznee, K., Dekker, J.P., Dame, R.T., Van Roon, H., Wuite, G.J.L., and Frese, R.N. (2011). Jumping mode atomic force microscopy on grana membranes from spinach. J. Biol. Chem. *286*, 39164–39171.

Trumpower, B.L., and Edwards, C.A. (1979). Purification of a reconstitutively active iron-sulfur protein (oxidation factor) from succinate . cytochrome c reductase complex of bovine heart mitochondria. J. Biol. Chem. *254*, 8697–8706.

Vasilev, C., Brindley, A. a, Olsen, J.D., Saer, R.G., Beatty, J.T., and Hunter, C.N. (2013). Nano-mechanical mapping of the interactions between surface-bound RC-LH1-PufX core complexes and cytochrome c_2 attached to an AFM probe. Photosynth. Res. *120*, 169–180.

Vasilev, C., Mayneord, G.E., Brindley, A.A., Johnson, M.P., and Hunter, C.N. (2019). Dissecting the cytochrome c_2 -reaction centre interaction in bacterial photosynthesis using single molecule force spectroscopy. Biochem. J. *476*, 2173–2190.

Wildling, L., Unterauer, B., Zhu, R., Rupprecht, A., Haselgrubler, T., Rankl, C., Ebner, A., Vater, D., Pollheimer, P., Pohl, E.E., et al. (2011). Linking of sensor molecules with amino groups to amino-functionalized AFM tips. Bioconjug. Chem. *22*, 1239–1248.

Wood, W.H.J., MacGregor-Chatwin, C., Barnett, S.F.H.S., Mayneord, G.E., Huang, X., Hobbs, J.K.J.K., Hunter, C.N.N., Matthew, P., and Johnson, M.P. (2018). Dynamic thylakoid stacking regulates the balance between linear and cyclic photosynthetic electron transfer. Nat. Plants *4*.

Yang, Z., Su, X., Wu, F., Gong, Y., and Kuang, T. (2005). Photochemical activities of plant photosystem I particles reconstituted into phosphatidylglycerol liposomes. J. Photochem. Photobiol. B Biol. *78*, 125–134.

Yoshizaki, F., Sugimura, Y., and Shimokoriyama, M. (1981). Purification, crystallization, and properties of plastocyanin from a green alga, Enteromorpha prolifera. J. Biochem. *89*, 1533–1539.

Yu, J., Wang, Q., Shi, X., Xinyong, M., Yang, H., Chen, Y.G., and Fang, X. (2007). Single-molecule force spectroscopy study of interaction between transforming growth factor β1 and its receptor in living cells. J. Phys. Chem. B *111*, 13619–13625.

Zhou, F., Liu, S., Hu, Z., Kuang, T., Paulsen, H., and Yang, C. (2009). Effect of monogalactosyldiacylglycerol on the interaction between photosystem II core complex and its antenna complexes in liposomes of thylakoid lipids. Photosynth. Res. *99*, 185–193.

4. Exploring the interaction between Plastocyanin and Cytochrome b_6f

4.1 Summary

Following the optimisation of the functionalisation steps in chapter 3, we attempted to use the established method to probe changes in the affinity between cytb_6f and Pc under different conditions, such as redox state and ionic strength. This chapter details the experiments and results of changing these different factors.

The two methods by which we measure affinity in our Single Molecule Force Spectroscopy (SMFS) experiments are the interaction frequency (how often the two components require pulling apart upon retraction), and unbinding force (the force required to separate the two components in the bound state). Force curves taken in the experiments show the expected separation distance of up to ca. 10nm, in agreement with the length of the linker used. Control experiments showed that saturation of the binding site on cytb_6f with free Pc injected into the imaging buffer decreased the interaction frequency, consistent with the notion that the SMFS experiment is probing a specific interaction between cytb_6f and Pc.

Previous experiments (see Chapter 3) were conducted with Pc in the oxidised state, and cyt b_6f in the reduced state (cytb_6f[Red] – Pc[Ox]). In this chapter, the redox states of each protein were systematically varied to observe the effect on binding of each of the four possible combinations. No significant change was observed between the pre-electron transfer (cytb_6f[Red] – Pc[Ox]) and post-electron transfer (cytb_6f[Ox] – Pc[Red]) states in either interaction frequency or unbinding force, however a significant reduction was seen in the interaction frequency when both proteins were in the same redox state (e.g. cytb_6f[Red] – Pc[Red]) compared to either the pre- or post – electron transfer states.

The effect of ionic strength on the interaction between cytb_6f and Pc measured in the SMFS experiments was also determined. As expected, the interaction frequency showed an exponential decay at increasing ionic strength, in agreement with a decreasing Debye length in the imaging media and consistent with the behaviour previously observed in bulk studies. The unbinding forces however remained unchanged, suggesting that once formed the interactions that sustain the full ET complex are unaffected by ionic strength.

The work in Chapter 3 revealed two force populations in the data describing the interaction between cytb_6f and Pc, one at ca. 310pN (as previously observed in native membranes by Johnson et al., 2014),

and a new population at ca. 220pN (Mayneord et al., 2019). Here the hypothesis that these may represent the full ET complex (at 310pN) and the encounter complex (at 220pN) was tested by investigating their response to ionic strength. This hypothesis was however refuted by the data since no change in the ratio between the two populations was observed. This observation, along with previous data from chapter 3 led to the suggestion that the two force populations arise from different orientations of the cytb_6f complex attached to the surface.

* A version of this work was published in Biochimica et Biophysica Acta (Mayneord et al., 2019). All rights and permissions for all visual data and artwork have been granted.

4.2 Introduction

One particularly well studied small diffusible redox protein is Pc, found in oxygenic photosynthetic systems in cyanobacteria and plant and algal chloroplasts, which transfers electrons from cytochrome b_6f (cytb_6f) to photosystem I (PSI) (reviewed in (Gross, 1993; Hope, 2000)). The redox active co-factor in Pc is a copper atom, which changes between +1 and +2 oxidation states (Haehnel et al., 1980). Pc accepts an electron from the *c*-type haem of cytochrome *f* and delivers it to the P700 special-pair chlorophylls of PSI. To achieve this transfer, Pc must diffuse over distances up to 250 nm between these two membrane integral complexes, through the narrow (ca. 10 nm wide) protein-crowded thylakoid lumen (Haehnel, 1984; Kirchhoff et al., 2011).

The interaction between b_6f and Pc has already been extensively studied via bulk phase measurements. Factors that sustain rapid electron transfer (ET) have been investigated by structural and mutational studies, which have highlighted the importance of complementary electrostatic interactions between two acidic residue patches on Pc ('Large region': D42, E43, D44, E45, and 'Small region': E59, E60, D61) and a basic patch of residues on cyt *f* (K58, K65, K66 and K187), as well as hydrophobic patches surrounding both the haem and copper cofactors on cyt *f* and Pc, respectively (Hope, 2000; Hyun Lee et al., 1995; Illerhaus et al., 2000; Modi et al., 1992; Sigfridsson, 1998; Soriano et al., 1996; Ueda et al., 2012). These features have been highlighted in figure 4.1.

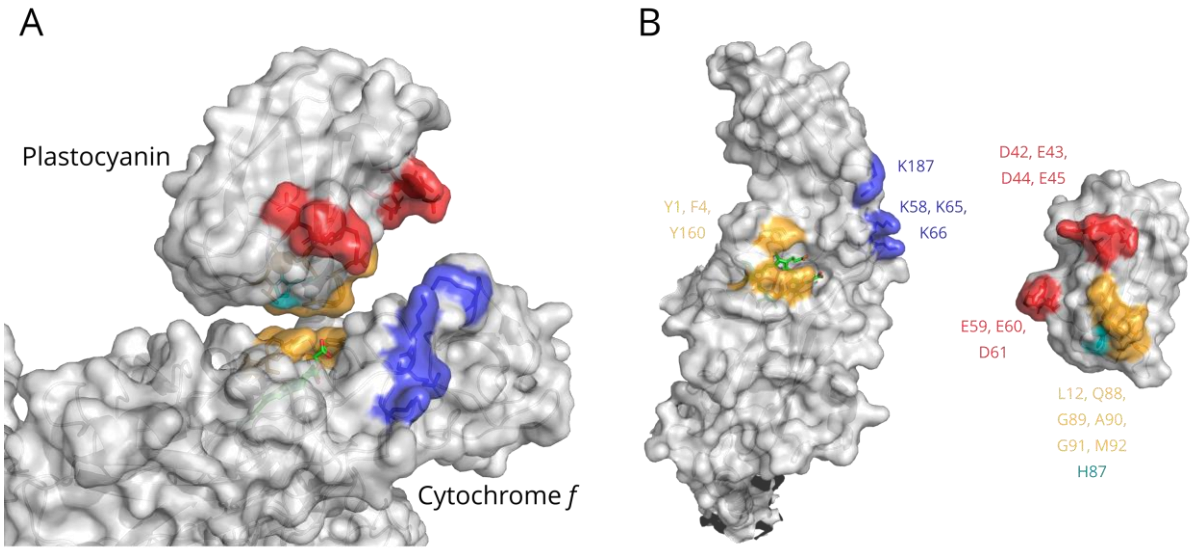

Figure 4.1 The binding interfaces Spinach Cytochrome f and Plastocyanin

Pc and cytochrome f with their relevant binding regions highlighted. Both structures from spinach; cytochrome b_6f – PDB: 6RQF *(Malone et al., 2019), and plastocyanin - PDB: 1AG6* (Xue et al., 1998). ***(A)***

*Plastocyanin and cytochrome f in a near - bound conformation for illustrative purposes, and (**B**) in an 'open book' view. Positive and negative residues are highlighted in blue and red respectively. Hydrophobic patches are shown in orange, and the His87 (accepted to be the path for electron transfer to cytochrome f haem and PSI P700 chlorophylls (Hope, 2000)) is shown in cyan.*

The importance of the encounter complex for ET rates is readily demonstrated by their dependence on the ionic strength of the aqueous medium (e.g. Illerhaus et al., 2000; Meyer et al., 1993; Qin and Kostić, 1993). As discussed in section 1.2.2, studies have found a bell-shaped response of ET rates to ionic strength. At high ionic strength the ET rate declines since the attractive electrostatic interactions are screened. At low ionic strength however, it is suggested that the transition from the initial encounter complex to the full ET complex is impeded, due to increased electrostatic interaction force, thus slowing down ET. Nuclear magnetic resonance (NMR) studies of biological ET complexes show that the encounter complexes are characterised by very small chemical shift perturbations spread out over relatively large areas of the proteins; thus, the interactions that establish ET complexes are highly dynamic and lack a single well-defined organisation, with the electrostatic interactions remaining fully-solvated and any salt-bridges being mediated by intervening water (Crowley et al., 2002; Ubbink and Bendall, 1997; Ueda et al., 2012; Volkov et al., 2005; Worrall et al., 2002).

While ensemble studies have been useful in defining the general characteristics of ET complexes, the averaging involved obscures the heterogeneity inherent within the system. Ideally it would be possible to quantify the forces involved in the putative encounter and full ET complexes at the single-molecule level and to understand their temporal, ionic strength and redox dependence. Our lab has previously used measurements of single cytb_6f-Pc interactions in an affinity mapping capacity, to understand the organisation of the cytb_6f complex in spinach thylakoids (Johnson et al., 2014). The SMFS statistics of this study were however limited by the relatively small number of membrane-embedded cytb_6f complexes. In this chapter, using the optimisations observed in the chapter 3 for attaching purified proteins to surfaces, a more in-depth study has been produced allowing a detailed investigation of the redox and salt dependence of the Pc : cytb_6f interaction at the single-molecule level.

4.3 Results

4.3.1 SMFS of the interaction between Cytochrome b_6f : Plastocyanin

Pc and dimeric cytb_6f complexes were purified from spinach (chapter 3). Surfaces and AFM probes were also generated as seen in chapter 3, utilising the Tris spiking method in GDN from section 3.3.14 (materials and methods 2.5.4.1 and 2.5.4.2). Following this, cytb_6f was pre-reduced using sodium ascorbate, Pc was pre-oxidized using potassium ferricyanide (cytb_6f[Red] – Pc [Ox]) and SMFS experiments were performed in larger data sets than those seen in chapter 3. Figure 4.2A shows an overlay of the surface topology and the adhesion events > 90pN. Good correlation can be seen between the points on the image where high unbinding forces are recorded (pink dots) and the 8 nm topographic features that correspond to immobilised cytb_6f complexes.

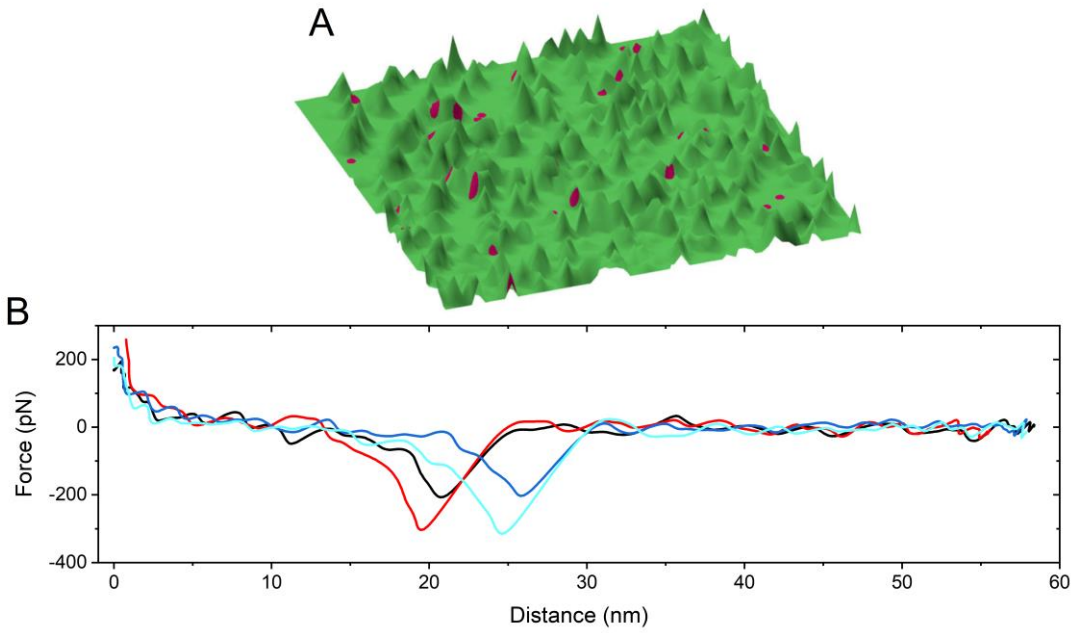

Figure 4.2 SMFS of the interaction between Cytochrome b_6f : Plastocyanin

*(**A**) 3D rendering of a subsection (250x250 nm^2) of the AFM height and adhesion data, reveals a coincidence between the regions of high unbinding force (pink dots) and the protrusions corresponding to cytb_6f molecules. (**B**) Examples of force-distance curves representing specific interactions. See results description for details.*

The density of cytb_6f on the surface is ca. 430 per 500 x 500nm scan window and the pixel density was 128 x 128; given that each pixel covers ca. 4 nm and the ~11 x 8 nm dimensions of cytb_6f (figure 3.9), each complex would be contacted roughly 9-12 times during the imaging process. The PeakForce

repetition rate was 0.5 kHz for these experiments, which corresponds to a dwell-time of the AFM probe on the surface of ca. 500 µs, slightly longer than the cyt*b*$_6$*f* -Pc ET time of 70-130 µs (Delosme, 1991; Haehnel et al., 1980). There is however an effective association rate between the cytb$_6$*f* on the surface and the Pc on the probe, hence only very infrequently would the entire 500µs dwell-time of the probe be available as a window for ET. The slight offset of the high adhesion force events from the peaks of the cyt*b*$_6$*f* complexes is most likely the result of an interaction between Pc molecules attached with an offset (i.e. not directly at the apex) on the AFM probe and cytb$_6$*f* complexes on the surface, together with a scan direction artefact during the image acquisition (Vasilev et al., 2013, 2019).

The unbinding forces were extracted and analysed using the MATLAB script discussed in section 3.3.8. Figure 4.2B shows examples of force-distance curves extracted. These curves show the unbinding following a separation of ca. 10nm, indicating that the flexible linker attaching Pc to the probe is fully extended before the interaction is ruptured, suggesting a specific Pc : cyt*b*$_6$*f* unbinding event. Some events occur at slightly larger distances, and are attributed to slight polymerisation of MPTMS, along with variations on the orientation of cytb$_6$*f* on the surface. This type of analysis allows the use the probe-sample separation distance as an initial selection criterion to extract FdCs with adhesions at separation distances over 5nm for further interrogation (Appendix, 8.1). Each dataset was statistically analysed to evaluate the frequency of the occurring interaction events (interaction frequency) as well as the most probable unbinding force (see Materials and methods section 2.6.4).

Figure 4.3 presents a statistical analysis of the distribution of the unbinding forces for over 6000 separate events, with probe-sample separation distances of at least 5nm. To further verify that these represent specific Pc-cyt*b*$_6$*f* unbinding events we tested the effect of saturating the available binding sites on the surface immobilised cyt*b*$_6$*f* complexes by injecting free oxidised Pc into the AFM liquid cell at a final concentration of 90 µM, several times higher than the reported K_D of 25 µM (Meyer et al., 1993). After approximately 5 minutes incubation with free Pc new data were recorded with the same imaging parameters. Analysis of the data obtained before and after the blocking of the docking site revealed a nearly 4-fold lower frequency for interaction between the cyt*b*$_6$*f* complex and the Pc attached to the AFM probe (Figure 4.3B), but that the distribution of unbinding forces was unaffected. The mean unbinding forces from gaussian fitting of 2 peaks on the distribution were 231 ± 3 pN and 314 ± 4 pN, and 231 ± 3pN and 310 ± 10 pN for the imaging buffer and '+90µM Pc' respectively (Figure 4.3A). Given the 25 µM K_D and 90 µM concentration of added Pc, the blocking control is expected to allow some residual binding events (Estimated only 78% occupancy based on ([Pc]/(K_D+[Pc])). A similarly lowered interaction frequency was found previously for the excess Pc control used for the affinity mapping study of cyt*b*$_6$*f* in grana membranes (Johnson et al., 2014). Following this validation of the experimental setup, the effect of different conditions could now be probed.

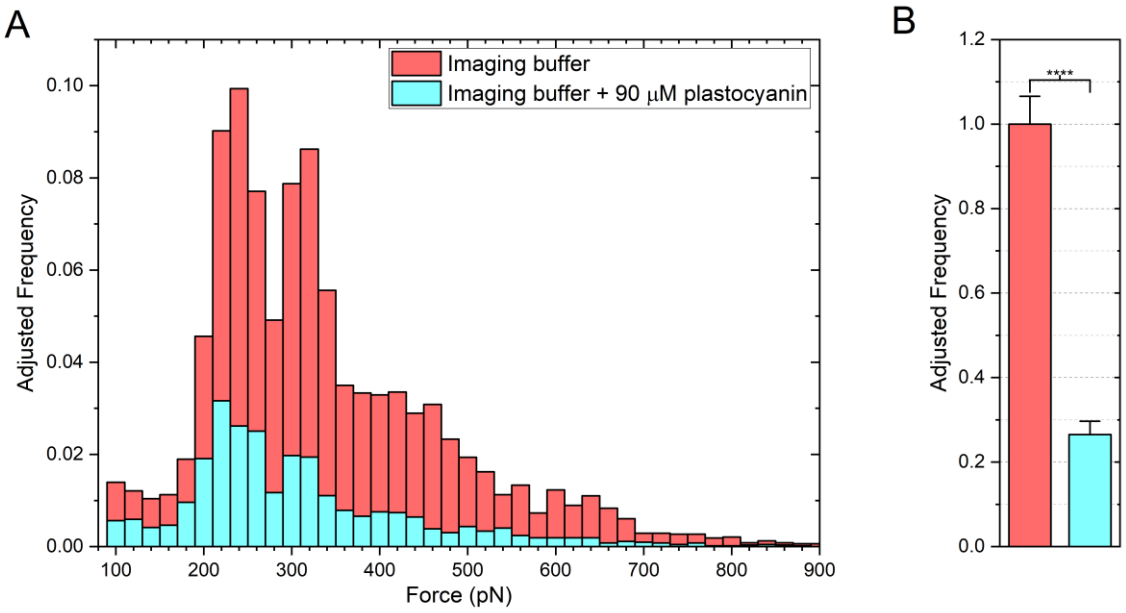

Figure 4.3 Effect of free plastocyanin on the interaction between Cytochrome b_6f : Plastocyanin

*(**A**) Distribution of forces measured, in the presence (cyan) and absence (red) of 90 μM free Pc in the imaging buffer. Mean from gaussian found to be 231 ± 3 pN and 314 ± 4pN for 'Imaging buffer' and 231 ± 3pN and 310 ± 10 pN for the '+90μM Pc' control. The cumulative frequency of each histogram was adjusted to reflect the interaction frequency plotted in (B), giving the adjusted frequency. (**B**) Mean frequency for the number of interactions observed between cytb_6f and Pc, using the same colour scheme as in (A). Frequency adjusted relative to 'Imaging buffer' sample. Imaging buffer was 10mM HEPES, pH 7.4, 10mM NaCl, 0.05% w/v GDN. Redox states of the participants were cytb_6f[Red] – Pc[Ox]. Unpaired t-test analysis was performed on the adjusted frequencies. Asterisk denotes a p-value of <0.0001. Error bars are ± standard error of the mean, n = 20-29 independent analysed images for each condition.*

4.3.2 Changes in binding dynamics between different redox states

Having established that the unbinding events correspond to *bone fide* Pc-cytb_6f interactions, the next assessment was the effect of the redox state of the partners by incubation with either sodium ascorbate (to reduce) or potassium ferricyanide (to oxidise). To ensure differences in probe preparation did not affect the interaction frequency (e.g. a probe with more Pc attached giving a higher interaction frequency), the initial experiment of cytb_6f[Red] – Pc[Ox] (Natively, the pre-ET state) was performed for 5 images, followed by a change in redox state to the given condition (thus creating a baseline). The adjusted frequency was thus a comparison of the new condition to the initial pre-ET

state. Four different experiments were conducted where cytb_6f — Pc were either in complementary redox states; cytb_6f[Red] – Pc[Ox] and cytb_6f[Ox] – Pc[Red], or in the same redox state; cytb_6f[Ox] – Pc[Ox] and cytb_6f[Red] – Pc[Red]. Figure 4.4 compares the cumulative binding frequencies and unbinding forces for all four redox pairs. It is evident that when the cytb_6f and the Pc are in the same redox state, the interaction frequency is substantially lower (by a factor of ca. 5) compared to the pre-ET state, in qualitative agreement with the previous findings on membrane-bound cytb_6f (Johnson et al., 2014). The results for the post ET state, cytb_6f[Ox] – Pc[Red], showed an equal (within experimental error) interaction frequency to the pre-ET state. Due to the low driving force (difference in midpoint potential of 30mV, Haehnel et al., 1980) for electron transfer in this complex the similar interaction frequencies for pre- and post-ET states likely reflect the reversible electron transfer between tip-attached Pc and surface-attached cytb_6f during the dwell time of the tip near the cytb_6f complex. In addition, the unbinding force distributions presented in figure 4.4 A-D also show that the unbinding forces present in the pre- and post-ET states were nearly identical, both displaying two lower populations, with most probable unbinding forces of 219 ± 64 pN and 311 ± 72 pN for cytb_6f[Red] – Pc[Ox], and 223 ± 63 pN and 313 ± 47 pN for cytb_6f[Ox] – Pc[Red]. The higher harmonics at ca. 400 and 650 pN in figure 4.4 A-B represent simultaneous unbinding events between two separate Pc molecules on the probe binding to two binding sites on the cytb_6f on the surface (either both sides of the dimer or two independent cytb_6f complexes), which is less likely than individual unbinding events given the low density of cytb_6f complexes on the surface. The forces observed for the cytb_6f[Red] – Pc[Red] and cytb_6f[Ox]–Pc[Ox] states are similar - 216 ± 68 pN and 314 ± 170 pN, and 212± 81 pN and 301 ± 155 pN, respectively, but the probability of such interactions is ca. 5-fold lower than for complementary redox pairs (Figure 4.4E). The higher of the two interaction forces (ca. 310pN) in all states corresponds well with the previous study on cytb_6f in the grana membrane (Johnson et al., 2014), which found a single most probable unbinding force of 312 ± 5pN. The present study identifies another probable unbinding force at a lower value (ca. 220 pN).

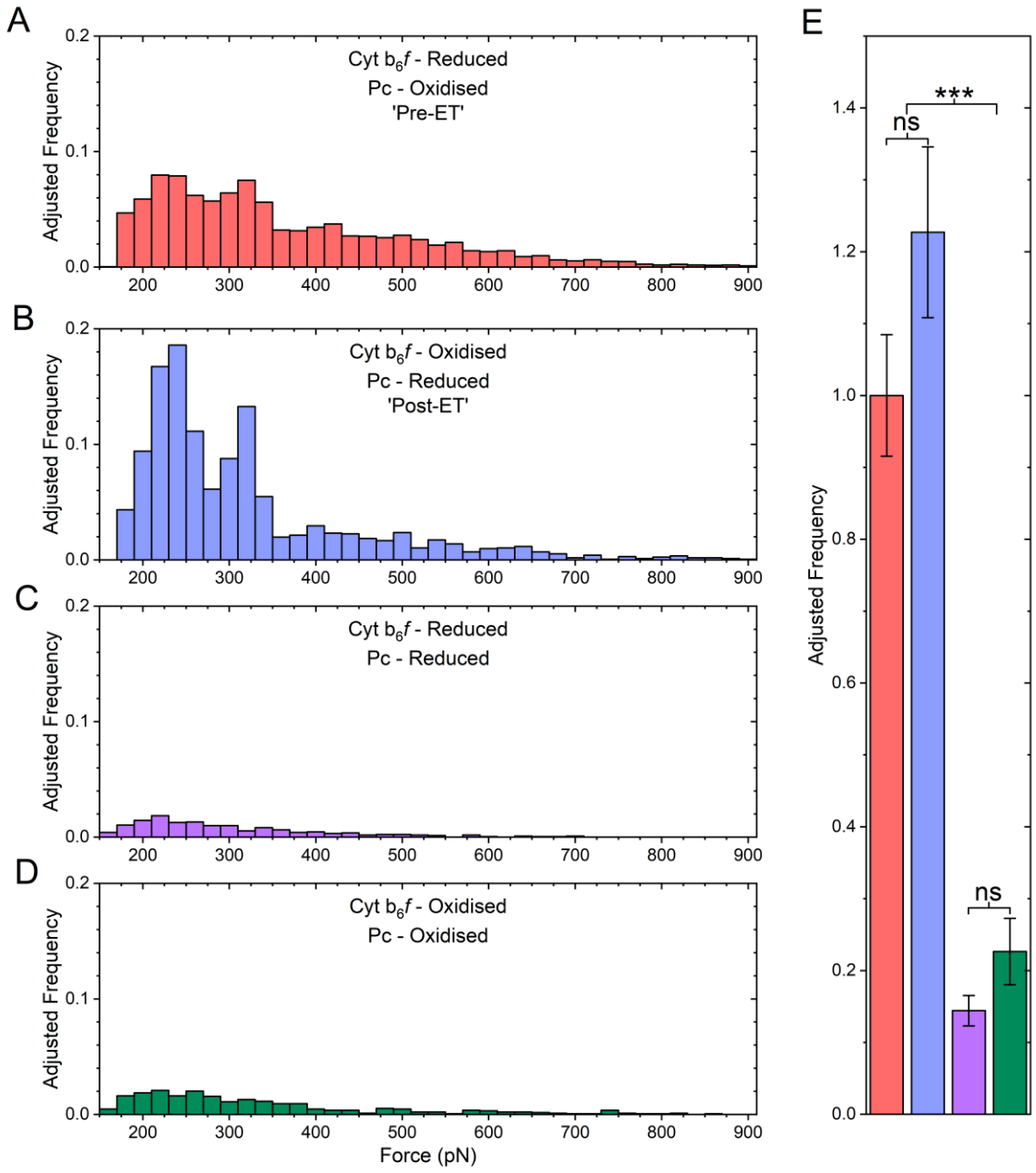

Figure 4.4 Redox dependence of the interaction between Cytochrome b_6f : Plastocyanin.

*Adjusted frequencies represent the total number of interactions occurring, adjusted to the pre-ET state (cytb_6f[Red] - Pc[Ox]). (**A-D**) Force distributions for the interaction between; (**A**) cytb_6f[Red] – Pc[Ox], (**B**) cytb_6f[Ox] - Pc[Red], (**C**) cytb_6f[Red] – Pc[Red], and (**D**) cytb_6f[Ox] – Pc[Ox]. For each, the cumulative frequency of the histogram reflects the adjusted frequency seen in (E). (**E**) Mean cumulative frequency for the interaction at different redox states. Frequencies adjusted relative to the Pre-ET state. Colours represent the data sets seen in A-D. One-way ANOVA of the adjusted frequencies to compare different states are indicated in asterisks/ns, and represent p-values as follows:*

cytb$_6$f[Red] – Pc[Ox] vs cytb$_6$f[Ox] – Pc[Ox] - 0.0007,
cytb$_6$f[Red] – Pc[Ox] vs cytb$_6$f[Red] – Pc[Red] - <0.0001,
cytb$_6$f[Red] – Pc[Ox] vs cytb$_6$f[Ox] – Pc[Red] - 0.2875,
cytb$_6$f[Ox] – Pc[Ox] vs cytb$_6$f[Red] – Pc[Red] - 0.9832,
cytb$_6$f[Ox] – Pc[Ox] vs cytb$_6$f[Ox] – Pc[Red] - <0.0001,
cytb$_6$f[Red] – Pc[Red] vs cytb$_6$f[Ox] – Pc[Red] - <0.0001.
Error bars are ± standard error of the mean, n = 25-87 independent analysed images for each condition.

4.3.3 Effect of ionic strength on Cytochrome *b$_6$f* : Plastocyanin interaction

In order to investigate the origin of the second unbinding force (at ca. 220 pN) further, the pre-ET state was measured as a function of the ionic strength of the medium. In the context of the SMFS experiments increasing the dielectric constant of the surrounding medium (the imaging buffer) should lead to a decrease of the interaction frequency due to a decrease of the Debye length, which in this case reflects the extent of the electrostatic effect exerted by the charged residues at the surfaces of cyt*b$_6$f* and Pc. Previous bulk phase studies have found a bell-shaped response of ET rate to ionic strength (Meyer et al., 1993). The suggested explanation has centred on the transition from the encounter complex to the full ET state; as the encounter complex is governed by electrostatic interactions, low ionic strengths (below 50mM) are suggested to impede the transition from encounter complex to full ET complex, thus slowing down ET at lower ionic strengths, leading to the bell shape. As such, an initial explanation for the bimodal distribution of unbinding forces was that the lower force (ca. 220pN) could represent the encounter complex, with a larger transition state barrier to the full ET complex if the cytb$_6$*f* on the surface were 'laying down' (figure 3.23). Complexes that were more 'upright' could potentially have a lower energetic barrier, facilitating easier entrance to the full ET complex (measured at ca. 310pN). If this were the case, the ratio between the populations would also be expected to change with ionic strength.

A series of SMFS measurements were conducted for this purpose (Figure 4.5), using the pre-ET state (cyt*b$_6$f*[Red] – Pc[Ox]) while varying the ionic strength of the imaging buffer by varying the salt concentration from 5 - 250mM NaCl, thus covering a broader range than physiologically relevant of salt concentrations (100-200 mM according to Izawa and Good, 1966; Staehelin, 1976). There appear to be no reports that measure the ionic strength of the luminal space occupied by Pc *in vivo*. As previously discussed with the examination of redox state, variation in tip preparations were negated by having an initial baseline experiment, this time in 5mM NaCl for 5 images, followed by changing the salt concentration to the given condition.

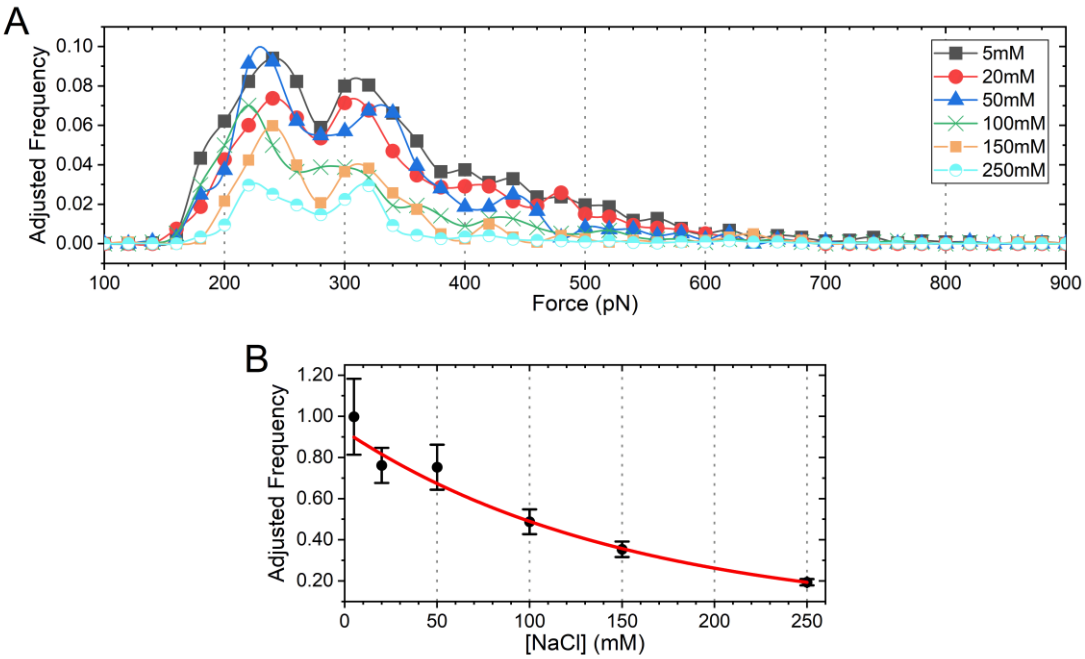

Figure 4.5 Effect of ionic strength on the unbinding forces and interaction frequency for Cytochrome b_6f : Plastocyanin

*(**A**) Multiple overlaid histograms representing the distributions of unbinding forces for separating cytb_6f[Red] – Pc[Ox] measured at different salt concentrations, with the cumulative sum adjusted relative to 5 mM NaCl. One-way ANOVA was used to test for a trend in the ratio between the two peaks and returned a p-value of 0.516. (**B**) Interaction frequency of each salt concentration adjusted relative to 5mM NaCl being 1. Error bars are ± standard error of the mean.*

Interestingly, changes in the ratio of the ca. 310 pN and 220 pN peaks in the distribution of unbinding forces in figure 4.5 were not found to follow a significant trend (following One-way ANOVA examination) over the entire range of salt concentrations, but the interaction frequency decreased significantly at higher salt concentrations (>50 mM NaCl). This trend is evident in figure 4.5B, where the interaction frequency is plotted against the salt concentration and the data follow the expected single exponential decay. At the highest concentration of 250 mM NaCl the interaction frequency is decreased by a factor of ca. 5. Since a similar pattern was observed for both force populations, the results suggest that the lower force peak is unlikely to arise specifically from the encounter complex.

4.4 Discussion

SMFS experiments have been performed to study the interaction of Pc with its native electron donor cytb_6f. The behaviour of single molecules, rather than the collective billions studied in bulk measurements, is arguably a more valid representation of intermolecular processes that occur *in vivo*. The previous AFM study of the Pc : cytb_6f interaction used grana membranes isolated from spinach, adsorbed onto a mica surface (Johnson et al., 2014). Although native membranes have the advantage of consistently presenting the luminal face of the cytb_6f complexes to incoming Pc molecules borne on the AFM probe, many thousands of interactions are required for statistical analysis. In this study, using purified cytb_6f complexes immobilised on silicon makes large numbers of molecules available for this approach and records a much larger number of unbinding events within a given scan area compared to cytb_6f in native membranes. This approach also ensures that the Pc targets only cytb_6f complexes rather than the heterogeneous protein complement of a native photosynthetic membrane. However, the downside to this approach is that it can introduce an intrinsic heterogeneity into the system, as the non-specific linkage of cytb_6f to the surface means that several orientations are possible. As discussed in section 3.3.13, introduction of a competitive agent into the linkage stage can reduce the probability of multiple linkage points, however it cannot offer any further specificity to the sites. This would ideally be achieved through the use of recombinant proteins with an engineered linkage point, such as a unique cysteine or hexa-His tag. Unfortunately, these options were not available for the current work. As such, there is a likely mixed orientation of cytb_6f complexes, arising from attachments to different lysine residues on the stromal and luminal faces of the complex. Nevertheless, there is good agreement between the present (Mayneord et al., 2019) and previous work (Johnson et al., 2014), in most results. In addition to the 310pN unbinding force previously observed, a second lower force at 220pN was also found.

4.4.1 Excess plastocyanin control

As discussed in section 1.4.1, a standard control for SMFS measurements is the addition of an excess of one of the components into the imaging buffer, to observe the effect of secluding one of the binding sites (Hinterdorfer et al., 1996, 2009; Lee et al., 1994). In our case, addition of 90 µM plastocyanin resulted in a ca. 4-fold drop in interaction frequency, in agreement with the ca. 80% occupancy expected from addition of 90 µM plastocyanin (K_D = 25 µM). This, in combination with the separation distance observed for the adhesion events is good evidence that the interaction being probed is between cytb_6f on the surface, and Pc on the AFM probe.

4.4.2 Ionic strength dependency

Due to the electrostatic nature of the complex between cytb$_6$*f* and Pc, many previous studies have observed the effect of varying ionic strength on the rate of ET. Due to the bell-shaped response to ionic strength previously found for the ET (Meyer et al., 1993), in addition to testing the effect of ionic strength on both the interaction frequency and unbinding force, we wished to understand why the force distributions were bimodal. The unbinding forces, or more specifically the ratio between the 220 and 310pN populations (220/310pN ratio) did not significantly change with ionic strength. The interaction frequency did change, following a single exponential decay in agreement with a decreasing Debye length at increasing ionic strength. The interaction frequency drops ca. 3.5-fold when comparing 50mM (the optimum found in bulk phase measurements (Meyer et al., 1993)) to 250mM NaCl. This would suggest that the physiologically relevant range of 100-200 mM (Izawa and Good, 1966; Kaiser et al., 1983; Staehelin, 1976) is far from being optimized for cyt*b$_6$f* : Pc binding.

The ratio between 220 and 310pN force populations was not affected by ionic strength (4.3.3), suggesting the 220pN population did not represent rupture of the encounter complex. However, this ratio did change when the orientation of cytb$_6$*f* changed, and when a different linkage method to Pc was used (figure 3.21). As seen in section 3.3.13, addition of 10µM Tris in the linkage stage lead to a change in the observed heights on the surface, which was correlated to the orientation of the cytb$_6$*f* on the surface. An accompanying change in the 220/310pN ratio was also observed (figure 3.22 and figure 4.3) which would suggest that the change in orientation of the cyt*b$_6$f* and Pc is associated with a change in ratio, lending credence to the orientation hypothesis. When the cytb$_6$*f* is laying down, it may seclude part of the binding interface, only allowing a partial complex formation. In addition, when K81 is chemically modified (section 3.3.11), this may also lead to the same partial complex formation. Such a transient complex might be expected to be easier to separate, when compared with the correctly oriented cyt*b$_6$f* – Pc ET complex. We cannot exclude the possibility that the ca. 220 pN unbinding force reflects a non-native association of Pc with the stromal surface of cyt*b$_6$f* complexes tethered in an inverted orientation, e.g. via interaction with a putative ferredoxin binding site.

4.4.3 Redox state changes

Previous bulk phase measurements of the Pc : cyt*b$_6$f* interaction have not been able to suggest redox specificity in the interaction, as many rely on observing absorbance changes from ET (such as stopped-flow), or simply have a time constraint (such as NMR) which means that averaging out of different redox states can occur on the timescale of the experiment. Our experiments here appear to be the first that have managed to probe the specificity of the interaction, due to their speed and independence from ET. We have found that it is the interaction frequency, rather than the unbinding

force, that shows a redox dependency; the unbinding forces required to disrupt the interactions between all reduced/oxidized combinations are similar, and it is only the frequency of interaction that changes. The previous study (Johnson et al., 2014), effectively only probed cytb_6f [Red] - Pc[Ox] and cytb_6f [Red] - Pc[Red] due to limitations such as the presence of PQ in the extracted grana membranes. The probing of the other possible redox states allowed us to form a more complete picture about the selectivity of the interaction. This study finds a high interaction frequency for the complementary redox pairs, whilst matching redox pairs appear to have a 5-fold decrease. The unbinding force measured is unchanged by any of the different redox matches. Thus, complementary redox states for the cytb_6f and Pc are essential for bringing about a highly probable interaction but once the association is established, the same level of force is required to disrupt it, regardless of redox states. These experiments therefore show that formation of the docking interface is under redox state control, as also suggested from molecular dynamics simulations of the analogous cyt bc_1 - cyt c_2 interaction (Singharoy et al., 2016).

Complementary charges on the cytb_6f and Pc cofactors must contribute to the electrostatic forces that initiate formation of the ET complex. Natively, continued turnover of the cytb_6f complex will regenerate cytb_6f [Red] and produce the strongly disfavoured cytb_6f [Red] - Pc[Red] pair. Our results suggest this would not lead to the deliberate dissociation of the complex in the cytb_6f [Red] - Pc[Red] state, but merely reduce the chances of reassociation following the dissociation. In addition, as Pc[Red] migrates through the lumen, it will also have a reduced affinity for cytb_6f[Red]. Nature likely uses this phenomenon to avoid 'product inhibition', in other words unproductive encounters between Pc and cytb_6f molecules in the same redox state, ensuring the efficiency and directionality of the electron transport process. Future studies can now focus on testing the roles of specific residues within the binding locus on the unbinding force and interaction frequency.

4.5 Bibliography

Crowley, P.B., Vintonenko, N., Bullerjahn, G.S., and Ubbink, M. (2002). Plastocyanin-cytochrome *f* interactions: the influence of hydrophobic patch mutations studied by NMR spectroscopy. Biochemistry *41*, 15698–15705.

Delosme, R. (1991). Electron transfer from cytochrome f to photosystem I in green algae. Photosynth. Res. *29*, 45–54.

Evans, E. (2001). Probing the relation between force - lifetime and chemistry in single molecular bonds. Annu. Rev. Biophys. *30*, 105–128.

Evans, E., and Ritchie, K. (1997). Dynamic strength of molecular adhesion bonds. Biophys. J. *72*, 1541–1555.

Friddle, R.W., Noy, a., and De Yoreo, J.J. (2012). Interpreting the widespread nonlinear force spectra of intermolecular bonds. Proc. Natl. Acad. Sci. *109*, 13573–13578.

Gross, E.L. (1993). Plastocyanin: Structure and function. Photosynth. Res. *37*, 103–116.

Haehnel, W. (1984). Photosynthetic electron transport in higher plants. Annu. Rev. Plant Physiol. *35*, 659–693.

Haehnel, W., Propper, A., and Krause, H. (1980). Evidence for complexed plastocyanin as the immediate electron donor of P-700. BBA - Bioenerg. *593*, 384–399.

Hinterdorfer, P., Baumgartner, W., Gruber, H.J., Schilcher, K., and Schindler, H. (1996). Detection and localization of individual antibody-antigen recognition events by atomic force microscopy. Proc. Natl. Acad. Sci. U. S. A. *93*, 3477–3481.

Hinterdorfer, P., Oijen, A. Van, Muller, D., Schmidt, T., and Seidel, C. (2009). Handbook of Single-Molecule Biophysics.

Hope, A.B. (2000). Electron transfers amongst cytochrome *f*, plastocyanin and photosystem I: kinetics and mechanisms. Biochim. Biophys. Acta *1456*, 5–26.

Hyun Lee, B., Hibino, T., Takabe, T., Weisbeek, P.J., and Takabe, T. (1995). Site-directed mutagenetic study on the role of negative patches on silene plastocyanin in the interactions with cytochrome *f* and photosystem i. J. Biochem. *117*, 1209–1217.

Illerhaus, J., Altschmied, L., Reichert, J., Zak, E., Herrmann, R.G., and Haehnel, W. (2000). Dynamic Interaction of Plastocyanin with the Cytochrome b_6f Complex. J. Biol. Chem. *275*, 17590–17595.

Izawa, S., and Good, N.E. (1966). Effect of Salts and Electron Transport on the Conformation of Isolated

Chloroplasts. II. Electron Microscopy. Plant Physiol. *41*, 544–552.

Johnson, M.P., Vasilev, C., Olsen, J.D., and Hunter, C.N. (2014). Nanodomains of Cytochrome b_6f and Photosystem II Complexes in Spinach Grana Thylakoid Membranes. Plant Cell *26*, 3051–3061.

Kaiser, W.M., Weber, H., and Sauer, M. (1983). Photosynthetic Capacity, Osmotic Response and Solute Content of Leaves and Chloroplasts From Spinacia oleracea Under Salt Stress. Zeitschrift Fur Pflanzenphysiologie *113*, 15–27.

Kirchhoff, H., Hall, C., Wood, M., Herbstova, M., Tsabari, O., Nevo, R., Charuvi, D., Shimoni, E., and Reich, Z. (2011). Dynamic control of protein diffusion within the granal thylakoid lumen. Proc. Natl. Acad. Sci. *108*, 20248–20253.

Lee, G.U., Kidwell, D.A., and Colton, R.J. (1994). Sensing Discrete Streptavidin Biotin Interactions With Atomic-Force Microscopy. Langmuir *10*, 354–357.

Malone, L.A., Qian, P., Mayneord, G.E., Hitchcock, A., Farmer, D.A., Thompson, R.F., Swainsbury, D.J.K., Ranson, N.A., Hunter, C.N., Johnson, M.P. (2019). Cryo-EM structure of the spinach cytochrome b_6f complex at 3.6 Å resolution, Nature *575,* 535–539.

Mayneord, G.E., Vasilev, C., Malone, L.A., Swainsbury, D.J.K., Hunter, C.N., and Johnson, M.P. (2019). Single-molecule study of redox control involved in establishing the spinach plastocyanin-cytochrome b_6f electron transfer complex. Biochim. Biophys. Acta - Bioenerg. *1860*, 591–599.

Meyer, T.E., Zhao, Z.G., Cusanovich, M. a, and Tollin, G. (1993). Transient kinetics of electron transfer from a variety of c-type cytochromes to plastocyanin. Biochemistry *32*, 4552–4559.

Modi, S., Nordling, M., Lundberg, L.G., Hansson, O., and Bendall, D.S. (1992). Reactivity of cytochromes c and F with mutant forms of spinach plastocyanin. BBA - Bioenerg. *1102*, 85–90.

Qin, L., and Kostić, N.M. (1993). Importance of protein rearrangement in the electron-transfer reaction between the physiological partners cytochrome f and plastocyanin. Biochemistry *32*, 6073–6080.

Sigfridsson, K. (1998). Plastocyanin, an electron-transfer protein. Photosynth. Res. *57*, 1–28.

Singharoy, A., Barragan, A.M., Thangapandian, S., Tajkhorshid, E., and Schulten, K. (2016). Binding Site Recognition and Docking Dynamics of a Single Electron Transport Protein: Cytochrome c_2. J. Am. Chem. Soc. *138*, 12077–12089.

Soriano, G.M., Ponamarev, M. V, Tae, G.S., and Cramer, W.A. (1996). Effect of the interdomain basic region of cytochrome *f* on its redox reactions in vivo. Biochemistry *35*, 14590–14598.

Staehelin, L.A. (1976). Reversible particle movements associated with unstacking and restacking of chloroplast membranes in vitro. J. Cell Biol. *71*, 136–158.

Ubbink, M., and Bendall, D.S. (1997). Complex of plastocyanin and cytochrome *c* characterized by NMR chemical shift analysis. Biochemistry *36*, 6326–6335.

Ueda, T., Nomoto, N., Koga, M., Ogasa, H., Ogawa, Y., Matsumoto, M., Stampoulis, P., Sode, K., Terasawa, H., and Shimada, I. (2012). Structural basis of efficient electron transport between photosynthetic membrane proteins and plastocyanin in spinach revealed using nuclear magnetic resonance. Plant Cell *24*, 4173–4186.

Vasilev, C., Brindley, A. a, Olsen, J.D., Saer, R.G., Beatty, J.T., and Hunter, C.N. (2013). Nano-mechanical mapping of the interactions between surface-bound RC-LH1-PufX core complexes and cytochrome c_2 attached to an AFM probe. Photosynth. Res. *120*, 169–180.

Vasilev, C., Mayneord, G.E., Brindley, A.A., Johnson, M.P., and Hunter, C.N. (2019). Dissecting the cytochrome c_2-reaction centre interaction in bacterial photosynthesis using single molecule force spectroscopy. Biochem. J. *476*, 2173–2190.

Volkov, A.N., Ferrari, D., Worrall, J.A.R., Ubbink, M., Reinle, W., Bernhardt, R., and Ubbink, M. (2005). The orientations of cytochrome *c* in the highly dynamic complex with cytochrome b_5 visualized by NMR and docking using HADDOCK. Protein Sci. *14*, 799–811.

Worrall, J.A.R., Liu, Y., Crowley, P.B., Nocek, J.M., Hoffman, B.M., and Ubbink, M. (2002). Myoglobin and cytochrome b_5: A nuclear magnetic resonance study of a highly dynamic protein complex. Biochemistry *41*, 11721–11730.

Xue, Y., Okvist, M., Hansson, O., and Young, S. (1998). Crystal structure of spinach plastocyanin at 1.7 A resolution. Protein Sci. *7*, 2099–2105.

5. Exploring the interaction between Plastocyanin and Photosystem I

5.1 Summary

Having established optimal conditions for SMFS experiments to investigate the cytb_6f : Pc ET complex, the next logical step was to extend the analysis to PSI, to which Pc is the native electron donor. To this end, PSI was purified from spinach thylakoids using an extensive modification of the protocol reported in Mazor et al., 2017. The purity of the PSI fraction obtained was confirmed by SDS-PAGE and 77K fluorescence and the intactness of the luminal Pc-binding site was confirmed by immunoblotting for the PsaF and PsaN subunits implicated in binding (Hippler et al., 1997 and Haldrup et al., 1999). The activity of this purified PSI fraction was confirmed by absorption spectroscopy.

PSI proved amenable to the same MPTMS method of attachment to the silicon surface successfully utilised for cytb_6f in Chapter 4. A concentration of 30 nM PSI was found to be optimal for producing surfaces with a density of complexes suitable for SMFS. The heights of the PSI particles attached to the surface were found to be in agreement with the expected height of the complex from the published crystal structures, suggesting the membrane plane was parallel with the silicon surface and therefore that either the stromal or luminal face of the complex was presented to the AFM probe. Initial experiments using a Pc functionalised AFM probe found a smaller unbinding force for the Pc : PSI interaction compared to the Pc : cytb_6f interaction. The location of these unbinding events was in good correlation with the topographic features of PSI resolved in the simultaneously recorded height image. The specific nature of the recorded interactions was confirmed by the injection of free unbound Pc into the imaging chamber. 90µM Pc yielded a ca. 2-fold decrease in the interaction frequency.

The effect of ionic strength on the Pc : PSI interaction was probed by varying the concentration of NaCl in the imaging buffer. The interaction frequency showed a single exponential decay with increasing ionic strength, as expected for screening between two charged bodies. The recorded unbinding forces appeared to be independent of ionic strength, although the possibility that the change could not be registered at the signal to noise level cannot be ruled out.

The redox dependency of the Pc-PSI interaction was probed by varying the redox state of Pc using ascorbate or ferricyanide as described in chapter 4. The interaction frequency dropped by a factor of 2 with Pc[Ox] compared to Pc[Red], in agreement with previous bulk phase studies (Drepper et al., 1996), whilst the unbinding forces were unchanged, in spite of the ca. 3-fold change observed

previously in bulk phase studies. This may reflect the poor signal to noise ratio in the experiments not being able to resolve the changes in unbinding forces, or it may reflect the $y \propto \ln(1/x)$ relationship between k_{off} and unbinding force (chapter 1.4.2), only leading to small changes in the force measured.

Since PSI was presumed to be excited to some extent by the 680 nm laser used in the AFM experiments it was not possible to perform a dark control as for *Rba.sphaeroides* RC-LH1 in Vasilev et al., 2013 to see if the binding of Pc was affected by photo-oxidation of PSI. As an alternative, an attempt was made to control PSI redox state under white light illumination via the inclusion or omission of methyl viologen (MV), capable of acting as an electron acceptor from PSI (Ke, 1973), in the imaging buffer. In principle the inclusion of MV should maintain PSI in an oxidised state whereas its absence might lead to net reduction of PSI via charge recombination. In contrast to this expectation no change in either the interaction frequency or the measured unbinding forces were observed with MV. One possible explanation is that the 30 ms half-time for PSI charge recombination is slow relative to the excitation rate with the 680 nm laser.

5.2 Introduction

As discussed in chapter 4.2, Pc carries electrons from cytb_6f to photosystem I (PSI) in oxygenic photosynthesis (reviewed in Hope, 2000). Just as with Pc and cytb_6f , the interaction between Pc and PSI must be highly specific and yet at the same time sufficiently transient in nature to sustain the rapid turnover of the electron transfer chain.

The PSI : Pc ET complex has been extensively studied via bulk phase kinetic measurements. Rather than the stopped-flow measurements commonly used for the Pc : cytb_6f interaction, PSI is frequently probed via flash induced kinetics (Bottin and Mathis, 1985; Drepper et al., 1996; Finazzi et al., 2005; Haehnel et al., 1971, 1980, 1994; Sigfridsson et al., 1997; Sigfridsson, 1997, 1998; Sigfridsson et al., 1996b, 1996a). Single flash excitation experiments (in which PSI is oxidised for single turnover via a short saturating pulse of light) revealed that the reduction of PSI following flash-induced photo-oxidation was biphasic. The oxidation rate was comprised of an initial fast phase (k_1) whose amplitude but not rate is dependent on the concentration of Pc, and a second slower phase (k_2), whose amplitude and rate are both dependent on Pc concentration. k_1 is thought to represent ET from pre-bound Pc and k_2 the ET following the relatively slow association of the two proteins in solution (with $k_{ET} >> k_{on}$). The rate-limiting step in the association of Pc and PSI, likely involves the transition from the 'encounter complex' previously discussed for ET complexes (section 1.2.2) to a full ET complex, as at high concentrations of Pc, PSI reduction via second order kinetics is limited to a ca. 110µs half time (Bottin and Mathis, 1985; Haehnel et al., 1980). An interesting extension of the flash excitation experiments is the ability to perform 'double flash' experiments, in which the interval between flashes can be varied to observe the effective dissociation of Pc [Ox] prior to Pc [Red] binding and transferring an electron (Drepper et al., 1996). These studies have found a redox selectivity present in the PSI – Pc interaction with a ca. 2 - fold decrease in the association (k_{on}) of Pc [Ox] compared to Pc [Red], thus avoiding 'product inhibition' of ET (Drepper et al., 1996). In addition, the dissociation (k_{off}) saw a ca. 2.5-fold increase in Pc [Ox] compared to Pc [Red], which is further increased to ca 4.5-fold when PSI becomes oxidised again (PSI [^{P}Ox] – Pc [Ox] compared to PSI [Red] – Pc [Red]) (Drepper et al., 1996). These resulted the changes in the dissociation constant (K_D), with values of 7µM for PSI [Red] – Pc [Red], 40µM for PSI [Red] – Pc [Ox] and 102µM for PSI [^{P}Ox] – Pc [Ox].

As expected, the interaction between PSI and Pc exhibits ionic strength dependency due to the electrostatic nature of the interaction. As with cytb_6f : Pc, the PSI : Pc ET rate exhibits a bell-shaped dependency on ionic strength (Sigfridsson, 1997; Sigfridsson et al., 1996b, 1997), with an optimal rate at ca. 50mM ionic strength. As previously discussed, this effect on overall ET rate represents the components becoming 'trapped' in the encounter complex (section 1.2.2) at lower ionic strengths due

to increased charge interactions according to coulombs law. This effect prolongs the lifetime of the encounter complex, as the energy required for rearrangement of the full ET complex is increased (Bottin and Mathis, 1985; Sigfridsson, 1997).

A cluster of lysine residues on PsaF, a luminal facing subunit of PSI is proposed to provide a complimentary electrostatic binding interface for Pc (Hope, 2000). This was first elucidated by cross linking (Hippler et al., 1989, 1996) and kinetic (Haldrup et al., 1999) studies and confirmed by mutational analysis in *C.reinhardtii* showing the importance of PsaF for fast ET to PSI both *in vivo* and *in vitro* (Respectively, Finazzi et al., 2005 and Hippler et al., 1997). In addition, the luminal PsaN subunit has also been implicated in Pc binding, with mutants lacking the protein showing a 45% decrease in ET rate (Haldrup et al., 1999).

To map the regions on the protein involved in forming the hydrophobic binding interface Ueda et al., 2012 used NMR, observing the chemical shifts in residues upon binding, and identified two hydrophobic tryptophan residues, W658 on psaA and W625 on psaB. Both the hydrophobic and electrostatic regions can be seen in figure 5.1 along with the complementary regions on Pc. Mutation studies have also been performed in *C.reinhardtii*, with mutants of the two equivalent hydrophobic residues giving rise to PSI complexes with hampered ET from Pc (Sommer et al., 2004). Mutation of charged residues surrounding the hydrophobic binding interface to expand the hydrophobic region were found to drastically increase the affinity of Pc for PSI, but gave the organism a light sensitive growth phenotype, due to the poor dissociation of Pc limiting PSI turnover (Kuhlgert et al., 2012). These results would suggest that while the hydrophobic region of the PSI binding interface appears small relative to the equivalent in cytb_6f, this may be optimised for a faster turnover of the complex.

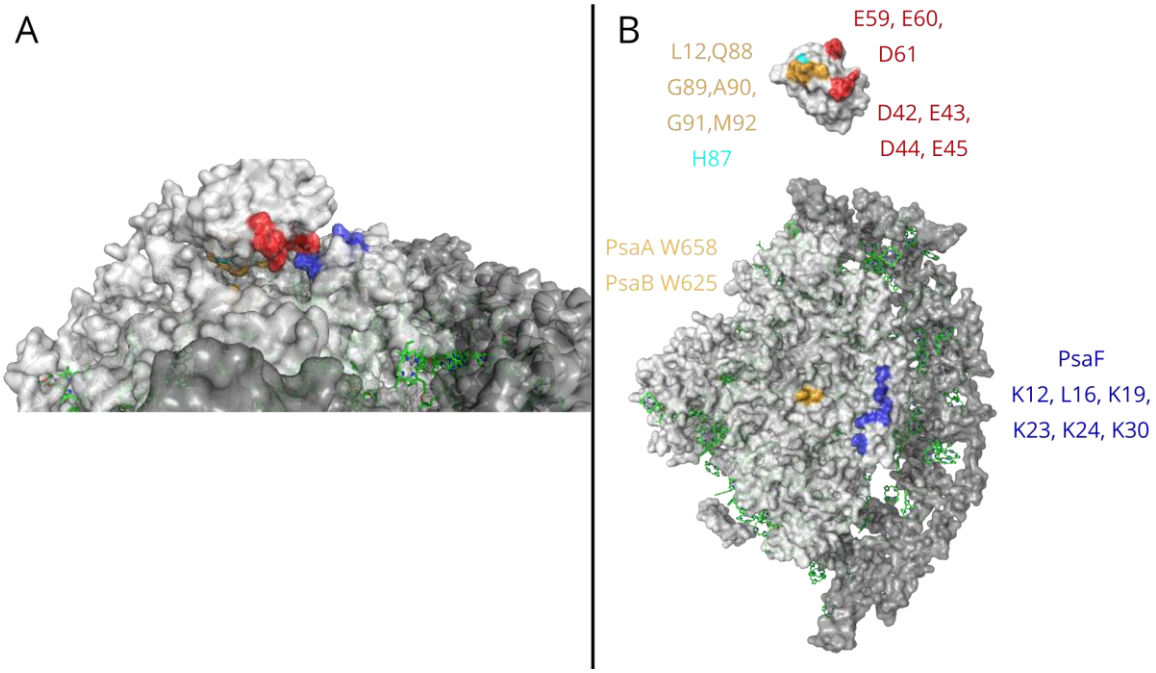

Figure 5.1 Binding interfaces between PSI and Plastocyanin

*Diagram showing the binding interfaces for the PSI : Pc interaction. Positive and negative residues are shown in blue and red respectively, hydrophobic residues in orange, and the histidine through which ET is thought to occur in cyan. (**A**) Both binding partners close to interaction, for diagrammatic purposes (**B**) Open book view of the binding interfaces, with known residues for interaction labelled. PDBs used: PSI: 2O01, (Amunts et al., 2007), Pc: 1AG6 - (Xue et al., 1998).*

Following the characterisation of the cytb_6f : Pc ET complex using SMFS in Chapter 4, it was logical to extend this analysis to the PSI : Pc interaction. The affinity mapping experiments originally used in Johnson et al., 2014 could not be repeated with isolated stromal lamellae membranes (Wood et al., 2018) given their protein complement containing both cytb_6f and PSI. Attempting to deconvolute the unbinding forces or the interaction frequencies would be not be feasible. Therefore, in this chapter, expanding on the work in the two previous chapters, PSI was immobilised on a SiOx surface, and the interaction was interrogated with a with a Pc-functionalised AFM probe.

5.3 Results

5.3.1 PSI purification method

A wide range of PSI purification protocols from plant material are available in the literature and have produced samples suitable for high-resolution structural determination (e.g. Amunts et al., 2007; Mazor et al., 2017; Qin et al., 2011, 2015). Here the method described by Mazor et al., 2017 for isolation of PSI from pea leaves was adapted for spinach. In brief, unstacked thylakoid membranes were isolated from spinach leaves and treated with αDDM for 5 minutes, to selectively deplete PSII, ATP synthase and cytb_6f. After centrifugation, the pellet was taken and frozen at -80°C. Following thawing, the membranes were solubilised with 1.5% (w/v) βDDM and centrifuged again to pellet insoluble material. The supernatant was applied to a DEAE anion exchange column, and an increasing salt concentration gradient was applied. Dark green fractions with PSI absorbance spectra were pooled and precipitated using 10% PEG6000, followed by centrifugation. The pellet was then resuspended and applied to a 10-35% sucrose gradient (Figure 5.2A). The dark green band (indicted by an arrow) was extracted, and a DEAE anion column was used to concentrate the sample and remove sucrose prior to being applied to another 10-35% sucrose gradient (figure 5.2B). The single band from this was extracted, and frozen until further use.

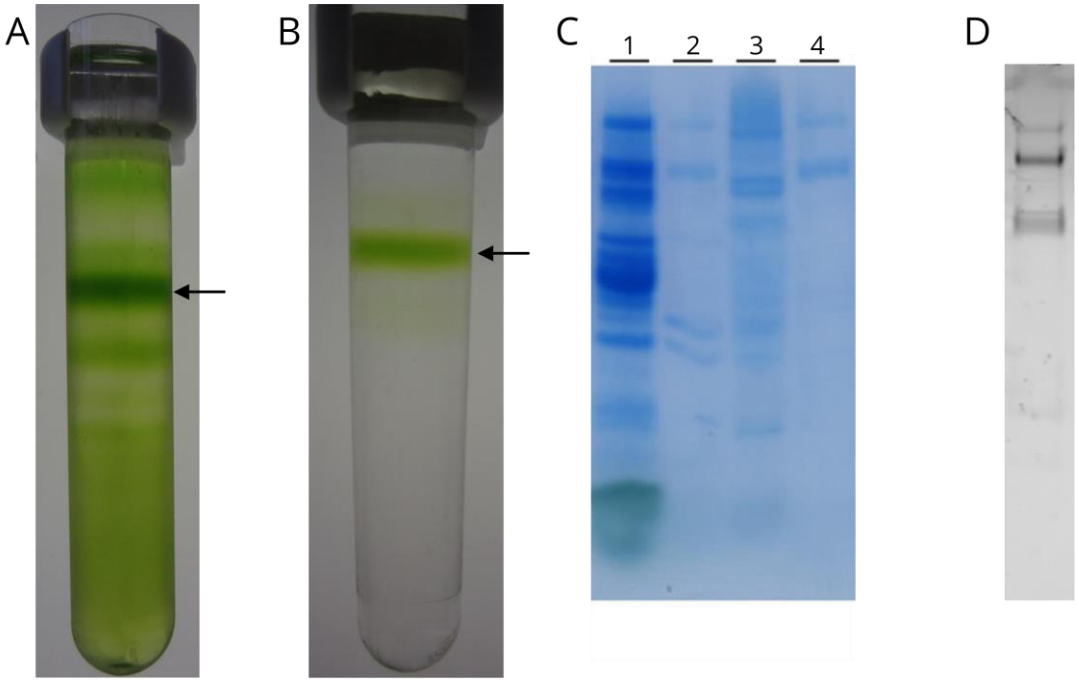

Figure 5.2 Mazor PSI purification method

*Purification process for the Mazor et al., 2017 method of purification of untagged PSI. (**A**) Initial sucrose gradient performed on the PEG6000 precipitated material. The dark band highlighted was extracted, had sucrose removed via DEAE column, and was run on a second sucrose gradient, producing the single band seen in (**B**). (**C**) SDS-PAGE of the stages of the purification to observe any loss or changes in material quality. Lanes: 1) βDDM solubilised material supernatant, 2) DEAE column loading flow through, 3) DEAE column PSI fractions pooled, 4) End purified product, showing only PsaA/B. (**D**) SDS-PAGE of the sample in lane 4 in (C) stained with Sypro-Ruby protein stain for higher sensitivity.*

Figure 5.2C shows the SDS-PAGE profile of each step during the purification process. It is clear that a significant amount of PSI is not binding to the DEAE column under these conditions since it is present in the flow through prior to application of the gradient (lane 2). Indeed, compared to the sample loaded onto the column (lane 1) the eluted fractions (lane 3) shows little further enrichment in PSI. Moreover, following PEG6000-induced precipitation, only the PSI core subunits (PsaA/B) are obvious on the gel (lane 4, and D) suggesting that the minor subunits are lost during the purification.

Following these results, the purification process was simplified by removing the PEG 6000 precipitation. Instead, following the selective enrichment by αDDM and the subsequent solubilisation of the enriched sample by βDDM, the supernatant was concentrated and applied to a single 10-35% sucrose gradient. The resultant sucrose gradient can be seen in figure 5.3A, with the extracted bands

indicated as middle (red) and bottom (black). Following this, absorbance spectra were taken of the samples, shown in figure 5.3B. Both the middle and bottom fractions had noticeably PSI-like absorption spectra, with chlorophyll Q_y peaks around 680nm (Ruban, 2013). The middle band had a slight blue shift from 680nm, which can be indicative of contamination with PSII, which has a spectral peak of 675nm (Ruban, 2013). SDS-PAGE (figure 5.3C) was performed on both samples, showing that the middle band contained a 37kDa size protein (labelled as unknown contaminant) not known to be a part of PSI, and was proposed to be CP43/47 from PSII, which would have blue-shifted the absorption spectrum as previously mentioned. The bottom fraction appeared to be cleaner, and as such was taken forward in the purification.

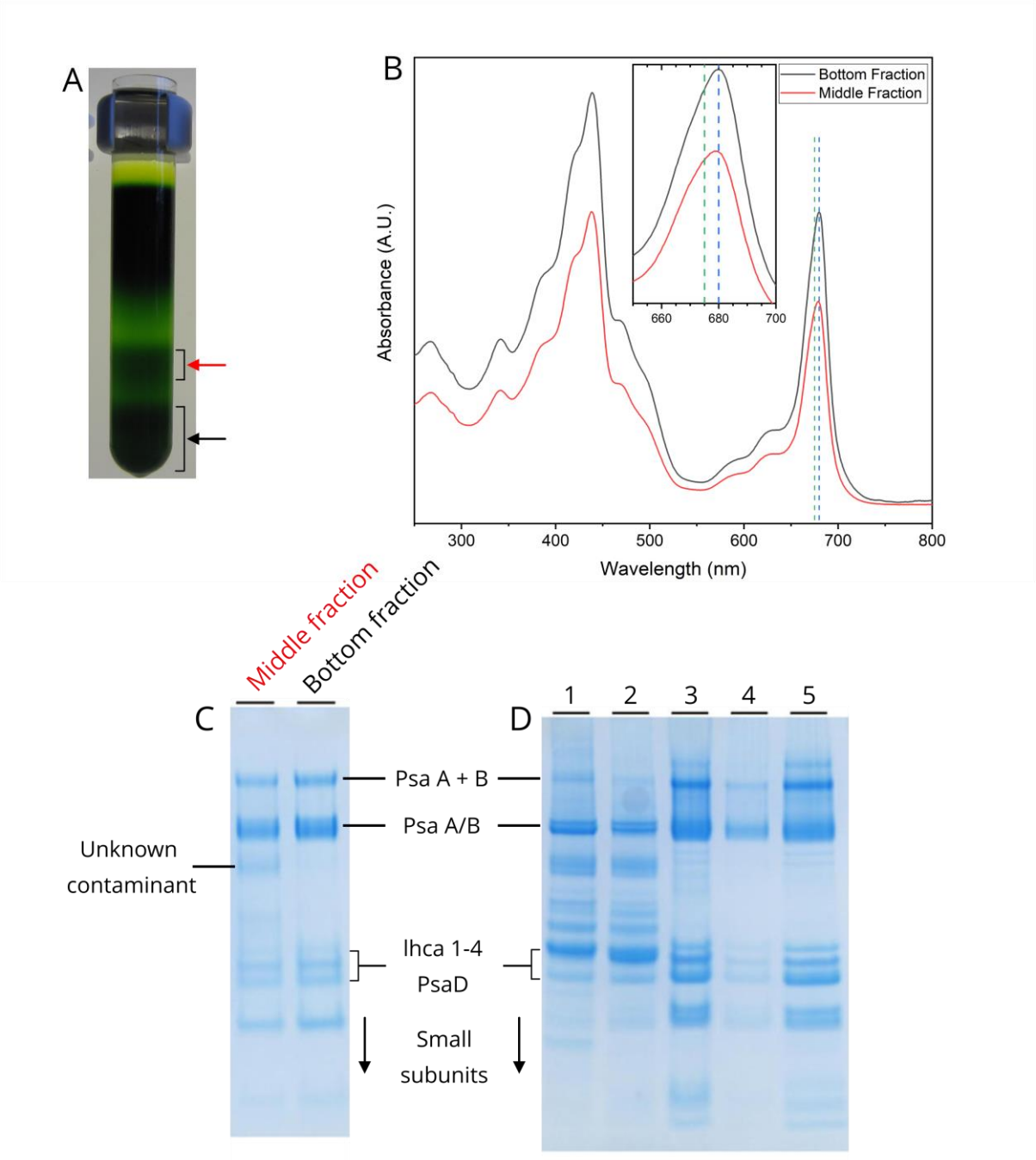

Figure 5.3 Simplified PSI purification method

*(**A**) Sucrose gradient of ßDDM solubilised material, producing 3 bands. As the top one was already known to contain LHCII (Crepin et al., 2016), the bottom two bands were taken. (**B**) Absorbance spectra for the bands extracted in (A). Dashed lines shown are 675nm (green) and 680nm (blue), indicating of PSII and PSI absorbance spectra peaks respectively (Ruban, 2013). Inlay shows magnified region for peaks. (**C,D**) SDS PAGE of samples throughout the purification process. (**C**) 2 bands from (A/B). (**D**) SDS-PAGE of the purification process. Bands: 1) Thylakoid membranes, 2) αDDM membrane pellet 3)*

Bottom band from sucrose gradient in (A), 4) DEAE column flow through following sample loading, 5) Concentrated PSI fractions from DEAE column.

The bottom band was applied to the DEAE column run in the previous iteration of the purification. Observing the protein complement before (figure 5.3D, lane 3) and after (lane 5) the column did not see a noticeable increase in purity of PSI. In addition, some PSI material is seen to be lost in the flow through loading the DEAE column (lane 4). For an additional measure, the bottom band from the sucrose gradient and the end PSI sample following the DEAE column were also tested via 77k fluorescence, seen in figure 5.4.

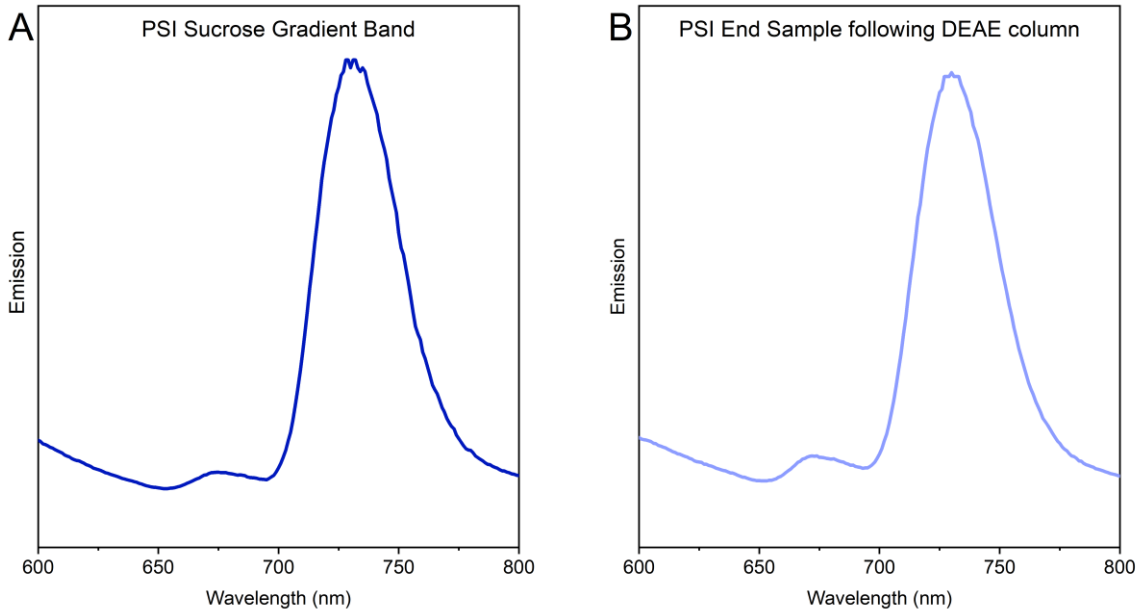

Figure 5.4 77K Fluorescence for PSI purification

*77K fluorescence of (**A**) the bottom sucrose gradient band seen in figure 5.3A and (**B**) the final purification product of fractions pooled from the DEAE column. The peak at 740nm is indicative of PSI, whilst the peak at 675nm is indicative of PSII. No significant change in purity was observed here from the DEAE column.*

The emission peak at ca. 740nm is indicative of PSI complex, whereas the 680 nm emission is from LHCII/LHCI (Lamb et al., 2015). This showed the DEAE column was not providing any further enrichment of PSI and indeed the SDS-PAGE in figure 5.3D shows that PSI was eluting at the loading stage of the column. As such the DEAE column was excluded from the purification process, and the

protocol would simply comprise of the solubilisation steps, followed by the sucrose gradient (materials and methods section 2.4.3).

Whilst the method would only require a single sucrose gradient when done on small samples, the scaling up of the purification to attain more material led to a decreased resolution on the sucrose gradient. As such, when using the larger SW32 rotor, 2 sucrose gradients were performed, with the first one (10-50%) producing 2 bands, comprised of the 'top' and 'middle + bottom' bands seen in figure 5.3. The bottom of the two bands was taken, and following desalting to remove sucrose, a second gradient (25-40%) also yielded two bands as seen in figure 5.5A. Once again performing 77K fluorescence on these two bands showed that the upper band presented a LHCII like emission spectrum, whilst the bottom band possessed the characteristic emission spectrum for PSI (figure 5.5B/C). Following this the lower band of the gradient was frozen at -80 °C until use, retaining the sucrose as a cryoprotectant. For further details on the purification process, see materials and methods section 2.4.4. In addition, an SDS PAGE was run on this sample, shown in figure 5.5D. The bands labelled clearly match those found previously from the purification of PSI-LHCI complex (Qin et al., 2011).

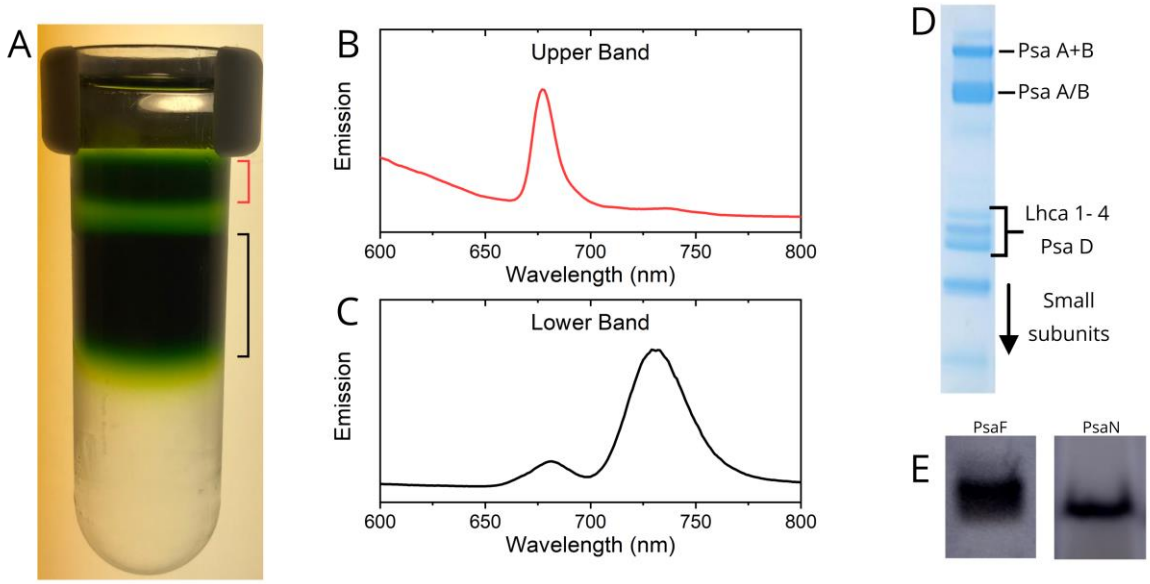

Figure 5.5 Scaled up purification of PSI

*(**A**) Second sucrose gradient from PSI purification, with the upper and lower bands indicated by red and black respectively. (**B/C**) 77K fluorescence of the bands seen in (A) (**D**) SDS – PAGE showing the end purification product following the PSI protocol, with bands labelled matching those seen in (Qin et al.,*

*2011) showing the SDS-PAGE visible components of the PSI – LHCI complex. (**E**) Western blot bands for PsaF and PsaN subunits on PSI.*

The intactness of the Pc binding site on the purified PSI complex was confirmed by immunoblotting the sample for the presence of the labile PsaF and PsaN subunits (figure 5.5E). The purified PSI complex was quantified via a Lowry protein assay for use in further experiments. For details on the assay, see materials and methods section 2.3.8.

5.3.2 Verification of PSI purification

The activity of the purified PSI was investigated by following its ability to oxidise Pc in the presence of 420 nm light using MV as an electron acceptor for PSI (Ke, 1973). Figure 5.6 shows the absorbance traces at 597nm (oxidised Pc), in the presence (black) and absence (red) of PSI. Illumination began at 10 seconds and lasted for 10 seconds. This yielded an initial rate of electron transfer rate of over 300 s^{-1} per PSI consistent with the range of values reported in the literature. For details on the experiment see materials and methods section 2.3.9.2.

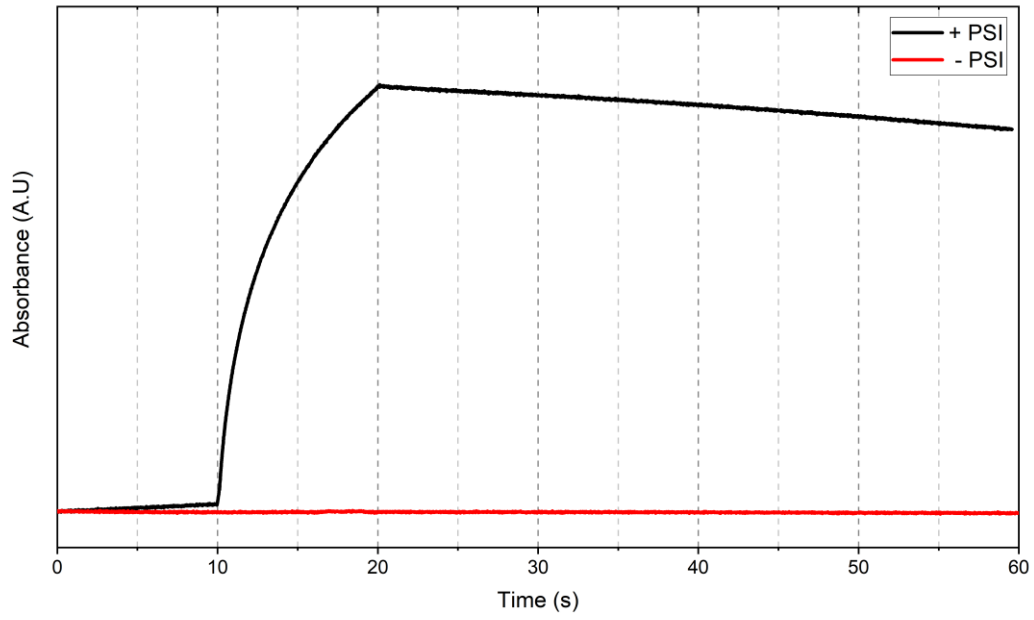

Figure 5.6 PSI bulk phase kinetics measurement

PSI kinetics measured by absorbance change at 597nm for Pc oxidation. Illumination began at 10 seconds and lasted for 10 seconds. PSI was omitted as a control, proving it was necessary for Pc oxidation. The initial change observed before illumination (0-10 seconds) in the PSI containing sample

reflects the low excitation of PSI from the light used for measuring absorbance. Both this oxidation and the oxidation upon illumination are absent when PSI is omitted. 'Deliberate' illumination used a 420nm light source, and 550nm filters were used on the detector side to minimise noise upon illumination. The re-reduction of Pc when the illumination ends is due to the slow reduction of Pc by MV.

5.3.3 Optimising surface distribution of PSI

The crystal structure of the PSI complex from pea shows lysine residues well distributed on both stromal and luminal faces, with a ratio of 11:6 (77 lysine residues on the stromal side and 42 on the luminal side). This should allow the effective immobilisation of the PSI complex using the MPTMS and SMCC linker chemistry described in Chapter 4, with a slight preference (assuming equal reactivity of all lysine residues) for the presentation of the luminal face to the Pc on the AFM probe. In addition, orientation was less likely to be an issue with PSI, as the dimensions of the complex show that, unlike cytb_6f, it is larger in the plane of the membrane, than perpendicular to it (effectively, it was 'wider' than it was 'tall'). As such it would be harder for the surface to form linkages with both sides of the complex.

Initial functionalisation steps prior to protein incubation were carried out as in chapter 4 (materials and methods section 2.5.3.1). Following this, an initial screening of 6 different protein concentrations were incubated with the NHS-ester terminated SMCC layer, in 10mM HEPES pH 7.4, 10mM NaCl, 0.03% βDDM. Figure 5.7A shows 6 different dilutions of the protein from 3 to 300nM, imaged by PF-QNM at a pixel density of 512 x 512 for a scan size of 1µm. As previously discussed (Chapter 3.3.3), controlling surface density by the concentration of the protein relies on the hydrolysis of the NHS-ester to compete with the reaction with primary amines on lysine residues. While 300 and 150nM appear to be covering the surface, 60nM appears to have a reduced density and 30nM appeared to give an ideal density for SMFS experiments, with areas of the surface still visible. Based on these results, a 30nM protein incubation was chosen, as this ensured a low enough surface density that the correlation between the height image and the location of adhesions could be used as an additional selection criterion when the user was shown FdCs in the MATLAB analysis tool (materials and methods section 2.6.4). The lower concentration of PSI required for optimal density compared to cytb_6f is thought to result from the increased number of surface exposed lysine residues, 119 compared to 89 for cytb_6f available for linkage. The MATLAB program discussed in 3.3.8 (Appendix, 8.2) was used to measure the heights of PSI complexes in the images of the 30nM protein incubation (figure 5.7B). The heights shown in the histogram would appear to match those expected from the crystal structure of PSI as seen in 5.7C. This suggests that this immobilisation method is able to successfully attach PSI complexes to the surface for SMFS experiments (materials and methods section 2.5.4.4).

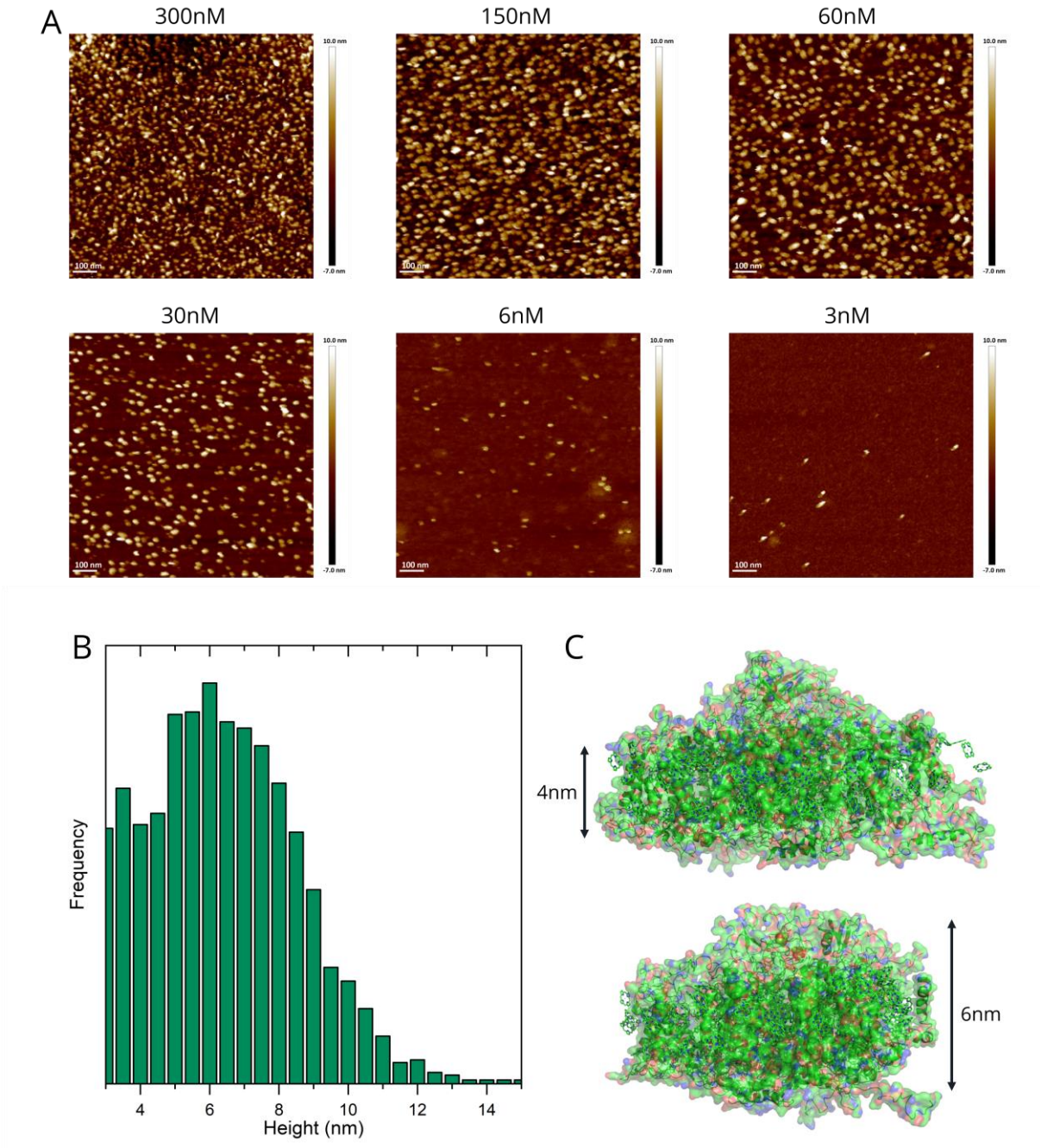

Figure 5.7 Surface immobilisation density testing of PSI

*(**A**) AFM images of the surfaces produced following SMCC generated monolayers, with 6 different concentrations of PSI on the surface (denoted above), for 45 minutes in 10mM HEPES, 10mM NaCl, 0.03% βDDM. (**B**) Histogram showing the distribution of peak heights measured in the 30nM incubation images. Peak heights were measured by a custom-built MATLAB script (Appendix 8.2). (**C**) Crystal structure of the pea PSI complex, showing the expected heights from the dimensions. (PDB: 2o01, Amunts et al., 2007)*

5.3.4 SMFS of the interaction between PSI : Plastocyanin

Performing the experiments under a continuous white light, it was assumed that PSI will become, then remain photo oxidised (PSI [^{P}Ox]) whilst being imaged if a suitable electron acceptor such as MV is present. As such no initial incubation to pre-set the redox state was deemed necessary, unlike with cytb_6f in Chapter 4. The Pc-functionalised AFM probe however was incubated with 1mM ascorbate to reduce Pc. While these probes were generated as those seen in chapter 4, a longer flexible PEG spacer with a length of 25nm, rather than the 10nm used for the cytb_6f : Pc experiments, allowed a larger separation distance between the interaction with the surface and adhesion events. This also gave a clearer indication of specific events than in the cytb_6f experiments. The PSI functionalised silicon surfaces were then scanned using the Pc[Red] AFM probes. Figure 5.8A shows a good correlation between the topographic features of PSI complexes on the silicon surface and the unbinding events extracted with the MATLAB script (red dots). In addition, figure 5.8B shows a sample of actual FdCs gathered.

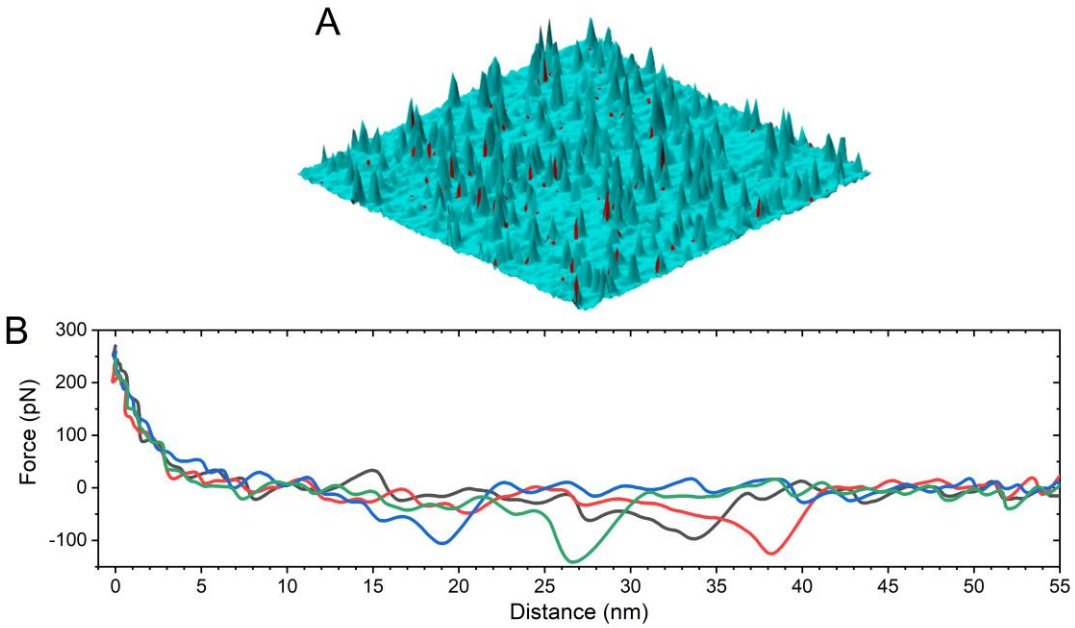

Figure 5.8 Example of force data from PSI : Plastocyanin experiments

*Example data taken from the force data extracted. (**A**) Overlay of the adhesion locations (red dots) onto the topology image taken from PF-QNM. The dots show good correlation with the locations of PSI on the surface, with some minor offset. Script used to generate the overlay in appendix section 8.3. (**B**) Example force curves extracted from the PF-QNM data collected on the PSI – Pc interaction. The adhesion offset of around 20nm is in agreement with the length of linker used to attach Pc, with the*

probe leaving the surface at ca. 6nm due to deformation, then the 20nm separation before any force is exerted.

AFM force curves are blighted by low level noise due to the frequency of movement and thermal fluctuations. In traditional slower SMFS experiments (like those discussed in 1.4.1), noise in the FdC are well below the signals measured in adhesion. In PF-QNM experiments, due to the much higher speed of motion being closer to the resonant frequency of the cantilever, the noise of oscillation in the FdCs is higher, around 50-60pN at the PeakForce frequency of 0.5kHz used. As a result, the noise threshold of 90pN was still applied to the data set, as it had been with the cytb_6f – Pc interaction, even though the unbinding force appeared to be close to this magnitude.

As in Chapter 4, free Pc was added to the imaging buffer at a concentration of 90 µM to determine if the observed unbinding events were due to specific interactions between Pc on the probe and PSI on the surface. Figure 5.9 shows the effect of 90 µM free Pc on both unbinding forces and interaction frequency obtained. The unbinding forces are unchanged, however the interaction frequency decreases by a factor of ca. 2. While the K_D for the interaction between reduced Pc (Pc [Red]) and photo-oxidised PSI (PSI [^{P}Ox]) has been published as 7µM (Drepper et al., 1996), a number of factors need to be considered. As previously mentioned, the experiment was performed under illumination by a white light source to photo-oxidise PSI on the surface, driving electron transfer to MV in the imaging buffer. As a result, injection of free reduced Pc into the imaging buffer will quickly yield oxidised Pc from PSI's turnover. Whilst slow donation of electrons from MV to Pc will occur (figure 5.6) it is unlikely to counter the turnover of PSI. As such, the pool of Pc would become oxidised, giving a resultant K_D of ca. 40µM for Pc [Ox] – PSI [Red] (Drepper et al., 1996). In addition, the PSI would then continue to turn over, thus resulting in Pc [Ox] – PSI [^{P}Ox] which has been shown to have a K_D of ca. 100µM (Drepper et al., 1996). With these considerations, the expected occupancy of Pc binding sites on surface attached PSI from 90µM Pc would be ca. 47%, leaving 53% available for interaction. Practically, due to MV's ability to donate electrons to Pc, it is likely that a small pool of the Pc remains reduced, giving a slightly different number from the 47% occupancy, resulting in the 45% interaction frequency (55% occupancy) observed upon addition of 90µM Pc.

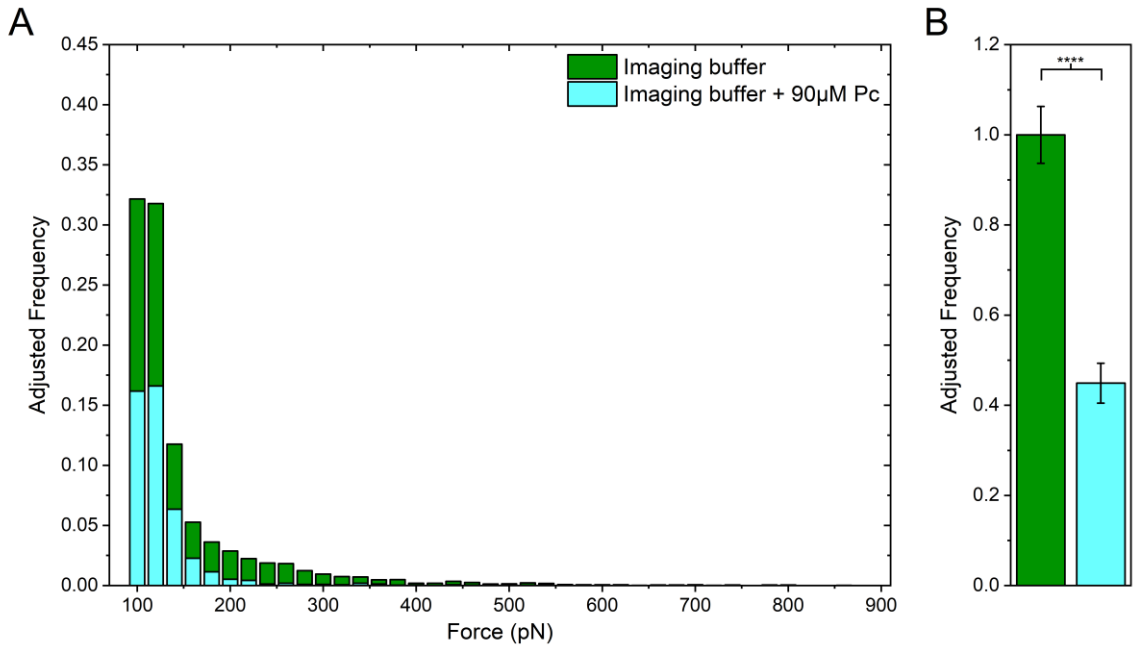

Figure 5.9 Effect of excess plastocyanin on PSI : Plastocyanin interaction

*SMFS experiments on the PSI : Pc interaction imaged in a buffer containing 10mM HEPES pH 7.4, 10mM NaCl, 0.1mM MV, 0.03% ϐDDM. (**A**) Distribution of forces measured for the PSI : Pc interaction, with the cumulative frequency being adjusted to the frequencies seen in (B). (**B**) Interaction frequency observed for the addition of free Pc in solution, set relative to the frequency before addition. Colours match those seen in (A). Unpaired t-test analysis was performed on the adjusted frequencies. Asterisk denotes a p-value of <0.0001. Error bars are ± standard error of the mean, n = 8-16 independent analysed images for each condition.*

To ensure the changed linker length did not affect the unbinding forces measured, the original SM(PEG)$_{24}$ linker was also briefly used and yielded the same result (data not shown). The reason for the greatly reduced unbinding force for the Pc : PSI interaction compared to the Pc : cyt*b*$_6$*f* is currently unknown. Western blot analysis showed subunits implicated in binding (PsaF and PsaN) were present (figure 5.5E), and the activity assay showed that PSI was still capable of oxidising Pc (Figure 5.6). In addition, the adhesion locations in figure 5.8 show good correlation with the topology of PSI, suggesting the interaction is still specific. This would suggest that the unbinding force for the PSI : Pc interaction is genuinely lower than for cyt*b*$_6$*f* : Pc. Fitting a gaussian curve over these regions was not feasible, as only a portion of the distribution is observed. As such, no mean unbinding forces are reported or discussed in this chapter, but the distribution of unbinding forces is still considered.

5.3.5 Effect of methyl viologen on the interaction between PSI : Plastocyanin

Since the 680 nm AFM laser used to monitor the deflection of the AFM cantilever coincides with the Q_y maximum of PSI absorption, it was assumed that even in the absence of the white light illumination PSI may still turnover. In our first experiments (5.3.4) MV was included in the imaging buffer to act as an electron acceptor for PSI allowing its stable photo-oxidation in the light by preventing charge recombination (section 1.1.2.6). In the absence of MV and white light illumination, the 30 ms charge recombination of the PSI primary donor $P700^+$ with the terminal acceptor F_A/F_B iron-sulphur cluster could result in a negligible steady state population of $P700^+$ (depending on the extent of illumination from the AFM laser), allowing PSI to be imaged in the reduced state. It was hoped this might give insight into the redox selectivity of the PSI : Pc interaction in the context of the redox state of PSI. For this experiment, initially each dataset was taken in an imaging buffer of 10mM HEPES, pH 7.4, 10mM NaCl, 5mM $MgCl_2$, 0.03% βDDM, with no white light illumination. Following several images, the tip was re-reduced using 1mM ascorbate and the imaging buffer was changed to include 1mM MV to obtain the second data set. As with the cytb_6f experiments, this meant that any deviations in tip functionalisation were accounted for as the comparisons between states utilised the same AFM probe. Figure 5.10 shows the effect of addition of 1mM MV in the imaging buffer on both the distribution of unbinding forces and the interaction frequency. The slight change in the dielectric constant upon addition of 1mM MV was considered negligible in comparison with the effect of ionic strength (see figure 5.11). Both the distribution of unbinding forces and the interaction frequency appear to be unchanged by the inclusion of MV.

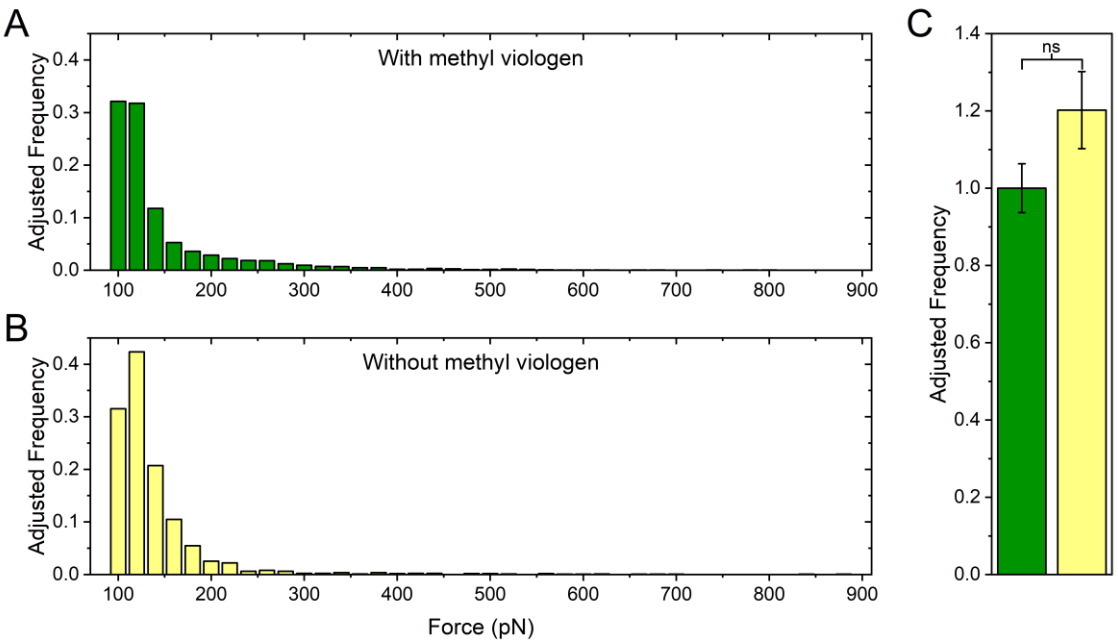

Figure 5.10 Effect of methyl viologen on the PSI : Plastocyanin interaction

*Distribution of unbinding forces for the PSI – Pc interaction in the presence (**A**) and absence (**B**) of MV as a PSI acceptor. Adjusted frequency calculated from the cumulative frequency of the histogram being equal to the frequencies seen in (C). (**C**) The interaction frequency for the interaction with the presence and absence of MV. Frequencies adjusted relative to the interaction when methyl viologen is present. Colours match those seen in (A) and (B). Unpaired t-test analysis was performed on the adjusted frequencies, returning a p-value of 0.1359 (Denoted by ns). Error bars are ± standard error of the mean, n = 16-26 independent analysed images for each condition.*

The lack of response to MV may reflect the location of the electron in PSI. Comparing the time for internal ET from $P700^+$ to the F_A/F_B iron sulphur clusters (ca. 200ns) and the time for charge recombination back to P700 (30ms) would suggest that the electron would spend nearly all it's time away from the chlorophylls (chapter 1.1.2.6, Itoh et al., 2001; Rutherford et al., 2012). Hence the location of the electron in PSI would effectively depend on the extent of illumination of PSI by the AFM laser, which is difficult to predict. A high illumination would be constantly generating $P700^+$, hence have very low occupancy of the P700 state, while a lower illumination could allow P700 to persist for short times between excitation events. The results seen in figure 5.10 suggest that the illumination from the laser is sufficiently high that no difference is seen from removing the electron via MV. Thus, even without MV the P700 may effectively spend most of its time in the $P700^+$ state due to the excitation provided by the AFM laser. The acceptance of the electron by other factors in the

system also cannot be ruled out, such as dissolved oxygen in the buffer. Nevertheless, 0.1mM MV was included in all other experiments with PSI unless stated otherwise, and all remaining experiments were performed under white light illumination.

5.3.6 Effect of ionic strength on the PSI : Plastocyanin interaction

As discussed in the introduction to this chapter the Pc : PSI ET complex depends on complimentary electrostatic interaction between positively charged lysine residues on the PsaF subunit of PSI and the acidic patch on Pc (Figure 5.1, Hippler et al., 1996). Similar to the interaction with cytb_6f, the PSI Pc oxidation has previously been shown to have a bell-shaped response to ionic strength (Sigfridsson, 1997; Sigfridsson et al., 1996b, 1997).

To probe the effect of ionic strength, the experiment was conducted in the same manner as the ionic strength experiments in section 4.3.3, using relative comparisons within datasets (a single AFM probe) to compare the interaction frequency. Figure 5.11 shows the effect of changing the salt concentration in the imaging buffer on both the distribution of forces and interaction frequency. As expected, the interaction frequency shows a single exponential decay in agreement with increased screening of two oppositely charged bodies at increasing ionic strength.

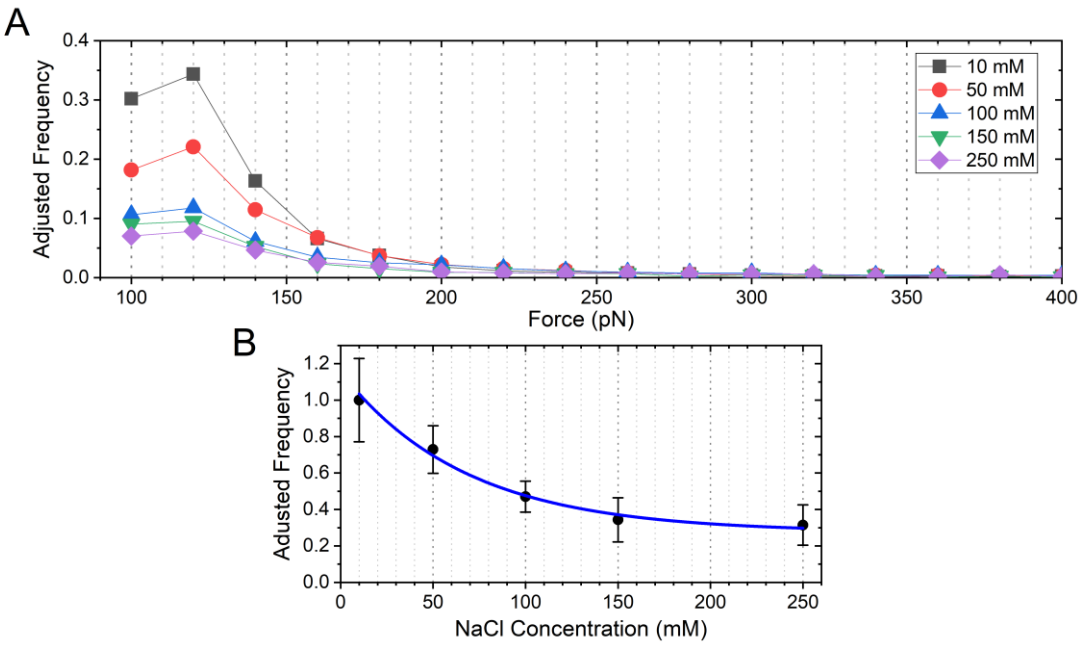

Figure 5.11 Effect of ionic strength on the PSI : Plastocyanin interaction

*The effect of ionic strength on both the forces (**A**) and interaction frequency (**B**) for the PSI : Pc interaction. No observable difference is seen in the distribution of forces for different salt concentrations in A, however the frequencies do decrease at increasing ionic strength. Adjusted*

frequencies in A are set so that the cumulative frequency for each salt concentration reflects the frequencies observed in B.

While there is no visible change in the distribution of unbinding forces measured with ionic strength, it cannot be ruled out that changes in the force do occur and are merely below the noise of this experimental setup.

5.3.7 Changes in binding between different redox states in the PSI : plastocyanin interaction

As previously discussed, PSI is assumed to turnover constantly due to the AFM laser (5.3.5). As a result, no clear control can be achieved over the PSI redox state for these experiments. Thus, in contrast to the experiments with cytb_6f, only the redox state of Pc could be varied. Previous measurements of the binding affinity in different redox states for PSI and Pc have shown a ca. 2-3-fold change in association (k_{on}) when observing illuminated PSI (PSI [^{P}Ox]) with Pc [Ox] and Pc [Red] (Drepper et al., 1996). In addition, the dissociation also appeared to show a redox dependency, with the Pc [Ox] form (Post – ET) showing a ca. 2.5-fold increase in k_{off} (Drepper et al., 1996).

Once again, SMFS experiments were performed assessing relative changes within each data set. Initially, the Pc functionalised AFM probe was either reduced (1mM sodium ascorbate) or oxidised (1mM potassium ferricyanide), and the PSI surface imaged under white light illumination. Following this, the probe borne Pc was changed to the opposite redox state, and another dataset was gathered. Performing the experiments in different orders ensured that the extraction and incubation stages, as well as the number of images taken prior to the data set did not affect the results. MV was excluded from these experiments due to its ability to donate electrons to Pc (figure 5.6).

Figure 5.12 shows the effect of the redox state of Pc on both the distribution of unbinding forces and the interaction frequency. The interaction frequency shows a ca. 2-fold decrease when in the Pc [Ox] (Post-ET) state compared to Pc [Red] (Pre-ET), in agreement with previous bulk phase studies (Drepper et al., 1996). The distribution of unbinding forces measured shows no significant difference between oxidised and reduced Pc.

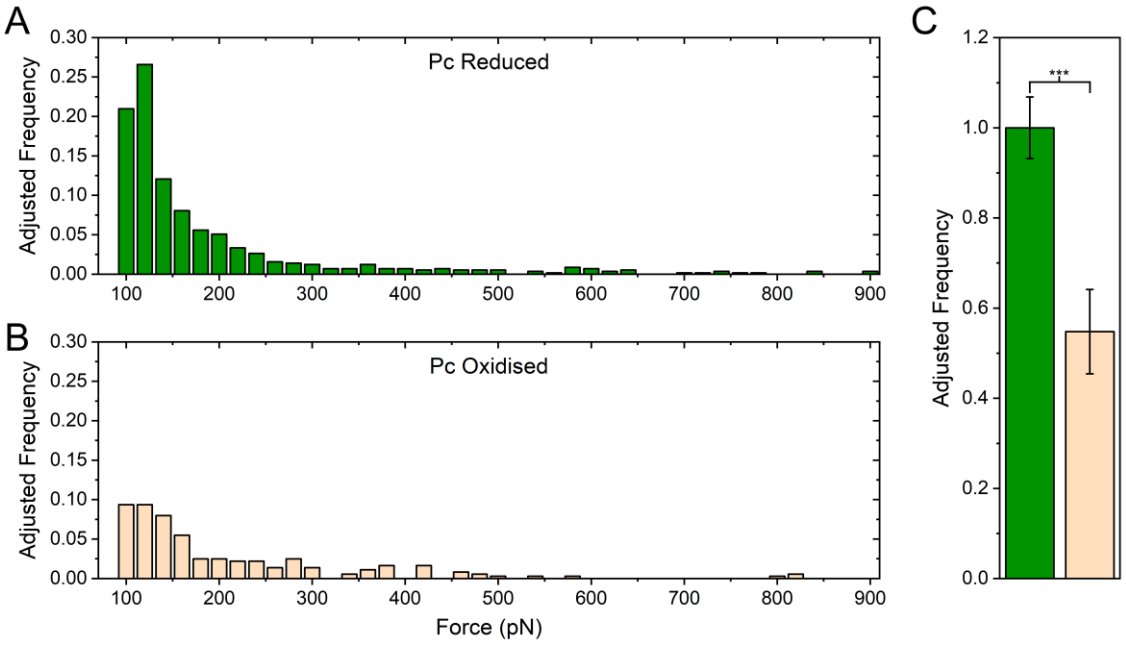

Figure 5.12 Effect of redox state of plastocyanin on the PSI : Plastocyanin interaction

*Distribution of forces when the AFM borne Pc is in a (**A**) Pc [Red] form and (**B**) in a Pc [Ox] form. Cumulative frequencies are adjusted so they reflect the frequencies seen in (C). (**C**) Interaction frequency for the reduced and oxidised forms of Pc on the AFM probe interacting with the PSI surface, with colours matching those seen in (A) and (B). The redox state was changed by incubation with potassium ferricyanide (Oxidation) or sodium ascorbate (Reduction) at 1mM for 5 minutes. Unpaired t-test analysis was performed on the adjusted frequencies. Asterisk denotes a p-value of 0.0007. Error bars are ± standard error of the mean, n = 18-25 independent analysed images for each condition.*

5.4 Discussion

5.4.1 SMFS controls performed on PSI : Plastocyanin

The reason for the low unbinding force measured between PSI and Pc is unknown. Control experiments (figure 5.8, 5.9) showed that the adhesion locations had good correlation with the PSI on the surface, and the interaction frequency decreased upon addition of 90 µM Pc into the imaging buffer (5.3.4). The conclusion from these results was that the unbinding forces measured were between PSI and Pc. The true 'mean unbinding force' could be lower than the 90pN limit that was placed at the low end of these experiments, although this cannot be determined due to noise.

One possible explanation for the relatively low force is the slightly smaller binding interface observed for PSI : Pc than that observed for cytb_6f : Pc. A previous study on *Chlamydomonas* revealed that mutation of the PsaB D612 and E613 residues that surround the two hydrophobic tryptophan residues W658 and W625 involved in Pc binding increases the affinity of the complex, but significantly slows turnover due to a lower k_{off} (Kuhlgert et al., 2012). The effect of slowed turnover was increased photoinhibition of PSII in the mutant strain, leading to a light-sensitive growth phenotype. Therefore, nature's selection of a small binding interface may reflect the need to balance fast ET with rapid turnover.

5.4.2 Effect of ionic strength on PSI : Plastocyanin

While the effect of ionic strength on the interaction was probed, only the interaction frequency data showed an effect. Once again, due to the poor signal to noise, a change in the unbinding forces cannot be ruled out, however non could be observed by our means.

5.4.3 Probing the effect of Redox state and Methyl viologen for PSI : Plastocyanin

While the probing of PSI [Red] was attempted via the removal of methyl viologen, the extent of illumination from the AFM laser meant that the P700 in PSI remained oxidised for significant periods. Although the use of larger cantilevers for the AFM probe may alleviate this issue, effectively shielding the surface underneath the probe, this could lead to either a loss of force resolution or higher noise, both of which are undesirable for these experiments. As such, it was assumed that we could not exert any control over the redox state of PSI on the surface. Future experiments could utilise an AFM laser at a longer wavelength where PSI doesn't absorb to understand the effect of light on the interaction.

The effect of the redox state of Pc however could be probed in our experiments, by incubation with reducing or oxidising agents prior to imaging. In addition, the exclusion of MV was made to ensure no electrons from PSI could be accepted by MV and donated to Pc, skewing the redox state being probed. The 2-fold change observed in the Pc[Ox] state relative to the Pc[Red] state is in agreement with the previous experiments performed to determine differences in the k_{on} (Drepper et al., 1996). This same study also found a 4.5-fold difference in the k_{off}, with the Pc[Ox] form dissociating faster than the Pc[Red] form, suggesting a redox selectivity in the system. The unbinding force can be correlated to the dissociation rate constant for the interaction (section 1.4.2), and as such a difference would be expected in the unbinding forces. The extent of this however would depend on the change in the reaction coordinate between these states (section 1.4.2). No change was observed in our experiments in the distribution of the unbinding forces measured, and again this may simply reflect the poor signal to noise ratio in the experiments obscuring a change below the threshold. Alternatively, the manifestation of the change in the unbinding forces may have been too small to show effect here, as a number of parameters in the Bell-Evans model for unbinding force are not known for PSI : Pc.

While this work explored a number of features for the PSI : Pc binding, it faced limitations from the low unbinding force of the interaction. While lower noise cantilevers for AFM probes could potentially be used, the high expense of the PeakForce-HIRS-SSB probes used in these experiments already was a limiting factor. A more prudent avenue forward would be the assessment of mutants of PSI previously characterised by bulk phase measurements, such as the mutants in Kuhlgert et al., 2012 which saw large increases in affinity from mutation of charged residues surrounding the hydrophobic binding interface.

5.5 Bibliography

Amunts, A., Drory, O., and Nelson, N. (2007). The structure of a plant photosystem I supercomplex at 3.4 Å resolution. Nature *447*, 58–63.

Bottin, H., and Mathis, P. (1985). Interaction of Plastocyanin with the Photosystem I Reaction Center: A Kinetic Study by Flash Absorption Spectroscopy. Biochemistry *24*, 6453–6460.

Crepin, A., Santabarbara, S., and Caffarri, S. (2016). Biochemical and spectroscopic characterization of highly stable photosystem II supercomplexes from arabidopsis. J. Biol. Chem. *291*, 19157–19171.

Drepper, F., Hippler, M., Nitschke, W., and Haehnel, W. (1996). Binding dynamics and electron transfer between plastocyanin and photosystem I. Biochemistry *35*, 1282–1295.

Finazzi, G., Sommer, F., and Hippler, M. (2005). Release of oxidized plastocyanin from photosystem I limits electron transfer between photosystem I and cytochrome b_6f complex in vivo. Proc. Natl. Acad. Sci. U. S. A. *102*, 7031–7036.

Haehnel, W., Doring, G., and Witt, H.T. (1971). On the Reaction between Chlorophyll-aIand its Primary Electron Donors in Photosynthesis. Zeitschrift Fur Naturforsch. - Sect. B J. Chem. Sci. *26*, 1171–1174.

Haehnel, W., Propper, A., and Krause, H. (1980). Evidence for complexed plastocyanin as the immediate electron donor of P-700. BBA - Bioenerg. *593*, 384–399.

Haehnel, W., Jansen, T., Gause, K., Klosgen, R.B., Stahl, B., Michl, D., Huvermann, B., Karas, M., and Herrmann, R.G. (1994). Electron transfer from plastocyanin to photosystem I. EMBO J. *13*, 1028–1038.

Haldrup, A., Naver, H., and Scheller, H.V. (1999). The interaction between plastocyanin and photosystem I is inefficient in transgenic Arabidopsis plants lacking the PSI-N subunit of photosystem I. Plant J. *17*, 689–698.

Hippler, M., Ratajczak, R., and Haehnel, W. (1989). Identification of the plastocyanin binding subunit of photosystem I. FEBS Lett. *250*, 280–284.

Hippler, M., Reichert, J., Sutter, M., Zak, E., Altschmied, L., Schroer, U., Herrmann, R.G., and Haehnel, W. (1996). The plastocyanin binding domain of photosystem I. EMBO J. *15*, 6374–6384.

Hippler, M., Drepper, F., Farah, J., and Rochaix, J.D. (1997). Fast electron transfer from cytochrome c6 and plastocyanin to photosystem I of Chlamydomonas reinhardtii requires PsaF. Biochemistry *36*, 6343–6349.

Hope, A.B. (2000). Electron transfers amongst cytochrome *f*, plastocyanin and photosystem I: kinetics and mechanisms. Biochim. Biophys. Acta *1456*, 5–26.

Itoh, S., Iwaki, M., and Ikegami, I. (2001). Modification of photosystem I reaction center by the extraction and exchange of chlorophylls and quinones. Biochim. Biophys. Acta - Bioenerg. *1507*, 115–138.

Johnson, M.P., Vasilev, C., Olsen, J.D., and Hunter, C.N. (2014). Nanodomains of Cytochrome b_6f and Photosystem II Complexes in Spinach Grana Thylakoid Membranes. Plant Cell *26*, 3051–3061.

Ke, B. (1973). The primary electron acceptor of photosystem I. BBA Rev. Bioenerg. *301*, 1–33.

Kuhlgert, S., Drepper, F., Fufezan, C., Sommer, F., and Hippler, M. (2012). Residues PsaB Asp612 and PsaB Glu613 of photosystem I confer pH-dependent binding of plastocyanin and cytochrome c_6. Biochemistry *51*, 7297–7303.

Lamb, J., Forfang, K., and Hohmann-Marriott, M. (2015). A practical solution for 77 K fluorescence measurements based on LED excitation and CCD array detector. PLoS One *10*, 1–12.

Mazor, Y., Borovikova, A., and Nelson, N. (2017). The Structure of plant photosystem I super-complex at 2.6A resolution. Nat. Plants *3*, 17014.

Qin, X., Wang, W., Wang, K., Xin, Y., and Kuang, T. (2011). Isolation and characteristics of the PSI-LHCI-LHCII supercomplex under high light. Photochem. Photobiol. *87*, 143–150.

Qin, X., Suga, M., Kuang, T., and Shen, J.R. (2015). Structural basis for energy transfer pathways in the plant PSI-LHCI supercomplex. Science (80-.). *348*, 989–995.

Ruban, A. (2013). The Photosynthetic Membrane: Molecular Mechanisms and Biophysics of Light Harvesting.

Rutherford, A.W., Osyczka, A., and Rappaport, F. (2012). Back-reactions, short-circuits, leaks and other energy wasteful reactions in biological electron transfer: Redox tuning to survive life in O_2. FEBS Lett. *586*, 603–616.

Sigfridsson, K. (1997). Ionic strength and pH dependence of the reaction between plastocyanin and photosystem 1. Evidence of a rate-limiting conformational change. Photosynth. Res. *54*, 143–153.

Sigfridsson, K. (1998). Plastocyanin, an electron-transfer protein. Photosynth. Res. *57*, 1–28.

Sigfridsson, K., Young, S., and Hansson, O. (1996a). Structural dynamics in the plastocyanin-photosystem 1 electron-transfer complex as revealed by mutant studies. Biochemistry *35*, 1249–1257.

Sigfridsson, K., He, S., Modi, S., Bendall, D.S., Gray, J., and Hansson, O. (1996b). A comparative flash-photolysis study of electron transfer from pea and spinach plastocyanins to spinach Photosystem 1. A reaction involving a rate-limiting conformational change. Photosynth. Res. *50*, 11–21.

Sigfridsson, K., Young, S., and Hansson, O. (1997). Electron transfer between spinach plastocyanin mutants and photosystem 1. Eur. J. Biochem. *245*, 805–812.

Sommer, F., Drepper, F., Haehnel, W., and Hippler, M. (2004). The Hydrophobic Recognition Site Formed by Residues PsaA-Trp ^{651} and PsaB-Trp ^{627} of Photosystem I in *Chlamydomonas reinhardtii* Confers Distinct Selectivity for Binding of Plastocyanin and Cytochrome c_6. J. Biol. Chem. *279*, 20009–20017.

Ueda, T., Nomoto, N., Koga, M., Ogasa, H., Ogawa, Y., Matsumoto, M., Stampoulis, P., Sode, K., Terasawa, H., and Shimada, I. (2012). Structural basis of efficient electron transport between photosynthetic membrane proteins and plastocyanin in spinach revealed using nuclear magnetic resonance. Plant Cell *24*, 4173–4186.

Vasilev, C., Brindley, A. a, Olsen, J.D., Saer, R.G., Beatty, J.T., and Hunter, C.N. (2013). Nano-mechanical mapping of the interactions between surface-bound RC-LH1-PufX core complexes and cytochrome c_2 attached to an AFM probe. Photosynth. Res. *120*, 169–180.

Wood, W.H.J., MacGregor-Chatwin, C., Barnett, S.F.H.S., Mayneord, G.E., Huang, X., Hobbs, J.K.J.K., Hunter, C.N.N., Matthew, P., and Johnson, M.P. (2018). Dynamic thylakoid stacking regulates the balance between linear and cyclic photosynthetic electron transfer. Nat. Plants *4*.

Xue, Y., Okvist, M., Hansson, O., and Young, S. (1998). Crystal structure of spinach plastocyanin at 1.7 A resolution. Protein Sci. *7*, 2099–2105.

6. Exploring the interaction between RC-LH1 and Cytochrome c_2

6.1 Summary

In this chapter the interaction between the reaction centre-light harvesting 1 complex (RC-LH1) and cytochrome c_2 (cyt c_2) from *Rba.sphaeroides* was investigated via SMFS. Compared to the plant photosynthetic ET complexes investigated in Chapters 3-5 the bacterial system offers a range of advantages. Firstly, the site-specific attachment of the RC-LH1 and cyt c_2 to the silicon surface and the AFM probe was possible due to the availability of recombinant proteins bearing poly-histidine tags. Secondly, a range of previously characterised mutants of the complimentary binding interface of the RC-LH1 and cyt c_2 proteins with altered affinity and ET rates are available, allowing the effect of individual residues on the interaction to be studied. The recombinant proteins were purified, and their activity was confirmed by spectroscopic assay.

For attachment of the 12xhis tagged RC-LH1 (RC^{12His}-LH1) complex to the silicon wafer an MPTMS monolayer was first derivatised with an SMCC crosslinker and then reacted with an amine-nitrilotriacetic acid (NTA) molecule. The NTA moiety was able to coordinate Ni^{2+} or Cu^{2+} cations and offer a binding site for the his tag of the RC^{12His}-LH1 protein. Similarly, for attachment of 6xhis tagged cyt c_2 (cyt c_2^{6His}) to the MPTMS monolayer on the AFM probe, an NTA terminated 15 nm PEGylated-SMCC linker molecule was utilised. The density of RC^{12His}-LH1 complexes on the silicon wafer could be controlled via the introduction of Tris as a competitive agent during the reaction of the amine-NTA with SMCC, which subsequently limits the number of attachment points for the complex. The specificity of the recorded interaction was supported by the coincidence between the recorded unbinding events and RC^{12His}-LH1 topology on the surface, and by the reduction in the number of unbinding events recorded in the presence of free cyt c_2 as a blocking agent. In addition, a negative control in which cyt c_2 was absent from the probe functionalisation process confirmed that the NTA linkages used in this chapter did not themselves give rise to non-specific adhesion events.

Using this experimental setup, the interaction between RC-LH1 and cyt c_2 was probed, and the effects of illumination, ionic strength and redox state of cyt c_2 on the interaction were investigated. In addition, a comparison was made between WT RC^{12His}-LH1 and a RC^{12His}-LH1 mutant in which glutamine 264 on the binding interface of the L-subunit of the RC was replaced by a glutamate QE(L264), which was previously shown to have a higher affinity for cyt c_2 .

6.2 Introduction

In purple non-sulphur photosynthetic bacteria cyt c_2 serves as an electron carrier between the cytochrome bc_1 (cyt bc_1) and RC-LH1 complexes in the periplasm of the chromatophore (Discussed in chapter 1.1.4). Unlike the cytb_6f : Pc and PSI : Pc ET complexes investigated in chapters 4 and 5, a high-resolution structure is available for the cyt c_2 : RC ET complex from *Rba.sphaeroides* (Axelrod et al., 2002), providing atomic level detail on the nature of the interaction and a blueprint for its targeted manipulation by mutation. The effect of specific mutations on the binding interface has been elucidated in a range of bulk phase ET kinetic studies (Gong et al., 2003; Tetreault et al., 2001, 2002). As seen previously for Pc in its interaction with cyt b_6f and PSI, the binding interface for the cyt c_2 : RC-LH1 ET complex is comprised of two regions; firstly, long range electrostatic forces between oppositely charged residues on the two proteins steers the formation of an encounter complex, and subsequently short-range hydrophobic and ∏-cation interactions between the residues surrounding the ET cofactors facilitate efficient ET (Reviewed in Hunter et al., 2008). The kinetic results of manipulations to the binding interfaces have been previously summarised (Gong et al., 2003; Hunter et al., 2008; Tetreault et al., 2001, 2002) and will not be extensively discussed here. Instead a brief summary of the residues involved in the interface will be presented.

Figure 6.1 presents a structural overview of the cyt c_2 : RC-LH1 ET complex. The longer range, charge-mediated interactions between the two proteins are separated by intervening water molecules in the Axelrod et al., 2002 structure. Complimentary electrostatic interactions are formed between negatively-charged acidic residues on the L subunit D155 (D(L155)), D(L257) and D(L261), and M subunit D88 (D(M88)), E(M95), D(M184) and D(M292) on the RC, and positively charged lysine residues, 10, 35, 95, 97, 99 and 103 on cyt c_2. Hydrogen bonds can be seen between Q(L258), N(M187) and N(M188) on the RC, with the backbone of residues K(99), T(101) and K(103) on the cyt c_2 (Abresch et al., 2008). Short-range hydrophobic interactions occur between Y(L162), L(M191) and V(M192) on the RC and F(102) and the haem group of the cyt c_2 (Gong et al., 2003). These short-range interactions also include a π-cation interaction between the aromatic ring of Y(M295) on the RC with R(32) on the cyt c_2 (Paddock et al., 2005). In addition, the location of Q(L264) has been shown in purple in figure 6.1 and is the location of the change in the aforementioned QE(L264) RC-LH1 mutant.

The distance between the 870 Bchl cofactors in RC-LH1 and haem in cyt c_2 is 14.2Å, giving a calculated ET rate of $5x10^6$ s^{-1} if going via Y(L162) on the RC (Hunter et al., 2008). This ET path would also account for the large ET rate decrease seen in YA(L162) mutants (Gong et al., 2003), and as such has been widely accepted as the native ET pathway between the proteins. The rate of ET also shows the

expected bell-shaped curve dependency on ionic strength, highlighting the importance of electrotactic interactions in steering formation of the encounter complex (Gerencsér et al., 1999).

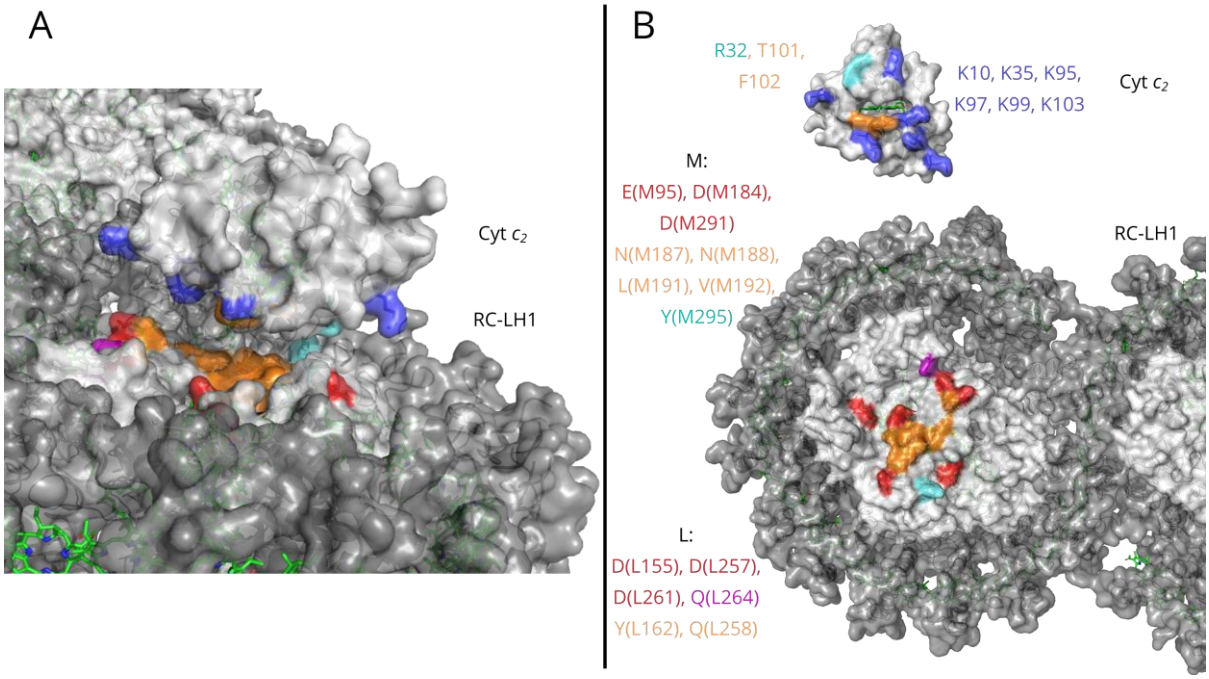

Figure 6.1 RC-LH1 : Cytochrome c_2 binding interfaces highlighted

*Binding interfaces highlighted for the interaction between RC-LH1 and cyt c_2. Acidic and basic residues involved in the interaction are shown in red and blue respectively. Hydrophobic residues involved in shorter range interactions are shown in orange, whilst the Pi-cation interacting residues are shown in cyan. Q(L264) is shown in purple as the location of the site of mutation in the QE(L264) high affinity mutant. Other parts of the reaction centre are shown in light grey, and the LH1 ring is shown in dark grey. (**A**) The nearly interacting complex between RC-LH1 and cyt c_2, moved apart for display purposes. (**B**) Open book form showing the binding interfaces for each component. (PDB: RC-LH1 dimer – 4V9G, (Qian et al., 2013), cyt c_2 – 1L9J, (Axelrod et al., 2002))*

Our lab has also previously used SMFS to probe the interaction between RC-LH1 and cyt c_2 in an initial study (Vasilev et al., 2013, 2019). In these experiments, the RC-LH1 and cyt c_2 were immobilised on freshly generated gold surfaces or probes respectively. Following this, the probes were used to scan over the surface, generating an image and showing the locations and magnitude of adhesions. The effect of light on the interaction was probed via the external illumination of the sample, and it was found that an interaction frequency decreases nearly 5-fold when no illumination was present. Whilst this initial study set the basis for SMFS using PF-QNM, it was limited to probing the effect of light on the interacting complex. In our study here, we hoped to gain a more complete understanding of how

the interaction responds to ionic strength and redox state, as well as utilise mutants to better understand the ET binding interfaces discussed throughout this thesis.

6.3 Results

6.3.1 RC-LH1 and Cytochrome c_2 purification

The WT and the QE(L264) mutant RC^{12His}-LH1 were purified from *Rba. sphaeroides* cells as previously described (see materials and methods section 2.4.5 and Friebe et al., 2016). In brief, following semi-aerobic growth, cells were harvested and lysed using a French pressure cell. Photosynthetic membranes (chromatophores) were then enriched on a sucrose step gradient, solubilised in βDDM and the RC^{12His}-LH1 complexes subsequently purified on a Ni^{2+} charged immobilized metal affinity chromatography (IMAC) column. After elution from the IMAC column using imidazole, the resulting RC^{12His}-LH1 sample was then concentrated and placed onto a size exclusion column to separate monomeric and dimeric forms of the complex and remove the imidazole. The ratio of the absorbance at 875nm (bacteriochlorophylls) and 280nm (aromatic residues of the protein) is commonly used to assess the purity of a sample, and the viability of the purified protein (Qian et al., 2005). A ratio of 1.6 has been suitable for structural work previously (Qian et al., 2013). Monomer fractions with Abs^{875nm} / Abs^{280nm} ratio over 1.7 were pooled, concentrated and frozen at -80°C until use. The end ratio (Abs^{875nm} / Abs^{280nm}) for the WT RC^{12His}-LH1 and QE(L264) RC^{12His}-LH1 was found to be 1.8 and 1.78 respectively. An extinction coefficient for the absorbance at 875nm of 3920$mM^{-1}cm^{-1}$ was used to quantify the proteins (Adams et al., 2011).

The purification of cyt c_2^{6His} is described in detail in materials and methods section 2.4.6. In brief, cyt c_2^{6His} was purified from a strain described in Vasilev et al., 2013, containing a 6xHis tag on the C terminus. Cells were grown and harvested as seen above for the RC^{12His}-LH1. After cell lysis, the cell homogenate was treated directly with 1% Triton. Following centrifugation and extrusion through a 0.45µm filter to remove unsolubilised material, the supernatant was applied to a Ni^{2+} charged IMAC column. Triton was removed in the washing stages and cyt c_2^{6His} was eluted in 400mM imidazole. The cyt c_2^{6His} fractions were then pooled, concentrated and applied to a size exclusion column. Fractions with an Abs^{417nm}/Abs^{280nm} ratio greater than 3 were pooled, concentrated and frozen at -80°C until use. The concentration could be measured by the absorbance at 550nm for the reduced form of the haem with an extinction coefficient of 30.8 $mM^{-1}cm^{-1}$ (Axelrod et al., 1994).

The initial verifications for the end products of all 3 purifications can be seen in figure 6.2, with both absorbance spectra and SDS-PAGE confirming the purity of the samples.

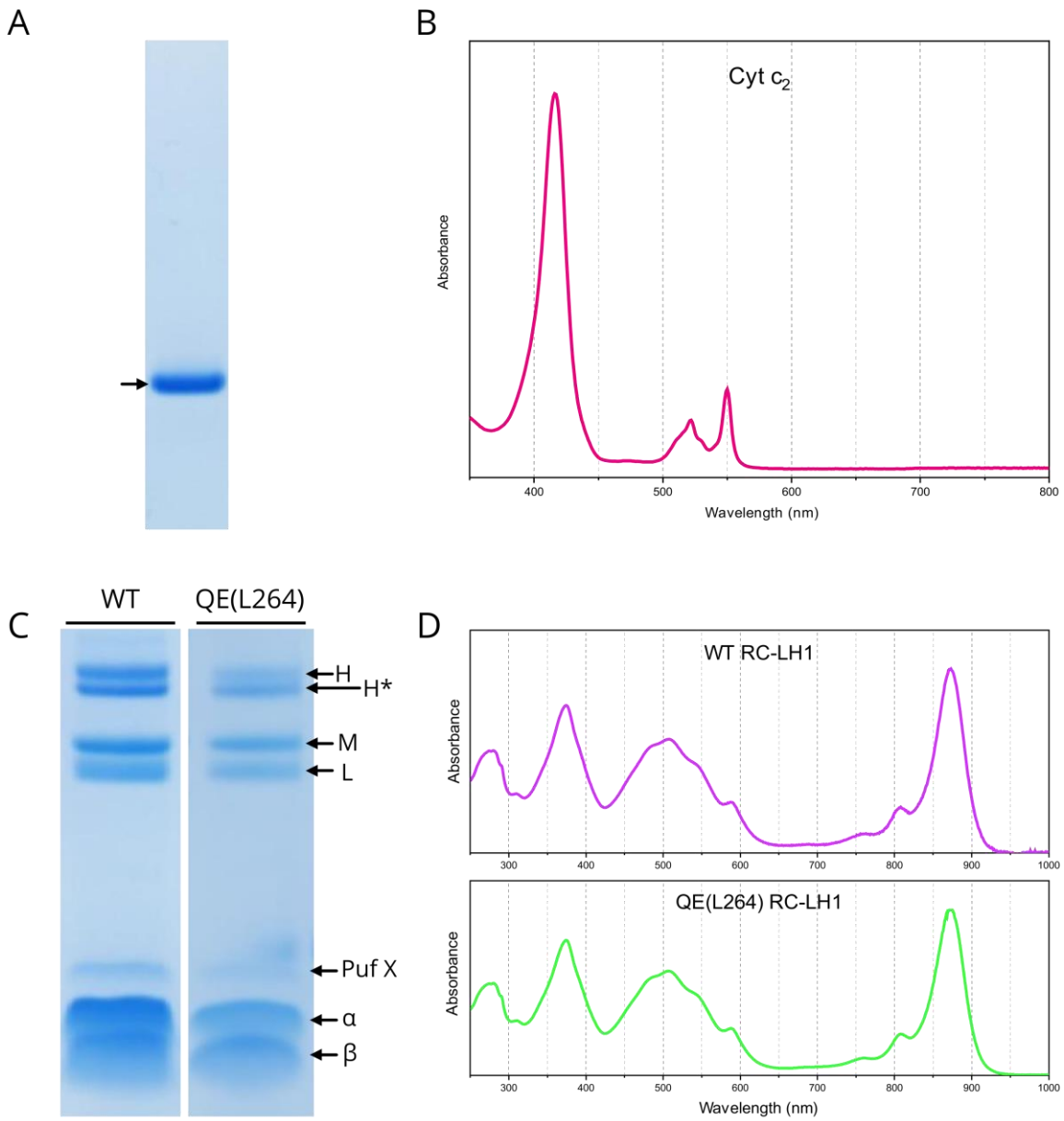

Figure 6.2 Purification of Cytochrome c_2 and WT and QE(L264) RC-LH1

*Proof of purifications for Cyt c_2^{6His}, and WT and the QE(L264) mutant of RC^{12His}-LH. (**A**) SDS-PAGE of the cyt c_2^{6His}, with the band indicated by black arrow. (**B**) Absorbance spectra for the end cyt c_2 sample. The Abs^{417}/Abs^{280} was found to be 4, which is high enough to be used for structural work (Axelrod et al., 1994). (**C**) SDS-PAGE of the RC^{12His}-LH1 purifications of WT and QE(L264) mutant as labelled. Band identities indicated by arrows. The duplication on the H subunit (H*) is the result of proteolysis of the thrombin cleavage site between the protein sequence and the 12xHis tag. The PufX subunit is also present in low quantities, in agreement with previous purifications (Qian et al., 2013). (**D**) Absorbance spectra from the RC^{12His}-LH1 purifications, both in agreement with previous studies of the complete*

intact complex. The Abs^{875nm}/Abs ^{280nm} was found to be 1.8 and 1.78 for the WT RC^{12His}-LH1 and QE(L264) RC^{12His}-LH1 respectively.

6.3.2 Verification of RC-LH1 purifications

In addition to the confirmation seen in figure 6.2, the ET activity of the purified His-tagged RC-LH1 and cyt c_2 complexes was confirmed by spectroscopic assay. The spectrophotometer described in section 5.3.2 for the PSI bulk phase kinetics was also used for the RC-LH1, however a 0.5W 880nm LED was used for the excitation of RC-LH1, with filters of 730nm used to minimise noise from illumination (For details see materials and methods, section 2.3.9.3). 20 µM cyt c_2^{6His} pre-reduced with ascorbate was added to 10nM RC^{12His}-LH1, together with 50µM of coenzyme Q_0 (Q_0) provided as an electron acceptor. This was measured for 10 seconds prior to a 10 second illumination of the sample. Figure 6.3 shows the 550 - 542 nm absorption change reflecting the oxidation of cyt c_2 by the WT and QE(L264) mutant RC^{12His}-LH1 samples. The QE(L264) mutant has been previously shown to exhibit a 30-fold higher affinity (30-fold lower K_D) over the WT form, with only minimal changes in the first order electron transfer rate (Tetreault et al., 2001). Unsurprisingly this is reflected in the steady state kinetics seen in figure 6.3 with the QE(L264) mutant exhibiting a 1.58 fold increase in initial ET rate compared to the WT. Whilst the higher affinity of the QE(L264) mutant might be expected to lower k_{off} compared to the WT, the use of 50mM NaCl (near optimum for RC-LH1 turnover (Gerencsér et al., 1999)) relieves this to some extent. The slow rate of cyt c_2^{6His} reduction following the end of illumination (t = 20 seconds onwards) reflects the slow uncatalyzed ET from Q_0 to cyt c_2. This rate was considered to be negligible at the start of illumination. The results confirmed the activity of the his-tagged complexes.

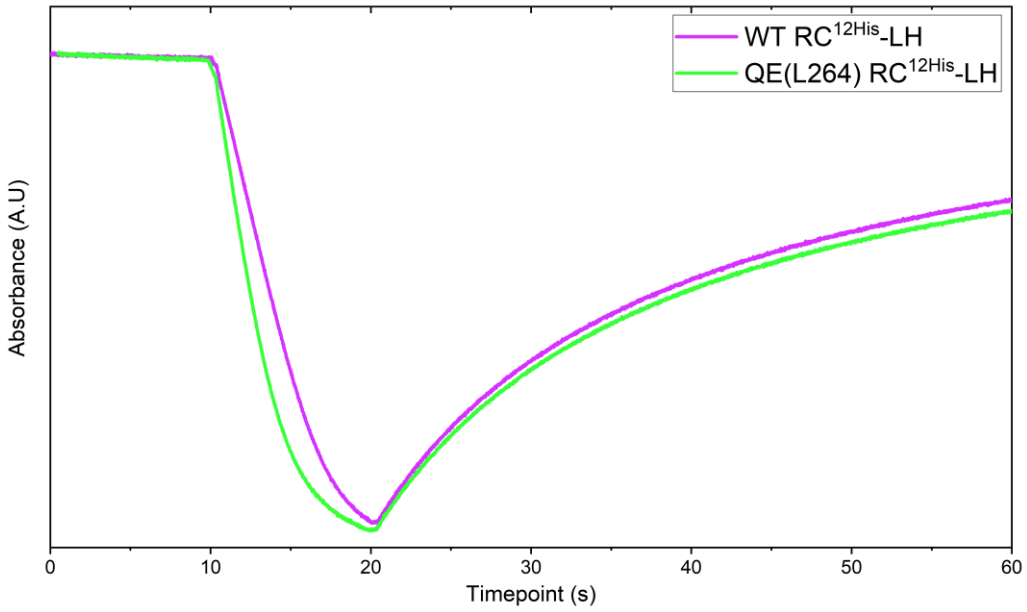

Figure 6.3 Flash kinetics of RC-LH1 WT and QE(L264)

Traces show the oxidation of cyt c_2 (550nm) minus the isosbestic point for the cyt c_2 $^{2+}$/ $^{3+}$ (542nm). The absorbance is measured for an initial 10 seconds, followed by illumination for a further 10 seconds. A slow initial rate (0-10 seconds) is observed following the start of absorbance measurements due to the light required to measure absorbance. Excitation was performed with 880nm 0.5watt THOR labs LED, and filters of 730nm were used to minimise noise. Initial rates for the ET were 204 and 321 s^{-1} for the WT and QE(L264) respectively. The re-reduction of cyt c_2^{6His} observed after illumination (20-60 seconds) is due to the Q_0 electron acceptor donating electrons to cyt c_2. The experiment was performed in 50mM HEPES, pH 7.4, 50mM NaCl, 0.03% βDDM.

6.3.3 Attachment of proteins to surfaces and storage

In previous SMFS experiments performed on RC-LH1 : cyt c_2 by SMFS the complexes were attached to gold surfaces (Vasilev et al., 2013). However, gold surfaces need to be freshly vaporized immediately prior to functionalisation to avoid contamination that can occur when stored for long periods. For this reason, they were avoided in the current work and the silicon methods used in previous chapters were adapted. In contrast to previous chapters, both the RC^{12His}-LH1 and cyt c_2^{6His} could be attached to the surface specifically, via the histidine tags used for purification. Figure 6.4 shows the linkages used for this purpose. In place of attaching proteins directly to the NHS esters on the SMCC monolayer generated, a chelating agent of Nα, Nα-Bis(carboxymethyl)-L-lysine (Amine - NTA) can be attached. Following incubation with either nickel or copper salts this then immobilises the divalent cation,

offering a binding location in the same manner as IMAC columns. This not only allows site-specific attachment to the surface but also provides orientation of the protein with the his-tag on the RC^{12His}-LH1 located on the cytoplasmic side of the complex leaving the cyt c_2 binding interface on the periplasmic surface exposed to the cyt c_2 functionalised probe.

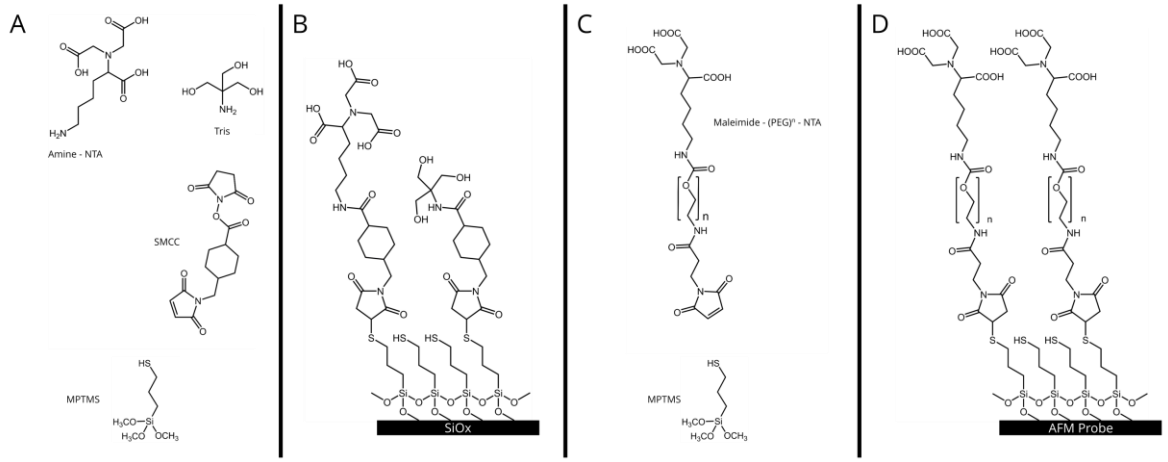

Figure 6.4 Surface chemistry utilised for fixing His tagged proteins

*(**A**) The independent linkage components used for the RC^{12His}-LH1 immobilisation on silicon wafer, with the end reacted product being shown in (**B**). (**C**) The independent linkage components used for attachment of cyt c_2^{6His} to AFM probes, with the end reacted products being down in (**D**). (By-products omitted for all end reacted products). The length of the PEG linker (n in C/D) was centred around a mean molecular weight of 2kDa, giving a mean value for n of 35, and a length of ca. 15nm. Abbreviations used: MPTMS, (3-Mercaptopropyl)trimethoxysilane; SMCC, succinimidyl 4-(N-maleimidomethyl)cyclohexane-1-carboxylate; Amine – NTA, Nα,Nα-Bis(carboxymethyl)-L-lysine.*

Unlike the covalent chemistry used for attachment of proteins in previous chapters, in the coordination of the RC^{12His}-LH and cyt c_2^{6his} his tags there is no competing hydrolysis reaction which allows control of protein density through concentration of incubation. An important objective is to ensure that a significant proportion of unbinding events probe only a single bound cognate pair at a time (Johnson and Thomas, 2018), which is usually achieved by a low concentration of the proteins at the incubation stage. Thus, another method was devised to control surface density of the proteins. At the incubation stage with amine - NTA, Tris could be added as a competitive agent to the amine-NTA (figure 6.4 A/B) as it was previously to lysine residues on cyt b_6f (Chapter 3). This would result in fewer chelating groups being available in a given area on the surface, thus lowering the final density of proteins attached. To establish the optimum conditions for achieving suitable surface density of RC-

LH1 complexes the concentration of Tris was varied between 50 µM and 5mM during the reaction between SMCC and 1mM amine-NTA. Following this the surfaces generated were incubated with 100mM $CuSO_4$, followed by 500nM RC^{12His}-LH1 (WT) (See materials and methods section 2.5.4.5). AFM images of these surfaces can be seen in figure 6.5, with a scan size of 1 µm, and pixel density of 512 x 512. 1mM Tris was found to give a good surface density of RC-LH1 complexes and was used in all the experiments subsequently described herein. The large lumps of material seen on the surfaces are aggregated protein, which could be removed by centrifugation of the protein sample immediately prior to surface incubation.

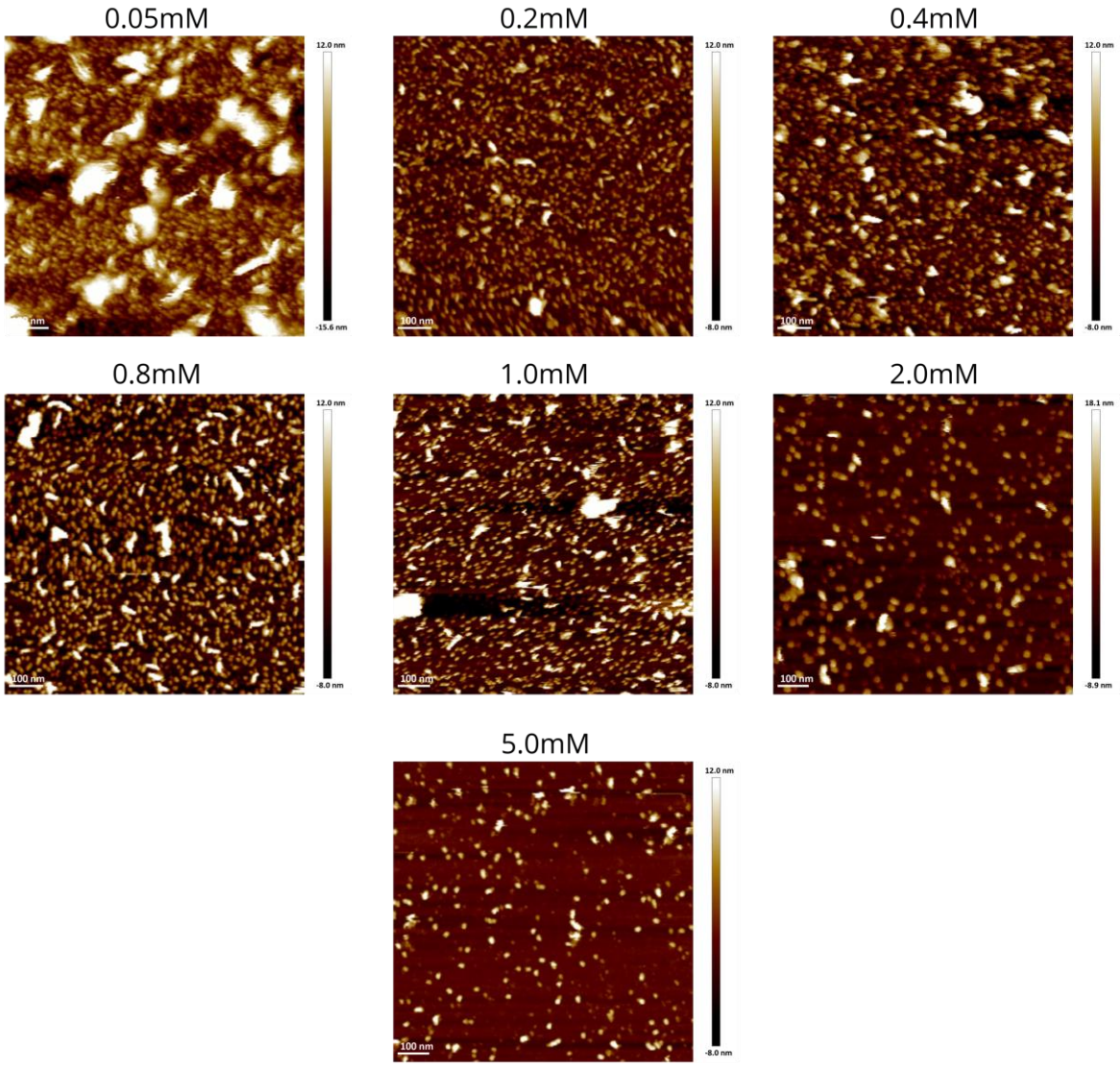

Figure 6.5 Surface immobilisation of RC-LH1 with Tris spiking

AFM images of the surfaces generated from incubating SMCC functionalised surfaces with 1mM Amine-NTA and the concentration of Tris displayed above the image. These incubations were performed in 10mM HEPES, pH 7.4, 10mM NaCl 0.03% ß-DDM. Following this, all surfaces were

incubated with 100mM $CuSO_4$ for 10 minutes, washed, incubated with 500nM WT RC^{12His}-LH1 for 10 minutes, washed again then imaged.

Another benefit of Cu^{2+}-NTA immobilisation method was the ability to store the wafers and AFM probes prior to attachment of the proteins. Other methods of chemical linkage used in Chapters 3-5 involved chemical groups that would, over time, hydrolyse or lose function in inorganic solvents, hence their commercial sale in desiccated powder form. The NTA groups terminating the surfaces generated as in figure 6.4 however do not degrade, allowing surfaces and probes to be generated in batches, and stored. Given the timescale for SMFS preparations, with cleaning and functionalisation stages usually taking up to 2 days, the ability to generate batches of surfaces that could then have proteins attached immediately prior to the experiments was advantageous.

To confirm that the surfaces remained viable following long-term storage (14 days) and that the RC-LH1 protein was attaching to the surface specifically via the poly-histidine tag, the control experiment shown in figure 6.6 was performed. Firstly, stored surfaces were imaged (fig 6.6A), these were then charged with $CuSO_4$, incubated with RC^{12His}-LH (Fig 6.6B) and washed with 400 mM imidazole (a competitor of the His-NTA interaction) and 100mM EDTA (to chelate divalent cations) (Figure 6.6C). These results showed that the stored surfaces retain the ability to specifically bind RC-LH1 by its His-tag.

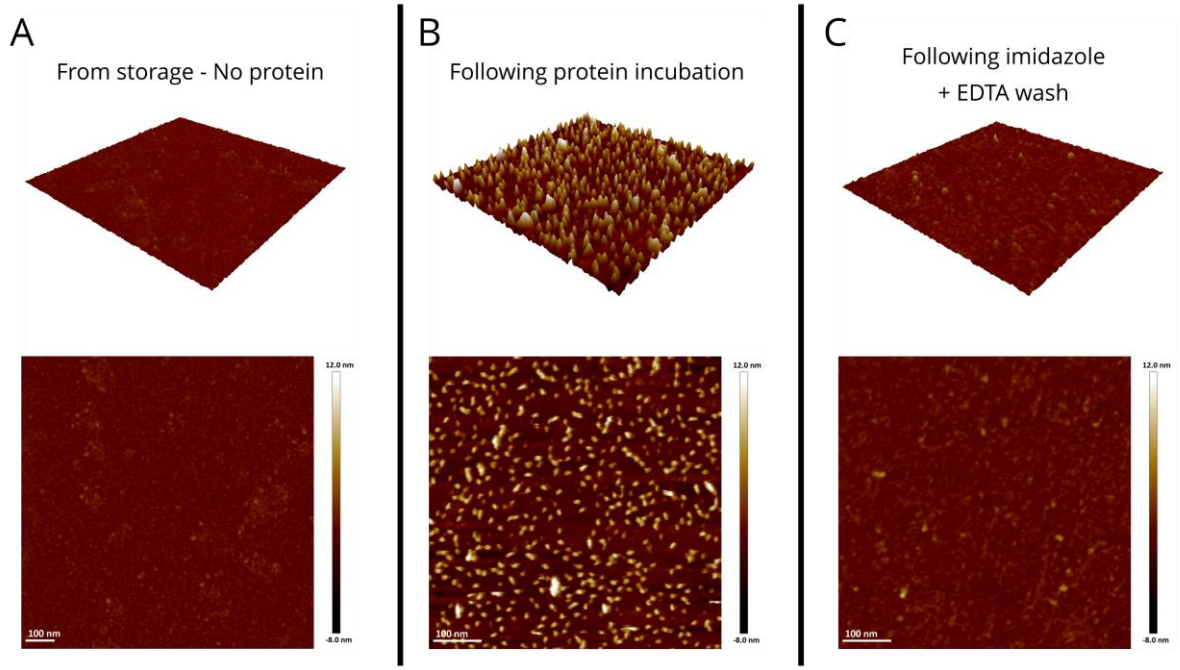

Figure 6.6 Testing of surface storage and linkage to NTA

*AFM images taken of surfaces following (**A**) Stored in storage buffer for 14 days, (**B**) Surface from A following 10-minute incubation with 100mM $CuSO_4$, then with 500nM WT RC^{12His}-LH1 for 10 minutes and (**C**) Surfaces from B after being washed with 200mM Imidazole, then 100mM EDTA.*

6.3.4 SMFS on the interaction between RC-LH1 : Cytochrome c_2

Figure 6.7 shows an example of the initial data obtained for a surface of WT RC-LH1 scanned across with a cyt c_2^{6His} [Red] functionalised probe, in the presence of external illumination. The coincidence between the topology of the bound RC^{12His}-LH1 complexes on the silicon surface in the AFM height images and the extracted unbinding events gives initial evidence that the measured interaction is specific. Looking at the individual FdCs for the data sets shown in figure 6.7B, some FdCs exhibited a slightly larger than 15nm separation distance (blue curve), however this could be accounted for by considering the size of the two proteins (5nm) added onto the linker.

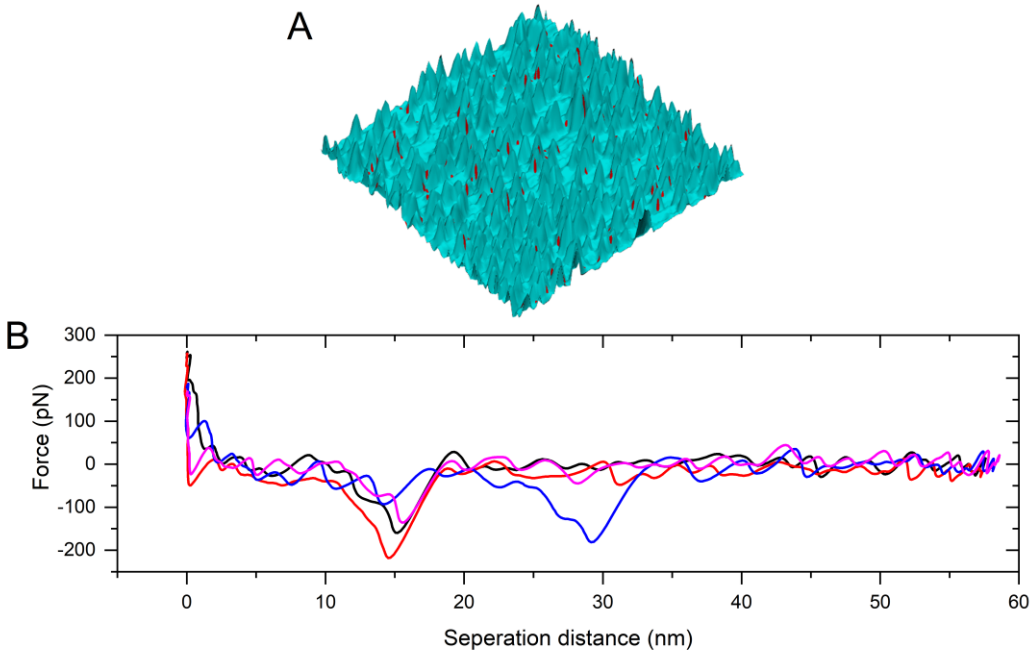

Figure 6.7 Example force data from the RC-LH1 – Cytochrome c_2 interaction

*(**A**) Overlay of the adhesion locations (shown in red) onto the height data from the AFM image, generated in custom MATLAB script (Appendix 8.3). Adhesion locations show strong correlation to the location of particles on the surface. (**B**) Example force-distance curves from initial data on the RC-LH1 – Cyt c_2 interaction. Measurements were performed in 10mM HEPES pH 7.4, 10mM NaCl, 0.03% βDDM.*

The measured distribution of unbinding forces for the RC-LH1 : cyt c_2 interaction is shown in figure 6.8A (for cyt c_2 [Red], under external illumination). A single gaussian fit gave an adjusted R-squared below 0.9, and as such 2 gaussians were fitted. These two populations gave mean unbinding forces of 116 ± 2 pN and 207 ± 11pN, both considerably lower than that previously reported in Vasilev et al., 2013 and 2019. It is important to distinguish however that a lower peak force repetition rate was used for these experiments; 0.5kHz as opposed to 1-2kHz. In addition, Bruker's SNL probes were used in Vasilev et al., 2013 and 2019, while in these experiments PeakForce-HIRS-SSB probes were used and had a lower spring constant. This combination would result in a lower loading rate upon retraction, however this is difficult to quantify due to Bruker's lack of transparency in PF-QNM as discussed in section 1.4.3. As such, these was accepted to be the normal unbinding forces going forward. The specificity of the recorded interaction was tested by the addition of 20µM free Cyt c_2^{6His}[Red] (a large excess compared to the reported K_D of 0.3µM (Tetreault et al., 2001)) to the imaging buffer (Lee et al., 1994). While both unbinding force populations were effectively unchanged following this addition (Fig 6.8A), the interaction frequency decreased to 35% of that seen prior to blocking, suggesting the

specific nature of the interaction (Fig 6.8B). The addition of 20µM free cyt c_2 should result in 98% occupancy of RC-LH1 on the surface given a K_D of 0.3 µM (20 / (20+0.3)). As such, the drop in binding frequency is smaller than expected (Fig 6.8B). At first, this would appear to reflect a similar situation to that proposed to occur in the PSI : Pc interaction (section 5.3.4), in which here, continued turnover of RC-LH1 would oxidise cyt c_2^{6His} in the imaging buffer, giving rise to photo-oxidised RC-LH1 (RC-LH1 [^{P}Ox]) and Cyt c_2 [Ox]. However, previous studies (Gerencsér et al., 1999) and indeed our own results for the effect of redox state discussed further on have found a higher affinity for RC-LH1 [^{P}Ox] : Cyt c_2 [Ox] than for RC-LH1 [^{P}Ox] : cyt c_2 [Red]. As such, this would not be a possible explanation for the results seen in figure 6.8 and the specificity of the remaining events needed to be confirmed.

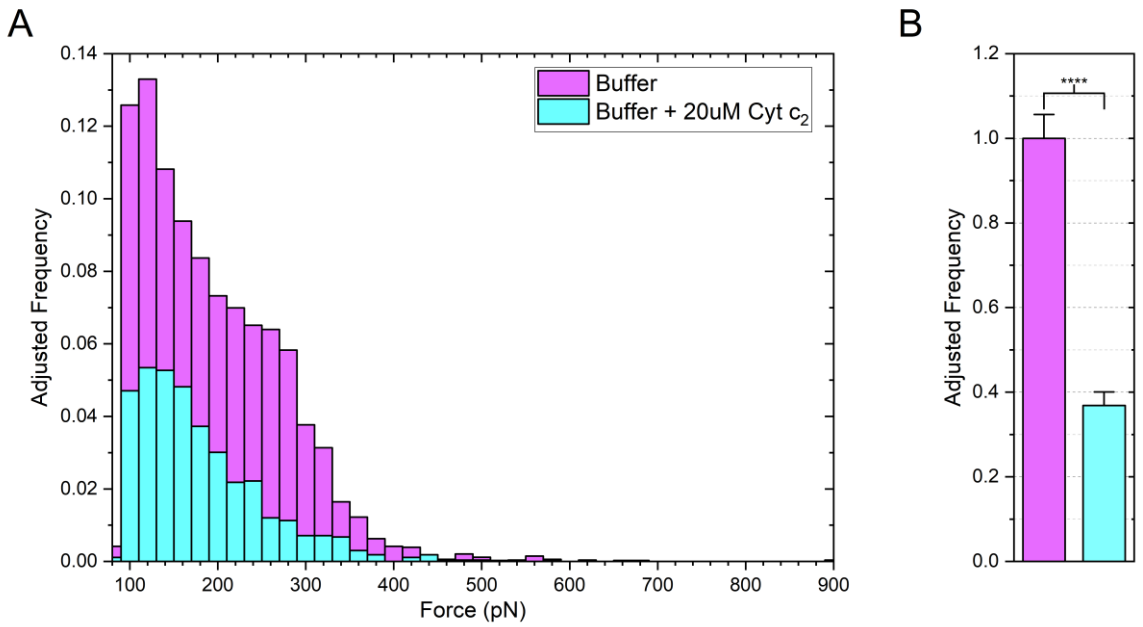

Figure 6.8 Effect of free Cytochrome c_2 on the RC-LH1 : Cytochrome c_2 interaction at 10mM NaCl

*Standard control of the interaction performed by addition of 20µM cyt c_2 into the imaging buffer. The cyt c_2^{6his} attached to the AFM probe was pre-reduced in 1mM ascorbate, and the measurements were performed under illumination. (**A**) Distribution of forces observed before and after addition of cyt c_2, with the cumulative frequencies adjusted to the state before addition of cyt c_2. Mean unbinding forces from gaussians were found to be 116 ± 2pN and 207 ± 11pN for Buffer sample, and 126 ± 3pN and 194 ± 37pN for Buffer + 20µM Cyt c_2 (**B**) Interaction frequency observed for the states seen in A, with colours matching. Unpaired t-test analysis was performed on the adjusted frequencies. Asterisk denotes a p-value of <0.0001. Error bars are ± standard error of the mean, n = 28-31 independent analysed images for each condition.*

To confirm the specificity of the residual unbinding events observed upon addition of 20µM cyt c_2^{6His}, an additional control was performed. The omission of one of the binding participants, in this case using an AFM probe that lacked cyt c_2 but still possessed a Cu^{2+}-NTA terminated monolayer (Vasilev et al., 2013) was performed. Figure 6.9 shows the distribution of unbinding forces, and the interaction frequency for when cyt c_2^{6His} is omitted (- cyt c_2). Following this the AFM probe was incubated in 20µM cyt c_2^{6His} for 10 minutes, then washed with imaging buffer. Once again, the SMFS measurements were taken with the newly functionalised probe (+ cyt c_2).

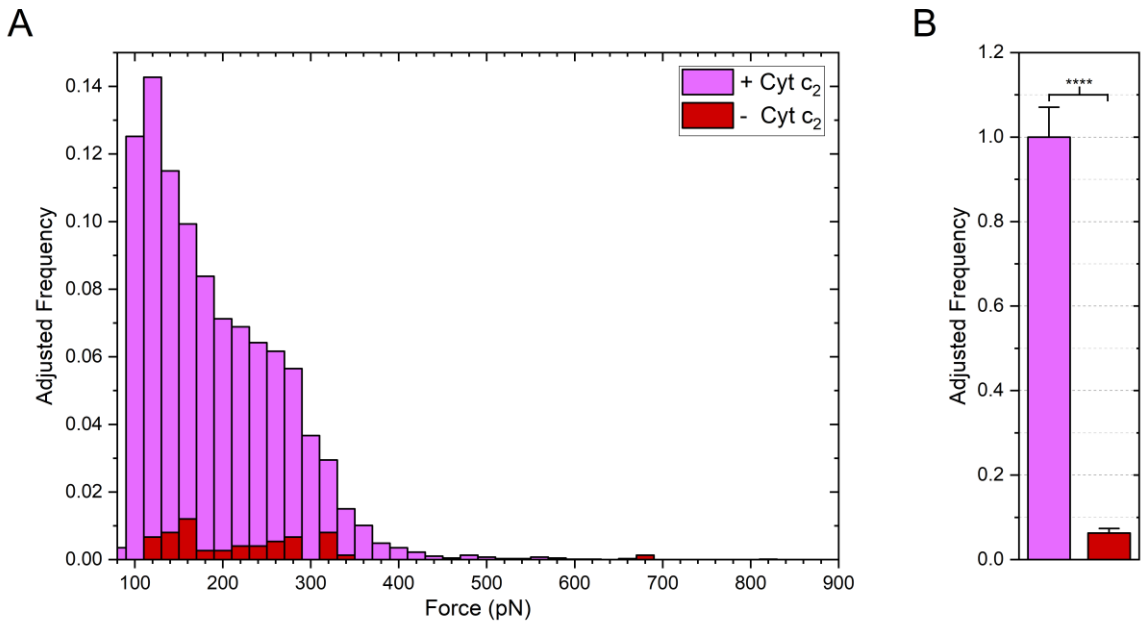

Figure 6.9 Negative control of SMFS on protein-absent surfaces

*Negative control of the interaction measured for the functionalised tip to the RC^{12His}-LH1 surface before (- Cyt c_2) and after (+ Cyt c_2) incubation with cyt c_2^{6His}. (**A**) Distribution of forces measured for the interaction, with the cumulative frequency adjusted relative to '+ Cyt c_2'. Mean unbinding force from gaussian was found to be 119 ± 2pN and 208 ± 12pN. (**B**) Interaction frequency for the system with and without cyt c_2^{6His} incubated with the AFM tip. Colours match those seen in (A). These measurements were performed under illumination, and in both cases the AFM probe was incubated with 1mM sodium ascorbate prior to measurements. Unpaired t-test analysis was performed on the adjusted frequencies. Asterisk denotes a p-value of <0.0001. Error bars are ± standard error of the mean, n = 13-21 independent analysed images for each condition.*

The interaction frequency when cyt c_2 is omitted is nearly 20 times lower than when the AFM probe is doped with cyt c_2^{6His}, and the forces show a more random distribution pattern. This is good evidence

that the remaining interactions and distribution of unbinding forces seen in figure 6.8 stem from a specific interaction between RC-LH1 and cyt c_2.

6.3.5 Effect of light on the interaction between RC-LH1 : Cytochrome c_2

While PSI (Chapter 5) absorbs the 680 nm AFM laser light efficiently, the oscillator strength of RC-LH1 in this spectral region is much lower (see figure 6.2D). As a result, the AFM laser itself would not be expected to induce significant turnover of the RC^{12His}-LH1. Therefore theoretically, by omitting the external white illumination present in previous experiments, the affinity of the RC-LH1[Red] state could be probed. Previous SMFS experiments showed that when RC-LH1 is photo-oxidised by white light illumination, the interaction frequency is increased relative to measurements in the dark (where only the 680 nm laser light was present) where RC-LH1 remains reduced (RC-LH1 [Red]) (Vasilev et al., 2013). However, since these previous SMFS experiments were conducted on gold surfaces it was important to establish if a similar effect could be seen on silicon as used here. Figure 6.10 shows the effect of white light illumination on the measured interaction frequency and distribution of unbinding forces. In contrast to the results in Vasilev et al., 2013, the interaction frequency is increased in the absence of white light illumination compared to in its presence. The distribution of unbinding forces does not appear to significantly change, with mean unbinding forces measured of 120 ± 2 pN and 210 ± 13 pN under white light illumination and 119 ± 2pN and 208 ± 7pN in its absence.

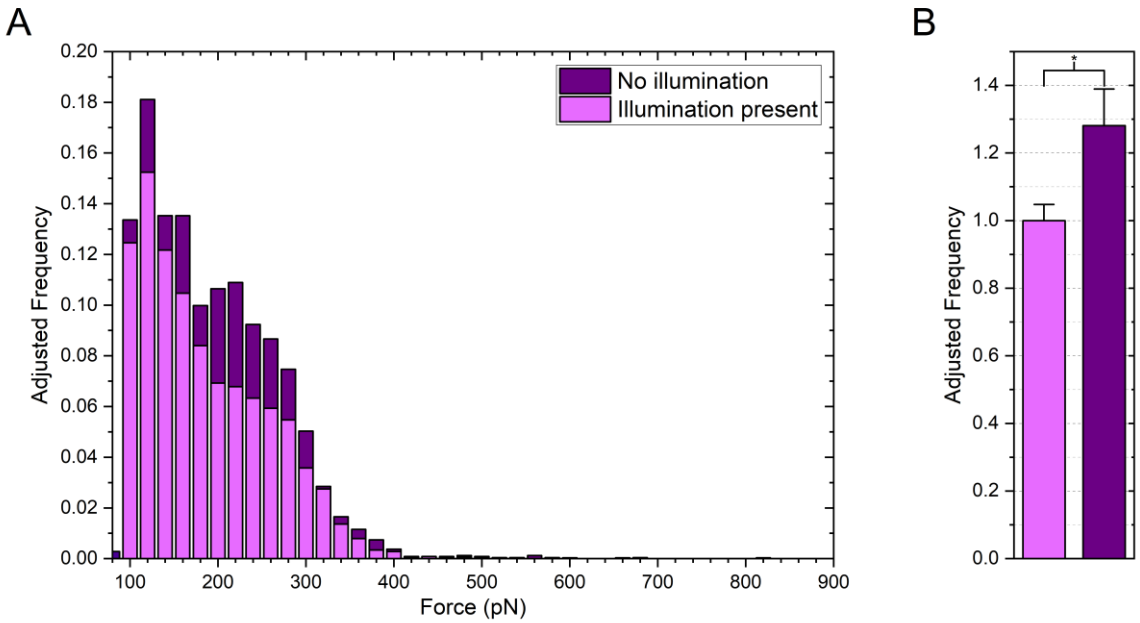

Figure 6.10 Effect of light on RC-LH1 : Cytochrome c_2 interaction

*(**A**) Distribution of forces observed for the interaction between RC-LH1 and cyt c_2 under illumination and under no illumination, with adjusted frequency set relative to being under illumination. Mean forces from gaussian were found to be 120 ± 2 pN and 210 ± 13pN under illumination and 119 ± 2pN and 208 ± 7pN in its absence. (**B**) Interaction frequency observed for the experiment, with the colour scheme matching that in (A). Unpaired t-test analysis was performed on the adjusted frequencies. Asterisk denotes a p-value of 0.0198. Error bars are ± standard error of the mean, n = 36-55 independent analysed images for each condition.*

The previous experiments in Vasilev et al., 2013 were performed utilising custom gold coated Bruker SNL probes. This contrasts with the experiments performed here, utilising the smaller Peakforce-HIRS-SSB probes. As such, the effective overspill from the 680 nm AFM laser is much larger in these experiments compared to using the SNL probes, due to the probes shape and smaller size. It is possible that the intensity of the laser light is sufficient to generate some photo-oxidation of RC-LH1 despite its low absorption in this region. However, this is unlikely to entirely explain the effect observed in figure 6.10, as the experiments do not simply show no effect of illumination (which would be expected if the AFM laser was illuminating), but actually show an increased binding frequency in its absence. In spite of this, all experiments herein were conducted in the presence of external white light illumination.

6.3.6 Effect of ionic strength on the interaction between RC-LH1 : Cytochrome c_2

As mentioned in the introduction to this chapter the RC-LH1 : cyt c_2 ET complex depends in part on complimentary electrostatic interactions which manifest as the bell-shaped dependency of ET rate on ionic strength as previously discussed (Gerencsér et al., 1999).

Figure 6.11 shows the effect of varying the concentration of NaCl from 10 – 500 mM on the binding frequency and unbinding forces measured for the RC-LH1 : cyt c_2 [Red] interaction under external illumination. In contrast to the results for the Pc : cytb_6f and Pc : PSI ET complexes examined in Chapters 4 and 5, changing the ionic strength did affect the distribution of unbinding forces. With increasing ionic strength, the ratio between the lower ca. 130pN and the higher ca. 230pN population decreases. The interactions frequencies seen in 6.11B observe the expected single exponential decay, in agreement with two oppositely charged bodies undergoing screening from one another.

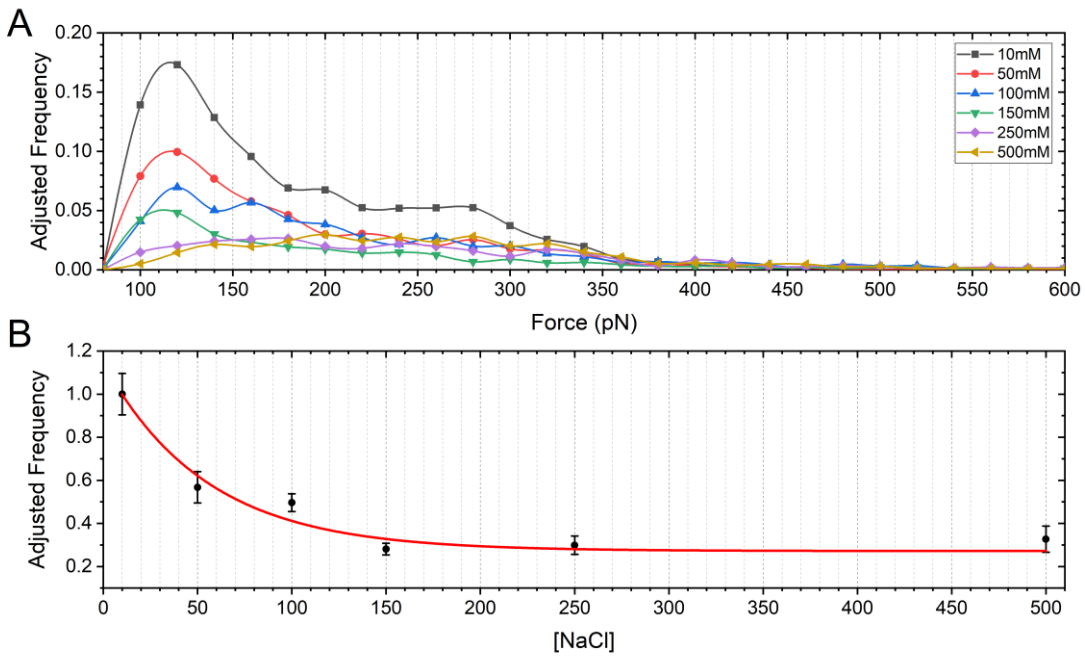

Figure 6.11 Effect of ionic strength on the RC-LH1 : Cytochrome c_2 interaction

*(**A**) Distribution of unbinding forces at different ionic strengths ranging from 10 – 500mM NaCl. The distribution of forces appeared to change, with the higher force population becoming more dominant at higher ionic strengths. (**B**) Effect of salt concentration on interaction frequency, with all points being adjusted relative to 10mM NaCl. Experiments were performed under illumination, and cyt c_2^{6His} on the AFM probe was reduced via ascorbate prior to measurements.*

The increase in the proportion of the higher force population at higher ionic strengths is counter to coulombs law, in which the increasing dielectric coefficient should weaken the attractive forces between opposite charges. However, considering the relationship between these two proteins previously described in bulk phase experiments, a reasonable explanation could be the lower population represents the encounter complex, whilst the higher population represents the full ET complex, which becomes stabilised by additional hydrophobic interactions (section 1.2.2). In this scenario, both force populations are visible at lower ionic strengths, with some interactions going into the full ET complex (230pN), but most not achieving this and being ruptured at the encounter complex stage (130pN), in agreement with the bell-shaped dependency of the ET rate on ionic strength (Gerencsér et al., 1999). As ionic strength is increased, screening of the two charged faces still occurs, leading to the single exponential decay in the interaction frequency, however complexes that do form have a greater probability of entering the full ET complex as the energy to do so is reduced, leading to the depletion of the lower force population at higher ionic strengths.

To ensure the effect of ionic strength observed is in fact on the RC-LH1 : cyt c_2 interaction, the addition of 20µM cyt c_2 was repeated, this time in buffer containing 250mM NaCl. Figure 6.12 shows the distribution of measured forces and interaction frequency observed under these conditions.

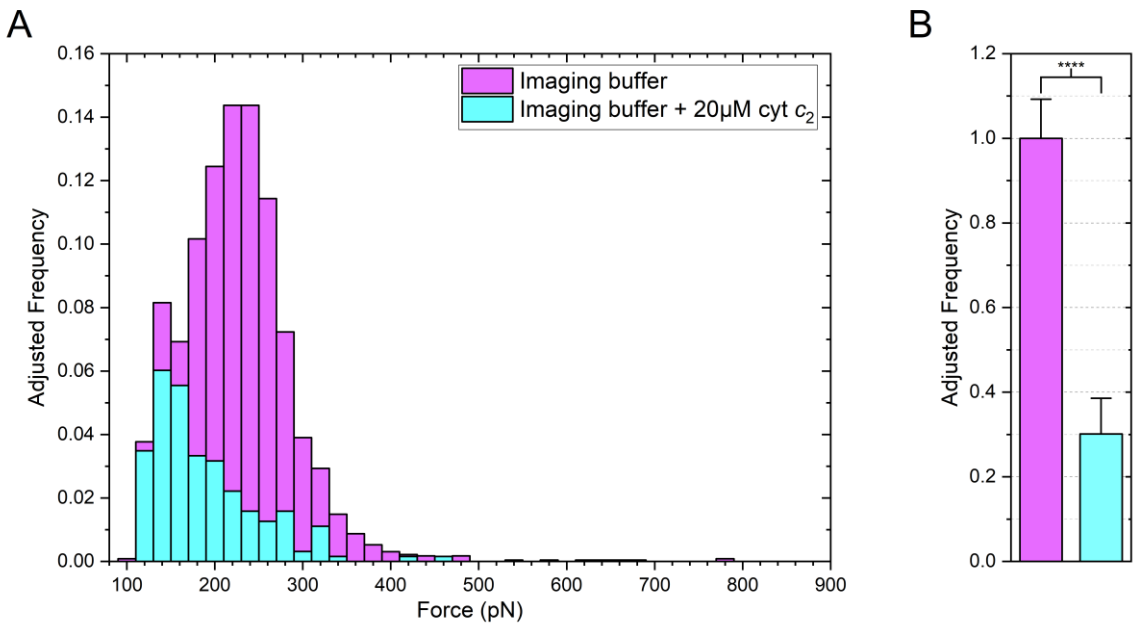

Figure 6.12 Effect of free Cytochrome c_2 on the RC-LH1 : Cytochrome c_2 interaction at 250mM NaCl

*A repeat of the control experiment seen in figure 6.8, here with 250mM NaCl in the imaging buffer. (**A**) The distribution of forces measured for the interaction, with cumulative frequencies adjusted to the*

*Imaging buffer sample. Mean forces from gaussian were found to be 224 ± 1 pN and 135 ± 1pN for Buffer sample, and 208 ± 13pN and 145 ± 1pN for Buffer + 20μM Cyt c_2. (**B**) The interaction frequency, with the same colour scheme as seen in (A). Unpaired t-test analysis was performed on the adjusted frequencies. Asterisk denotes a p-value of <0.0001. Error bars are ± standard error of the mean, n = 8-16 independent analysed images for each condition.*

Once again, the decrease in interaction frequency to around a third is observed. This would suggest the interaction remains between the RC^{12His}-LH1 and cyt $c_2{}^{6His}$. The forces observed in figure 6.12A appear to show a change in distribution upon addition of 20μM cyt $c_2{}^{6His}$, with the dominant force population being the higher and lower, for Imaging buffer and + cyt c_2 samples respectively. The reason for this is unknown. The remaining forces following incubation with 20μM cyt c_2 are not thought to reflect non-specific forces, as they are not observed in the absence of cyt c_2 attached to the AFM probe as seen in figure 6.9.

6.3.7 Probing mutants of RC-LH1 for their interaction with Cytochrome c_2

A range of mutants of the RC-LH1 : cyt c_2 binding interface have been previously described (Tetreault et al., 2001, 2002). The RC-LH1 mutant QE(L264) in which the glutamine at position 264 on the L subunit is mutated to glutamic acid maintains the residue size, however gives an additional charge to the delocalised region as shown in figure 6.1. Kinetics performed in Tetreault et al., 2001 showed that this change yielded a 30-fold decrease in the K_D for cyt c_2 (increase in affinity) compared to the WT RC-LH1 and a ca. 2-fold increase in the first order electron transfer rate (k_{ET}). Since it would be predicted that this mutation would affect the measured unbinding force in SMFS experiments it represented a good initial test case for extending the analysis of ET complexes to encompass the effect of specific residues on the interaction (Gerencsér et al., 1999; Tetreault et al., 2001, 2002).

Surfaces were prepared in parallel utilising the WT or QE(L264) RC^{12His}-LH1 and probed via SMFS. All previous SMFS experiments in this thesis involved relative changes measured on the same surfaces, with the same AFM probe, in different conditions. Redox changes could be carried out via incubation of the surfaces or probes with redox agents. Ionic strength changes could be probed via changing the imaging buffer. All these measurements allowed the same tip and surface to undergo changes and observe the relative result. Probing a mutated protein however would require two separate surfaces to be generated and scanned. While differences in surface coverage could be minimised by generating them in batches, the use of two different protein samples could still introduce variation. Differences in surface density were countered using the MATLAB script seen in chapter 3.3.13 to count the number of particles in a given scan area for each dataset. The cumulative frequencies of interaction were then

normalised for the same number of RC^{12His}-LH1 on the surface, rather than for each image as was the case for previous experiments. Surfaces were generated as previously discussed, and SMFS experiments were used to probe the interaction between cyt c_2^{6His} on the AFM probe with either WT or QE(L264) RC-LH1 in either order. Given the observed effect of ionic strength on the interaction, these experiments were performed at both 10mM and 250mM NaCl.

Figure 6.13 shows the unbinding force distributions and interaction frequencies for the WT and QE(L264) RC-LH1 : cyt c_2 complexes. The measured interaction frequency was not significantly different between the WT and QE(L264) mutant at either 10 mM or 250 mM NaCl (Figure 6.13). However, the mean unbinding forces were significantly different. At 10mM NaCl, the WT exhibited 2 unbinding force populations, with means of 138 ± 1 pN and 222 ± 10pN, while the QE(L264) showed a single population with a mean of 155 ± 8 pN (unable to fit a second population). Measuring the interaction in 250mM NaCl yielded the opposite response, with the QE(L264) mutant exhibiting two populations with means of 135 ± 1pN and 208 ± 4, while the WT only showed a single peak, with a mean of 255 ± 2pN.

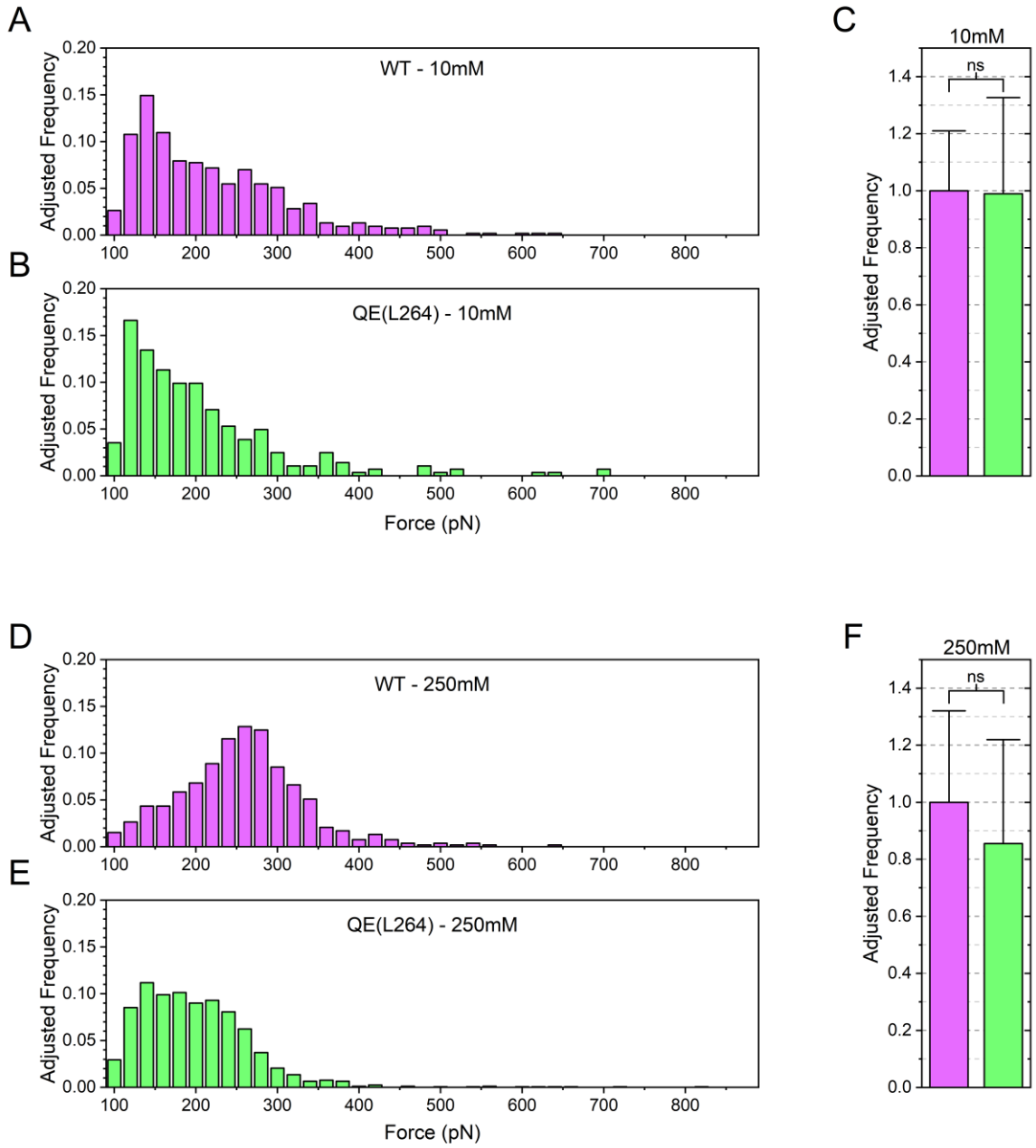

Figure 6.13 Probing the WT and QE(L264) mutant RC-LH1 : Cytochrome c_2 interaction

*Distribution of forces and interaction frequencies for the WT and QE(L264) RC^{12His}-LH1 at 10mM and 250mM NaCl. (**A**) WT RC^{12His}-LH1 in 10mM, 2 peaks found with means of 138 ± 1 pN and 222 ± 10pN, (**B**) QE(L264) RC^{12His}-LH1 in 10mM with only a single peak apparent, mean force: 155 ± 8 pN, (**C**) Interaction frequency for WT and QE(L264) in 10mM NaCl. Unpaired t-test analysis returned a p-value of 0.8182. Error bars are ± standard error of the mean, n = 6 independent analysed images for each condition. (**D**) WT RC^{12His}-LH1 in 250mM with mean force: 255 ± 2pN, (**E**) QE(L264) RC^{12His}-LH1 in 250mM, 2 peaks with means of: 135 ± 1pN and 208 ± 4pN (**F**) Interaction frequency for WT and*

QE(L264) in 250mM NaCl. Unpaired t-test analysis returned a p-value of 0.8182. Error bars are ± standard error of the mean, n = 6 independent analysed images for each condition.

6.3.8 Effect of redox state on the interaction between RC-LH1 : Cytochrome c_2

As discussed above, the redox state of the RC-LH1 could not be controlled independently due to the AFM laser excitation (section 6.3.5). As such, only the redox state of the cyt c_2 was changed for the experiments exploring redox state, and the surfaces were externally illuminated to ensure homogenous photo-oxidation. In principle this allows the RC-LH1 [^{P}Ox] : cyt c_2 [Red] and RC-LH1 [^{P}Ox] : cyt c_2 [Ox] combinations to be investigated. Figure 6.14 shows the unbinding forces and the interaction frequency for different redox states of the cyt c_2 interacting with WT RC^{12His}-LH1 at 10mM [NaCl]. The mean unbinding forces for cyt c_2 [Red] (134 ± 1 and 219 ± 4 pN) were not significantly different compared to cyt c_2 [Ox] (138 ± 2pN and 244 ± 2 pN). The interaction frequency saw no statistically significant difference. The large change observed in the cyt c_2 [Ox] state in (C) is merely the result of a large change in one data set, which was thought to be an anomaly. The remaining datasets with this removed are plotted in (D) and (E). Curiously, the ratio between the lower (130pN) and higher (230pN) populations appears to change between the redox states, with the higher population (purported the full ET complex) more prevalent in the cyt c_2 [Ox] state.

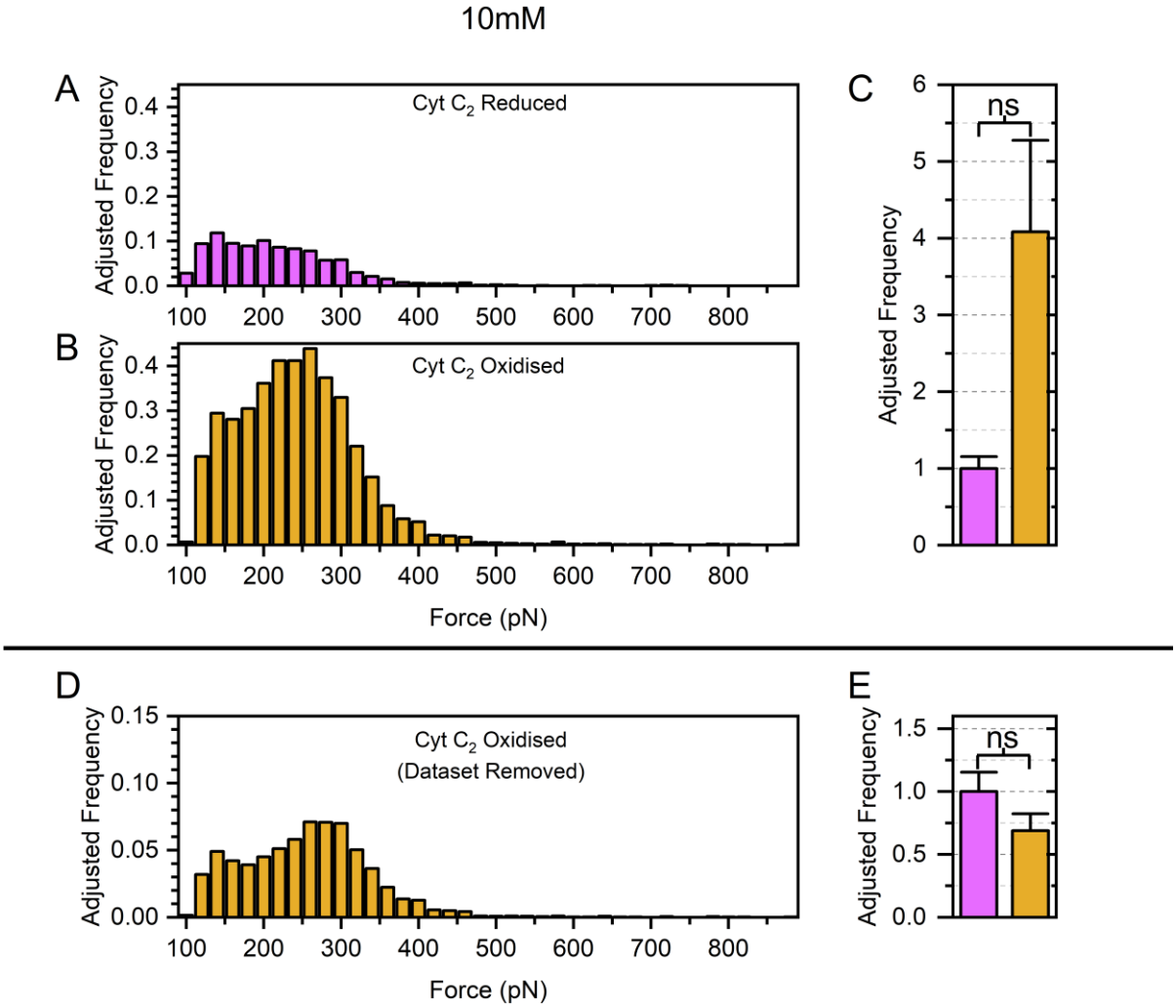

Figure 6.14 Effect of Redox state on RC-LH1 : Cytochrome c_2 interaction at 10mM NaCl

*Distribution of unbinding forces and interaction frequency for cyt c_2 being in different redox states measured at 10mM NaCl. (**A**) Distribution of forces measured for RC-LH1 [^{p}Ox] : cyt c_2 [Red], giving two peaks in force with means of 134 ± 1 pN and 219 ± 4 pN. (**B**) Forces for RC-LH1 [^{p}Ox] : cyt c_2 [Ox], giving two peaks with means of 138 ± 2 pN and 244 ± 2 pN. (**C**) The interaction frequency for the different redox states of cyt c_2. Colours match the scheme shown in (A) and (B). Unpaired t-test analysis returned a p-value of 0.2226, n=13 independent images analysed for each condition. The large difference observed in the interaction frequency is the result of a few data points in which there was a large difference, however this was not found to be statistically significant. This is shown in both (D) and (E), where the data set with the large difference has been removed. Following this removal, the unpaired t-test analysis returned a value of 0.2749, n=8-13 independent images analysed for each condition. Error bars in (C) and (E) are ± the standard error of the mean.*

If the hypothesis presented in section 6.3.6 regarding the two force populations is correct, this would suggest that the cyt c_2 [Ox] has a smaller energy barrier to entering the full ET state than the cyt c_2 [Red], seen by the preference in unbinding forces for the 230pN unbinding force over the 130pN. The results from probing the interaction at 250mM [NaCl] are shown in figure 6.15. In both cases, only single peaks could be found by gaussian fitting, with means of 265 ± 1 pN for cyt c_2 [Red] and 235 ± 1 for cyt c_2 [Ox]. The interaction frequencies did see a statistically significant change, with the cyt c_2 [Ox] state having an over 3.5-fold increase in the number of interactions, this would suggest that the cyt c_2 [Ox] state is binding more frequently.

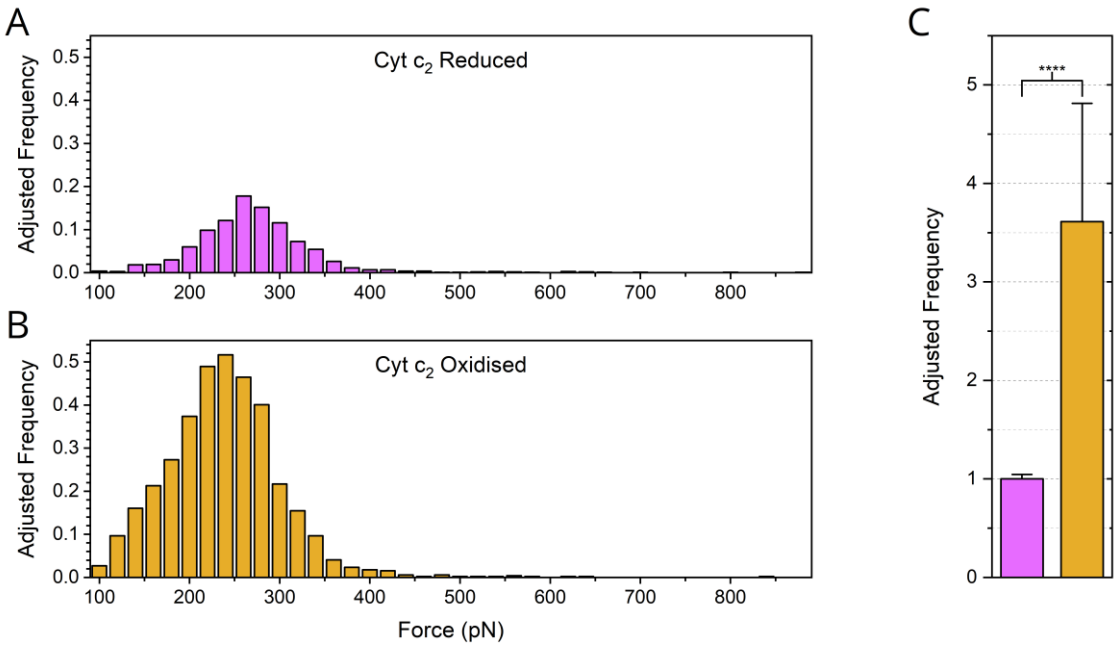

Figure 6.15 Effect of Redox state on RC-LH1 : Cytochrome c_2 interaction at 250mM NaCl

*Distribution of unbinding forces and interaction frequency for cyt c_2 being in different redox states measured at 250mM NaCl. (**A**) Distribution of forces measured for RC-LH1 [^{p}Ox] : cyt c_2 [Red], giving a mean unbinding force of 266 ± 1 pN, and (**B**) for RC-LH1 [^{p}Ox] : cyt c_2 [Ox], giving a mean force of 236 ± 1 pN. (**C**) The interaction frequency for the different redox states of cyt c_2. Unpaired t-test analysis was performed on the adjusted frequencies. Asterisk denotes a p-value of <0.0001. Error bars are ± standard error of the mean, n = 11-13 independent analysed images for each condition. Opposite to figure 6.14, the changes observed between cyt c_2^{6His} [Red] and cyt c_2^{6His} [Ox] are statistically significant in this dataset, with a ca. 3.5-fold increase in the oxidised state being observed over the reduced state.*

6.4 Discussion

To add to the previous experiments on the nature of ET complexes, the RC-LH1 : cyt c_2 interaction was probed via SMFS. *Rba.sphaeroides* was an ideal candidate, as the photosynthetic machinery of the chromatophore is produced in photoheterotrophic, photoautotrophic and heterotrophic anaerobic conditions (Cohen-Bazire et al., 1957), allowing the production of potentially deleterious mutations of the photosynthetic machinery. The RC-LH1 : cyt c_2 interaction has already been extensively studied via traditional bulk phase measurements (Abresch et al., 2008; Devanathan et al., 2004; Gerencsér et al., 1999; Gong et al., 2003; Ke et al., 1970; Moser and Dutton, 1988; Paddock et al., 2005; Tetreault et al., 2001, 2002). In addition, there have also already been explorations of the interaction via SMFS experiments performed by our lab (Vasilev et al., 2013, 2019). Following purifications of both RC^{12His}-LH1 and cyt $c_2{}^{6His}$, their kinetic verifications, and optimisations of the immobilisation chemistry, the effect of light, ionic strength and redox state of cyt c_2 were probed.

6.4.1 SMFS controls performed on the RC-LH1 : Cytochrome c_2 interaction

Initial controls of adding 20 µM cyt $c_2{}^{6His}$ into the imaging buffer only found a 65% decrease in the interaction frequency at both 10 and 250mM [NaCl]. One possible explanation for the discrepancy between expected occupancy and the results seen in figure 6.8/12 is that the transience of the interaction allows for a higher interaction rate than normal with 20 µM cyt $c_2{}^{6His}$ present. With a dwell time of 600µs for the AFM probe and surface, this is comparable to the 300 µs average lifetime of the complex (Overfield et al., 1979). If an untethered cyt c_2 were to dissociate, then given the limited diffusion space for the cyt $c_2{}^{6His}$ tethered to the probe it could have a high probability of binding to the RC^{12His}-LH1 on the surface, thus competing with the high concentration of cyt $c_2{}^{6His}$ in solution. Another explanation is the sequestering of the added cyt $c_2{}^{6His}$ on the surface, becoming chelated to any possible free NTA-Cu^{2+} available on the surface. It is assumed however that all sites on the surface are saturated upon the initial incubation with RC^{12His}-LH during surface preparation, and due to no obvious change in the height image measured upon addition of cyt $c_2{}^{6His}$, this is unlikely to represent a significant enough proportion to explain the results.

6.4.2 Effect of light on the RC-LH1 : Cytochrome c_2 interaction

Contrary to previous experiments on gold immobilised complexes (Vasilev et al., 2013), figure 6.10 found a higher interaction frequency when illumination was absent, compared to when it was present. No feasible explanation could be generated that would reconcile these results with other results seen

in the chapter. Further experiments involving the use of the original SNL probes, along with different light intensities for illumination may offer further insights but have not been performed at this time.

6.4.3 Effect of ionic strength on the interaction

The interaction frequency showed an exponential decay with increasing ionic strength, in agreement with two charged bodies undergoing screening. In contrast to our results in previous chapters, changes in the distribution of unbinding forces were seen with RC-LH1 : cyt c_2. There appeared to be two populations present in the data. At low ionic strengths, the lower force population was more prominent, while at increasing ionic strengths, the distribution of forces appeared to shift, with the higher population becoming the more the prominent at ionic strengths above 150mM. The explanation offered for this result is that the two force populations represent two stages within the binding, the encounter complex and the full ET complex (section 1.2.2). The size of this barrier has been proposed to change with ionic strength, leading to the lower end of the bell-shaped curve seen for the relationship between ET rate and ionic strength. While normally different energetic barriers can be probed by varying the loading rate of a SMFS experiment, this was not possible to attain with the current information on PF-QNM for reasons discussed in chapter 1.4.3. It is believed this offers a feasible explanation for the results observed in the ionic strength dependency.

6.4.4 Mutants being probed by SMFS experiments

Attempts to measure the interaction frequency change between the WT and QE(L264) RC^{12His}-LH1 did not appear to work. While the QE(L264) has shown to exhibit a 30-fold higher affinity, most likely shared between both k_{on} and k_{off}, no effect was observed for the interaction frequency. As discussed in section 6.3.7, previous experiments had focused on observing relative changes in the interaction between a single probe and surface under different conditions. It is likely that, in spite of attempts to adjust for variation between samples, attempting to utilise different protein samples resulted in a variation in the interaction frequency between these that effectively cancelled out. The unbinding force distributions for the WT and QE(L264) however had a curious manifestation, with the measurements at 10mM NaCl only allowing the fitting of a single population for the QE(L264) mutant, and at 250mM NaCl, the lower force population still remained dominant. As the QE(L264) mutation adds an additional negative charge to the binding interface, it might be expected to increase the transition state barrier to the full ET complex, as seen in figure 6.16. This was also previously suggested in Tetreault et al., 2001. As such, the higher population is not prevalent in the QE(L264) force distribution at 10mM NaCl, as fewer interactions can reach the full ET complex compared to the WT at the same ionic strength. In contrast, at 250mM NaCl, the encounter complex is less stabilised, thus

leading to a smaller gap between the encounter complex and the transition state, and as such the higher force population becomes more prevalent as more interacting complexes can reach the full ET stage. This contrasts with the WT RC^{12His}-LH, in which both force populations are present at 10mM NaCl, and at 250mM NaCl only the higher force population is prevalent, suggesting most interacting complexes can enter the full ET state before rupture. Testing of the QE(L264) RC-LH1 : cyt c_2 interaction at a range of ionic strengths could test this theory further.

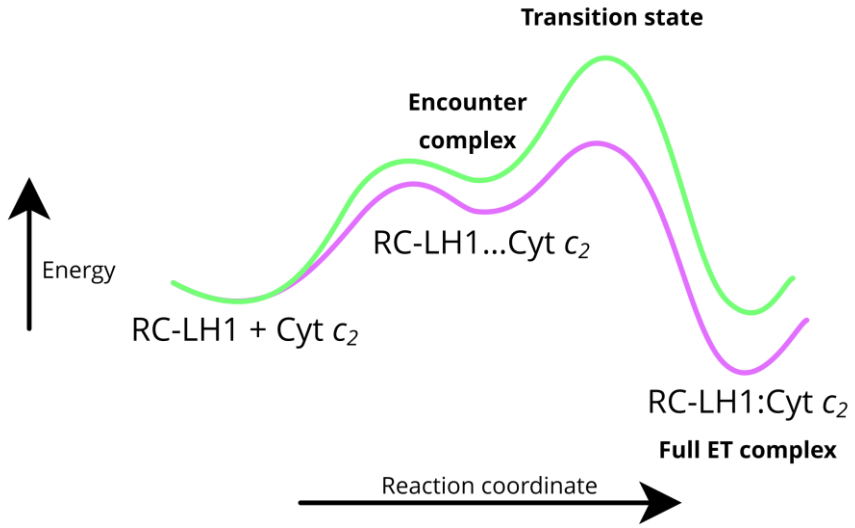

Figure 6.16 Energy diagram for the WT and QE(L264) mutant RC-LH1 interaction with Cytochrome c_2

Free energy diagram for the RC-LH1 : cyt c_2 association process for WT (Purple) and QE(L264) (Green) RC-LH1 at high ionic strengths. Reproduced with permission from American Chemical Society, adapted from Tetreault et al., 2001. The initial, unbound states are arbitrarily set to equal.

6.4.5 Effect of Redox state on the interaction

Whilst the effect of redox state on the interaction has technically been probed previously via changing the illumination, the redox state of cyt c_2 was not changed in the prior experiments (Vasilev et al., 2013, 2019). As shown by the previous experiments, the redox state of the RC-LH1 could not be guaranteed, and as such only the redox state of cyt c_2 was probed.

Comparing the two force populations, both are present in both the oxidised and reduced forms of cyt c_2 at 10mM [NaCl] (Figure 6.14). The ratio between the two appears to shift however, continuing with our theory for the two force populations, cyt c_2 [Ox] appears to favour the full ET complex, whilst the cyt c_2 [Red] appears to favour the encounter complex at 10mM [NaCl]. Comparing these unbinding forces measured at 250mM [NaCl], here only a single population was present in both cyt c_2 redox

states, assumed to be the full ET complex. The differences in the mean unbinding force in each redox state at 250mM [NaCl] were not thought to be significant given the underlying noise level in the experiments. Observing both these results together, it would suggest that the cyt c_2 [Ox] has a lower energy barrier to enter the full ET complex with RC-LH1 than the cyt c_2 [Red]. This would facilitate the higher proportion of events entering the full ET state at the lower ionic strength, whilst at the higher ionic strength the barrier could be lowered in both states so that no observable difference is seen between them. The reason for the higher interaction frequency for cyt c_2 [Ox] compared to cyt c_2 [Red] in 250mM, but not at 10mM [NaCl] is also unknown.

Previous bulk phase kinetics have suggested that 'product inhibition' can occur in the interaction between RC-LH1 and cyt c_2, where the cyt c_2 [Ox] appears to have a higher affinity for RC-LH1 than cyt c_2 [Red] (Gerencsér et al., 1999; Hunter et al., 2008; Moser and Dutton, 1988) and the apparent lower transition state barrier for cyt c_2 [Ox] compared to cyt c_2 [Red] might explain this.

The difference in the interaction frequencies seen at 10 and 250mM [NaCl] could be reconciled with this hypothesis if we assume that cyt c_2 [Ox] can dissociate prior to the interaction being ruptured. If cyt c_2 [Ox] has the proposed lower energetic barrier to the full ET, this may also cause a faster dissociation of the complex, compared to cyt c_2 [Red] which must overcome the comparatively larger barrier. At 10mM, this may result in the higher association of cyt c_2 [Ox] for RC-LH1 being obscured by the faster dissociation, whilst at 250mM [NaCl] the barrier may be lowered enough that the same extent of dissociation is occurring in both reduced and oxidised forms of cyt c_2. This could be probed further by testing the effect of a wider range of ionic strengths on both redox states to observe the effect on the distribution of the two populations, and the interaction frequency.

6.5 Bibliography

Abresch, E.C., Paddock, M.L., Villalobos, M., Chang, C., and Okamura, M.Y. (2008). Interaction between Cytochrome c 2 and the Photosynthetic Reaction Center from Rhodobacter sphaeroides : Role of Interprotein Hydrogen Bonds in Binding and Electron Transfer †. Biochemistry *47*, 13318–13325.

Adams, P.G., Mothersole, D.J., Ng, I.W., Olsen, J.D., and Hunter, C.N. (2011). Monomeric RC–LH1 core complexes retard LH2 assembly and intracytoplasmic membrane formation in PufX-minus mutants of Rhodobacter sphaeroides. Biochim. Biophys. Acta - Bioenerg. *1807*, 1044–1055.

Axelrod, H.L., Feher, G., Allen, J.P., Chirino, a J., Day, M.W., Hsu, B.T., and Rees, D.C. (1994). Crystallization and X-ray structure determination of cytochrome c2 from Rhodobacter sphaeroides in three crystal forms. Acta Crystallogr. D. Biol. Crystallogr. *50*, 596–602.

Axelrod, H.L., Abresch, E.C., Okamura, M.Y., Yeh, A.P., Rees, D.C., and Feher, G. (2002). X-ray structure determination of the cytochrome c2: reaction center electron transfer complex from Rhodobacter sphaeroides. J. Mol. Biol. *319*, 501–515.

Cohen-Bazire, G., Sistrom, W.R., and Stanier, R.Y. (1957). Kinetic studies of pigment synthesis by non-sulfur purple bacteria. J. Cell. Comp. Physiol. *49*, 25–68.

Devanathan, S., Salamon, Z., Tollin, G., Fitch, J., Meyer, T.E., and Cusanovich, M. a (2004). Binding of Oxidized and Reduced Cytochrome c 2 to Photosynthetic Reaction Centers : Plasmon-Waveguide Resonance Spectroscopy. 16405–16415.

Friebe, V.M., Delgado, J.D., Swainsbury, D.J.K., Gruber, J.M., Chanaewa, A., van Grondelle, R., von Hauff, E., Millo, D., Jones, M.R., and Frese, R.N. (2016). Plasmon-Enhanced Photocurrent of Photosynthetic Pigment Proteins on Nanoporous Silver. Adv. Funct. Mater. *26*, 285–292.

Gerencsér, L., Laczkó, G., and Maróti, P. (1999). Unbinding of oxidized cytochrome c from photosynthetic reaction center of Rhodobacter sphaeroides is the bottleneck of fast turnover. Biochemistry *38*, 16866-75.

Gong, X.M., Paddock, M.L., and Okamura, M.Y. (2003). Interactions between Cytochrome c2 and Photosynthetic Reaction Center from Rhodobacter sphaeroides: Changes in Binding Affinity and Electron Transfer Rate Due to Mutation of Interfacial Hydrophobic Residues Are Strongly Correlated. Biochemistry *42*, 14492–14500.

Hunter, N., Daldal, F., Thurnauer, M., and Beatty, T. (2008). The Purple Phototrophic Bacteria.

Johnson, K., and Thomas, W.E. (2018). How do we know when single molecule force spectroscopy really tests single bonds. 2032–2039.

Ke, B., Chaney, T.H., and Reed, D.W. (1970). The electrostatic interaction between the reaction-center bacteriochlorophyll derived from Rhodopseudomonas spheroides and mammalian cytochrome c and its effect on light-activated electron transport. BBA - Bioenerg. *216*, 373–383.

Lee, G.U., Kidwell, D.A., and Colton, R.J. (1994). Sensing Discrete Streptavidin Biotin Interactions With Atomic-Force Microscopy. Langmuir *10*, 354–357.

Moser, C.C., and Dutton, P.L. (1988). Cytochrome c and c2 binding dynamics and electron transfer with photosynthetic reaction center protein and other integral membrane redox proteins. Biochemistry *27*, 2450–2461.

Overfield, R.E., Wraight, C.A., and Devault, D. (1979). Microsecond photooxidation kinetics of cytochrome c2 from Rhodopseudomonas sphaeroides: in vivo and solution studies. FEBS Lett. *105*, 137–142.

Paddock, M.L., Weber, K.H., Chang, C., and Okamura, M.Y. (2005). Interactions between cytochrome c2 and the photosynthetic reaction center from Rhodobacter sphaeroides: the cation-pi interaction. Biochemistry *44*, 9619–9625.

Qian, P., Hunter, C.N., and Bullough, P.A. (2005). The 8.5 Å projection structure of the core RC-LH1-PufX dimer of Rhodobacter sphaeroides. J. Mol. Biol. *349*, 948–960.

Qian, P., Papiz., M.Z., Jackson, P.J., Brindley, A.A., Ng, I., Olsen, J.D., Dickman, M.J., Bullough, P.A., and Hunter, C.N. (2013). Three-Dimensional Structure of the Rhodobacter sphaeroides RC-LH1-PufX Complex: Dimerization and Quinone Channels Promoted by PufX. Biochem. *52*, 7575–7585.

Tetreault, M., Rongey, S.H., Feher, G., and Okamura, M.Y. (2001). Interaction between cytochrome c2 and the photosynthetic reaction center from Rhodobacter sphaeroides: effects of charge-modifying mutations on binding and electron transfer. Biochemistry *40*, 8452–8462.

Tetreault, M., Cusanovich, M., Meyer, T., Axelrod, H., and Okamura, M.Y. (2002). Double Mutant Studies Identify Electrostatic Interactions That Are Important for Docking Cytochrome c_2 onto the Bacterial Reaction Center. Biochemistry *41*, 5807–5815.

Vasilev, C., Brindley, A. a, Olsen, J.D., Saer, R.G., Beatty, J.T., and Hunter, C.N. (2013). Nano-mechanical mapping of the interactions between surface-bound RC-LH1-PufX core complexes and cytochrome c 2 attached to an AFM probe. Photosynth. Res. *120*, 169–180.

Vasilev, C., Mayneord, G.E., Brindley, A.A., Johnson, M.P., and Hunter, C.N. (2019). Dissecting the cytochrome c 2 -reaction centre interaction in bacterial photosynthesis using single molecule force spectroscopy. Biochem. J. *476*, 2173–2190.

7. Concluding remarks and future work

The work described in this thesis first sought to establish the optimum conditions for studying biological ET complexes using the PF-QNM method for SMFS. In chapter 3, several different methods of attaching the proteins to the AFM probe and silicon surface were tested, and an optimal method selected that ensured the complexes were sufficiently well distributed for reliable statistics to be obtained. In chapter 4, the effect of ionic strength and redox state of the participants involved in the spinach cytb_6f : Pc ET complex were explored using the methodology developed in Chapter 3. The results provided evidence that the binding frequency of Pc to cytb_6f was under redox state control, while the unbinding force was not. A similar pattern of redox selectivity was observed for the spinach PSI : Pc ET complex studied in Chapter 5, suggesting that faster turnover is ensured by control at the level of association (analogous to k_{on}) rather than dissociation (analogous to k_{off}). Finally, to utilise the simple recombinant genetics of bacterial systems, the attachment chemistry established in Chapter 3 was adapted for poly-histidine tagged RC-LH1 and cyt c_2 complexes from *Rba.sphaeroides*, and the effect of mutation on the binding interface was also probed. Unlike the spinach complexes studied in Chapters 4 and 5 the unbinding force populations in RC-LH1 : cyt c_2 ET complex were strongly influenced by changing the ionic strength of the reaction medium. These results suggest that the PF-QNM SMFS technique has the ability under certain circumstances to distinguish between the encounter complex and the full ET complex.

The techniques used here had several drawbacks that became apparent during the course of the experiments. The most obvious was the presence of the AFM laser for the detection of the cantilever deflection. The 680nm laser was found to excite both PSI and RC-LH1 on the surface, obstructing studies into affinity changes under different photo-oxidation states. The use of higher wavelength lasers could be a possible solution to this in future work, as neither complex should absorb significantly above 1000nm. Another limiting factor identified was the noise level present in the PF-QNM FdC's, this was particularly an issue for studying the PSI : Pc ET complex in chapter 5. The use of higher quality cantilevers, with higher resonant frequencies could resolve this issue in the future. Finally, and undoubtedly the largest issue for the experiments was the lack of transparency from the AFM manufacturer Bruker on the real-time processing of FdC's for PF-QNM mode. While this method provided the fast motion required to perform these experiments on transient complexes, the obscured real-time corrections applied in this method, taking multiple 'ramp events' with the surface to produce a single FdC meant that the loading rate could not be accurately obtained from the data. As an alternative, the use of Quantitative Imaging (QI™) mode from JPK™ could offer a solution to this, as a single FdC is generated from a single interaction with the surface at each pixel, and more recent

developments in the technique now allow imaging speeds equivalent to PF-QNM. Utilising the QI technique, it should be possible to quantify the forces that sustain biological ET complexes in greater detail by varying the repetition rate for ramping events, thus changing the loading rate of the experiment. In principle this would provide a more accurate measure of the loading rate, allowing the dynamic force spectrum to be determined for each ET complex studied.

In order to circumvent issues associated with the orientation of complexes on the surface, mutants of Pc, PSI and cytb_6f complexes with site-specific tags similar to those utilised for RC-LH1 and cyt c_2 in Chapter 6 could be developed. A further optimisation would be to ensure the complexes are fixed in a more native membrane environment such as in proteoliposomes. Unfortunately, efforts to follow this approach in chapter 3 failed but given more time this may prove fruitful, though the incorporation of complexes into these membranes would still be random and thus orientation would remain an issue. Ideally, using recombinant genetics to generate thylakoids or chromatophores deficient in the alternative binding partner (e.g. for the study of RC-LH1, they would be deficient in cyt bc_1), would allow simple isolation of these membranes, and probing via the soluble binding partner attached to the probe by a specific site. Since both *Rba.sphaeroides* and *C.reinhardtii* are capable of producing photosynthetic membranes with deficiencies in their photosynthetic apparatus so long as alternative sources of energy are provided, this may offer a useful next stage for extending and validating these experiments. In addition, the use of recombinant genetics to probe different isoforms of the proteins involved under different conditions could elucidate the roles for these further, not only for Pc but also Fd in its interaction with PSI and potentially cytb_6f in CEF.

Several themes have become apparent in these studies. Firstly, the plant complexes display a clear redox selectivity for the pre-ET state, with Pc having a higher affinity for cytb_6f when oxidised, and for PSI when reduced. Such redox selectivity of association ensures that non-productive encounters are minimised, maximising the turnover of the photosynthetic electron transport chain. This same effect is not present in the RC-LH1 : cyt c_2 system however, where the post-ET state appears to be favoured. While this matches bulk phase kinetic studies on the RC-LH1 : cyt c_2 interaction, its purpose in native chromatophores has not been explained. Given the small diffusional space of the chromatophore, this may simply reflect the lack of selective pressure for the binding interface to avoid product inhibition, when diffusion between complexes within this small area is already fast and other components of the electron flow are rate limiting for the overall turnover of the chromatophore. The larger space of the thylakoid lumen in plants however may impose that Pc selectively associates with each of its binding partners in the correct pre-ET state, otherwise the long 250nm diffusion distance of Pc from cytb_6f in the grana stacked regions to PSI in the stromal lamellae regions may become limiting.

While the transition from the encounter complex to the full ET complex may broadly reflect a rate limiting step in the association, an important consideration is the native ionic strength in which these complexes act. Previously ionic strengths of ca. 100-200mM have been suggested for both the chromatophores and the thylakoid membranes. As such, while it would appear that the association of these complexes is far from optimum at this ionic strength, the encounter complex will generally not become rate limiting in these interactions.

Overall, this work on utilising PF-QNM for fast-SMFS is still in relatively early stages, and whilst these interactions have been initially explored, further supplementary work involving mutants of all the participants' binding interfaces could help better characterise both the interactions themselves, and the properties observed by SMFS.

8. Appendix

8.1 MATLAB SMFS analysis script

```
%                        PROGRAM TO ANALYSE PFQNM FILES FOR FORCES
%                                        INPUTS:
%                                   RUN IN MATLAB 64 BIT
%Code from Guy E Mayneord
%If used in publishing data please give acknowledgement to G.E.Mayneord.
%================================================================================
=======%
clear variables;
close all;
warning('off','all');
% Check screen size for figures later on.
figure_size=get(0, 'screensize');
% Ask if it is a new analysis, or continuing from a previous one (See function at
bottom)
continuation_or_new=initial_asking_for_continuation(figure_size);
% If it is a new analysis
if continuation_or_new == 1
    % GUI element to allow selection of a directory where the data is
    file_locations_name = uigetdir();
    % Get only .pfc files from this directory
    file_locations = dir(fullfile(file_locations_name, '*.pfc'));
    % Popup for entering the parameters of the analysis
    [tip_deflection_sensitivity, tip_spring_constant, minimum_force_parameter,
minimum_seperation_distance, maxmimum_seperation_distance,
date_of_measurements]=input_parameters_ui(file_locations(1).name);
    %Preallocation of the data recorded.
    Writing_info=cell(5000,7);
    Writing_info_counter=0;
    %Self contained section just to make a new directory for the interesting
    %curves, 1 directory up from the data folder

Interesting_curve_directory=file_locations_name(1:(max(strfind(file_locations_name,
'\'))));
    Interesting_curve_directory=strcat(Interesting_curve_directory, 'Interesting
curve directory\');
    mkdir(Interesting_curve_directory);
    %These parameters are set to 1 here, however if the analysis is
    %continuing from a previous session that was quit before ending, then
    %these are assigned below in the other if clause ('Continuation code'), below.
    starting_image_point=1;
    previous_curve_number_in_file=1;
    %Save these parameters before we start, so that if we have to use the
    %continuation code then it has the same order of the files in particular.
    save('001_Tip_parameters_saved', 'file_locations_name',
'tip_deflection_sensitivity', 'tip_spring_constant', 'minimum_force_parameter',
'minimum_seperation_distance', 'maxmimum_seperation_distance',
'date_of_measurements');
    save('004_File_directory_list', 'file_locations');
    %Pause to allow the saving of these files. Without this it can
```

```
    %sometimes run into issues
    pause(0);
%If its continuing from a previous session:
elseif continuation_or_new ==0
    %Load in other parameters from before stopping
    load('001_Tip_parameters_saved.mat');
    load('002_Current_state.mat');
    load('003_Data_backup.mat');
    load('004_File_directory_list');
    %Method for chosing between home and work etc. and then save them
    %again.
    file_locations_name = files_location_choice(file_locations_name, figure_size);
    save('001_Tip_parameters_saved', 'file_locations_name',
'tip_deflection_sensitivity', 'tip_spring_constant', 'minimum_force_parameter',
'minimum_seperation_distance', 'maxmimum_seperation_distance',
'date_of_measurements');
    pause(0);
    %Perform the preallocation
    Writing_info=cell(5000,7);
    %Write in the values from before
    Writing_info(1:Writing_info_counter,:)=Writing_info_to_save;
    clear Writing_info_to_save
    starting_image_point=Current_state(1);
    previous_curve_number_in_file=Current_state(2);
    %Get the interesting curve directory name again, but dont need to write the
directory.

Interesting_curve_directory=file_locations_name(1:(max(strfind(file_locations_name,
'\'))));
    Interesting_curve_directory=strcat(Interesting_curve_directory, 'Interesting
curve directory\');
end
clear continuation_or_new;
pause(0)

%Import Bruker's tools to open the AFM files.
import NSMatlabUtilities.*
NSMU=NSMatlabUtilities();
%Calculate the minimum force value in raw deflection data (value for searching in
the raw data).
Deflection_value_search=((minimum_force_parameter/tip_spring_constant)/tip_deflecti
on_sensitivity)/-1000;
%Correction value is the reverse of this, for converting the raw deflection
%data to force values.
correction_value=1000*tip_spring_constant*tip_deflection_sensitivity;

%Correction for issue over 4k/1080p font sizes.
if figure_size(4) > 1500
    fontsize_for_checkbox=10;
else
    fontsize_for_checkbox = 8;
end

%Set visibility of the approach curve off
approach_curve_visibility='on';
```

```
%Start a loop, to go through each image.
for current_file_probe = starting_image_point:length(file_locations)
    %Pull out the file name
    filename=file_locations(current_file_probe).name;
    disp(' ');
    disp('
++++++++++++++++++++++++++++++++++++++++++++++++++++++++++++++++++++++++++++++++');

disp('==========================================================================
==================================');
    disp('                                                  New file!');
    disp(['                                  ' filename]);

disp('==========================================================================
==================================');
    disp('
++++++++++++++++++++++++++++++++++++++++++++++++++++++++++++++++++++++++++++++++');
    disp(' ');
    directory_and_filename=char(strcat(file_locations_name, '\', filename));
    %Open up the file
    NSMU.Open(directory_and_filename);
    %Find number of pixels per line
    [size_of_image_pix, ~] = NSMU.GetForceVolumeScanLinePixels();
    %Number of force curves in image
    NumberOfCurves = NSMU.GetNumberOfForceCurves();
    %In the analysis window, show the height image, and change the force
    %curve being shown, and the location of that force curve on the image.
    Main_figure=figure('Name','Analysis window','NumberTitle','off', 'MenuBar',
'none', 'ToolBar', 'none', 'units','normalized', 'Position', [0 0 1 1 ],  'Color',
'w');
    %Open the height image data.
    [height_image_data, ~, ~] = NSMU.GetPeakForceCaptureImageData(NSMU.METRIC);
    subplot(2,3,5)
    image(flipud(height_image_data),'CDataMapping','scaled');
    axes_for_plot=gca;
    %Set z limits for the height.
    axes_for_plot.CLim=[-7, 12];
    set(gca,'YDir','normal');
    axis('tight', 'square');
    set(gca,'XTick',[], 'YTick', []);
    colormap('default');
    %Display the filename above the image
    title((regexprep(filename, '_', ' ')), 'FontSize', 18, 'FontWeight', 'bold');
    xlabel(NSMU.GetScanSizeLabel());
    hold on;

Close_down_button=uicontrol('Parent',Main_figure,'Style','pushbutton','Callback',
{@close_figure_down, figure_size}, 'String','Quit
analysis','Units','normalized','Position',[0.25 0.26 0.06 0.03],'Visible','on',
'FontSize', 10, 'FontWeight', 'bold');
    uipanel('Title','Last saved force curve','Position',[0.70 0.25 0.2 0.1],
'FontSize', 12, 'Background', 'w');
    uipanel('Title','Current Progress','Position',[0.70 0.38 0.2 0.07], 'FontSize',
12, 'Background', 'w');
```

```
    uicontrol('style', 'text', 'units', 'normalized', 'position', [0.75 0.4 0.1
0.02], 'string', strcat(num2str(current_file_probe), '/',
num2str(length(file_locations))), 'FontSize', 15, 'FontWeight', 'bold',
'Background', 'w');
    please_wait_sign=uicontrol('style', 'text', 'units', 'pix', 'position',
[((figure_size(3)/2)-100) ((figure_size(4)*0.75)-13) 200 26], 'string', 'Please
Wait...', 'FontSize', 15, 'BackgroundColor',[1 1 1]);
    %Check if this is the first time we are going through the list (if it
    %is, we need so start where we left off) and if it is not then we need
    %to start from 1 again.
    if current_file_probe == starting_image_point
        curve_number_for_start=previous_curve_number_in_file;
    %If we've moved on from the image that we stopped on.
    elseif current_file_probe ~= starting_image_point
        curve_number_for_start = 1;
    end
    %Section to do calculations for the whole image to save time. Take them
    %from first curve
    [~, xRetrace, ~, ~, ~, ~] = NSMU.CreatePeakForceForceCurveZplot(1, NSMU.METRIC,
1);
    %This will be the same for the entire image(change of probably only 1
    %data point), so only calculate it once per image. Find the first time
    %it goes above the minimum seperation distance in the list, and the
    %final time it is below (effectively pull out the bounds that we should
    %search in).
    array_location_lower=find(xRetrace>minimum_seperation_distance, 1);
    array_location_higher=find(xRetrace<maxmimum_seperation_distance, 1, 'Last');
    Current_FC_on_screen=uicontrol('style', 'text', 'units', 'normalized',
'position', [0.3 0.93 0.4 0.05], 'string', strcat('Current curve: 0/',
num2str(NumberOfCurves)), 'FontSize', 15, 'FontWeight', 'bold', 'Background', 'w');
    for current_curve_number = (curve_number_for_start : NumberOfCurves)
        %Open FC data
        [xTrace, xRetrace, yTrace, yRetrace, ~, ~] =
NSMU.CreatePeakForceForceCurveZplot(current_curve_number, NSMU.METRIC, 1);
        %Take the 10-60% back region (40-90% from the front)
        %Use the approach curve for fitting, more consistent.
        %Baseline
        Fit_for_scanning_region=polyfit((xTrace((round((length(xTrace))-
(6*(length(xTrace)/10)))):(9*(length(xTrace)/10)))),(yTrace((round((length(xTrace))
-(6*(length(xTrace)/10)))):(9*(length(yTrace)/10)))),1);

Baseline_fitting_function=(Fit_for_scanning_region(1).*xTrace)+Fit_for_scanning_reg
ion(2);
        %Adjust the data for the baseline.
        yRetrace=(yRetrace-Baseline_fitting_function);
        yTrace=(yTrace-Baseline_fitting_function);
        %So now they have the corrected data, find the minimum from the
        %entire set, and see if it is above the minimum
        if (min(yRetrace))<Deflection_value_search &&
(yRetrace(1)*correction_value)>30
            %If it is more than the lowest searching value, then we
            %progress further. Pull out the data in the searching areas.
            %Here we search for peaks in the 'scanning region' we set out
            %in the initial parameters, then search for which are over the
            %minuimum force value, if any peaks flag up in this region, we
```

```
            %will shown the FC.

trough_searching=findpeaks(yRetrace(array_location_lower:array_location_higher)*-1,
'MinPeakHeight', Deflection_value_search*-1);
            %Check if the trough_searching list is empty, if it is then
            %theres nothing, if it isnt empty then theres values here.
            if ~isempty(trough_searching)
                %Save current place in analysis.
                background_saving_parameters(Writing_info, Writing_info_counter,
current_file_probe, current_curve_number);
                %Correct signal data to actual force
                yRetrace=yRetrace*correction_value;
                yTrace=yTrace*correction_value;
                delete(Current_FC_on_screen);
                Current_FC_on_screen=uicontrol('style', 'text', 'units',
'normalized', 'position', [0.3 0.93 0.4 0.05], 'string', strcat('Current curve: ',
num2str(current_curve_number), '/', num2str(NumberOfCurves)), 'FontSize', 20,
'FontWeight', 'bold', 'Background', 'w');
                delete(please_wait_sign);
                subplot(2,3,[1 3]);
                %Plot the approach and retract curves, with the option to
                %hide the approach curve.
                retract_curve_plotted=plot(xRetrace, yRetrace, 'b', 'LineWidth',
3);
                hold on;
                approach_curve_plotted=plot(xTrace, yTrace,'r', 'LineWidth', 3);
                set(approach_curve_plotted,'visible', approach_curve_visibility);
                %Display the location in the data set for this image.
                set(gca,'XTick',(-50: 10:(max(xRetrace)+10)), 'XLim', ([0 inf]));
                xlabel('Piezo movement (nm)', 'FontWeight', 'bold');
                ylabel('Force (pN)', 'FontWeight', 'bold');
                set(gca, 'FontSize', 18);
                dcm_obj=datacursormode;

set(dcm_obj,'DisplayStyle','datatip','SnapToDataVertex','off','Enable','on','Update
Fcn',@cursor_custom);
                uicontrol('Parent',Main_figure,'Style','pushbutton','Callback',
{@button_save, Interesting_curve_directory, filename, current_curve_number,
xRetrace, yRetrace, xTrace, yTrace}, 'String','Save Force
curve','Units','normalized','Position',[0.92 0.725 0.07 0.05],'Visible','on',
'FontSize', 10, 'FontWeight', 'bold');
                %Checkbox for approach curve
                if strcmp(approach_curve_visibility, 'on') == 1
                    checkmark_value=1;
                elseif strcmp(approach_curve_visibility, 'off') == 1
                    checkmark_value=0;
                end
                approach_figure_checkbox =
uicontrol('style','check','Units','normalized','position',[0.92 0.67 0.075
0.02],'string','Show Approach curve','Value', checkmark_value,'BackgroundColor',[1
1 1], 'FontSize', fontsize_for_checkbox, 'FontWeight',
'bold','callback',{@change_approach_visibility, approach_curve_plotted});
                %Select height image figure, and plot the location of this
adhesion.
                subplot(2,3,5);
```

```
                %Quick calculation for the x y positions
                x_location_in_image=mod(current_curve_number, size_of_image_pix);
                y_location_in_image=fix(current_curve_number/size_of_image_pix);
                current_pixel_position_plotted=plot(x_location_in_image,
y_location_in_image, 'o', 'MarkerSize', 6.5 ,'MarkerEdgeColor','r',
'MarkerFaceColor', 'r');
                currkey=0;
                % do not move on until enter key is pressed
                while currkey~=1
                    pause; % wait for a keypress
                    currkey=get(gcf,'CurrentKey');
                    if strcmp(currkey, 'return')
                        currkey=1;
                    else
                        currkey=0;
                    end
                end
                please_wait_sign=uicontrol('style', 'text', 'units', 'pix',
'position', [((figure_size(3)/2)-60) ((figure_size(4)*0.75)-13) 200 26], 'string',
'Please Wait...', 'FontSize', 15, 'BackgroundColor',[1 1 1]);
                %When we exit this, find out if it was visible, and take this
                %value into the next one (means it persists between fcs)
                approach_curve_visibility=get(approach_curve_plotted,'visible');
                c_info={};
                try %#ok<TRYNC>
                    c_info=getCursorInfo(dcm_obj);
                end
                %Remove the force curve shown previously now, and remove
                %the location for it on the height image.
                delete(retract_curve_plotted);
                delete(approach_curve_plotted);
                delete(current_pixel_position_plotted);
                %if c_info is not empty, then something was selected
                if ~isempty(c_info)
                    all_points_selected_x={};
                    all_points_selected_y={};
                    for each_point_selected = 1:length(c_info)
                        x_value_selected=c_info(each_point_selected).Position(1);
                        y_value_selected=c_info(each_point_selected).Position(2);
                        all_points_selected_x{end+1}=x_value_selected;
                        all_points_selected_y{end+1}=y_value_selected;
                    end
                    %Also just add this to adjust for if 3 points are
                    %accidentally selected, only take the first two.

length_of_points_selected=floor(length(all_points_selected_x)/2);
                    %If only 1 point is selected, this is true and thus just
                    %extract them out. (floor 1/2 = 0)
                    if length_of_points_selected == 0
                        Writing_info_counter=Writing_info_counter+1;
                        x_value_selected=all_points_selected_x{1};
                        y_value_selected=all_points_selected_y{1};
                        Writing_info=data_appending_to_list(x_value_selected,
y_value_selected, current_curve_number, x_location_in_image, y_location_in_image,
current_file_probe, filename, Writing_info_counter, Writing_info);
```

```
                    %If it is larger than 0, then at least 2 points were
                    %selected (selected and baseline for each 2 selected).
                    elseif length_of_points_selected > 0
                        for each_selected_point_number =
1:length_of_points_selected
                            Writing_info_counter=Writing_info_counter+1;
                            %if there is multiple clicks, the seperation
                            %distance in this wont be changed, is still true
                            %just not the correct baseline, so only change y
                            %value.

x_value_selected=all_points_selected_x{(each_selected_point_number*2)-1};

y_value_selected=all_points_selected_y{(each_selected_point_number*2)-1} -
all_points_selected_x{(each_selected_point_number*2)};
                            Writing_info=data_appending_to_list(x_value_selected,
y_value_selected, current_curve_number, x_location_in_image, y_location_in_image,
current_file_probe, filename, Writing_info_counter, Writing_info);
                        end
                    end
                else
                    %If nothing is selected
                    pause(0);
                end
            end
        end
    end
    NSMU.Close();
    %Close down the entire figure
    close(Main_figure);
end

analysis_program_filename=strcat('Analysed by: ', convertCharsToStrings(mfilename),
',\n');
Writing_info=Writing_info(1:Writing_info_counter, :);
size_of_writing=size(Writing_info);
size_of_writing=size_of_writing(1);

%Initially save the parameters that are saved as mat files
parameter_folder=strcat(file_locations_name, '\Parameters saved for back up');
mkdir(parameter_folder);
save((strcat(parameter_folder, '\Total data from analysis')), 'Writing_info');
save((strcat(parameter_folder, '\Saved analysis parameters')),
'file_locations_name', 'tip_deflection_sensitivity', 'tip_spring_constant',
'minimum_force_parameter', 'minimum_seperation_distance',
'maxmimum_seperation_distance', 'date_of_measurements');

output_location=strcat(file_locations_name, '\', date_of_measurements, ' Total
force and seperation data for analysis.csv');
fid=fopen(output_location,'w');
fprintf(fid,[analysis_program_filename]);
fprintf(fid,['Output from analysis program - all data' '\n']);
fprintf(fid,[' ' '\n']);
fprintf(fid,['Force of adhesion (pN),' 'Seperation distance (nm), \n']);
```

```
for current_writing_data = (1:size_of_writing)
    Total_information=Writing_info(current_writing_data,:);
    fprintf(fid, [char(Total_information{3}) ',' char(Total_information{4}) '\n']);
end
fclose(fid);

%Now sort the data after printing it all
final_image_analysed=Writing_info{(size_of_writing), 1};
final_image_analysed=str2num(final_image_analysed);
Writing_sorted_data={};
Collated_adhesion_numbers={};
%loop through all possible file allocations
for j = 1:final_image_analysed
    %loop through all the files
    current_image_list={};
    for i = 1:size_of_writing
        if str2num(Writing_info{i, 1}) == j %#ok<*ST2NM>
            current_image_list(end+1)={Writing_info(i,:)};
        end
    Writing_sorted_data(j)={current_image_list}; %#ok<*SAGROW>
    end
end

output_location=strcat(file_locations_name, '\', date_of_measurements, ' Output
from analysis program.csv');
fid=fopen(output_location,'w');
fprintf(fid,[analysis_program_filename]);
fprintf(fid,['Output from analysis program' '\n']);
fprintf(fid,[' ' '\n']);
Tip_parameters_d=num2str(tip_deflection_sensitivity);
Tip_parameters_s=num2str(tip_spring_constant);

min_seperation_distance_s=num2str(minimum_seperation_distance);
max_seperation_distance_s=num2str(maxmimum_seperation_distance);
minimum_force_parameter_s=num2str(minimum_force_parameter);

fprintf(fid,['Tip spring constant:' '\n']);
fprintf(fid,[Tip_parameters_s 'N/m', '\n']);
fprintf(fid,[' ' '\n']);
fprintf(fid,['Tip deflection sensitivity:' '\n']);
fprintf(fid,[Tip_parameters_d 'nm/v', '\n']);
fprintf(fid,[' ' '\n']);
fprintf(fid,['Minimum force parameter:' '\n']);
fprintf(fid,[minimum_force_parameter_s 'pN', '\n']);
fprintf(fid,[' ' '\n']);
fprintf(fid,['Minimum seperation distance parameter:' '\n']);
fprintf(fid,[min_seperation_distance_s 'nm' '\n']);
fprintf(fid,[' ' '\n']);
fprintf(fid,['Maximum seperation distance parameter:', '\n']);
fprintf(fid,[max_seperation_distance_s 'nm' '\n']);
fprintf(fid,[' ' '\n']);

collated_writing={};

for element_1 = (1:length(Writing_sorted_data))
```

```
    %Pulls out the elements list
    image_list=Writing_sorted_data{element_1};
    image_name=image_list{1};
    image_name=(image_name{2});
    fprintf(fid,['Source image:' ',' char(image_name) '\n']);
    fprintf(fid,['Force (pN),' 'Seperation distance (nm),' 'Pixel location number,'
'X location of pixel,' 'Y location of pixel,' '\n']);
    for element_2 = 1:length(image_list)
        %Pulls out the specific data point (adhesion) in an image
        specific_datapoint_information=image_list{element_2};
        file_name=specific_datapoint_information{2};
        adhesion_force=num2str(specific_datapoint_information{3});
        seperation_distance=num2str(specific_datapoint_information{4});
        pixel_location_in_image=num2str(specific_datapoint_information{5});
        x_axis_location=num2str(specific_datapoint_information{6});
        y_axis_location=num2str(specific_datapoint_information{7});
        %Now need to write this information
        fprintf(fid,[adhesion_force ',' seperation_distance ','
pixel_location_in_image ',' x_axis_location ',' y_axis_location '\n']);
    end
    collated_temp={image_name; num2str(element_2)};
    fprintf(fid,[char(image_name) '\n']);
    fprintf(fid,['End' ',' 'End' '\n']);
    fprintf(fid,['Interaction count:' '\n']);
    fprintf(fid,[num2str(element_2) '\n']);
    fprintf(fid,[' ' '\n']);
    fprintf(fid,[' ' '\n']);
    collated_writing(element_1)={collated_temp};
end
fclose(fid);

output_location=strcat(file_locations_name, '\', date_of_measurements, ' Adhesions
per image output.csv');
fid=fopen(output_location,'w');
fprintf(fid,[analysis_program_filename]);
fprintf(fid,['Collated adhesion data from images:' '\n']);
fprintf(fid,['\n']); %#ok<*NBRAK>
fprintf(fid,['\n']);

fprintf(fid,[',' 'Image name' ',' 'Adhesion count' '\n']);
%This was changed here so that the adhesion count was now adhesion
%count_out, if this stops it working go back.
for adhesion_count = (1:length(collated_writing))
    writing_dataset=collated_writing{adhesion_count};
    file_name_dataset=writing_dataset{1};
    adhesion_count_out=writing_dataset{2};
    fprintf(fid,[',' char(file_name_dataset) ',' char(adhesion_count_out) '\n']);
end
fclose(fid);

% Section for sorting out the data by condition
file_name_for_sorting=Writing_info{1,2};
file_name_for_sorting=strsplit(file_name_for_sorting, '.');
file_name_for_sorting=file_name_for_sorting(1);
```

```
current_file_name=file_name_for_sorting;

output_location=strcat(file_locations_name, '\', date_of_measurements, ' Forces and
seperation distance for conditions.csv');
fid=fopen(output_location,'w');
fprintf(fid,[analysis_program_filename]);
fprintf(fid,['Collated adhesion data for each condition:' '\n']);
fprintf(fid,['\n']);
fprintf(fid,['\n']);
fprintf(fid,[char(current_file_name)]);
fprintf(fid,['\n']);
fprintf(fid,['Force (pN)' ',' 'Seperation Distance (nm)' '\n']);

%Convert this back to string as otherwise the string comparison doesnt work
%and thus we never write
current_file_name=file_name_for_sorting;

for counting_number = drange(1:size_of_writing)
    file_name_for_sorting=Writing_info(counting_number,2);
    file_name_for_sorting=file_name_for_sorting{1};
    %Knocks the end bit off, which would be eg .003.pfc
    file_name_for_sorting=strsplit(file_name_for_sorting, '.');
    file_name_for_sorting=file_name_for_sorting(1);
    %If theyre the same
    if strcmp(current_file_name,file_name_for_sorting) == 1
        Total_information=Writing_info(counting_number,:);
        fprintf(fid, [(Total_information{3}) ',' (Total_information{4}) '\n']);
    %But if weve found a new file name, so need to set it up, AND write the
    %first value, which has triggered this recognition.
    elseif strcmp(current_file_name,file_name_for_sorting) == 0
        %change to new value
        fprintf(fid,['End' ',' 'End' '\n']);
        fprintf(fid, [char(current_file_name)]);
        current_file_name=file_name_for_sorting;
        fprintf(fid,['\n']);
        fprintf(fid,['\n']);
        fprintf(fid,['\n']);
        fprintf(fid,['\n']);
        fprintf(fid,['\n']);
        fprintf(fid,[char(current_file_name)]);
        fprintf(fid,['\n']);
        fprintf(fid,['Force (pN)' ',' 'Seperation Distance (nm)' '\n']);
        Total_information=Writing_info(counting_number,:);
        fprintf(fid, [(Total_information{3}) ',' (Total_information{4}) '\n']);
    end
end
fprintf(fid,['End' ',' 'End' '\n']);
fprintf(fid, [char(current_file_name)]);
fclose(fid);
fclose('all');

disp(' ');
disp('================================');
disp('Analysis complete, Outputs saved');
disp('================================');
```

```
delete 001_Tip_parameters_saved.mat;
delete 002_Current_state.mat;
delete 003_Data_backup.mat;
delete 004_File_directory_list.mat;

function button_save(input_ui_var,~, Interesting_curve_directory, filename,
current_curve_number, xRetrace, yRetrace, xTrace, yTrace)
    Int_curve_save=strcat(Interesting_curve_directory, '\' , filename, '-',
num2str(current_curve_number), '.csv');
    fid=fopen(Int_curve_save,'w');
    fprintf(fid,['Retract Curve' ',' ',' 'Approach Curve' '\n']);
    fprintf(fid,['Distance' ',' 'Force' ',' 'Distance' ',' 'Force' '\n']);
    for data_point_in_save = 1:length(xRetrace)
        fprintf(fid,[num2str(xRetrace(data_point_in_save)) ','
num2str(yRetrace(data_point_in_save)) ',' num2str(xTrace(data_point_in_save)) ','
num2str(yTrace(data_point_in_save)) '\n']);
    end
    fclose(fid);
    output_for_saving_file=['Force Curve ', num2str(current_curve_number), ' - ',
filename, ' saved to interesting curves folder'];
    uicontrol('style', 'text', 'units', 'normalized', 'position', [0.71 0.26 0.18
0.045], 'string', output_for_saving_file, 'FontSize', 10, 'FontWeight', 'bold',
'Background', 'w');
    set(input_ui_var,'str','SAVED','backg', 'g');
end

function Writing_info = data_appending_to_list(x_value_selected, y_value_selected,
current_curve_number, x_location_in_image, y_location_in_image, current_file_probe,
filename, Writing_info_counter, Writing_info)
    source_image_number=num2str(current_file_probe);
    source_image_w=string(filename);
    force_of_adhesion_w=num2str(abs(y_value_selected));
    seperation_distance_w=num2str(abs(x_value_selected));
    pixel_location_w=num2str(current_curve_number+1);
    x_location_w=num2str(x_location_in_image);
    y_location_w=num2str(y_location_in_image);
    Writing_info((Writing_info_counter),:)={source_image_number; source_image_w;
force_of_adhesion_w; seperation_distance_w; pixel_location_w; x_location_w;
y_location_w};
    pause(0);
end


function [deflection_sensitivity, spring_constant, minimum_force_parameter,
minimum_seperation_distance, maximum_seperation_distance, text_to_add] =
input_parameters_ui(first_file_name)
size_for_ui=get(0, 'screensize');
S.fh = figure('units','pixels',...
              'position',[((size_for_ui(3)/2)-300) ((size_for_ui(4)/2)-450) 600
900],...
              'menubar','none',...
              'name','Analysis Parameters',...
              'numbertitle','off',...
              'resize','off');
```

```
uipanel('Title','Tip Parameters','Position',[0.1 0.8 0.8 0.18], 'FontSize', 12);
uipanel('Title','Analysis Parameters','Position',[0.1 0.58 0.8 0.2], 'FontSize',
12);
eg_fc_panel=uipanel('Position',[0.1 0.31 0.8 0.25], 'FontSize', 12);
uipanel('Title','Any additional text to add','Position',[0.1 0.14 0.8 0.15],
'FontSize', 12);
S.deflection_sensitivity = uicontrol('style','edit','units','pix','FontSize',
9,'position',[210 792 180 30],'string','Deflection Sensitivity');
S.spring_constant = uicontrol('style','edit','units','pix','FontSize',
9,'position',[210 742 180 30],'string','Spring Constant');
S.minimum_force_parameter = uicontrol('style','edit', 'units','pix','FontSize',
9,'position',[210 640 180 30],'string','Minimum force');
S.minimum_seperation_distance = uicontrol('style','edit', 'units','pix',
'FontSize', 9, 'position',[210 590 180 30], 'string','Minimum seperation
distance');
S.maximum_seperation_distance = uicontrol('style','edit','units','pix','FontSize',
9,'position', [210 540 180 30], 'string','Maximum seperation distance');
uicontrol('style', 'text', 'units', 'pix', 'position', [90 830 120 20], 'string',
'First Filename:', 'FontSize', 9);
uicontrol('style', 'text', 'units', 'pix', 'position', [210 829 180 30], 'string',
first_file_name, 'FontSize', 7, 'FontWeight', 'bold');
uicontrol('style', 'text', 'units', 'pix', 'position', [90 795 120 20], 'string',
'Deflection Sensitivity:', 'FontSize', 9);
uicontrol('style', 'text', 'units', 'pix', 'position', [90 745 120 20], 'string',
'Spring Constant:', 'FontSize', 9);
uicontrol('style', 'text', 'units', 'pix', 'position', [90 643 120 20], 'string',
'Minimum force: ', 'FontSize', 9);
uicontrol('style', 'text', 'units', 'pix', 'position', [90 592 120 30], 'string',
'Minimum Seperation Distance:', 'FontSize', 9);
uicontrol('style', 'text', 'units', 'pix', 'position', [90 542 120 30], 'string',
'Maximum Seperation Distance:', 'FontSize', 9);
uicontrol('style', 'text', 'units', 'pix', 'position', [200 215 200 15], 'string',
'Text to add into file names', 'FontSize', 9);
uicontrol('style', 'text', 'units', 'pix', 'position', [390 796 30 20], 'string',
'm/v', 'FontSize', 11);
uicontrol('style', 'text', 'units', 'pix', 'position', [392 746 30 20], 'string',
'N/m', 'FontSize', 11);
uicontrol('style', 'text', 'units', 'pix', 'position', [390 644 30 20], 'string',
'pN', 'FontSize', 11);
uicontrol('style', 'text', 'units', 'pix', 'position', [390 585 30 30], 'string',
'nm', 'FontSize', 11);
uicontrol('style', 'text', 'units', 'pix', 'position', [390 535 30 30], 'string',
'nm', 'FontSize', 11);
uicontrol('style', 'text', 'units', 'pix', 'position', [390 437 65 42], 'string',
'Maximum Seperation Distance', 'FontSize', 8, 'BackgroundColor',[1 1 1],
'ForegroundColor', 'r');
uicontrol('style', 'text', 'units', 'pix', 'position', [168 437 65 42], 'string',
'Minimum Seperation Distance', 'FontSize', 8, 'BackgroundColor',[1 1 1],
'ForegroundColor', 'b');
uicontrol('style', 'text', 'units', 'pix', 'position', [128 365 45 40], 'string',
'Minimum Force', 'FontSize', 8, 'BackgroundColor',[1 1 1], 'ForegroundColor', 'm');
uicontrol('style', 'text', 'units', 'pix', 'position', [260 326 100 15], 'string',
'Searching Region', 'FontSize', 8, 'BackgroundColor',[1 1 1, 0], 'ForegroundColor',
[1 0.4 0.0]);
```

```
S.text_to_add = uicontrol('style','edit','units','pix','FontSize',
9,'position',[125 175 350 30],'string','Text to add');
S.pb = uicontrol('style','pushbutton','units','pix','FontSize', 10,'position',[210
50 180 30],'string','Continue','callback',{@pb_call});
eg_fc=[120,105,91,78,66,55,45,36,28,21,15,10,6,3,1,0,0,0,0,0,0,0,0,0,0,0,0,0,0,0,0,
-1,-3,-6,-10,-15,-21,-28,-36,-45,-55,-66,-78,-91,-105,-120,-136,-153,-171,-190,-
210,0,0,0,0,0,0,0,0,0,0,0,0,0,0,0,0,0,0,0,0,0,0,0,0,0,0,0,0,0,0,0,0,0,0,0,0,0,0
,0,0,0,0,0,0,0,0,0];
eg_fc_1_y=[150,-250];
eg_fc_2_x=[20,20];
eg_fc_3_x=[80,80];
eg_fc_4_x=[1,100];
eg_fc_4_y=[-90, -90];
ax=axes(eg_fc_panel);
plot(ax, eg_fc, 'k', 'LineWidth', 3);
hold on;
plot(ax, eg_fc_2_x, eg_fc_1_y, 'b', 'LineWidth', 3);
hold on;
plot(ax, eg_fc_3_x, eg_fc_1_y, 'r', 'LineWidth', 3);
hold on;
plot(ax, eg_fc_4_x, eg_fc_4_y, 'm', 'LineWidth', 3);
hold on;
rectangle('Position',[20 -300 60 210], 'FaceColor', [1 0.4 0.0 0.25], 'LineStyle',
'none');
hold on;
xlabel('Seperation Distance (nm)');
ylabel('Force (pN)');
uicontrol(S.deflection_sensitivity)  % Make the editbox active.
uiwait(S.fh)  % Prevent all other processes from starting until closed.
    function [] = pb_call(varargin)
    % Callback for the pushbutton.
        deflection_sensitivity =
str2double(get(S.deflection_sensitivity,'string'));
        spring_constant = str2double(get(S.spring_constant,'string'));
        minimum_force_parameter =
str2double(get(S.minimum_force_parameter,'string'));
        minimum_seperation_distance =
str2double(get(S.minimum_seperation_distance,'string'));
        maximum_seperation_distance =
str2double(get(S.maximum_seperation_distance,'string'));
        text_to_add = get(S.text_to_add,'string');
        close(S.fh);
    end
end

function close_figure_down(~,~, figure_size)
    close_down_prompt=figure('Name','Close window','NumberTitle','off', 'Position',
[(figure_size(3)/2)-200 (figure_size(4)/2)-100 400 200], 'resize','off');
    set(close_down_prompt, 'MenuBar', 'none');
    set(close_down_prompt, 'ToolBar', 'none');
    uicontrol('Parent',close_down_prompt,'Style','pushbutton','Callback',
@quitting_analysis, 'String','Close','Units','normalized','Position',[0.4 0.3 0.2
0.2],'Visible','on', 'FontWeight', 'bold');
    uicontrol('style', 'text', 'units', 'pix', 'position', [50 160 300 30],
'string', 'Are you sure you want to quit?', 'FontSize', 9, 'FontWeight', 'bold');
```

```
end

function quitting_analysis(~,~)
    close all;
    disp('=========================================');
    disp('              Analysis Quit');
    disp('=========================================');
    disp('      Please use Ctrl + C to end code');
    disp('=========================================');
end

function txt = cursor_custom(~,event_obj)
% Customizes text of data tips
pos = get(event_obj,'Position');
txt = {['Peizo movement: ',num2str(round(pos(1)*10)/10), ' nm'],...
              ['Force: ',num2str(round(abs(pos(2)))), ' pN']};
end

function change_approach_visibility(varargin)
% Callback for pushbutton.
approach_plot_for_visibility=varargin{3};
switch get(approach_plot_for_visibility,'visible')
    case 'on'     % The text is visible, make it invisible.;
        set(approach_plot_for_visibility,'visible', 'off');
    case 'off'    % The text is invisible, make it visible.
        set(approach_plot_for_visibility,'visible', 'on');
end
end

function background_saving_parameters(Writing_info, Writing_info_counter,
current_file_probe, current_curve_number)
    Writing_info_to_save=Writing_info(1:Writing_info_counter, :);
    Current_state=[current_file_probe, current_curve_number];
    save('003_Data_backup', 'Writing_info_to_save', 'Writing_info_counter');
    save('002_Current_state', 'Current_state');
end

function answer_for_continuation = initial_asking_for_continuation(figure_size)
    close_down_prompt=figure('Name','Initial checking','NumberTitle','off',
'Position', [(figure_size(3)/2)-200 (figure_size(4)/2)-100 400 200],
'resize','off');
    set(close_down_prompt, 'MenuBar', 'none');
    set(close_down_prompt, 'ToolBar', 'none');
    answer_for_continuation =
uicontrol('Parent',close_down_prompt,'Style','pushbutton','Callback',
@new_button_push, 'String','New analysis','Units','normalized','Position',[0.55 0.3
0.3 0.15],'Visible','on', 'FontWeight', 'bold');
    answer_for_continuation =
uicontrol('Parent',close_down_prompt,'Style','pushbutton','Callback',
@continuation_button_push,
'String','Continuing','Units','normalized','Position',[0.15 0.3 0.3
0.15],'Visible','on', 'FontWeight', 'bold');
    uicontrol('style', 'text', 'units', 'pix', 'position', [50 130 300 30],
'string', 'Are you continuing from previous analysis, or starting a new analysis?',
'FontSize', 9, 'FontWeight', 'bold');
```

```
    function new_button_push(~,~)
        answer_for_continuation=1;
        uiresume()
    end
    function continuation_button_push(~,~)
        answer_for_continuation=0;
        uiresume()
    end
    uiwait;
    close all;
end

function file_locations_name = files_location_choice(file_locations_name,
figure_size)
    d = dialog('Position',[(figure_size(3)/2)-200 (figure_size(4)/2)-100 400
200],'Name','Location choice', 'resize','off');
    uicontrol('Parent',d,...
           'Style','text',...
           'Units','normalized',...
           'Position',[0.3 0.7 0.4 0.2],...
           'String', 'Where are you doing the analysis?');

    uicontrol('Parent',d,...
           'Style','popup',...
           'Units','normalized',...
           'Position',[0.3 0.4 0.4 0.2],...
           'String',{'Home', 'Work', 'Laptop'},...
           'Callback',@popup_callback);

    uicontrol('Parent',d,...
           'Units','normalized',...
           'Position',[0.3 0.1 0.4 0.2],...
           'String','Select',...
           'Callback','delete(gcf)');

    choice = 'Home';

    % Wait for d to close before running to completion
    uiwait(d);

       function popup_callback(popup,~)
          idx = popup.Value;
          popup_items = popup.String;
          choice = char(popup_items(idx));
       end
   resulting_location=choice;
   if strcmp(resulting_location,'Work') == 1
        changed_string='C:\Users\Guy Ewart Mayneord\Google Drive\Locally stored
files for analysis (TEMP)';
    elseif strcmp(resulting_location,'Home') == 1
        changed_string='D:\GoogleDrive\Locally stored files for analysis (TEMP)';
    elseif strcmp(resulting_location,'Laptop') == 1
        changed_string='C:\Users\Guy Ewart Mayneord\Google Drive\Locally stored
files for analysis (TEMP)';
    end
```

```
    extracted_data=file_locations_name((strfind(file_locations_name, 'Files
location')-1):end);
    file_locations_name=strcat(changed_string, extracted_data);
end
```

8.2 MATLAB script for obtaining peak heights and counting particles on surface

```
%Simply give it the folder with the corrected spm files (please flatten in
%nanoscope)
% It will output a csv file with the results in that folder

%Set this to change the bottom limit
%=========================================================================%
bottom_limit=2.5;
%=========================================================================%
import NSMatlabUtilities.*

NSMU=NSMatlabUtilities();

% Allows the user to give the directory where the spm files are located
file_locations_name = uigetdir();
%Find all the spm files in the given folder
found_AFM_files = dir(fullfile(file_locations_name, '*.spm'));

local_maxima_collected=cell(10000,2);
maxima_counter=0;

image_size_info=cell(0);

for i = 1:length(found_AFM_files)
    file_directory_root=strcat(file_locations_name, '\', found_AFM_files(i).name);
    %Open each spm file.
    NSMU.Open(file_directory_root);
    %Open up height data
    [z_info_data, scale_units, type_desc] = NSMU.GetImageData(1, NSMU.METRIC);
    scan_size_text=string(NSMU.GetScanSizeLabel());
    scan_size_text=split(scan_size_text, [":","("]);
    scan_size_text=str2double(scan_size_text(2));
    %Find regions below the bottom threshold and convert to 0 to stop noise
    %in data.
    bottom_threshold=find(z_info_data < bottom_limit);
    z_info_data(bottom_threshold)=0;
    scan_size=NSMU.GetScanSizeLabel();
    NSMU.Close();
    %Scan size given as a sting, remove unwanted bits.
    scan_size=split(scan_size, ': ');
    scan_size=split(scan_size{2}, '(');
    units_val=split(scan_size{2}, ')');
    units_val=units_val{1};
    scan_size=str2double(scan_size{1});
    if units_val== 'µm'
        scan_size=scan_size*1000;
    end
    [x,y] = meshgrid(linspace(0,scan_size_text,(length(z_info_data))));
    ix = find(imregionalmax(z_info_data));

    new_maxima_counted=maxima_counter+(length(ix));
    local_maxima_collected(maxima_counter+1:new_maxima_counted,
1)=num2cell(z_info_data(ix));
```

```
    local_maxima_collected(maxima_counter+1:new_maxima_counted,
2)={found_AFM_files(i).name};
    image_size_info(end+1)={{found_AFM_files(i).name, scan_size, length(ix)}};
    maxima_counter=new_maxima_counted;
end


local_maxima_collected=local_maxima_collected(1:maxima_counter, :);


%Convert this back to string as otherwise the string comparison doesnt work
%and thus we never write

file_name_for_sorting=local_maxima_collected{1,2};
file_name_for_sorting=strsplit(file_name_for_sorting, '.');
file_name_for_sorting=file_name_for_sorting{1};
current_file_name=file_name_for_sorting;

total_output_list=cell(1,1);

current_output_list=cell(1,1);
current_output_list(end+1)={current_file_name};


for counting_number = drange(1:maxima_counter)
    file_name_for_sorting=local_maxima_collected{counting_number,2};
    file_name_for_sorting=strsplit(file_name_for_sorting, '.');
    file_name_for_sorting=file_name_for_sorting{1};
    %If theyre the same
    comparison = strcmp(current_file_name,file_name_for_sorting);
    if comparison == 1
        current_output_list(end+1)={local_maxima_collected{counting_number,1}};
    end
    %But if weve found a new file name, so need to set it up, AND write the
    %first value, which has triggered this recognition.
    if comparison == 0
        %change to new value
        current_file_name=file_name_for_sorting;

total_output_list{end+1}=current_output_list(2:(length(current_output_list)));
        current_output_list=cell(1,1);
        current_output_list(end+1)={current_file_name};
    end
end
total_output_list{end+1}=current_output_list(2:(length(current_output_list)));


new_directory=strcat(file_locations_name, '\Heights calculated per condition');
mkdir(new_directory);


for i = 2:length(total_output_list)
    current_name=string(total_output_list{i}{1});
    output_location=strcat(new_directory, '\', current_name, '.csv');
    fid=fopen(output_location,'w');
```

```
    file_name_for_sorting=local_maxima_collected{1,2};
    file_name_for_sorting=strsplit(file_name_for_sorting, '.');
    file_name_for_sorting=file_name_for_sorting{1};

    fprintf(fid,['Peak heights from MATLAB program' '\n']);
    fprintf(fid,['\n']);
    fprintf(fid,['\n']);
    fprintf(fid,['\n']);
    fprintf(fid,[file_name_for_sorting '\n']);
    fprintf(fid,['\n']);
    fprintf(fid,['Height (nm),' '\n']);
    for j = 2:length(total_output_list{i})
        fprintf(fid, [num2str(total_output_list{i}{j}) ', \n']);
    end

    fprintf(fid,['End']);
    fclose(fid);
end

output_location=strcat(new_directory, '\Peaks counted.csv');
fid=fopen(output_location,'w');
fprintf(fid,['Peaks counted in MATLAB program' '\n']);
fprintf(fid,['\n']);
fprintf(fid,['\n']);
fprintf(fid,['\n']);
fprintf(fid,['Image source,' 'Peaks counted,' 'Scan Size,' 'Peaks per 1um^2,'
'\n']);

for i = 1:length(image_size_info)
    file_name=image_size_info{i}{1};
    scan_size=image_size_info{i}{2};
    number_of_peaks=image_size_info{i}{3};
    peaks_per_um=(1000000/(scan_size^2))*number_of_peaks;
    fprintf(fid,[file_name ',' num2str(number_of_peaks) ',' num2str(scan_size) ','
num2str(peaks_per_um) '\n']);
end
fprintf(fid,['End']);
fclose(fid);


disp('=====================================');
disp('              Finished!');
disp('=====================================');
```

8.3 MATLAB script for overlaying extracted adhesion locations on topology

```
%Makes a mesh with an overlaid image.
%Select the AFM file to extract the height data from
[file_locations_name, AFM_file_folder] = uigetfile({'*.pfc'; '*.spm';'*.*'},'Select
the AFM file');
AFM_file_for_image=strcat(AFM_file_folder, file_locations_name);
%Select the .mat data backup generated at the end of an analysis run of the
%main SMFS script.
[mat_file, adhesion_locations_folder] = uigetfile('*.mat', 'Select the .mat file');
Adhesion_locations=strcat(adhesion_locations_folder, mat_file);
load(Adhesion_locations);

total_list={};
names_list={};
previous_name=Writing_info{1,1};
names_list{end+1}=Writing_info{1,2};
locations_temp_list=cell(0,2);

%Sort out all the AFM file names analysed in this run.
for i = 1:length(Writing_info)
    current_name=Writing_info{i,1};
    %if it matches
    if strcmp(current_name, previous_name) == 1
        locations_temp_list(end+1, :)={(Writing_info{i, 6}), (Writing_info{i, 7})};
    %New one found
    elseif strcmp(current_name, previous_name) == 0
        total_list{end+1}=locations_temp_list;
        locations_temp_list=cell(0,2);
        names_list{end+1}=Writing_info{i,2};
        previous_name=current_name;
    end
end

total_list{end+1}=locations_temp_list;
names_list=reshape(names_list, length(names_list), 1);
File_choice=choosedialog (names_list);

chosen_file=names_list{File_choice};
chosen_data=total_list{1, File_choice};
x_data_to_plot=str2double(chosen_data(:,1));
y_data_to_plot=str2double(chosen_data(:,2));
scatter(x_data_to_plot, y_data_to_plot, 50, 'r', 'filled');
xlim([0 128])
ylim([0 128])
set(gcf,'position',[10,10,1000,1000])
set(gca,'xtick',[],'ytick',[])
box on
set(gca,'Color','cyan')
set(gca, 'Position', [0,0,1,1])
graphy=gcf;
graphy.InvertHardcopy = 'off';
saveas(gcf, 'Temp_image_for_overlay.png');
close(graphy);
```

```
import NSMatlabUtilities.*
NSMU=NSMatlabUtilities();
NSMU.Open(AFM_file_for_image);
afm_file_extension=split(AFM_file_for_image, '.');
afm_file_extension=afm_file_extension{end};
if strcmp(afm_file_extension, 'pfc') == 1
    [z_info_data, scale_units, type_desc] =
NSMU.GetPeakForceCaptureImageData(NSMU.METRIC);
elseif strcmp(afm_file_extension, 'spm') == 1
    [z_info_data, scale_units, type_desc] = NSMU.GetImageData(1, NSMU.METRIC);
end
NSMU.Close()
figure('units','normalized','outerposition',[0 0 1 1]);
output=surf(z_info_data);
%=======================================
zlim([-10 90]);
%^^^Vary this to vary the topology height.
%=======================================
im1=imread('Temp_image_for_overlay.png');
output.EdgeColor= 'none';
axis off
set(output, 'CData', im1, 'FaceColor', 'texturemap', 'FaceAlpha', 1);
material dull
light
axis vis3d
view(-200,30);
lightangle(-60,30)
output.FaceLighting = 'gouraud';
output.AmbientStrength = 0.2;
output.DiffuseStrength = 0.5;
output.SpecularExponent = 25;
output.BackFaceLighting = 'unlit';

delete('Temp_image_for_overlay.png');


function choice = choosedialog (names_list)

    d = dialog('Position',[800 500 600 150],'Name','Image selection');
    txt = uicontrol('Parent',d,...
           'Style','text',...
           'Position',[175 80 250 40],...
           'String','Select a the file used');

    popup = uicontrol('Parent',d,...
           'Style','popup',...
           'Position',[50 70 500 25],...
           'String',names_list,...
           'Callback',@popup_callback);

    btn = uicontrol('Parent',d,...
           'Position',[250 20 100 25],...
           'String','Select',...
           'Callback','delete(gcf)');
```

```
    choice = 1;

    % Wait for d to close before running to completion
    uiwait(d);

       function popup_callback(popup,event)
          idx = popup.Value;
          popup_items = popup.String;
          choice= idx;
       end
end
```